Engineering the Flow of Energy and Charge Carriers in Hybrid Plasmonic Systems and Catalysts

by

Steven Anthony Chavez

A dissertation submitted in partial fulfillment
of the requirements for the degree of
Doctor of Philosophy
(Chemical Engineering)
in the University of Michigan
2022

Doctoral Committee:

Professor Suljo Linic, Chair
Assistant Professor Xiwen Gong
Assistant Professor Somin Lee
Assistant Professor Andrej Lenert

Steven A. Chavez

stchavez@umich.edu

ORCID iD: 0000-0001-8469-625X

Dedication

This dissertation is dedicated to my mother, Teresa Echevarria, whose tremendous sacrifices have allowed me to accomplish all of my goals, and to my sister, Elizabeth Chavez, for whom I have always strived to be a role model. Thank you both for your invaluable support over the years.

I also dedicate this dissertation to all Latinos and Latinas pursuing graduate degrees in STEM. Work hard, take risks and develop the talents you need to succeed in the world. I hope this accomplishment helps pave the way forward for you all.

Acknowledgements

The opportunity to compose this dissertation directly results from over 11 years of discipline, resilience, and passion. As a first-generation, low-income student, my initial objective for my academic career never involved becoming a professional scientist. If you asked me how I ended up pursuing a doctoral degree at the beginning of my graduate studies, I would say it was only through a series of coincidences. I now recognize that my innate thirst for knowledge served as the driving force for this trajectory that I could have only navigated with the help of well-intentioned individuals. None of this would be possible without the programs and people that helped me excel throughout the years. Their guidance and support have positioned me to obtain my doctoral degree and develop into the best possible version of myself. I am proud to say that I have become an encapsulation of their efforts, and I have continuously used what they taught me as a catalyst to drive my own journey forward. I'd like to thank everyone who made this experience unforgettable and life-changing throughout the remainder of this section.

Obtaining my Ph.D. in and of itself would not have been possible without the guidance of my doctoral adviser Prof. Suljo Linic. I can honestly say I have never met someone as dedicated to their career as Suljo. His genuine passion for rigorous, world-changing science is contagious and has been a constant motivator for me over the years. Under his guidance, I developed a sincere curiosity for fundamental science and an understanding of how breakthroughs in basic mechanistic research could lay the groundwork for developing novel clean energy technologies. He has demonstrated his confidence in my abilities as a scientist by continuously challenging me with some of the lab's most complex projects. These projects have led me to develop knowledge related

to solar energy conversion technologies to the degree that I never thought was possible. He has continuously pushed me to challenge the boundaries of what is possible with the scientific endeavors I pursue. His critical and skeptical nature has impacted how I view my own knowledge related to the observations I make, the opinions I form, and the conclusions I draw. It is safe to say that the caliber of my Ph.D. work would not be at the level it is at without him as a mentor. Now that my journey in his group has come to an end, I am confident that I can excel in any technical environment, and for that, I am truly grateful.

I would next like to thank several UM faculty members for their time and dedication to my dissertation work over the past 6 years. First and foremost, I'd like to thank the members of my dissertation committee: Prof. Andrej Lenert, Prof. Somin Lee, Prof. Mark Barteau, and Prof. Xiwen Gong. Prof. Lenert and Prof. Lee have been a part of my committee from the beginning. Their feedback was critical when I developed the initial stages of my dissertation proposal. Specifically, Andrej has continuously pushed me from the photonics aspect of my work (as well as letting me use his integrating sphere for my absorption measurements). At the same time, Prof. Lee was vital in developing my understanding of plasmonics fundamentals through her EECS 526 course. I want to thank Prof. Barteau (now at Texas A&M) for his invaluable feedback during my preliminary examination and his adept introduction to chemical kinetics during ChE 528. Finally, I would like to thank Prof. Gong for serving as a last-minute addition to my committee. Her energy as a new professor is refreshing, and her feedback during my data meeting helped clarify some of the finer points of my work presented throughout this document. While not a part of my committee, I'd like to give a special shout out to Prof. Omolola (Lola) Eniola-Adefeso. She is the epitome of what I strive to be – a highly successful person of color who is at the top of her field and advocates

for diversity, equity, and inclusion in all aspects of her career. She has gone out of her way to advocate for me more times than I can count, and I appreciate her more than she knows.

I want to thank the staff in the Chemical Engineering (ChE) Department, the Michigan Center for Materials Characterization (MC^2), and the Lurie Nanofabrication Facility (LNF) for all their support over the years. Susan Hamlin and Kelly Raickovich from ChE deserve special thanks for being generally amazing people who do their jobs effectively (and for letting me be the ChE "grill master" for the past six years). Pilar Herrera-Fierro from the LNF also deserves special thanks for training me meticulously and always looking out for me as a fellow Latino. Its poetic that she is retiring the same year I am graduating – I wish her all the best.

I have been in the Linic Lab a long time, and the type of students that persevere through its rigor never cease to amaze me. I'll first address the group members who were present when I started: Matthew Morabito, Paul Hernley, Brittany Farrell, Timothy Van Cleve, Calvin Boerigter, Umar Aslam, Joseph Quinn, and Valentina Igenegbai. Brittany, Tim, Matt, and Calvin all served as great resources for my initial development in the lab, and their advice was always valuable. It was also a pleasure seeing Valentina and Joe progress throughout their Ph.D. work. They are both highly talented researchers, and I am fortunate that I had the opportunity to learn from them throughout my time here.

I worked directly with Paul for my first year and a half in the group. He was instrumental in teaching me fundamental skills related to conducting research and concepts related to photonics and finite element modeling, which most of this dissertation focuses on. He is also one of the most resourceful engineers I have ever met – the man can build anything. Working with Paul was consistently enjoyable – I couldn't have asked for a better mentor to get started with. I also worked directly with Umar for a significant portion of the work presented in this dissertation. His

motivation to continuously improve himself in all aspects served as a tremendous source of energy and inspiration for me during our time together. He taught me the fundamentals of plasmonic catalysis, and within a couple of weeks, we were having high-level conversations daily. Working with him was one of the most intellectually stimulating and rewarding periods of my scientific career. I am happy to say that I became good friends with Umar and Paul outside of the lab. Our experiences together showed me that people who genuinely enjoy working together conduct the best science.

I would also like to acknowledge the members of the Linic Lab who joined after me: John Hemmerling, Sean Dix, Jacques Esterhuizen, Rachel Elias, Rawan Almallahi, Yi Zhang, James Wortman, Shawn Lu, Aarti Mathur, Shiuan-Bai Ann, Han-Ting Chen, Claire Yin, Ahmet Sert, and Jianchao (Charles) Zhao. It was a privilege getting to know John and Sean throughout their time in the lab. Discussions with John about photochemistry have been particularly fruitful, and Sean has been the one "affirming" me from day one. I am thankful for Jacques's support throughout my time here. I'll miss our one-on-one lunches, but I am excited to see what he comes up with for the remainder of his dissertation work. Conversations with Rawan are always delightful, and I'm sure she is making her family proud with all of her hard work. I have particular respect for James' work ethic – I'm sure he will be highly successful in the near future. My relationship with Shawn can only be described as "unique," but I greatly appreciate how close we have become in such a short amount of time. Aarti reminds me of myself when I first joined the lab – ambitious, fun, and hardworking. I know she will take her project far and will have a blast doing so. I have not interacted much with the newer lab members, but I'll leave them with some advice that I hope will serve them well throughout their time in the lab – just get the data.

Rachel gets her own paragraph because she's Rachel. We have indirectly directly worked with each other for the past 5 years. I have seen her take a project with little to no direction and turn it into a meaningful study. She is undoubtedly one of the hardest workers in the lab, and it has been a pleasure seeing her mature as a scientist. She has also been critical in helping me mature during my time in Ann Arbor. She has always been there for me when times were rough in and out of the lab. I will forever be thankful for our friendship, and I can't wait to see where her career takes her. I could not have asked for a better person to be my number one "lab buddy."

Outside of the lab, my time in graduate school was particularly spectacular due to the incredible friends I made throughout the process. Each of these individuals has always had my back whenever I needed it, and I appreciate them all to the highest degree. Thank you, Lydia Atangcho, for taking me into your friend group when I arrived in Michigan. I am glad we became best friends in the early years. Thank you, Dylan Neale, for being my first roommate and continuously being in my life despite all you've had going on. I couldn't ask for a better friend to start and finish this journey with. Thank you, Ruben Villegas, for demonstrating that hard work always pays off and serving as a role model for me during my time here. Thank you, Scott Johnson, and Victor Fuentes, for the fun times we always shared (in and out of the weight room). Thank you, Mario Gutierrez, for being unique, always showing me a good time, and helping me hold it down as the other Latino in our department. Thank you, Vyas Ramasubramani, for being that one friend who is always consistent and enjoyable to be around in any situation. I hope we continue to stay in touch on the West coast. Thank you, Tejas Navaratna, Carlos Anaya, and Phillip Vu, for always being willing to discuss science with me (regardless of the circumstances…) and for being generally incredible people. Thank you, Brandon Buchanan, for being one of the funnest and most down to earth people I know. Thank you to my current roommates, Colin Hunter and Brandon

Smith, whose unique personalities and paths in life have constantly kept me grounded outside of the lab. A special shout out to Robert (Bobby) Graham. Our similar life philosophies allowed us to connect instantly as friends, and I have greatly enjoyed growing with him as both a scientist and human being. Lastly, I'd also like to thank Valentina Guevara for making the last few months of my time in Ann Arbor particularly special.

I next want to thank all the incredible friends and mentors I had during my undergraduate studies at UC Berkeley. I would not have been able to navigate the rigor of the Berkeley undergraduate curriculum (much less make it to graduate school) without their guidance and support. Thank you, Robert Ixta, Emmanuel "Big Manny" Flores, and Ivet Ramirez, for being my emotional rocks throughout my undergraduate experience. Thank you, Diana Lizarraga and Hugo Ramirez, for continuously advocating for me, mentoring me in life, and ensuring I took advantage of as many opportunities as possible. Thank you, Dr. Ian Sharp (now a professor at TU Munich), for mentoring me during my time at Lawrence Berkeley Lab and being an overall spectacular human being.

I next want to acknowledge my friends from my hometown (Riverside, California) who have followed my academic journey for the past 11 years. Thank you to the guys: Eddie Hernandez, Luis Vital, Arturo Murillo, Eric Murillo, Jesus Munguia, and Erick Arguello for keeping in touch and always cheering me on. Thank you, Christian Alcaraz, who was my best friend during my brief stint at UC Riverside and continuously pushed me to live up to my full potential. Special shout out to my chemistry and calculus teachers from Ramona High School, Marc and Kelly Silva. I want to give Kelly a special thanks – if it wasn't for you, I wouldn't have made it to college in the first place. Thank you for recognizing my potential, giving me an avenue

to express my passion for science, and pushing me to pursue that passion to the highest degree. You changed my life.

I would like to thank my family for their continued support over the years. My dad has not been in my life much, but he keeps in contact and continuously wishes me success. I hope this accomplishment will make him proud. Thanks to my sister Elizabeth for always cheering me on and helping take care of my mom throughout the time I've been away. I have always strived to be a role model for her. Elizabeth, I know you are still in the process of figuring out your path in life, but just know that I'll always be here for you.

Last but not least, I'd like to thank my mother, Teresa Echevarria. Being a single mother is never easy. She demonstrates her immense love for my sister and I through the unquantifiable number of sacrifices she makes to promote our health, success, and well-being. Now that I am older, I can see precisely how significant those sacrifices are and their effect on her life. While I wish there could have been a better way, I acknowledge that I would not be in this position without each one of those sacrifices. Completing this dissertation and acquiring my doctoral degree will be my first step in paying her back for everything she's done for me. Thanks for everything, mom. I love you.

Table of Contents

List of Tables

List of Figures

List of Supplementary Figures

Abstract

The emission of greenhouse gases due to the combustion of fossil fuels (i.e., coal, oil, and natural gas) is unanimously recognized as the primary driver of climate change. One attractive option for shifting away from a fossil fuel-based economy involves utilizing the sun's energy to produce electricity and chemicals renewably. In this context, nanostructures of plasmonic metals (Ag, Au, or Cu) have emerged as a popular platform to improve and enable solar energy conversion technologies because of their ability to harvest solar energy via the creation of surface plasmons. These plasmons decay to form energetic charge carriers (i.e., electron-hole pairs) within the nanostructures that can potentially be stored as electricity or used to drive chemical reactions. In practice, these processes often require the extraction of the excited charge carrier from the plasmonic nanostructure into another material (e.g., a molecule, semiconductor, or another metal) before they lose energy. Unfortunately, the ultrafast recombination rates of charge carriers within metal nanostructures significantly limits the efficiency of this extraction process. This drawback limits the number of viable applications for plasmonic nanomaterials.

This dissertation presents a combined experimental/theoretical approach to study whether energy/charge can be extracted from plasmonic materials by interfacing them with non-plasmonic materials to form "hybrid plasmonic" nanostructures. The first part of this dissertation sheds light on the factors governing the flow of energy and charge in hybrid plasmonic nanomaterials. We demonstrate that coating plasmonic nanostructures with thin layers of non-plasmonic materials can result in localized charge carrier formation (absorption) in the non-plasmonic component. Our results suggest that the plasmonic component preferentially dissipates light energy through the

formation of charge carriers directly in the non-plasmonic component, effectively bypassing the charge recombination process. We reveal that two primary factors govern the energy transfer process: (1) the intensity of the electric field generated by the plasmonic nanostructure and (2) the availability of direct electronic excitations in the non-plasmonic material. We use these results to develop a unifying physical framework leading to molecular control of charge carrier generation in all hybrid plasmonic systems.

The second part of this dissertation investigates how the efficiency of this energy/charge localization process is affected in the limit of strong light-matter coupling. The strong coupling of optical absorbers (e.g., molecules or semiconductors) to plasmonic nanostructures fundamentally alters the physical properties of the coupled system via the formation of hybrid light-matter states. Our results show that the light absorption efficiencies in strongly coupled absorbers surpass those weakly coupled. These efficiencies are highest in configurations where the strongly coupled molecules interact directly with the incoming photon flux. We use these results to propose design principles for engineering nanostructured systems that allow for high efficiencies of charge carrier localization into strongly coupled absorbers. We also show that the strong coupling of molecular absorbers to optical cavities can improve their charge transport properties. The collective work presented in this dissertation provides a comprehensive framework for designing hybrid plasmonic materials applicable to solar energy conversion technologies related to mitigating climate change.

Chapter 1 Motivation and Significance

1.1 Summary

This chapter introduces our global demand for energy and how our society currently satisfies this demand. We discuss the consequences of our current fossil fuel-based economy and introduce the sun as a potential renewable energy source to displace fossil fuels. Finally, we outline the scope of this dissertation in the context of improving and enabling solar energy conversion technologies.

1.2 The Global Energy Challenge

Energy is a basic human need that underpins all aspects of modern-day society. We use energy to power our homes, grow/distribute our food, enable the internet, purify our water, and more. This on-demand access to energy has allowed the global population to increase by 7 billion over the past 200 years (**Figure 1.1** – red).[1] As the global population grows and our modern society becomes more technologically advanced, the demand/consumption of energy will increase accordingly (**Figure 1.1** – blue).[2] In fact, the energy information agency (EIA) projects a 50% increase in global energy demand by 2050.[3] Energy companies will therefore need to push production to increasingly larger scales to satisfy this energy demand.[4] The main challenge is ensuring that the energy demand can be satisfied while simultaneously curtailing harm to humans and the environment.

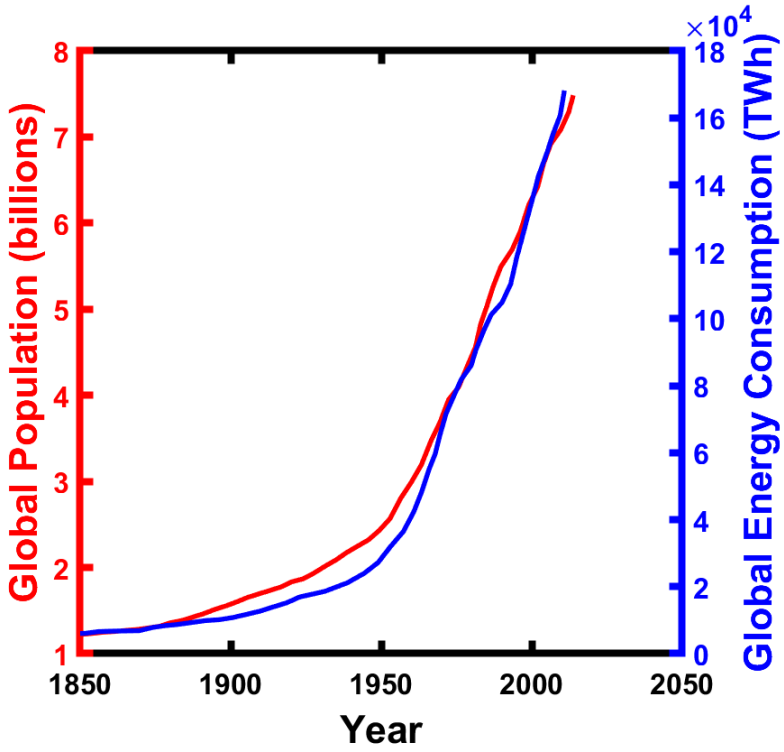

Figure 1.1 Correlation between global population and global energy consumption. The population data is from Ref.[1], and the energy consumption data is from Ref.[5]

1.2.1 Current State of Energy Consumption

In 2020, the United States (U.S.) consumed ~93 quadrillion British thermal units of energy.[2] **Figure 1.2** shows a breakdown of this energy consumption by energy source. The data show that 79% of the U.S. energy consumption is from fossil-derived resources such as petroleum, coal, and natural gas. Nuclear power (9%) and renewables (12%) make up the remaining fraction. On the global scale, energy consumption leans more heavily on fossil fuels due to the lack of renewable energy technologies. The dependence on fossil fuels will only increase as industrializing countries continue to develop. Consequently, scientists expect fossil fuels to remain the dominant supplier of global energy in 2050.[3]

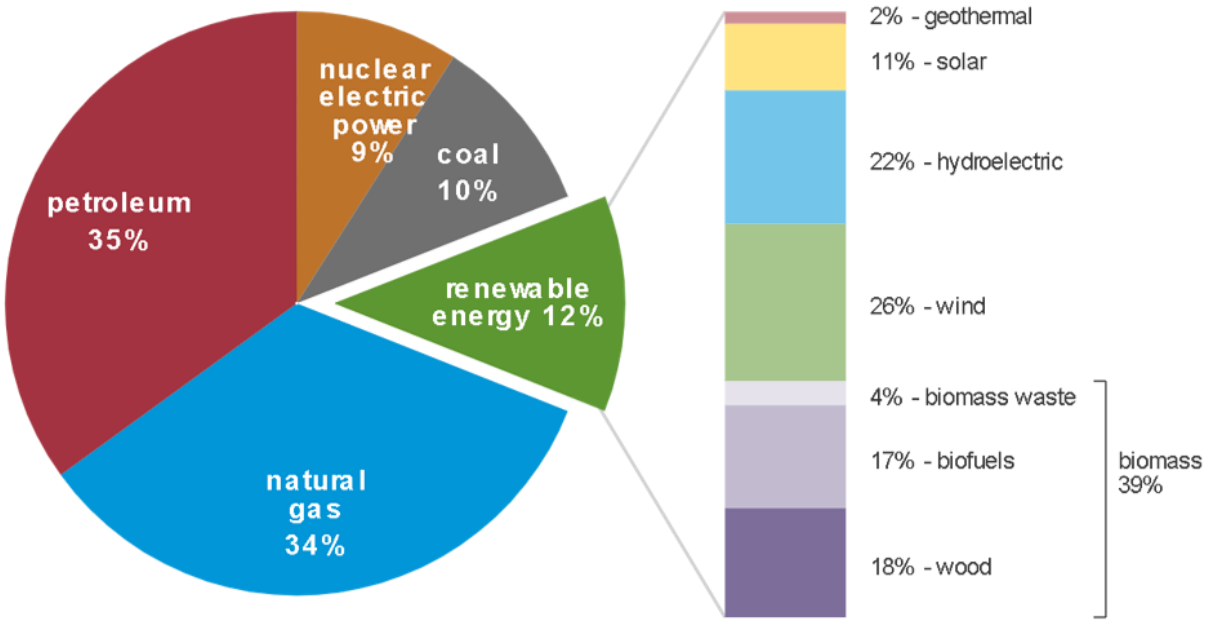

Figure 1.2 U.S. primary energy consumption by energy source in 2020. Note from reference – the sum of components may not equal 100% because of independent rounding. Adapted from Ref.[2]

1.2.2 Concerns with a Fossil Fuel-based Economy

Fossil fuels comprise a significant portion of our energy portfolio because they are readily available and energy-dense. They can be readily transported via our pipeline-based infrastructure and stored for long periods without losing their potency. These features make them one of the world's most reliable energy resources, especially with an increasing understanding of how to utilize them safely. Unfortunately, fossil fuel usage faces its own set of challenges related to sustainability.

One issue with fossil fuels is that they are not renewable resources. Fossil fuels form from the decomposition of vegetation and wildlife within the Earth over hundreds of millions of years.[6] Comparing this formation rate to the rate of fossil fuel consumption (~seconds), it is clear that we will eventually run into a supply issue. While many reports have tried to predict how long our fossil fuel reserves will last, the conclusions typically vary by several decades.[7,8] The best approach

is thus to adopt renewable energy technologies that can potentially mitigate some of the other main problems associated with fossil fuels.

The primary issue with fossil fuels is that their combustion results in the emission of greenhouse gases, mainly carbon dioxide (CO_2). For example, the combustion of fossil fuels produced approximately 84% of the total global energy in 2019 demand while simultaneously producing ~37 billion tons of CO_2.[9] The steady rise in energy demand/consumption over time has led to steadily increasing concentrations of CO_2 in the atmosphere, which has now reached over 400 ppm (**Figure 1.3**). These increasingly high levels of atmospheric CO_2 are the primary driver of various global health and environmental problems.

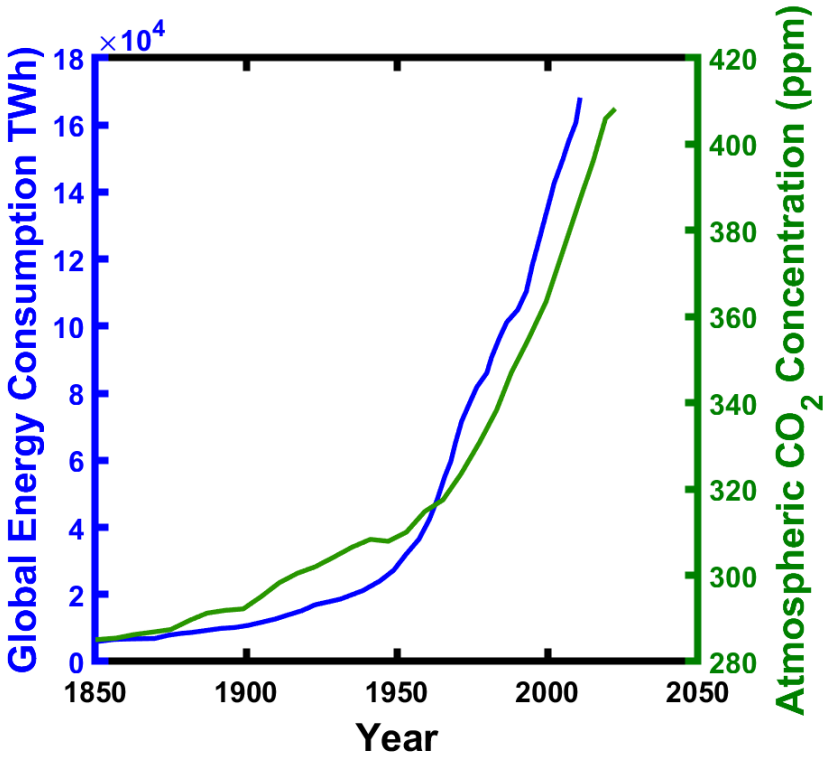

Figure 1.3 The correlation between global energy consumption and atmospheric CO_2 concentration. The energy consumption data is from Ref.[5]and the CO_2 data is from Refs.[10,11]

Numerous climate models and reports show that elevated amounts of greenhouse gases in the atmosphere increase average global temperatures.[12–14] The data in **Figure 1.4** show that the

~100 ppm increase in atmospheric CO_2 concentration over the past 100 years resulted in a ~1.5 °C change in the average global surface temperature.[14] This rise in global temperature will increase the severity/frequency of natural disasters, lead to more droughts/famines and increase the levels and acidity of the oceans.[14–17] These consequences indicate that climate change presents an existential threat to humanity and underscore the need to implement zero-emission energy technologies.

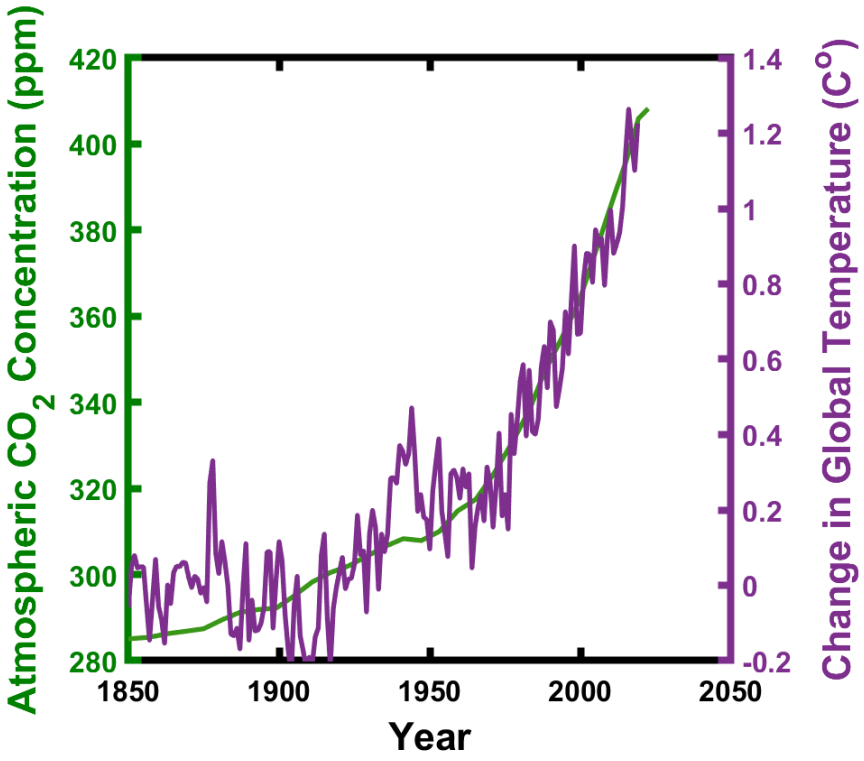

Figure 1.4 Correlation between atmospheric CO2 concentration and the change in global temperature. The CO_2 data is from Refs.[10,11], and the global temperature data is from Ref.[14]

1.3 Solar Energy as a Solution to Climate Change

One attractive option for shifting away from a fossil fuel-based economy involves utilizing the sun's energy to produce electricity and chemicals renewably. The sun delivers energy to the surface of the earth at an average rate of ~120,000 TW. This amount of solar energy is enough to

satisfy the yearly global energy demand in just one hour.[18] We can therefore view the sun as an inexhaustible energy source that can potentially power our energy planet for the foreseeable future.

1.3.1 Solar Cells for Renewable Electricity Production

Solar photovoltaics (i.e., solar cells) are currently the most common solar energy conversion technology. They work by using semiconducting materials to absorb sunlight and subsequently generate electricity. They are a relatively mature technology, and their production is projected to increase over the next several decades as they are cheaper than coal and natural gas in many world regions.[19–21] The main benefit of implementing solar cells is that they generate orders of magnitudes less pollution and CO_2 emissions compared to fossil fuels.[22,23]

Despite decades of research and development, the implementation of solar cells into our current energy infrastructure faces significant hurdles. One major challenge solar cells face is sunlight's daily and seasonal intermittency.[24] While electricity production from solar cells typically matches daily energy demand (i.e., society consumes the most energy during daylight hours), they cannot generate power at night or under weather conditions that obscure sunlight. This intermittency inherently limits the amount of energy that solar cells generate. One possible way to solve this problem is to store the generated electricity in batteries to be used on-demand. However, batteries also face cost limitations at large scales, discharge slowly over long periods, and generate large amounts of waste.[25,26]

1.3.2 Solar Fuels as a Next-generation Solar Energy Conversion Technology

Solar-to-chemical energy conversion technologies have recently been recognized as the top emerging solution to climate change because they can displace fossil fuels with "solar fuels."[27–31] The overall objective of these technologies is to use light to convert water and CO_2 into chemical

fuels and feedstocks. By storing solar energy in chemical bonds, we can generate energy sources that 1) rival the energy density of fossil fuels, 2) can be stored in high quantities for long periods as liquid/gaseous fuels, and 3) can be readily incorporated into our current pipeline-based energy infrastructure.

1.4 Scope of Dissertation

This dissertation focuses on developing photonic approaches to improve and enable solar-to-chemical and solar-to-electrical energy conversion technologies. We focus on a class of optically active materials known as plasmonic metal nanostructures. These materials can harvest the energy of visible light and subsequently use it to drive chemical reactions or improve the efficiency of solar cells.[32,33] These processes require the transfer of light energy harvested by the plasmonic nanostructure to some other non-plasmonic material that can perform a function. These non-plasmonic materials include molecules (in the case of photochemistry or sensing), semiconductors (in the case of solar cells or photodetectors), and even other metals that can potentially be more active for catalytic reactions. The primary aim of this dissertation was to elucidate the mechanism of energy transfer from photoexcited plasmonic metals to non-plasmonic materials (e.g., catalytic metals, semiconductors, molecules) to enable the design of hybrid plasmonic materials that can utilize solar energy with high efficiencies. We can compartmentalize the research presented throughout this document into three main focuses.

The first portion of this dissertation research focuses on designing bimetallic hybrid plasmonic materials for applications in plasmonic catalysis. Plasmonic catalysis has recently emerged as an attractive option for mitigating climate change because it utilizes sunlight to produce chemicals that can directly displace fossil fuels. In plasmonic catalysis, photochemical reactions are driven directly on the surface of metal nanoparticles that can harvest the energy of

visible light.[32,34–38] Despite its immense potential, the widespread application of plasmonic catalysis has been limited by the fact that light-harvesting 'plasmonic metals' such as silver (Ag), gold (Au), and copper (Cu) have low chemical reactivity compared to non-light harvesting 'catalytic metals' used in industry such platinum (Pt) and palladium (Pd). Throughout these two chapters, we study how bimetallic plasmonic nanomaterials comprised of a light-harvesting plasmonic metal and a catalytically active non-plasmonic metal can drive photochemistry. We focus on the mechanism of energy transfer between plasmonic and non-plasmonic metals, which was not extensively explored when this dissertation work began.

The second portion of this dissertation research focuses on understanding the energy transfer mechanisms in hybrid plasmonic metal-molecule and metal-semiconductor systems. Understanding energy transfer in metal-molecule systems is essential for designing photocatalytic materials that can use light to activate chemical bonds. Similarly, energy transfer in metal-semiconductor systems is important for improving the efficiency of photovoltaic devices. The main advantage of using plasmonic materials in this application is to localize light into thin semiconductor layers. Using thinner layers can decrease materials costs, which comprise a large portion of solar cell implementation capital.

The final portion of this dissertation work explores energy transfer in the strong light-matter coupling regime. Strong coupling of light absorbers to confined optical modes has shown the capability to fundamentally alter a coupled system's physical properties via the formation of hybrid light-matter states. We explore how strong light-matter coupling affects light absorption in strongly coupled hybrid plasmonic systems. We note that enhancing light absorption is critical for enabling a range of solar energy conversion technologies including photocatalysis, photodetection, and photovoltaics. The chapters of this dissertation are organized a follows:

- **Chapter 2** provides an introduction to the field of plasmonics. We focus on the physical properties of metals that allow them to localize light to the nanoscale. We also introduce the field of hybrid plasmonics and discuss its current state and associated challenges.
- **Chapter 3** provides an overview of the experimental and computational methods utilized throughout this dissertation. We introduce the synthesis/nanofabrication techniques utilized to prepare various nanomaterials throughout this dissertation. We then describe the experimental tools to characterize their physical, optical, and electrical properties. Finally, we emphasize an introduction to finite element modeling of electrodynamics since these models underpin a significant portion of the conclusions presented throughout this dissertation work.
- **Chapter 4** outlines our initial results studying energy transfer in hybrid metal-metal systems. We introduce the design of Ag-Pt core-shell nanoparticles as a platform for studying energy flow in bimetallic systems. We present the first data showing that introducing a thin layer of Pt to the surface of plasmonic Ag nanocubes biases the plasmon decay towards absorption. We end the chapter by describing our initial hypothesis into the energy transfer mechanism between a plasmonic metal and a non-plasmonic metal.
- **Chapter 5** presents a thorough investigation of the factors governing energy transfer from plasmonic metals to non-plasmonic metals. We show that excited plasmonic nanoparticles preferentially dissipate electromagnetic energy confined to their surface through direct, momentum-conserved interband transitions in non-

plasmonic metals. We generalize this conclusion by studying bimetallic metal nanoparticles of varying size, shape, and composition.

- **Chapter 6** shows how we can use Raman nanothermometry to probe how bimetallic plasmonic nanoparticles localize light energy. We show that adding a Pt layer to the surface of Ag nanocubes results in an increase photothermal response. We investigate how to optimize bimetallic plasmonic nanoparticles to achieve high light absorption rates.
- **Chapter 7** shows that we can generalize our proposed model for energy transfer to other hybrid plasmonic materials. We achieve this by studying energy transfer mechanisms in metal-semiconductor and metal-molecule systems. We show that the exact mechanisms responsible for energy transfer in bimetallic hybrid systems govern energy transfer in all hybrid plasmonic systems. We discuss how these results benefit the design of various solar energy conversion technologies.
- **Chapter 8** expands our energy transfer analysis in hybrid systems to the strong light-matter coupling regime. Specifically, we explore how plasmonic and photonic nanostructures can localize light into strongly coupled molecular absorbers. We show that optical cavities typically used in the strong coupling literature suffer from significant losses. We present design principles using other plasmonic nanostructures that can mitigate these losses.
- **Chapter 9** investigates whether photogenerated charge can be extracted from strongly coupled molecular absorbers. Electrical measurements suggest that charge transport is improved in the limit of strong light-matter coupling. Photoelectrical

measurements suggest the presence of a photogenerated current unique to the strongly coupled systems.

- **Chapter 10** summarizes the findings presented throughout this dissertation. We highlight the impact of these findings and place them in the context of current research in the field of hybrid plasmonics. We also outline opportunities for utilizing hybrid plasmonic nanomaterials in and out of the strong coupling regime to improve/enable the next generation of solar energy conversion technologies.

1.5 References

(1) World Population Growth - Our World in Data https://ourworldindata.org/world-population-growth (accessed Dec 23, 2021).

(2) U.S. energy facts explained - consumption and production - U.S. Energy Information Administration (EIA) https://www.eia.gov/energyexplained/us-energy-facts/ (accessed Dec 23, 2021).

(3) EIA projects nearly 50% increase in world energy usage by 2050, led by growth in Asia - Today in Energy - U.S. Energy Information Administration (EIA) https://www.eia.gov/todayinenergy/detail.php?id=42342 (accessed Dec 24, 2021).

(4) Chu, S.; Cui, Y.; Liu, N. *Nat. Mater. 2017 161* **2016**, *16* (1), 16–22.

(5) Energy Production and Consumption - Our World in Data https://ourworldindata.org/energy-production-consumption (accessed Dec 23, 2021).

(6) Fossil Fuels | National Geographic Society https://www.nationalgeographic.org/encyclopedia/fossil-fuels/ (accessed Dec 24, 2021).

(7) Shafiee, S.; Topal, E. *Energy Policy* **2009**, *37* (1), 181–189.

(8) 2020, B. S. R. of W. E. **2020**, *68*.

(9) Jackson, R. B.; Friedlingstein, P.; Andrew, R. M.; Canadell, J. G.; Le Quéré, C.; Peters, G. P. *Environ. Res. Lett.* **2019**, *14* (12), 121001.

(10) NASA - Global Mean CO2 Mixing Ratios (ppm) https://data.giss.nasa.gov/modelforce/ghgases/Fig1A.ext.txt (accessed Dec 23, 2021).

(11) NOAA - Keeling Curve Data https://gml.noaa.gov/webdata/ccgg/trends/co2/co2_mm_mlo.txt (accessed Dec 23, 2021).

(12) Risbey, J. S.; Lewandowsky, S.; Langlais, C.; Monselesan, D. P.; O'Kane, T. J.; Oreskes, N. *Nat. Clim. Chang. 2014 49* **2014**, *4* (9), 835–840.

(13) Hausfather, Z.; Drake, H. F.; Abbott, T.; Schmidt, G. A. *Geophys. Res. Lett.* **2020**, *47* (1), e2019GL085378.

(14) Masson-Delmotte, V.; Zhai, P.; Chen, Y.; Goldfarb, L.; Gomis, M. I.; Matthews, J. B. R.; Berger, S.; Huang, M.; Yelekçi, O.; Yu, R.; Zhou, B.; Lonnoy, E.; Maycock, T. K.; Waterfield, T.; Leitzell, K.; Caud, N. **2021**.

(15) Full Report | National Climate Assessment https://nca2014.globalchange.gov/report (accessed Dec 24, 2021).

(16) Church, J. A.; White, N. J.; Aarup, T.; Wilson, W. S.; Woodworth, P. L.; Domingues, C. M.; Hunter, J. R.; Lambeck, K. .

(17) Allemand, D.; Osborn, D. *Reg. Stud. Mar. Sci.* **2019**, *28*, 100558.

(18) Solar Energy: Frequently Asked Questions. **2020**.

(19) World Energy Outlook 2020 – Analysis - IEA https://www.iea.org/reports/world-energy-outlook-2020 (accessed Dec 25, 2021).

(20) Ray, D. L. **2018**.

(21) Energy Information Administration, U. **2021**.

(22) Kreith, F.; Norton, P.; Brown, D. *Energy* **1990**, *15* (12), 1181–1198.

(23) Sherwani, A. F.; Usmani, J. A.; Varun. *Renew. Sustain. Energy Rev.* **2010**, *14* (1), 540–544.

(24) Kannan, N.; Vakeesan, D. *Renew. Sustain. Energy Rev.* **2016**, *62* (C), 1092–1105.

(25) Castillo, A.; Gayme, D. F. *Energy Convers. Manag.* **2014**, *87*, 885–894.

(26) Rarotra, S.; Sahu, S.; Kumar, P.; Kim, K. H.; Tsang, Y. F.; Kumar, V.; Kumar, P.; Srinivasan, M.; Veksha, A.; Lisak, G. *ChemistrySelect* **2020**, *5* (20), 6182–6193.

(27) Walter, M. G.; Warren, E. L.; McKone, J. R.; Boettcher, S. W.; Mi, Q.; Santori, E. a; Lewis, N. S. *Chem. Rev.* **2010**, *110*, 6446–6473.

(28) Fabian, D. M.; Hu, S.; Singh, N.; Houle, F. A.; Hisatomi, T.; Domen, K.; Osterloh, F.; Ardo, S. *Energy Environ. Sci.* **2015**, *8* (10), 2825–2850.

(29) Montoya, J. H.; Seitz, L. C.; Chakthranont, P.; Vojvodic, A.; Jaramillo, T. F.; Nørskov, J. K. *Nat. Publ. Gr.* **2017**, *16*.

(30) Lewis, N. S.; Crabtree, G.; Nozik, A. J.; Wasielewski, M. R.; Alivisatos, P.; Kung, H.;

Tsao, J.; Chandler, E.; Walukiewicz, W.; Spitler, M.; Ellingson, R.; Overend, R.; Mazer, J.; Gress, M.; Horwitz, J.; Ashton, C.; Herndon, B.; Shapard, L.; Nault, R. M. *Basic Research Needs for Solar Energy Utilization. Report of the Basic Energy Sciences Workshop on Solar Energy Utilization, April 18-21, 2005*; 2005.

(31) Lewis, N. S. *Science* **2016**, *351* (6271).

(32) Linic, S.; Christopher, P.; Ingram, D. B. *Nat. Publ. Gr.* **2011**, *10*.

(33) Atwater, H. a; Polman, A. *Nat. Mater.* **2010**, *9* (3), 205–213.

(34) Christopher, P.; Xin, H.; Marimuthu, A.; Linic, S. *Nat. Mater.* **2012**, *11* (12), 1044–1050.

(35) Christopher, P.; Xin, H.; Linic, S. *Nat. Chem.* **2011**, *3* (6), 467.

(36) Linic, S.; Aslam, U.; Boerigter, C.; Morabito, M. *Nat. Mater.* **2015**, *14* (6), 567–576.

(37) Xiao, M.; Jiang, R.; Wang, F.; Fang, C.; Wang, J.; Yu, J. C. *J. Mater. Chem. A* **2013**, *1* (19), 5790.

(38) Kale, M. J.; Avanesian, T.; Christopher, P. *ACS Catal.* **2014**, *4* (1), 116–128.

Chapter 2 Introduction to Plasmonics

2.1 Summary

This chapter provides a brief introduction to the field of plasmonics. We begin by describing the physical properties of metals that are responsible for plasmon excitation. We focus on the dielectric function of metals and discuss how it governs the excitation of localized and propagating surface plasmons at metal/dielectric interfaces. We then introduce the metallic nanostructures utilized throughout this dissertation work, including Fabry-Perot optical cavities, plasmonic nanohole arrays, and plasmonic metal nanoparticles. We emphasize plasmonic metal nanoparticles, as these are the materials mainly studied throughout this dissertation. We highlight the excitation of localized surface plasmons unique to nanoparticles and the fundamental decay pathways affecting the plasmon lifetime. Finally, we end the chapter by discussing the current literature on using plasmonic nanomaterials to direct energy and charge into other materials.

2.2 Plasmonics Fundamentals

Plasmonics is a sub-field of nanophotonics that explores how light can be confined to sub-wavelength volumes.[1–6] It originated from mathematical predictions that electromagnetic radiation can couple to the free conduction electrons present at the interface between a metal and a dielectric.[7,8] This coupling results in the localization of light energy to the metal-dielectric interface and can thus enable applications that require the confinement of light below the diffraction limit.[9] The ability of nanostructured metals to confine light to the nanometer length scale has catapulted plasmonics to the forefront of research in microscopy, sensing, optical communications, bio-

optics, and beyond.[10,11] In this context, understanding how to engineer plasmonic nanomaterials from the physics perspective is critical in optimizing their efficiency in the applications mentioned above. Throughout the remainder of this section, we will introduce the physics governing the creation of surface plasmons in nanostructured metals.

2.2.1 The Dielectric Function

The optical behavior of metals is grounded in classical electrodynamics. A complex, frequency-dependent material property known as the complex dielectric function, ε(ω), describes a metal's response to electromagnetic radiation. We write the mathematical form of, ε(ω) in the limit of a spatially localized response as:

$$\varepsilon(\omega) = \varepsilon_1(\omega) + i\varepsilon_2(\omega) \tag{2.1}$$

where ε_1 is the real component of the dielectric function, ε_2 is the imaginary component, *i* is the complex number, and ω is the photon frequency. Generally, ε_1 describes the polarizability of a metal in response to electromagnetic radiation, and ε_2 describes the ability of a photon of a given frequency to induce an optical excitation within the metal. While we will discuss ε(ω) throughout this text in the context of metals, it is essential to note that ε(ω) describes how any material interacts with light. **Figure 2.1** shows an example of ε_1 and ε_2 as a function of frequency for various molecular processes.

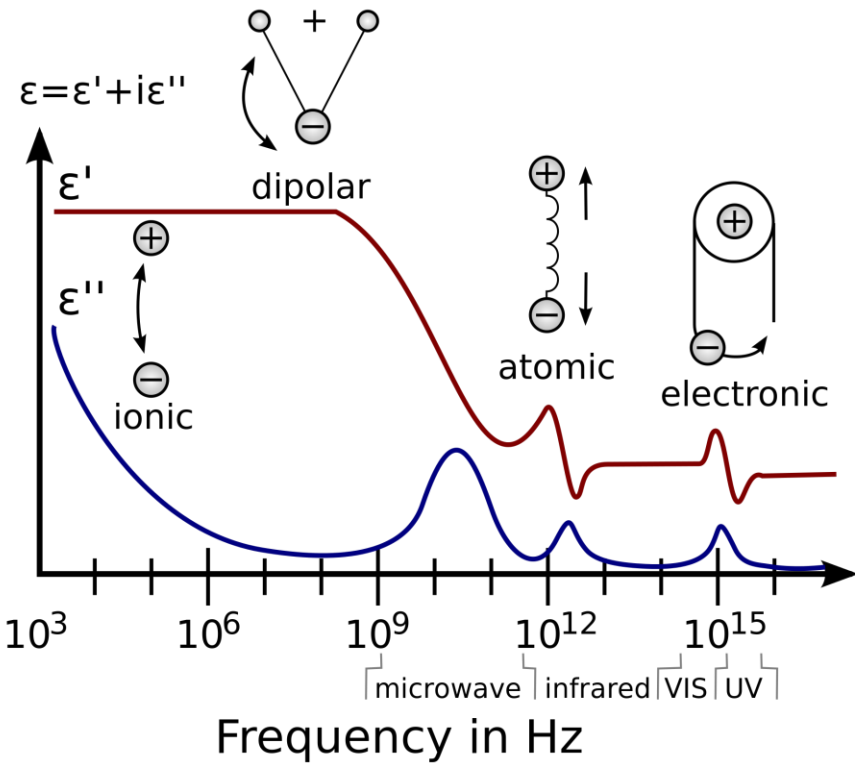

Figure 2.1 The frequency response of various dielectric mechanisms. Here, ε' and ε" represent the real and imaginary components of the dielectric function. The various processes include atomic/electronic resonances at high energies and dipolar/ionic relaxation at low energies. Adapted from Ref. [12]

One can also quantify the optical properties of a material is via the complex refractive index:

$$\tilde{n}(\omega) = n(\omega) + ik(\omega) \tag{2.2}$$

where n is the refractive index of the material and k is known as the extinction coefficient. The complex refractive index and complex dielectric function are related by the equation:

$$n(\omega) + ik(\omega) = \sqrt{\varepsilon_1(\omega) + i\varepsilon_2(\omega)} \tag{2.3}$$

This leads to the following relations:

$$\varepsilon_1 = n^2 - k^2 \tag{2.4}$$

$$\varepsilon_2 = 2nk \tag{2.5}$$

Throughout this dissertation, we will use both the complex dielectric function (Equation 2.1) and the complex refractive index (Equation 2.2) to define the optical properties of our materials. We use the relations in Equation 2.4 and Equation 2.5 to convert between them.

2.2.2 Surface Plasmon Polaritons

The materials properties introduced in the previous section govern how a material interacts with electromagnetic radiation. Knowing their physical significance, one can describe the formation of surface plasmons. Surface plasmons are delocalized electron oscillations that can arise at any interface where ε_1 changes signs across the interface. The first fundamental excitation in plasmonics is a specific type of surface plasmon known as the surface plasmon polariton (SPP). SPPs are non-localized plasmons that propagate along the interface between a dielectric (such as air) and a metal.[1] The name originates from the fact that they involve both the collective motion of charge in the metal (plasmon) and the oscillation of electromagnetic waves in the dielectric (polariton).[13]

The most straightforward geometry that can support a SPP is a metal slab interfaced with air (**Figure 2.2**). For a photon to excite an SPP along this interface, the photon and resulting SPP must have the same direction and momentum. Unfortunately, a photon from free space has less momentum than a typical SPP. This problem can be mitigated by utilizing momentum-coupling approaches such as prism or grating coupling.[14] Once an SPP is formed, it confines electromagnetic energy to the interface. This feature of SPPs makes them attractive for various applications such as SPP-based circuits[4], biosensors[15], second harmonic generation[16], and much more. We discuss SPPs in **Chapter 8** of this dissertation when discussing the coupling of plasmonic nanohole arrays to dye molecules.

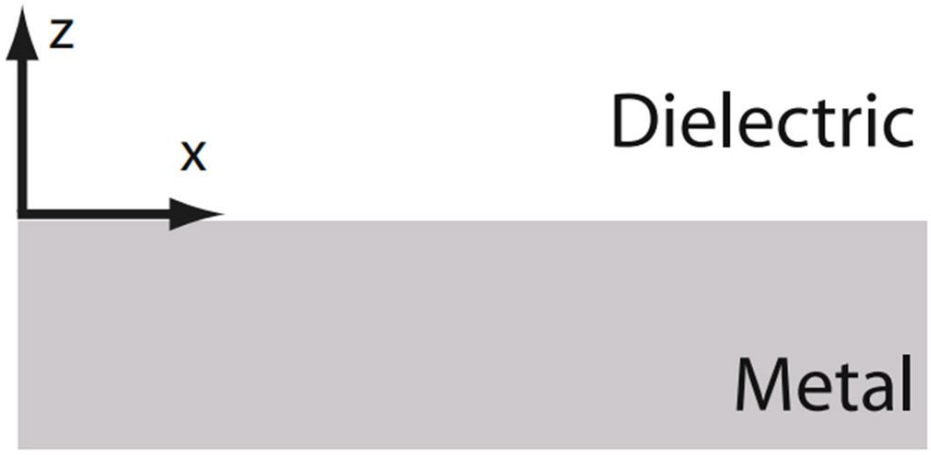

Figure 2.2 Schematic of SPP propagation along a metal/dielectric interface. An electromagnetic wave with the correct momentum constraints can couple to the interface between a metal and dielectric. The wave will propagate along this interface until it decays or reradiates. Adapted from Ref.[1]

2.2.3 Localized Surface Plasmons

The second fundamental excitation in plasmonics is a localized surface plasmon (LSP). While SPPs consist of electron oscillations propagating at a metal-dielectric interface, LSPs are non-propagating electron oscillations confined to specific locations in space. LSPs are most commonly found in metal nanoparticles with diameters much smaller than the wavelength of visible light. When the electric field of incoming light interacts with a metal nanoparticle, it induces a force on the freely-moving delocalized electron cloud of the nanoparticle. This force causes the electron cloud to shift and results in a polarization of the nanoparticle, as shown in **Figure 2.3**. As the electron cloud moves, the Coulombic attraction between the positive nuclei of the nanoparticle induces a restoring force on the electron cloud. This restoring force causes the electron cloud to oscillate. This oscillation of the electron cloud is maximized at a resonant frequency that depends on the charge distribution throughout the nanoparticle and the electron cloud density.[17] This resonant oscillation is known as localized surface plasmon resonance (LSPR). The majority of this dissertation focuses on LSPR in metal nanoparticles as opposed to

SPPs introduced in the previous section. The following section discusses the criteria for establishing LSPR in metal nanoparticles and the effects on the nanoparticle optical properties.

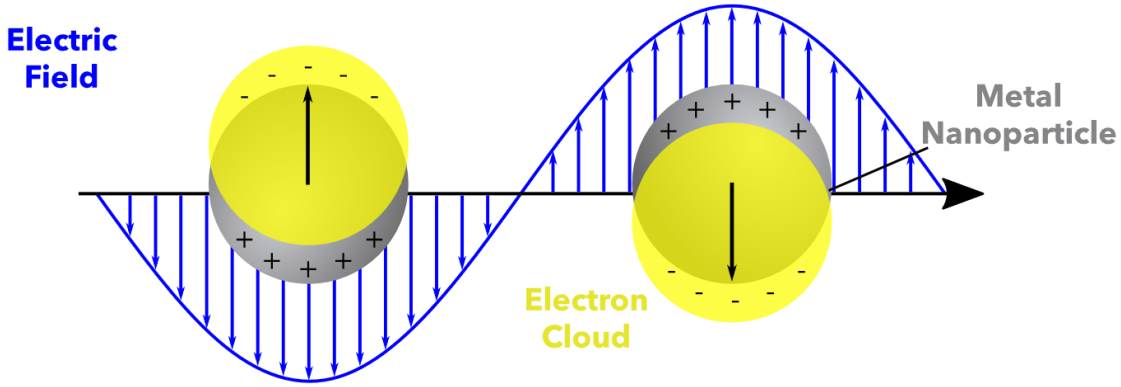

Figure 2.3 Localized surface plasmon resonance in plasmonic nanoparticles. A schematic of how incoming electromagnetic radiation can polarize a plasmonic metal nanoparticle by inducing forces of the free electron cloud. The oscillation of the electron cloud as the wave changes phase results in a localized surface plasmon excitation.

2.3 Types of Plasmonic Nanostructures

Nanostructures that confine light are ubiquitous in the field of plasmonics. This section introduces the types of metallic nanostructures utilized throughout this dissertation. We begin by describing the physical criteria for light confinement in Fabry-Perot cavities and plasmonic nanohole arrays. We then introduce the physics governing plasmon excitation and decay in plasmonic nanoparticles.

2.3.1 Fabry-Perot Optical Cavities

A Fabry-Perot optical cavity is a photonic structure formed from two parallel, highly reflecting surfaces (i.e., mirrors) spaced anywhere from nanometers to kilometers apart.[18] They are widely used in laser science and spectroscopy to measure and control light of various wavelengths. These cavities operate based on the concept of interference. Broadband light entering the cavity undergoes multiple internal reflections between the two parallel mirrors (**Figure 2.4a**). Most of the light within the cavity is lost due to destructive interference and does not escape the

cavity (i.e., transmission through the cavity at these wavelengths is zero). However, in-phase light constructively interferes and produces a sharp transmission peak in the optical transmission spectra (**Figure 2.4b**). The back and forth reflection of light within the cavity results in a standing electromagnetic wave. This phenomenon results in high electric field enhancements between the two mirrors.

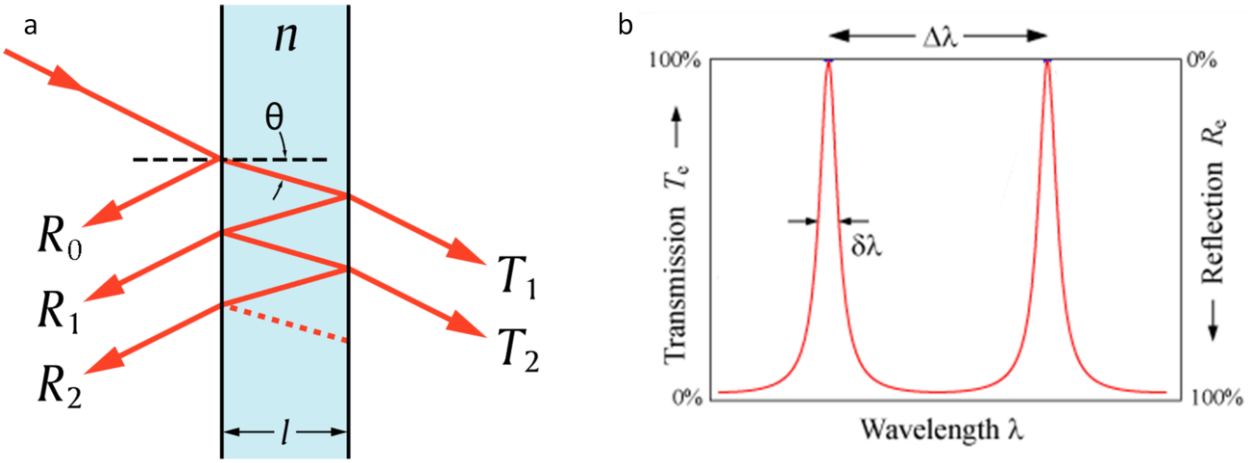

Figure 2.4 Characteristics of Fabry-Perot optical cavities. **a)** Schematic of light reflecting back and forth between two parallel mirrors in an optical cavity. **b)** Example transmission spectra for a Fabry-Perot optical cavity. Adapted from Ref. [19]

We can calculate the wavelength of maximum transmission (λ) from a Fabry-Perot cavity with the following equation:

$$2lcos\theta = m\lambda \tag{2.6}$$

where l is the length of the cavity (i.e., the spacing between the two mirrors), θ is the angle of incidence between the mirror/incoming photon, and m is an integer. At normal incidence, it is clear from equation 2.6 that increasing the distance between the two mirrors increases the wavelength of the photon (and thus the electric field) that the cavity confines. In **Chapter 8** and **Chapter 9** of this dissertation, we take advantage of this fact when we tune this wavelength to match up with molecular resonances to induce strong light-matter coupling.

2.3.2 Plasmonic Nanohole Arrays

Plasmonic nanohole arrays are a type of plasmonic nanostructure consisting of periodic arrays of holes milled into opaque metal films. These arrays provide the momentum necessary to couple light into the metal film, resulting in the formation of SPP modes on the surface of the hole array.[20] The coupling of light to form SPP modes leads to extraordinary optical transmission through the sub-wavelength holes at specific frequencies.[20,21] At these wavelengths, the hole array acts to confine electromagnetic energy to the surface of the array in the form of elevated fields. The following equation approximates the condition for these transmission wavelengths (λ_T) for a 2-dimensional hole array milled into a metal film [22]:

$$\lambda_T = \frac{P}{C}\sqrt{\frac{\varepsilon_m \varepsilon_d}{\varepsilon_m + \varepsilon_d}} \tag{2.7}$$

Here, P is the period of the array, ε_m is the metal's dielectric function, and ε_d is the dielectric function of the material in contact with the array. C is an indexing factor given by $(i^2+j^2)^{0.5}$ for a square array and by $(i^2+ij+j^2)^{0.5}$ for a hexagonal array. Equation 2.7 shows that the SPP mode of the array is easily tuned by adjusting the period of the array. We take advantage of this in Chapter 8 when we couple molecular resonances to plasmonic hole arrays. **Figure 2.5** shows an example of a hole array and its enhanced transmission.

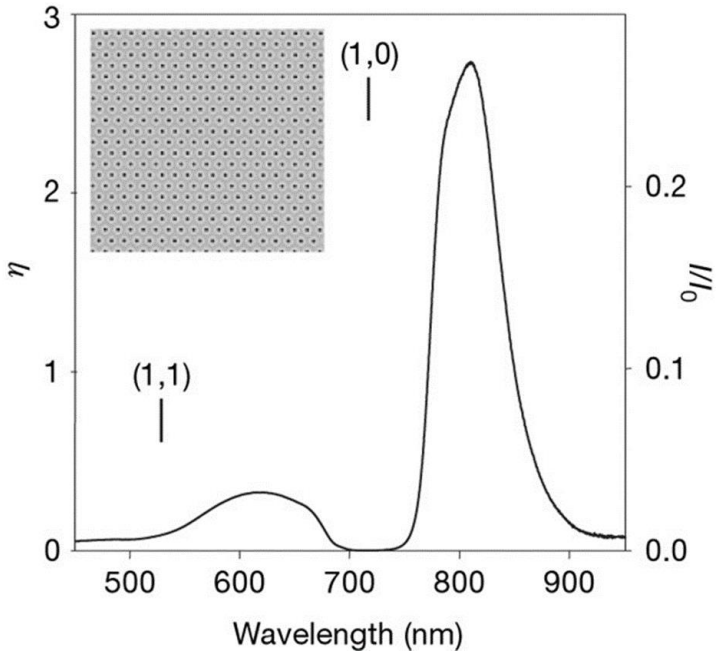

Figure 2.5 Characteristics of plasmonic nanohole arrays. An example transmission spectra for a triangular hole array milled into a 225-nm-thick Au film supported on a glass substrate. The transmission spectrum was measured using collimated white light and illuminated at normal incidence. The absolute transmission is plotted on the left axis, and the transmission normalized to the hole area is plotted on the right. Inset – an image of the hole array. Adapted from Ref.[20]

2.3.3 Plasmonic Metal Nanoparticles

Nanoparticles of plasmonic metals (e.g., Ag, Au, Cu, and Al) have emerged as an important class of optically active materials because of their ability to support LSPs via the excitation of LSPR.[23–25] As described above, the excitation of LSPR allows plasmonic metal nanoparticles to confine the energy of visible light to the nanoscale. This feature has made them a critical research topic in various fields such as photocatalysis[26–28], surface-enhanced Raman spectroscopy[29–31], photovolatics[32,33], photothermal heating[34–37], biosensing[38,39], and many others. This section presents a detailed introduction to the fundamental physics of plasmonic metal nanoparticles. These are the nanomaterials utilized throughout the majority of this dissertation.

We begin by describing the criteria for establishing LSPR in metal nanoparticles. One of the critical features of LSPR in metal nanoparticles is their extremely high optical extinction cross-

section (σ_{ext}). Generally, σ_{ext} quantifies a nanoparticle's ability to interact with light and can be up to tens of times larger than the nanoparticle's geometric cross-section at the LSPR frequency.[40] In the case of a spherical nanoparticle, Mie theory can show that σ_{ext} is related to the metal's complex dielectric function via Equation 2.8:

$$\sigma_{ext} \sim \frac{\varepsilon_2}{[\varepsilon_1 + 2\varepsilon_m]^2 + {\varepsilon_2}^2} \tag{2.8}$$

where ε_m is the dielectric constant of the surrounding medium.[41] According to this equation, σ_{ext} is largest when the denominator approaches zero. This observation helps us identify the requirements for establishing LSPR in metal nanoparticles. The denominator approaches zero when ε_2 is small and when $\varepsilon_1 = -2\ \varepsilon_m$. **Figure 2.6** shows the values of ε_1 and ε_2 as a function of wavelength for some common transition metals. The data show that while Ag, Au, Cu, and Ni have $\varepsilon_1 \approx -2\ \varepsilon_m$ in the visible wavelength range (i.e., between 400 nm and 700 nm), only Ag, Au, and Cu have low ε_2 in that same wavelength range. These features suggest that it is easiest to induce LSPR with visible light in Ag, Au, and Cu nanoparticles, explaining why these metals are typically considered "plasmonic" metals. **Figure 2.7a** shows the experimentally measured and theoretically calculated values of σ_{ext} for Au and Ag nanospheres. The sharp peaks in σ_{ext} are indicative of large LSPR at that wavelength.

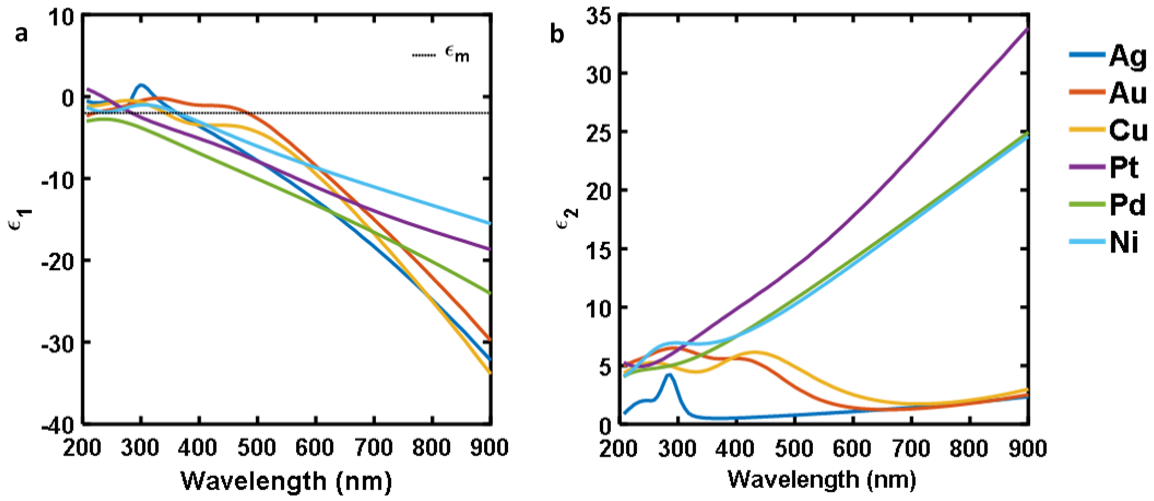

Figure 2.6 Dielectric properties of metals. a) the wavelength-dependent real part of the dielectric function for various plasmonic and non-plasmonic metals. The dashed line indicates where $\varepsilon_1 = -2\ \varepsilon_{m,air}$. **b)** the wavelength-dependent imaginary dielectric function for various plasmonic and non-plasmonic metals. Adapted from Ref. [26]

The second main feature of LSPR is that it acts to confine the energy of visible light to the nanoparticle surface in the form of elevated electric fields. The data in **Figure 2.7b** and **Figure 2.7c** show contour plots of the simulated electric field enhancement ($|E|^2/|E_0|^2$) surrounding the Ag and Au nanospheres shown in **Figure 2.7a,** respectively**.** We see that $|E|^2/|E_0|^2$ for Ag and Au nanospheres of these specific sizes can be ~35 to ~140. The magnitude of this enhancement depends on several factors, including the nanoparticle composition, shape, size, and surrounding dielectric medium.[42–44] For decades, researchers have exploited these high electric fields at the surface of photoexcited plasmonic nanoparticles for sensing applications. These applications include surface-enhanced Raman spectroscopy (SERS)[45] and the detection of fluorescently labeled proteins in biological systems[38].

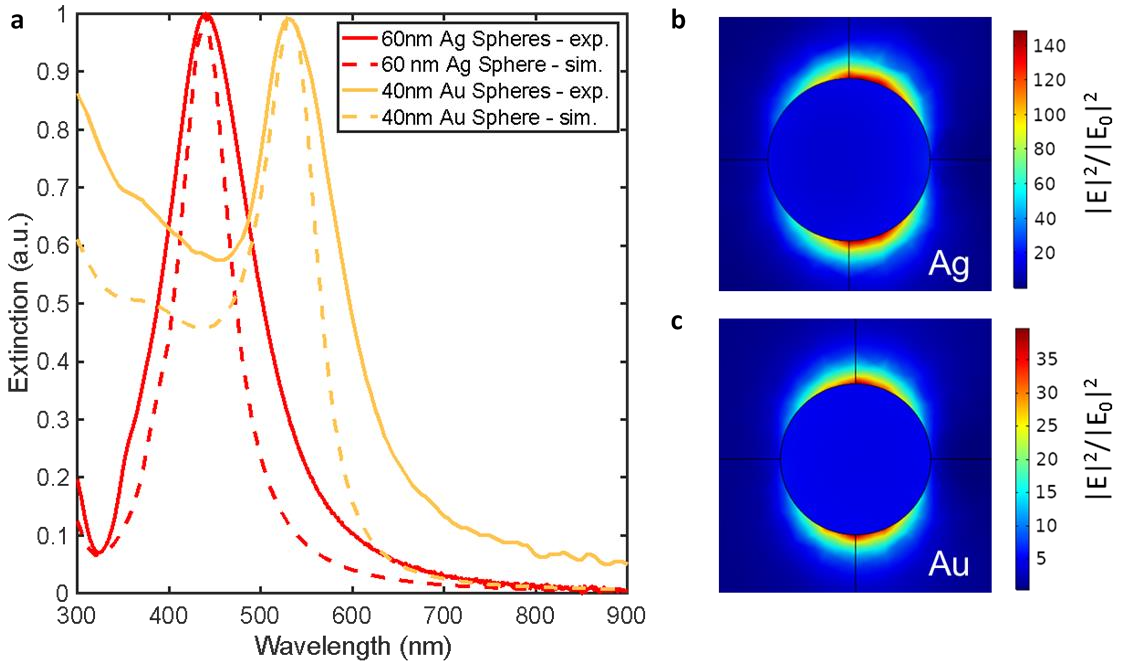

Figure 2.7 Characteristics of plasmon excitation. **a)** The experimentally measured and simulated optical extinction spectra in water for 40 nm Au and 60 nm Ag nanospheres. **b)** the contour plots of the electric field enhancement ($|E|^2/|E_0|^2$) corresponding to the data in (a). Adapted from Ref. [46]

The energy of these LSPR-confined electric fields subsequently dissipates through either radiative photon scattering or nonradiative photon absorption (**Figure 2.8**). Radiative scattering involves photon emission or reflection into the far-field, while absorption occurs via the excitation of energetic charge carriers, i.e., electron-hole pairs, within the nanoparticles.[47–49] These charge carriers thermalize via electron-electron collisions (~100s of femtoseconds) and subsequently electron-phonon collisions (~100s of picoseconds).[46] This thermalization process can lead to nanoparticle heating under LSPR conditions.[37,50,51] This dissertation mainly focuses on determining whether charge carriers generated within the nanoparticles via absorption can be localized into attached materials to perform a function. Thus, light absorption is the quantity we focus on throughout the rest of this section.

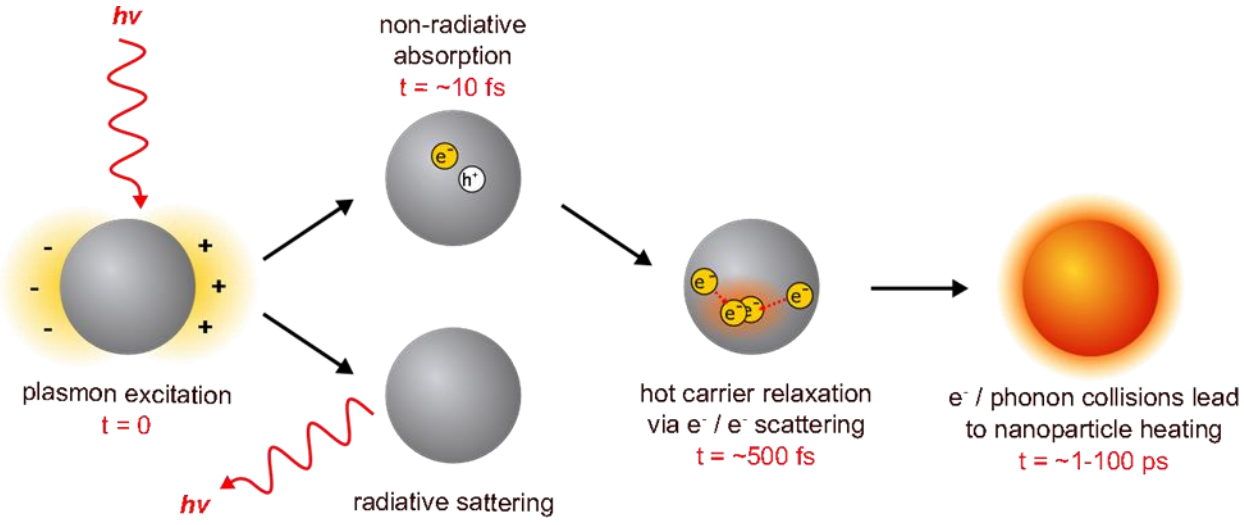

Figure 2.8 Dynamics of plasmon decay. A schematic of the sequential plasmon excitation and decay processes in a photoexcited Ag nanoparticle and their associated timescales. Adapted from Ref.[46]

Light absorption in metal nanoparticles occurs through the excitation of electrons in full bands (orbitals) below the metal Fermi level (E_f) to empty bands above E_f (**Figure 2.9**). One type of excitation involves transitions from full *s* states below E_f to empty *s* states above E_f known as intraband transitions. These transitions inherently do not conserve momentum (*k*) and thus are characterized by relatively slow characteristic timescales of 10^{13}-10^{15} s^{-1} that depend on the nanoparticle geometry and photon energy. As a result, these processes require a third entity to provide the required momentum for the transition. One way to provide this momentum is via collision with a nanoparticle phonon (**Figure 2.9a**). For nanoparticles with diameters of ~10s of nanometers, the plasmon decay constant (γ) for this process is $\gamma_{ph} = 10^{13}$-10^{14} s^{-1}.[52,53] The second way to conserve momentum is via the simultaneous excitation of two electrons from a single photon (**Figure 2.9b**). This process is characterized by a decay process that depends on the photon energy (E_{ph}) where $\gamma_{el} = 10^{15} (E_{ph}/E_f)^2$ s^{-1}. This process is ~10^{13}-10^{14} s^{-1} for Ag nanoparticles in the visible wavelength range.[54] The third way to conserve momentum in intraband transitions is via collisions with the nanoparticle surface (geometry-assisted), also known as Kreibig decay (**Figure**

2.9c).[55] The rate constant for this process is $\gamma_{geom} = v_f/R$, where R is the nanoparticle radius, and v_f is the Fermi velocity. The value of γ_{geom} ranges from ~10^{13}-10^{14} s^{-1} for Ag nanoparticles of 10 nm and 100 nm diameters, respectively.[52] The last type of excitation in metals occur via transitions from full *s* states below E_f to empty *d* states above E_f known as interband transitions (**Figure 2.9d**). These transitions conserve momentum and thus are characterized by a faster rate constant. These rate constants are wavelength-dependent but typically γ_{inter} = ~10^{15} s^{-1}. [52,56]

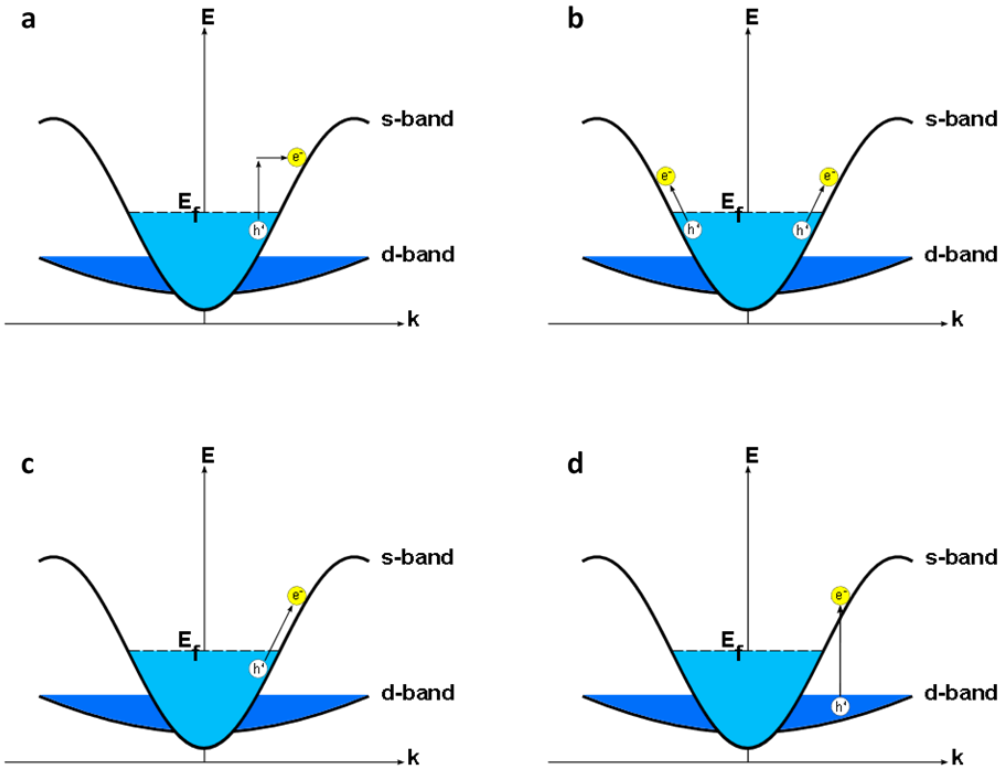

Figure 2.9 Optical excitations in metals. The diagrams in this Figure depict the representative electronic structure band diagrams for typical transition metals. We plot the energy (E) of the s-band and d-band as a function of the momentum (k). We designate the Fermi level with E_f. The various types of optical excitations in metal nanoparticles are: **a)** phonon-assisted intraband transitions. **b)** multi-electron intraband transitions. **c)** surface-assisted intraband transitions. **d)** direct interband transitions.

All four nonradiative plasmon decay mechanisms discussed above play a critical role in the lifetime of the LSPR optical response and the energy distribution of carriers generated within

the plasmonic nanoparticles. Due to their inherently rate constant, excitations through *d*-to-*s* interband transitions are the dominant decay pathway when energetically accessible. Recent theoretical calculations have investigated the contributions of the various decay pathways to absorption as a function of particle size and photon energy.[57] These calculations are compared to a semi-infinite slab. The data show that direct transitions dominate above a specific photon energy in all cases. At the same time, surface/geometry contributions are negligible for the semi-infinite surface and become more relevant as the nanoparticle diameter decreases.

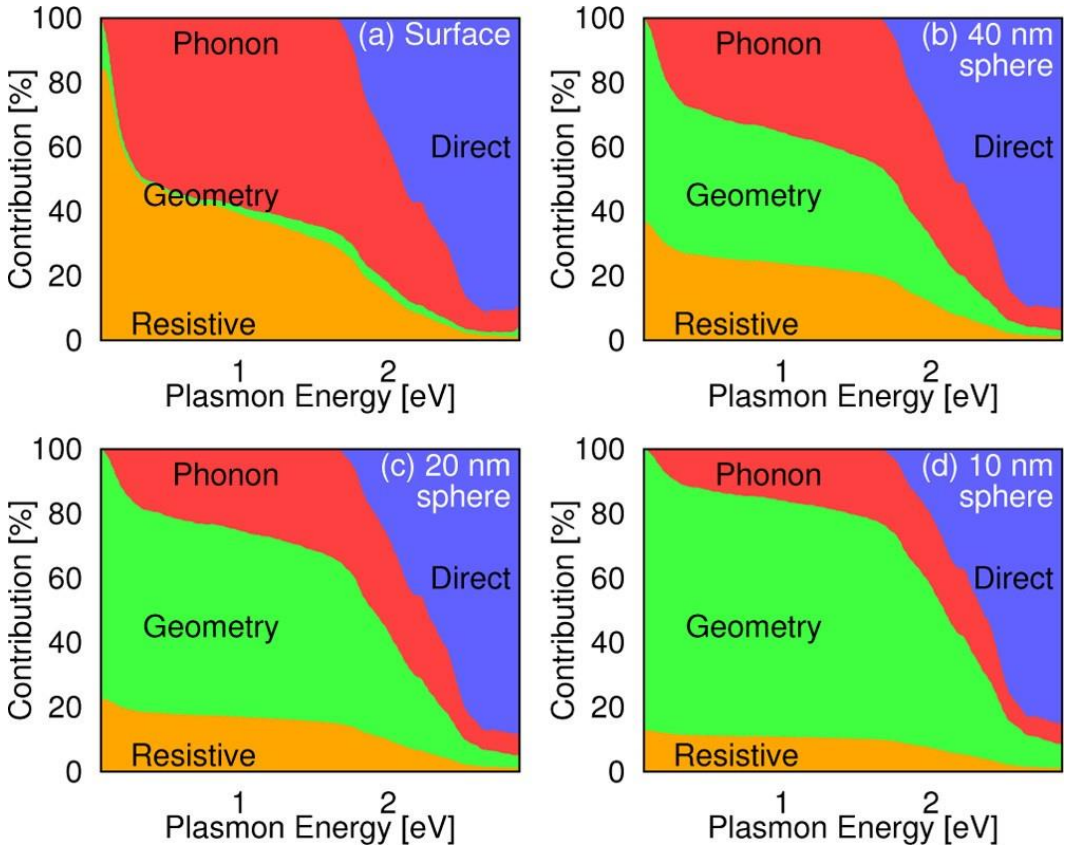

Figure 2.10 Comparison of nonradiative plasmon decay mechanisms in metals. The relative contributions of various nonradiative plasmon decay mechanisms to absorption in a semi-infinite gold surface and spherical gold nanoparticles of various sizes as a function of plasmon energy. These mechanisms include classical resistive losses as well as geometry-assisted, phonon-assisted, and direct excitations. Adapted from Ref. [57]

The following sections introduces the current state of understanding in the field of hybrid plasmonic nanomaterials. While it mainly focuses on studies performed on plasmonic nanoparticles, it is essential to note that phenomena associated with the metal's electronic structure

(e.g., interband transitions) are still relevant when describing other systems. On the contrary, geometry-dependent mechanisms (e.g., surface-assisted transitions) are not as important. The rate constants of these geometry-independent transitions play a key role in how metals confine electric fields regardless of their structure, so keeping them in mind throughout the next section is important.

2.4 Current Understanding of Energy and Charge Transfer in Hybrid Plasmonic Materials

The previous section introduced three types of plasmonic/photonic nanomaterials that can confine light below the diffraction limit in the form of elevated electric fields. As discussed in **Section 2.3.3,** these elevated fields lead to high light absorption (i.e., charge carrier generation) rates within the metal nanostructures. These high light absorption rates make plasmonic nanomaterials ideal for hot electron applications such as photodetection, photovoltaics[32,33], and photocatalysis[26,28,58]. In this context, designing hybrid materials to extract charge carriers from plasmonic nanomaterials requires a deep understanding of the physical mechanisms governing the flow of LSPR energy between plasmonic and non-plasmonic materials. This section introduces the current understanding (as of the beginning of this dissertation work) of how we can extract energy and charge from photoexcited plasmonic nanostructures into other materials (e.g., molecules, semiconductors and other metals).

2.4.1 The Indirect Transfer Mechanism

The first mechanism by which plasmonic nanoparticles transfer LSPR energy/charge to attached materials is the *indirect transfer mechanism* (**Figure 2.11** – green).[28,59–62] This mechanism involves the initial formation of hot charge carriers within the nanoparticle via the decay of LSPR. If these charge carriers have enough energy, they can transfer across the plasmonic/nonplasmonic

interface into unoccupied states. These unoccupied states are the lowest unoccupied molecular orbital (LUMO), the conduction band, and the empty s-band states for adsorbed molecules, semiconductors, and metals. Once in the other material, the charge carriers can impart energy into the attached material or be subsequently used in some other charge carrier-driven process such as powering an electrical circuit or driving a chemical reaction.[63–66]

The probability of energy/charge transfer to other materials through this indirect mechanism depends on the position of the unoccupied states in the molecule, semiconductor, or metal relative to the plasmonic metal's Fermi level. Unoccupied states near E_f will experience the largest energy/charge transfer rates since their formation follows a Fermi-Dirac distribution. This circumstance means that most of the generated charge carriers have energy near E_f and can therefore have a high probability of transferring into states similar in energy. Unoccupied states far from E_f (such as in semiconductors with wide band gaps) experience lower energy/charge transfer rates since fewer charge carriers have the energy needed to transfer. It is also important to note that even for low energy charge carriers near E_f, ultrafast recombination times in metals hinder their lifetime and thus also prevent them from being extracted. Thus, while this mechanism can play an important role in plasmonic energy transfer processes, it is ultimately hindered by fast thermalization rates within the plasmonic metal and limited to unoccupied states near E_f.

2.4.2 The Direct Transfer Mechanism

The second mechanism by which plasmonic nanoparticles transfer LSPR energy/charge to attached materials is the *direct transfer mechanism* (**Figure 2.11** – blue). [28,59–62] This mechanism involves the direct excitation of electrons (or holes) from full states in the plasmonic metal to empty states in the non-plasmonic material. This energy/charge transfer mechanism is characterized by the formation of direct, momentum-conserved electronic transitions (**Figure 2.9**)

at the plasmonic/nonplasmonic interface. These can arise from hybridized metal-molecule states that form via strong chemisorption in metal-molecule systems[67,68] or from interfacial states arising from strong electronic mixing in metal-semiconductor systems[69,70]. The main advantage of the direct transfer mechanism is that it does not compete with the thermalization process in the plasmonic component. Since the decay of LSPR energy directly injects charge into the non-plasmonic component, the efficiency of this direct mechanism is high compared to the indirect mechanism. Unfortunately, only a few metal-molecule and metal-semiconductor systems (cited above) have demonstrated this mechanism. As of the beginning of this dissertation work, metal-metal systems are thought to operate by the indirect mechanism.[71,72]

2.4.3 The Direct Excitation Mechanism

The third mechanism by which plasmonic nanoparticles transfer LSPR energy/charge to attached materials is the *direct excitation mechanism* (**Figure 2.11** – purple). [28,59–62] This mechanism involves the direct, LSPR electric-field mediated excitation of charge carriers from occupied states to unoccupied states in the attached material. Along with the indirect transfer mechanism, this mechanism is the most widely observed and studied. It is known as plasmon-induced resonance energy transfer (PIRET) in the metal-semiconductor literature and has been demonstrated in various contexts.[44,73] Recently, Kazuma et al. extended this mechanism to metal-molecule systems via the detailed study of dissociation reactions on plasmonic nanoparticles.[74]

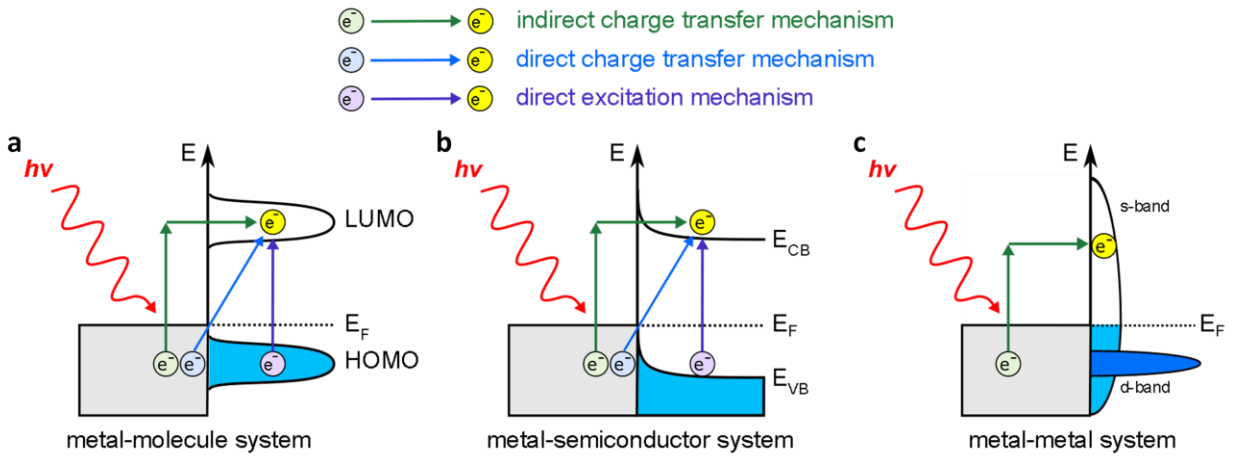

Figure 2.11 Mechanisms of energy and charge transfer in hybrid plasmonic materials (before dissertation). a-c) Schematics detailing the accepted energy/charge transfer mechanisms in metal-molecule, metal-semiconductor, and metal-metal systems hybrid plasmonic systems. The molecular orbitals, band structure, and density of states are shown for the molecule, semiconductor, and metal systems, respectively.

2.5 Current Limitations in Hybrid Plasmonics

The ability of hybrid plasmonic materials to funnel visible light energy into attached materials via LSPR makes them attractive for solar energy conversion technologies. They are specifically attractive for hot electron applications such as photodetection, photovoltaics[32,33], and photocatalysis[26,28,58]. The overall viability of hybrid plasmonic nanomaterials to improve these technologies depends on the ability to extract charge carriers from the plasmonic component before they thermalize. This fact leads to two main concerns for the field of hybrid plasmonics. First, the ultrafast thermalization of these charge carriers (**Figure *2.8***) significantly limits the efficiency of charge carrier extraction. This detail inherently limits the number of viable applications of hybrid plasmonics to those that can either bypass these fast thermalization rates or see significant improvements in quantum efficiencies even when transfer rates are low. The next limitation is the lack of literature describing energy transfer in hybrid metal-metal systems. Understanding this mechanism is key in applications that rely on metal alloys to perform chemical work, such as plasmonic photocatalysis.[59]

This dissertation work addresses both of these limitations. First, we investigate the mechanisms of energy transfer in hybrid metal-metal systems. We accomplish this by utilizing a combined experimental/computational approach to study bimetallic plasmonic nanoparticles. We then use our findings to revisit energy transfer mechanisms in hybrid metal-semiconductor and metal-molecule systems. Finally, we use our findings to maximize energy transfer in hybrid plasmonic systems by exploiting new physics known as strong light-matter coupling.

2.6 References

(1) Maier, S. A. *Plasmonics : Fundamentals and Applications*; Springer, 2007.

(2) Giannini, V.; Fernández-Domínguez, A. I.; Heck, S. C.; Maier, S. A. Plasmonic Nanoantennas: Fundamentals and Their Use in Controlling the Radiative Properties of Nanoemitters. *Chem. Rev.* **2011**, *111*, 3888–3912

(3) Ciracì, C.; Hill, R. T.; Mock, J. J.; Urzhumov, Y.; Fernández-Domínguez, A. I.; Maier, S. A.; Pendry, J. B.; Chilkoti, A.; Smith, D. R. Probing the Ultimate Limits of Plasmonic Enhancement. *Science* **2012**, *337*, 1072–1074.

(4) Ozbay, E. Plasmonics: Merging Photonics and Electronics at Nanoscale Dimensions. *Science* **2006**, *311*, 189–193.

(5) Giannini, V.; Fernández-Domínguez, A. I.; Heck, S. C.; Maier, S. A. Plasmonic Nanoantennas: Fundamentals and Their Use in Controlling the Radiative Properties of Nanoemitters. *Chem. Rev.* **2011**, *111*, 3888–3912.

(6) Gerasimov, V. V; Knyazev, B. A.; Nikitin, A. K.; Barnes, W. L. Surface Plasmon–Polariton Length Scales: A Route to Sub-Wavelength Optics. *J. Opt. A Pure Appl. Opt.* **2006**, *8*, S87.

(7) Sommerfeld, A. Ueber Die Fortpflanzung Elektrodynamischer Wellen Längs Eines Drahtes. *Ann. der Phisik* **1899**, *303*, 233–290.

(8) Zenneck, J. Über Die Fortpflanzung Ebener Elektromagnetischer Wellen Längs Einer Ebenen Leiterfläche Und Ihre Beziehung Zur Drahtlosen Telegraphie. *Ann. Phys.* **1907**, *328*, 846–866.

(9) Gramotnev, D. K.; Bozhevolnyi, S. I. Plasmonics beyond the Diffraction Limit. *Nat. Photonics 2010 42* **2010**, *4*, 83–91.

(10) Hutter, E.; Fendler, J. H. Exploitation of Localized Surface Plasmon Resonance. *Adv.*

Mater. **2004**, *16*, 1685–1706.

(11) Willets, K. A.; Van Duyne, R. P. Localized Surface Plasmon Resonance Spectroscopy and Sensing. *http://dx.doi.org/10.1146/annurev.physchem.58.032806.104607* **2007**, *58*, 267–297.

(12) Mauritz, K. Dielectric Spectroscopy https://web.archive.org/web/20060118002845/http://www.psrc.usm.edu/mauritz/dilect.html (accessed Dec 15, 2021).

(13) Zeng, S.; Baillargeat, D.; Ho, H.-P.; Yong, K.-T. Nanomaterials Enhanced Surface Plasmon Resonance for Biological and Chemical Sensing Applications. *Chem. Soc. Rev* **2014**, *3426*, 3426.

(14) Homola, J.; Koudela, I.; Yee, S. S. Surface Plasmon Resonance Sensors Based on Diffraction Gratings and Prism Couplers: Sensitivity Comparison. *Sensors Actuators B Chem.* **1999**, *54*, 16–24.

(15) Homola, J. Present and Future of Surface Plasmon Resonance Biosensors. *Anal. Bioanal. Chem.* **2003**, *377*, 528–539.

(16) Valev, V. K. Characterization of Nanostructured Plasmonic Surfaces with Second Harmonic Generation. *Langmuir* **2012**, *28*, 15454–15471.

(17) K. Lance Kelly; Eduardo Coronado; Lin Lin Zhao, and; Schatz*, G. C. The Optical Properties of Metal Nanoparticles: The Influence of Size, Shape, and Dielectric Environment. **2002**.

(18) Ismail, N.; Calil Kores, C.; Geskus, D.; Pollnau, M.; Fabry, C.; Pérot, A.; Llorens, J. M.; Buencuerpo, J.; Postigo, P. A. Fabry-Perot Resonator: Spectral Line Shapes, Generic and Related Airy Distributions, Linewidths, Finesses, and Performance at Low or Frequency-Dependent Reflectivity. *Opt. Express, Vol. 24, Issue 15, pp. 16366-16389* **2016**, *24*, 16366–16389.

(19) Fabry–Pérot interferometer https://en.wikipedia.org/wiki/Fabry–Pérot_interferometer#cite_note-Williams2007-5 (accessed Dec 20, 2021).

(20) Genet, C.; Ebbesen, T. W. Light in Tiny Holes. *Nature* **2007**, *445*, 39–46.

(21) Ebbesen, T. W.; Lezec, H. J.; Ghaemi, H. F.; Thio, T.; Wolff, P. A. Extraordinary Optical Transmission through Sub-Wavelenght Hole Arrays. *Nature* **1998**, *391*, 667–669.

(22) Salomon, A.; Wang, S.; Hutchison, J. A.; Genet, C.; Ebbesen, T. W. Strong Light-Molecule Coupling on Plasmonic Arrays of Different Symmetry. *ChemPhysChem* **2013**, *14*, 1882–1886.

(23) Kelly, K. L.; Coronado, E.; Zhao, L. L.; Schatz, G. C. The Optical Properties of Metal Nanoparticles: The Influence of Size, Shape, and Dielectric Environment. *J. Phys. Chem.*

B **2002**, *107*, 668–677.

(24) Link, S.; El-Sayed, M. A. Spectral Properties and Relaxation Dynamics of Surface Plasmon Electronic Oscillations in Gold and Silver Nanodots and Nanorods. *J. Phys. Chem. B* **1999**, *103*, 8410–8426.

(25) El-Sayed, M. A. Some Interesting Properties of Metals Confined in Time and Nanometer Space of Different Shapes. *Acc. Chem. Res.* **2001**, *34*, 257–264.

(26) Aslam, U.; Rao, V. G.; Chavez, S.; Linic, S. Catalytic Conversion of Solar to Chemical Energy on Plasmonic Metal Nanostructures. *Nat. Catal.* **2018**, *1*, 656–665.

(27) Zhang, X.; Li, X.; Reish, M. E.; Zhang, D.; Su, N. Q.; Gutiérrezgutiérrez, Y.; Moreno, F.; Yang, W.; Everitt, H. O.; Liu, J. Plasmon-Enhanced Catalysis: Distinguishing Thermal and Nonthermal Effects. *Nano Lett* **2018**, *18*, 1714–1723.

(28) Zhang, Y.; He, S.; Guo, W.; Hu, Y.; Huang, J.; Mulcahy, J. R.; Wei, W. D. Surface-Plasmon-Driven Hot Electron Photochemistry. *Chem. Rev.* **2018**, *118*, 2927–2954.

(29) Stiles, P. L.; Dieringer, J. A.; Shah, N. C.; Van Duyne, R. P. Surface-Enhanced Raman Spectroscopy SERS: Surface-Enhanced Raman Spectroscopy Raman Scattering: Inelastic Scattering of a Photon from a Molecule in Which the Frequency Change Precisely Matches the Difference in Vibrational Energy Levels. *Annu. Rev. Anal. Chem* **2008**, *1*, 601–626.

(30) Brus, L. Noble Metal Nanocrystals: Plasmon Electron Transfer Photochemistry and Single-Molecule Raman Spectroscopy. *Acc. Chem. Res.* **2008**, *41*, 1742–1749.

(31) Rao, V. G.; Aslam, U.; Linic, S. Chemical Requirement for Extracting Energetic Charge Carriers from Plasmonic Metal Nanoparticles to Perform Electron-Transfer Reactions. *J. Am. Chem. Soc* **2019**, *141*, 647.

(32) Enrichi, F.; Quandt, A.; Righini, G. C. Plasmonic Enhanced Solar Cells: Summary of Possible Strategies and Recent Results. *Renew. Sustain. Energy Rev.* **2018**, *82*, 2433–2439.

(33) Atwater, H. a; Polman, A. Plasmonics for Improved Photovoltaic Devices. *Nat. Mater.* **2010**, *9*, 205–213.

(34) El-Sayed, I. H.; Huang, X.; El-Sayed, M. A. Selective Laser Photo-Thermal Therapy of Epithelial Carcinoma Using Anti-EGFR Antibody Conjugated Gold Nanoparticles. *Cancer Lett.* **2006**, *239*, 129–135.

(35) Xiaohua Huang, †; Ivan H. El-Sayed, ‡; Wei Qian, † and; Mostafa A. El-Sayed*, †. Cancer Cell Imaging and Photothermal Therapy in the Near-Infrared Region by Using Gold Nanorods. *J. Am. Chem. Soc.* **2006**, *128*, 2115–2120.

(36) Tao, P.; Ni, G.; Song, C.; Shang, W.; Wu, J.; Zhu, J.; Chen, G.; Deng, T. Solar-Driven

Interfacial Evaporation. *Nat. Energy* **2018**, *3*, 1031–1041.

(37) Baffou, G.; Cichos, F.; Quidant, R. Applications and Challenges of Thermoplasmonics. *Nat. Mater.* **2020**, *19*, 946–958.

(38) Kabashin, A. V.; Evans, P.; Pastkovsky, S.; Hendren, W.; Wurtz, G. A.; Atkinson, R.; Pollard, R.; Podolskiy, V. A.; Zayats, A. V. Plasmonic Nanorod Metamaterials for Biosensing. *Nat. Mater.* **2009**, *8*, 867–871.

(39) Stuart, D. A.; Haes, A. J.; Yonzon, C. R.; Hicks, E. M.; Van Duyne, R. P. Biological Applications of Localised Surface Plasmonic Phenomenae. *IEE Proc. Nanobiotechnol.* **2005**, *152*, 13–32.

(40) Langhammer, C.; Kasemo, B.; Zorić, I. Absorption and Scattering of Light by Pt, Pd, Ag, and Au Nanodisks: Absolute Cross Sections and Branching Ratios. *J. Chem. Phys.* **2007**, *126*, 194702.

(41) Kreibig, U.; Vollmer, M. *Optical Properties of Metal Clusters*; Springer Series in Materials Science; Springer Berlin Heidelberg: Berlin, Heidelberg, 1995; Vol. 25.

(42) Kelly, K. L.; Coronado, E.; Zhao, L. L.; Schatz, G. C. The Optical Properties of Metal Nanoparticles: The Influence of Size, Shape, and Dielectric Environment. *J. Phys. Chem. B* **2003**, *107*, 668–677.

(43) Hao, E.; Schatz, G. C. Electromagnetic Fields around Silver Nanoparticles and Dimers. *J. Chem. Phys.* **2004**, *120*, 357.

(44) Linic, S.; Christopher, P.; Ingram, D. B. Plasmonic-Metal Nanostructures for Efficient Conversion of Solar to Chemical Energy. *Nat. Publ. Gr.* **2011**, *10*.

(45) Stiles, P. L.; Dieringer, J. A.; Shah, N. C.; Van Duyne, R. P. Surface-Enhanced Raman Spectroscopy. **2008**.

(46) Linic, S.; Chavez, S.; Elias, R. Flow and Extraction of Energy and Charge Carriers in Hybrid Plasmonic Nanostructures. *Nat. Mater.* **2021**, 1–9.

(47) Hartland, G. V; Besteiro, L. V; Johns, P.; Govorov, A. O. What's so Hot about Electrons in Metal Nanoparticles?

(48) Bernardi, M.; Mustafa, J.; Neaton, J. B.; Louie, S. G.; Barnes, W. L.; Dereux, A.; Ebbesen, T. W.; Tame, M.; Fakonas, J. S.; Lee, H.; *et al.* Theory and Computation of Hot Carriers Generated by Surface Plasmon Polaritons in Noble Metals. *Nat. Commun.* **2015**, *6*, 7044.

(49) Sundararaman, R.; Narang, P.; Jermyn, A. S.; Goddard III, W. A.; Atwater, H. A.; Kolesov, R.; Schuller, J. A.; Atwater, H. A.; Polman, A.; Jacob, Z.; *et al.* Theoretical Predictions for Hot-Carrier Generation from Surface Plasmon Decay. *Nat. Commun.* **2014**, *5*, 5788.

(50) Baffou, G.; Quidant, R. Thermo-Plasmonics: Using Metallic Nanostructures as Nano-Sources of Heat. *Laser Photon. Rev.* **2013**, *7*, 171–187.

(51) Govorov, A. O.; Richardson, H. H. Generating Heat with Metal Nanoparticles. *Nano Today* **2007**, *2*.

(52) Khurgin, J. B. How to Deal with the Loss in Plasmonics and Metamaterials. *Nat. Nanotechnol.* **2015**, *10*, 2–6.

(53) Hartland, G. V. Optical Studies of Dynamics in Noble Metal Nanostructures. *Chem. Rev.* **2011**, *111*, 3858–3887.

(54) Abelès, F. *Optical Properties of Solids.*; North-Holland Pub. Co.;;American Elsevier: Amsterdam ;New York, 1972.

(55) Khurgin, J. B.; Levy, U. Generating Hot Carriers in Plasmonic Nanoparticles: When Quantization Does Matter? *ACS Photonics*, 2020, *7*, 547–553.

(56) Khurgin, J. B.; Sun, G. Scaling of Losses with Size and Wavelength in Nanoplasmonics and Metamaterials. *Appl. Phys. Lett.* **2011**, *99*, 211106.

(57) Brown, A. M.; Sundararaman, R.; Narang, P.; Goddard, W. A.; Atwater, H. A. Nonradiative Plasmon Decay and Hot Carrier Dynamics: Effects of Phonons, Surfaces, and Geometry. *ACS Nano* **2016**, *10*, 957–966.

(58) Corte, E.; Besteiro, L. V; Alabastri, A.; Baldi, A.; Tagliabue, G.; Demetriadou, A.; Narang, P. Challenges in Plasmonic Catalysis . **2021**, *18*, 22.

(59) Linic, S.; Aslam, U.; Boerigter, C.; Morabito, M. Photochemical Transformations on Plasmonic Metal Nanoparticles. *Nat. Mater.* **2015**, *14*, 567–576.

(60) Ahlawat, M.; Mittal, D.; Govind Rao, V. Plasmon-Induced Hot-Hole Generation and Extraction at Nano-Heterointerfaces for Photocatalysis. *Commun. Mater. 2021 21* **2021**, *2*, 1–15.

(61) Kazuma, E.; Jung, J.; Ueba, H.; Trenary, M.; Kim, Y. Real-Space and Real-Time Observation of a Plasmon-Induced Chemical Reaction of a Single Molecule. *Science* **2018**, *360*, 521–526.

(62) Christopher, P.; Moskovits, M. Hot Charge Carrier Transmission from Plasmonic Nanostructures. *Annu. Rev. Phys. Chem* **2017**, *6817*.

(63) Tagliabue, G.; Jermyn, A. S.; Sundararaman, R.; Welch, A. J.; DuChene, J. S.; Pala, R.; Davoyan, A. R.; Narang, P.; Atwater, H. A. Quantifying the Role of Surface Plasmon Excitation and Hot Carrier Transport in Plasmonic Devices. *Nat. Commun.* **2018**, *9*, 3394.

(64) Cortés, E.; Xie, W.; Cambiasso, J.; Jermyn, A. S.; Sundararaman, R.; Narang, P.; Schlücker, S.; Maier, S. A. Plasmonic Hot Electron Transport Drives Nano-Localized

Chemistry. *Nat. Commun.* **2017**, *8*.

(65) Christopher, P.; Xin, H.; Linic, S. Visible-Light-Enhanced Catalytic Oxidation Reactions on Plasmonic Silver Nanostructures. *Nat. Chem.* **2011**, *3*, 467.

(66) Mubeen, S.; Lee, J.; Singh, N.; Krämer, S.; Stucky, G. D.; Moskovits, M. An Autonomous Photosynthetic Device in Which All Charge Carriers Derive from Surface Plasmons. *Nat. Nanotechnol.* **2013**, *8*, 247–251.

(67) Boerigter, C.; Campana, R.; Morabito, M.; Linic, S. Evidence and Implications of Direct Charge Excitation as the Dominant Mechanism in Plasmon-Mediated Photocatalysis. *Nat. Commun.* **2016**, *7*.

(68) Boerigter, C.; Aslam, U.; Linic, S. Mechanism of Charge Transfer from Plasmonic Nanostructures to Chemically Attached Materials. *ACS Nano* **2016**, *10*, 6108–6115.

(69) Wu, K.; Chen, J.; McBride, J. R.; Lian, T. Efficient Hot-Electron Transfer by a Plasmon-Induced Interfacial Charge-Transfer Transition. *Science* **2015**, *349*, 632–635.

(70) Tan, S.; Argondizzo, A.; Ren, J.; Liu, L.; Zhao, J.; Petek, H. Plasmonic Coupling at a Metal/Semiconductor Interface.

(71) Zheng, Z.; Tachikawa, T.; Majima, T. Single-Particle Study of Pt-Modified Au Nanorods for Plasmon-Enhanced Hydrogen Generation in Visible to Near-Infrared Region. *J. Am. Chem. Soc.* **2014**, *136*, 6870–6873.

(72) Zheng, Z.; Tachikawa, T.; Majima, T. Plasmon-Enhanced Formic Acid Dehydrogenation Using Anisotropic Pd–Au Nanorods Studied at the Single-Particle Level. *J. Am. Chem. Soc.* **2015**, *137*, 948–957.

(73) Li, J.; Cushing, S. K.; Meng, F.; Senty, T. R.; Bristow, A. D.; Wu, N. Plasmon-Induced Resonance Energy Transfer for Solar Energy Conversion. *Nat. Photonics* **2015**, *9*, 601–607.

(74) Kazuma, E.; Jung, J.; Ueba, H.; Trenary, M.; Kim, Y. Real-Space and Real-Time Observation of a Plasmon-Induced Chemical Reaction of a Single Molecule. *Science* **2018**, *360*, 521–526.

Chapter 3 Experimental and Computational Techniques

3.1 Summary

This chapter provides a brief introduction to experimental and computational techniques used throughout the work presented in this dissertation. It begins with a summary of methods to synthesize plasmonic metal nanoparticles. This chapter focuses on the synthesis of colloidal Ag nanoparticles since they serve as the platform for the experimental work presented in the first several chapters of the manuscript. The synthesis of each type of multicomponent plasmonic system, where we interface the plasmonic Ag nanoparticles with other materials (e.g., semiconductors, molecules, or other metals), is presented explicitly in their respective chapters. We then describe several nanofabrication techniques used to fabricate the optical cavities studied in the last part of the dissertation. Next, we introduce materials characterization techniques utilized to determine the composition of the hybrid, multicomponent systems presented throughout the dissertation. We subsequently introduce the spectroscopic techniques used for characterizing the optical characteristics of the colloidal nanoparticle systems/the thin film optical cavities and describe the electrical measurements performed on the optical cavities to investigate their charge transport properties. Finally, we introduce the methodology behind the finite element electrodynamics models that underpin all discussions and analyses throughout the document.

3.2 Nanoparticle Synthesis Techniques

Synthesizing well-defined monometallic plasmonic nanoparticles of specific shapes and sizes is key in engineering their optical properties.[1,2] The following section briefly introduces the methodology behind synthesizing the nanoparticles used throughout this dissertation.

3.2.1 Colloidal Synthesis of Metal Nanoparticles

We prepare the metal nanoparticles discussed in this dissertation via a common solution-phase approach known as colloidal synthesis.[3] Colloidal synthesis methods typically employ four major components. These consist of the solvent, a metal precursor, a reducing agent, and a polymeric stabilizer. A typical synthesis procedure involves mixing the four ingredients into a closed, heated reaction vessel. The reducing agent gives electrons to the metal precursor to form metal clusters. As these clusters form, the polymeric stabilizer attaches to the exposed metal facets to dictate the growth and stabilize the clusters in solution. The metal precursor continuously depletes as it is reduced onto the small metal clusters, resulting in the formation of colloidal metal nanoparticles suspended in solution by the polymeric stabilizer.

This colloidal synthesis method is highly flexible because of the vast options for the four components listed above. Ascorbic acid, ethylene glycol, sodium citrate, and sodium borohydride are typical examples of reducing agents, while metal nitrites, metal chlorides, and transition metal complexes typically serve as metal precursors. Common polymeric stabilizers include citrate, polyvinyl alcohol (PVA), citrate, and polyvinyl pyrrolidone (PVP). The choice of these various ingredients is important in directing the metal nanoparticle growth. For example, one can control the shape of various metal nanoparticles simply by changing the capping agent or adding ionic species to the solution.[4] Collectively, the flexibility of the synthesis components makes colloidal

nanoparticle synthesis an ideal method for the creation of metal nanoparticles with specific size, shape, and composition for our studies.

We mainly employ Ag nanocubes of varying sizes throughout the work presented in this dissertation. Generally, we prepare these nanocubes by modifying a well-established polyol method.[5] PVP acts as the polymeric stabilizer in this method, and silver nitrate ($AgNO_3$) serves as the metal precursor. Ethylene glycol acts as both the solvent and the reducing agent. Throughout the dissertation, the specific synthesis procedures used in each study are presented either in the main body of the chapter or in the chapter's Supporting Information section.

3.3 Nanofabrication Techniques

The final part of the dissertation focuses on analyzing light-matter interactions in optical cavities. The section below describes the nanofabrication techniques used to fabricate the cavity and control systems presented in that portion of the dissertation. The equipment we used related to each process introduced in this section is located at the University of Michigan's Lurie Nanofabrication Facility.

3.3.1 Electron-beam Evaporation

We deposited our metal thin films for our optical cavities using a physical vapor deposition technique known as electron-beam evaporation (EBE).[6] EBE is a high-vacuum evaporation technique that uses an electron beam to vaporize high-purity metals contained in a metal crucible that lies opposite from the sample. Electrons are created by passing a current through a tungsten filament and then accelerated toward the crucible under extremely low pressures. The high vacuum is critical in preventing vaporized metal from colliding with air molecules as they traverse the chamber and deposit on the sample. The small point sources and long throw distances used in these

evaporators minimize heat transfer to the substrate and allow for highly directional depositions. This feature allows the thin films fabricated via this method to be highly uniform.

We deposited the metal films to fabricate the optical cavities using an Angstrom Engineering Evovac Evaporator. Briefly, we cleaned glass slides or coverslips in piranha solution (3:1 mixture of sulfuric acid to 30% hydrogen peroxide) for 30 minutes and dried them with pressurized N_2 before the evaporation step. Next, we mounted the samples in the evaporator across from a crucible containing solid Ag. We pumped down the chamber to $< 3x10^{-6}$ torr and performed the evaporation under vacuum at a rate of 1-5 A/s. We present the specific evaporation details for each sample in the chapter discussed.

3.3.2 Spin Coating

Spin coating is a fabrication technique used for depositing thin films of material (typically polymer films) onto flat substrates.[7] Spin coating a material onto a substrate typically occurs in the following manner. First, a solution (either aqueous or non-aqueous) is prepared to contain a solvent and the material of interest. For polymer films, the solvent is heated to dissolve the polymer and then cooled to room temperature. A small amount of this polymer-loaded solvent is deposited onto the substrate. The substrate is either immobile (static spinning) or already spinning as a set rotation speed (dynamic spinning). Static and dynamic spinning have their unique advantages/disadvantages. The choice between the two depends on the solvent, the material of interest, and the final desired properties of the thin film. Static spinning is superior when considering low spin speeds or highly viscous solutions, while dynamic spinning is superior for fast spinning spends and less viscous solutions.[8]

Once the polymer-solution is added to the substrate, it spins at a constant speed for a set amount of time. The centrifugal force from the high rotation speeds (commonly >1000 rpm)

spreads the polymer solution across the substrate as the solvent evaporates. The final thickness of the film is mainly governed by the spin speed and duration, although other factors such as humidity, ambient temperature, etc. can play significant factors. [8] Generally, the thickness of the film is proportional to the inverse of the spin speed squared.[8]

We performed the spin coating of the dye-polymer films presented in the strong coupling studies on a Laurell Spinner Ws-650-23B. A static spinning method was employed, where we deposited 0.5 mL of the polymer-dye solution onto an immobile sample (e.g., metal-coated glass slides). The spread time was set equal to 0s and the spin time varied from 30 s to 4 5s. We present the specific spin coating details in the chapters they are utilized.

3.4 Materials Characterization Techniques

The characterization of the physical properties (e.g., shape, size, composition, etc.) of the plasmonic nanostructures presented throughout their dissertation is critical in determining the success of the synthesis methods and the structure-property relationships related to their optical properties. We have employed various techniques to characterize our nanomaterials post-synthesis and post-fabrication. In particular, we utilized electron microscopy to determine the nanoscale morphology of our materials and associated x-ray spectroscopies to determine their elemental composition. We have also used optical metrology techniques to determine the thicknesses of our metal and polymer thin films for our optical cavities.

3.4.1 Scanning Transmission Electron Microscopy

The primary nanoparticle characterization technique used in this work was scanning transmission electron microscopy (STEM).[9] STEM works by rastering a highly focused beam of electrons across a sufficiently thin sample. Electrons impinging on the sample either transmit

through the sample or scatter via interactions with the nanomaterial. A dark field detector collects the scattered electrons and yields information about the thickness of the sample and the material's elemental composition based on the contrast of the image. Thicker materials or materials with higher elemental weight will scatter the electrons more and thus provide higher contrast. This feature makes dark-field imaging ideal for obtaining high-resolution (atomic level) STEM images of the material of interest.[10] A bright-field detector collects electrons that transmit directly through the sample to provide bright field images complementary to the dark field images.[11] Together, these images can provide information into the atomic structure and composition of the materials of interest.

We obtained the STEM images presented throughout this dissertation on a JEOL 3100 double CS-corrected transmission electron microscope utilizing an accelerating voltage of 300 kV. The samples for STEM characterization were prepared by drop-casting the nanoparticle solution onto 200 mesh carbon-on-copper grids. Each sample was plasma-cleaned under vacuum in the TEM for 5 minutes before spectra were acquired. We obtained and analyzed all STEM data at the University of Michigan's Center for Materials Characterization.

3.4.2 Energy Dispersive X-ray Spectroscopy

We use energy-dispersive x-ray spectroscopy (EDS) to characterize the elemental composition of a material of interest in STEM.[12] This technique works by collecting x-rays emitted by the atoms in the sample when the electron beam ionizes them. The energy of the emitted x-rays is characteristic of the element's atomic structure and thus serves as a unique identifier of the elements comprising the material. We obtain EDS elemental maps of all Ag-Pt nanoparticles presented throughout this dissertation using the Ag Lα and Pt M transition peaks. We obtained and analyzed all EDS data at the University of Michigan's Center for Materials Characterization.

3.4.3 Variable-Angle Spectroscopic Ellipsometry

We measured the thicknesses and dielectric properties for the molecule-loaded polymer films presented throughout this dissertation via variable angle spectroscopic ellipsometry (VASE) measurements. Generally, ellipsometry is an optical technique that takes advantage of light polarization to determine the dielectric properties of thin films.[13] In the case of spectroscopic ellipsometry, the sample is illuminated with polarized broadband light. A detector then measures the change in polarization upon transmission or reflection. The polarization change is recorded as a function of wavelength and at different incident angles and compared to a model. The model then pieces together the wavelength-dependent dielectric properties of the material. We extract the thickness of the thin film can by fitting the model to a transparent region of the sample.

We performed the VASE measurements presented throughout this dissertation utilizing a Woollam M-2000 ellipsometer. Briefly, we performed reflection measurements at three different angles (55°, 65°, and 75°) to obtain measurements for the elliptically polarized light's p- and s-components. We fit the reflection data to a thin film model, allowing us to extract the optical properties and film thicknesses. We obtained and analyzed all VASE data at the University of Michigan's Lurie Nanofabrication Facility.

3.5 Optical Characterization Techniques

Determining the optical behavior of the plasmonic nanomaterials presented throughout this study is a crucial requirement for understanding how these materials harvest and confine the energy of visible light. We have characterized the optical properties of our nanomaterials using a variety of optical spectroscopies. These include extinction and absorption spectroscopies as well as vibrational spectroscopies. We present a brief introduction to these techniques below.

3.5.1 Ultraviolet-visible Spectroscopy

UV-vis spectroscopy (UV-vis) is a common optical characterization technique used to determine how various materials interact with light at different wavelengths.[14] These samples can be simple molecules, organic or inorganic complexes, nanoparticles, or even solids such as powders or thin films. A measurement is typically performed by passing monochromatic light at various wavelengths through the sample. A detector collects the photons that pass through the sample (i.e., the transmission) and subtracts it from the incident light to calculate the light extinction. Light extinction is the sum of various ways the sample can interact with light. It includes light absorption (the nonradiative excitation of electrons within the material), scattering (the radiative emission of a photon, typically from a nanoparticle), and reflection (typically from solids). While extinction measurements usually are not relevant for molecular samples (since scattering is generally negligible), they are essential for characterizing the plasmonic metal nanoparticles presented throughout this dissertation since they can scatter light at high rates.

This dissertation used a ThermoFisher Scientific Evolution 300 spectrophotometer to perform all UV-vis measurements. We diluted aqueous nanoparticle samples are to 3 mL in a quartz cuvette cleaned with piranha solution. A baseline is collected by preparing a cuvette with the nanoparticle solvent (water) and subtracted from the final measurement to prevent contributions from the solvent itself.

3.5.2 Integrating Sphere Absorption Measurements

As mentioned in the previous section, UV-vis spectroscopy directly measures light extinction (i.e., absorption + scattering + reflection). It only directly measures the sample's absorption when the scattering and reflection processes are negligible. Measuring the absorption of a sample yields information about the energy of electronic excitations readily available in the

material. This information is important in the context of plasmonic nanoparticles since it allows us to determine the energy of the charge carriers we are generating within the nanoparticles when photoexciting them. In order to measure the absorption of our nanoparticle samples, we used a combination of UV-vis spectroscopy coupled with integrating sphere absorption spectroscopy.

We obtained our nanoparticle absorption measurements using an optical integrating sphere (LabSphere) coupled to a silicon photodiode detector (Newport Corporation). We illuminated our samples with monochromatic light as a function of wavelength. We obtained our monochromatic light by passing broadband light from a 1000 W Xenon lamp through a Cornerstone 260 monochromator. We measured the absorption for the optical cavity and respective control systems presented in the strong coupling studies with a UV-vis-NIR spectrophotometer (Shimadzu, UV-3600i Plus) with an integrating sphere attachment (Shimadzu, UV-3600i Plus)

3.5.3 Surface-enhanced Raman Spectroscopy

Surface-enhanced Raman spectroscopy (SERS) is an optics-based analytical tool used to detect molecules on the surfaces of plasmonic metal nanoparticles.[15] It is a surface-sensitive, vibrational spectroscopy technique that takes advantage of the high electric fields present at the surface of plasmonic metal nanoparticles to enhance the Raman scattering process. In traditional Raman spectroscopy, a high-intensity laser forces the polarization of a molecule's electron cloud.[16] In the framework of quantum mechanics, the molecule is said to be excited into a virtual energy state high in energy. When the molecule relaxes, it most often relaxes back to its original vibrational energy state. This process is known as Rayleigh scattering. If the molecule relaxes to a higher energy level, it is called Stokes scattering, and the reverse process is known as anti-Stokes scattering. Regardless of the initial/final position of the molecule, excitation into a virtual energy state is an inherently low probability process. However, the Raman enhancement factor scales with

the fourth power of the electric field interacting with the molecule.[15] SERS takes advantage of this fact to enhance the Raman scattering up to 10^{12} times.[16] This allows SERS to detect even single molecules.[17,18]

We conducted the wavelength-dependent Raman studies presented in this dissertation using a Horiba LabRAM HR DuoScan™ system under excitation from either a 532 nm diode-pumped solid-state laser or a 785 nm diode laser. We focused the laser beam with an objective microscope at a magnification of 50×. Raman scattering was detected at an angle of 180° using a Peltier-cooled (-71 ℃) charge-coupled device (CCD) camera.

3.6 Electrical Characterization Techniques

We performed electrical measurements on the strongly coupled optical cavities to investigate their charge transport properties. We performed these measurements in a two-electrode set-up consisting of a working electrode and a counter electrode connected to a potentiostat (Reference Gamry 3000 Potentiostat in this work). These two-electrode measurements measure the complete voltage dropped across the entire system and are commonly used in systems that exhibit relatively low currents or when the total voltage is the parameter of interest.[19] The potentiostat controls/measures the input and output current/voltage between the working and counter electrodes. The quantity that it measures depends on the experiment. The remainder of the section briefly describes the two electrical measurement techniques used in this work. THe specific details of our measurements are described in the associated chapter.

3.6.1 Linear Sweep Voltammetry

Linear sweep voltammetry (LSV) is one of the most common voltammetric methods. In a 2-electrode LSV measurement, the current at the working electrode is measured while varying the

voltage between the working and counter electrode.[20] In this dissertation, we use LSV to monitor how the current across an optical cavity as a given voltage changes in and out of the strong coupling regime.

3.6.2 Chronopotentiometry

Chronopotentiometry (CP) is an electrical characterization technique that measures the voltage of a system subject to different inputs while maintaining a constant current.[21] In this dissertation, we use CP to measure the voltage generated across an optical cavity under illumination by setting the current to zero. We then investigate how this voltage changes for a given light intensity in and out of the strong light-matter coupling regime.

3.6.3 Chronoamperometry

Chronoamperometry (CA) is the complementary measurement technique to chronopotentiometry. CA is an electrical characterization technique that measures the current of a system subject to different inputs while maintaining a constant voltage. In this dissertation, we use CA to measure the current by optical cavities under illumination at varying applied voltages. We then investigate how the characteristics of the photocurrent change in and out of the strong light-matter coupling regime.

3.6.4 Electrochemical Impedance Spectroscopy

Electrochemical impedance spectroscopy (EIS) is an electrical technique used to probe the impedance characteristics of a system. The technique involves passing a small amplitude alternating current through the system over a wide range of frequencies to generate impedance spectra. We use EIS in this dissertation to measure the resistances across optical cavities in and out of the strong light-matter coupling regime.

3.7 Finite-element Method Electrodynamics Modeling

Electrodynamics modeling has continuously played a critical role in plasmonics research.[22] It has proven crucial in understanding the delicate interactions between light and matter at the nanoscale and exploiting these interactions to enable various technologies. Throughout this dissertation, we utilize finite element method (FEM) electrodynamics models to understand the interplay between plasmonic and non-plasmonic components present in hybrid plasmonic nanomaterials. The objective is to capture phenomena related to the individual components of multicomponent plasmonic systems that we cannot probe experimentally. This section presents an overview of the methodology used in modeling various nanomaterials presented throughout this dissertation. We begin with an introduction to the FEM and discuss its advantages in the context of modeling electrodynamics. We then present the details regarding the models utilized throughout this dissertation. We begin with the modeling of core-shell hybrid plasmonic metal nanoparticles and end with the modeling of Fabry-Perot optical cavities and nanohole arrays.

3.7.1 Introduction to Finite Element Models

The electrodynamics phenomena investigated throughout this dissertation can be described by a set of coupled partial differential equations known as Maxwell's equations.[23] Solving these equations for a given system gives a complete description of its physical properties related to optics and electromagnetism. While this makes them particularly powerful tools for investigating a wide variety of systems in physics and engineering, solving them analytically for a given system is essentially impossible. Thus, we turn to numerical methods solved by computers to aid in studying relevant electrodynamics phenomena throughout this dissertation.

We use finite element method (FEM) modeling throughout this dissertation to investigate the optical behavior of nanostructured systems. FEM modeling is a numerical technique used to

solve coupled partial differential equations using additional constraints provided by physics.[24]The technique involves compartmentalizing a model geometry into discrete elements (i.e., domains or sections). The partial differential equations are approximated with numerical equations within each element, solved, and then reassembled into a more extensive system of equations that can capture the physical phenomena of the entire problem. The benefits of this approach include extensive freedom in forming the elements, allowing the modeling of complex geometries and irregular shapes.[25] Throughout this dissertation, we use COMSOL Multiphysics Finite Element method software to model our systems of interest. We outline the details for each simulation throughout the remainder of the section.

3.7.2 Overview of Model Set-up and Definitions

This section provides an overview of the electrodynamics models using COMSOL Multiphysics. We created all of our FEM models using COMSOL Multiphysics' '*Wave Optics'* module. They are 3-dimensional, time-independent models solved in the frequency domain. Dielectric properties for the materials were either obtained from COMSOL's materials database or obtained experimentally (described in the relevant chapter). The remainder of the section lists the boundary conditions used throughout the models described in the following sections.

- *Perfectly matched layer (PML)* – This is a condition applied to a particular domain in the model for mimicking a nonreflecting infinite domain. It essentially sets up a perfectly absorbing domain to eliminate nonphysical reflections that would otherwise be present in the models. We used the PML boundary condition in the core-shell nanocube models to approximate the optical behavior of the nanoparticles sitting in free space.
- *Perfect electric conductor (PEC)* – This condition sets the tangential component of the incident electric field to zero. It is typically used to model a lossless metallic surface or

impose symmetry in the magnetic field. We use the PEC boundary condition in the core-shell nanocube model to impose symmetry perpendicular to the polarization of the plane wave incident on the nanoparticle.

- *Perfect magnetic conductor (PMC)* – This condition sets the tangential component of the incident magnetic field to zero. It is typically used to model a high impedance surface or impose symmetry in the electric field. We use the PEM boundary condition in the core-shell nanocube model to impose symmetry parallel to the polarization of plane wave incident on the nanoparticle.
- *Scattering boundary condition (SBC)* – This condition makes a boundary transparent to incoming and scattered plane waves. We use the SBC in the core-shell nanocube model to define a surface over which we calculate the scattered field.
- *Periodic boundary condition (PBC)* – This condition relates two boundaries through geometric periodicity. It is typically used to extend the geometry in a periodic fashion to model repetitive structures such as a unit cell. We use the PBC in the optical cavity and nanohole array models to extend the geometry repetitively in the XY plane. The type of PBC used is Floquet periodicity, which is ideal for frequency-domain problems.
- *Transition boundary condition (TBC)* – This condition represents a discontinuity in the tangential electric field. It is typically used to model geometric domains that are geometrically thin but not electrically thin. We use the TBC in the optical cavity models to represent the optically thin metal films comprising the cavity.
- *Port* – This condition defines where electromagnetic energy enters or exits the model. We use ports in the optical cavity and nanohole array models to launch light into the system and to receive the transmission light coming out of the system.

The following sections outline the three main models presented throughout this dissertation.

3.7.3 Modeling of Core-Shell Nanoparticles

We show a schematic of the model geometry used in the core-shell nanocube simulations in **Figure 3.1**. We encase a core-shell nanocube of the desired dimensions in two concentric spheres. We split the combined sphere/nanocube geometry is into ¼ in order to reduce computational costs. We implemented symmetry conditions (described below) to capture the behavior of the complete system. We define the outer sphere as a PML to ensure we do not include nonphysical reflections from the model in the simulations. The inner sphere and the nanocube are physical domains assigned the dielectric properties of the materials we want to model. We define our electromagnetic excitation as a plane wave defined: $E = E_0 e^{-ikx}$ and polarized in the z-direction.

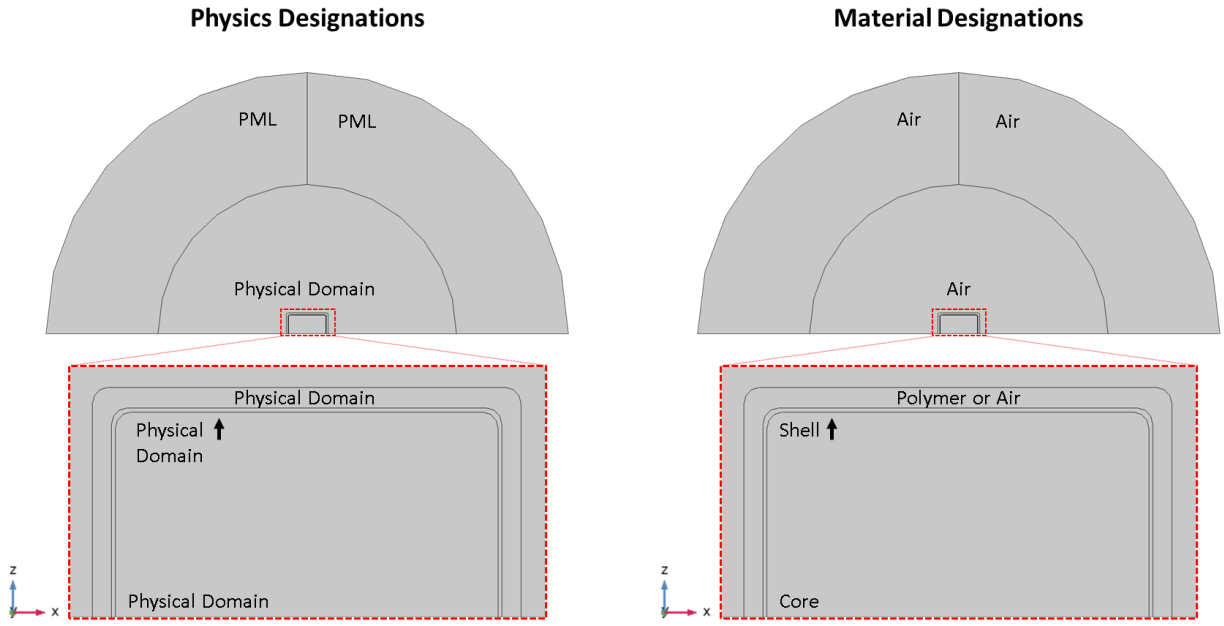

Figure 3.1 Physical and material designations for the nanocube models. Schematics of the model geometry used in the core-shell nanocube simulations. The physics designations show what portions of the model are real (physical domains) or virtual (PML domains). The material designations designate the material selection for each domain in the model.

We show the boundary conditions used in the core-shell nanocube model in **Figure 3.2**. We use the PEC and PMC boundary conditions to impose symmetry in the model. These are required to preserve the electromagnetic phenomena across the Y and Z boundaries. We include an SBC on the outer surface of the PML to define a surface over which we can approximate the scattered field.

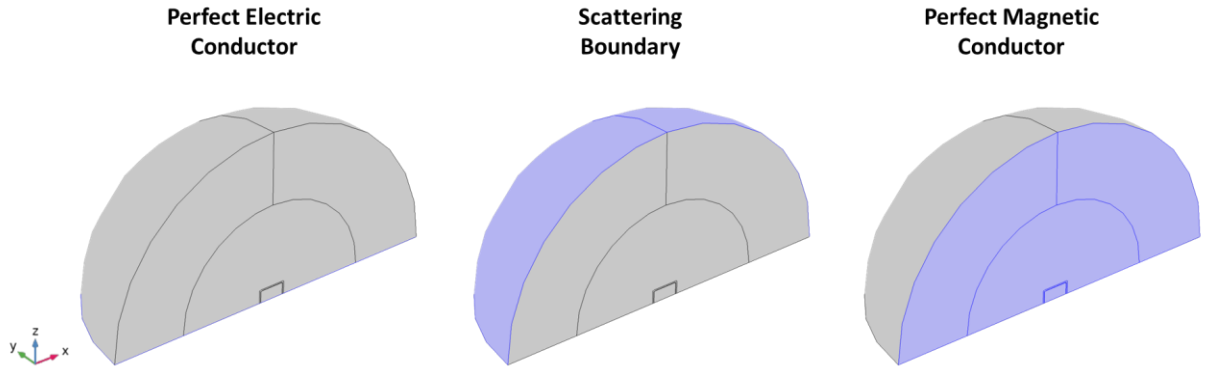

Figure 3.2 Boundary conditions used in the nanocube models. Schematics of the model geometry used in the core-shell nanocube simulations and the boundary conditions on their relevant surfaces (shown in purple).

3.7.4 Modeling of Fabry-Perot Optical Cavities

We show a schematic of the model geometry used in the optical cavity simulations in **Figure 3.3**. We create a five-layer system by first sandwiching a dye/polymer domain between two metallic domains. We then place these metallic domains between air domains. Collectively, these domains represent a unit cell of an optical cavity suspended in air. All physical domains are assigned the dielectric properties of the materials we model.

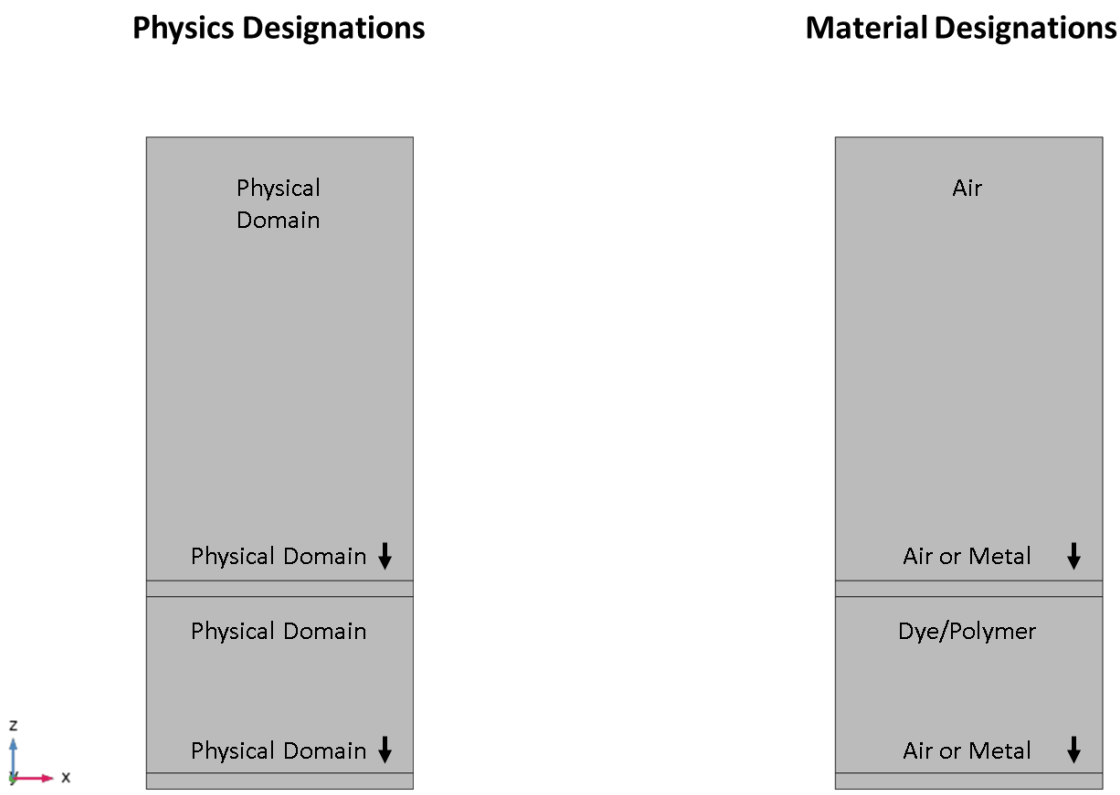

Figure 3.3 Physical and material designations for the optical cavity models. Schematics of the model geometry used in the optical cavity simulations. The physics designations show what portions of the model are real (physical domains) or virtual (PML domains). The material designations designate the material selection for each domain in the model.

We show the boundary conditions used in the optical cavity model in **Figure 3.4**. We set port boundary conditions at the top and bottom of the model geometry to launch and absorb electromagnetic radiation. We implemented Floquet PBC's on the boundaries in the X and Y directions to approximate an optical cavity extending infinitely in the XY plane. We incorporated TBC's into the model to approximate the cavity's optically thin Ag layers.

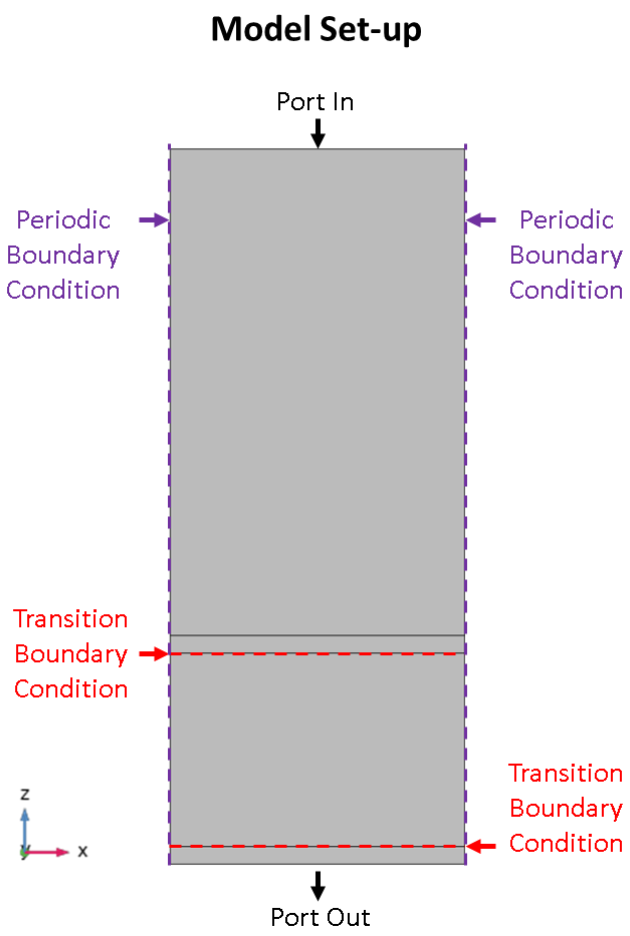

Figure 3.4 Boundary conditions used in the optical cavity models. Schematics of the model geometry used in the optical cavity simulations and the boundary conditions on their appropriate boundaries.

3.7.5 Modeling of Plasmonic Nanohole Arrays

We show a schematic of the model geometry used in the nanohole array simulations in **Figure 3.5**. We create a nanohole array characterized by its period (P) and hole diameter (d). The holes are defined as air, while the array is defined as metal. We define the dye/polymer film layer as the domain on top of the nanohole array. All physical domains are assigned the dielectric properties of the materials we model.

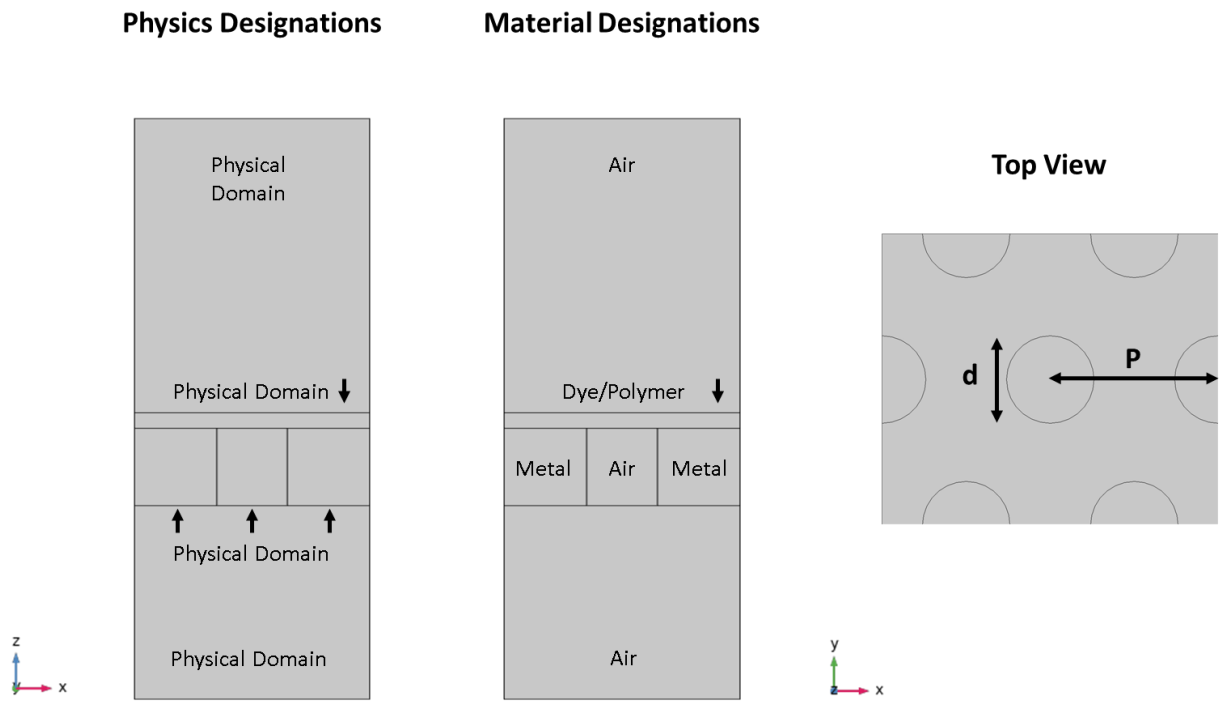

Figure 3.5 Physical/material designations and parameters for the nanohole array models. Schematics of the model geometry used in the nanohole array simulations. The physics designations show what portions of the model are real (physical domains) or virtual (PML domains). The material designations designate the material selection for each domain in the model. The diagram to the far right shows a top view of the nanohole array geometry indicating the array's diameter (d) and period (P).

We show the boundary conditions used in the nanohole array model in **Figure 3.4**. We set port boundary conditions at the top and bottom of the model geometry to launch and absorb electromagnetic radiation. We implemented Floquet PBC's on the boundaries in the X and Y directions to approximate a nanohole array extending infinitely in the XY plane.

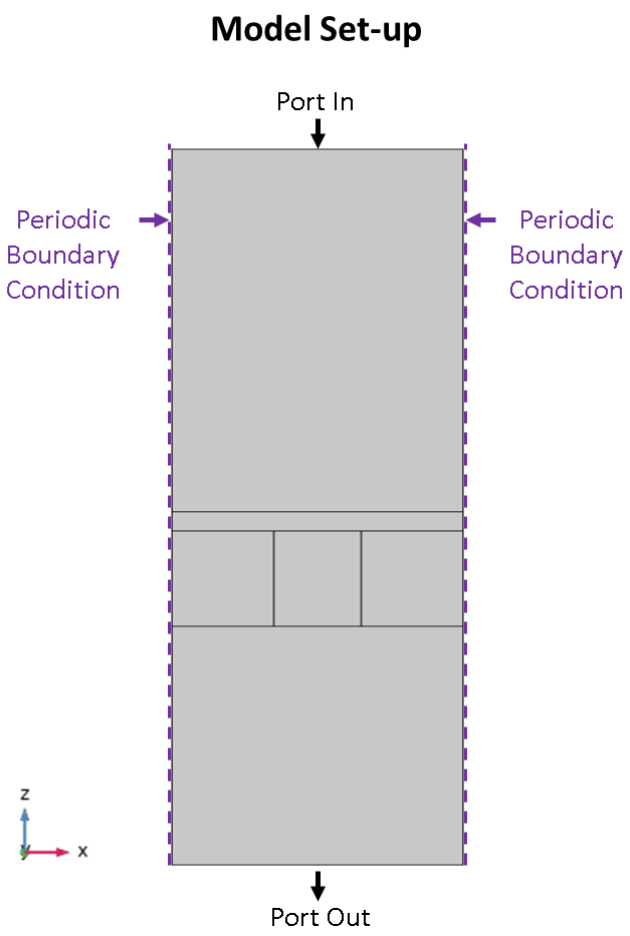

Figure 3.6 Boundary conditions used in the nanohole array models. Schematics of the model geometry used in the nanohole array simulations and the boundary conditions on their appropriate boundaries.

3.8 References

(1) Kelly, K. L.; Coronado, E.; Zhao, L. L.; Schatz, G. C. *J. Phys. Chem. B* **2002**, *107* (3), 668–677.

(2) Linic, S.; Christopher, P.; Ingram, D. B. *Nat. Mater.* **2011**, *10* (12), 911–921.

(3) Wiley, B.; Sun, Y.; Mayers, B.; Xia, Y. *Chem. – A Eur. J.* **2005**, *11* (2), 454–463.

(4) Sun, Y. *Science.* **2002**, *298* (5601), 2176–2179.

(5) Im, S. H.; Lee, Y. T.; Wiley, B.; Xia, Y. *Angew. Chemie* **2005**, *117* (14), 2192–2195.

(6) Minton, P. E. *Handbook of Evaporation Technology*; 1986.

(7) Scriven, L. E. *MRS Online Proc. Libr. 1988 1211* **2011**, *121* (1), 717–729.

(8) Spin Coating: Complete Guide to Theory and Techniques | Ossila https://www.ossila.com/pages/spin-coating (accessed Dec 7, 2021).

(9) Muller, D. A. *Nat. Mater. 2009 84* **2009**, *8* (4), 263–270.

(10) Pennycook, S. J.; Jesson, D. E. *Ultramicroscopy* **1991**, *37* (1–4), 14–38.

(11) XU, P.; Kirkland, E. J.; Silcox, J.; Keyse, R. *Ultramicroscopy* **1990**, *32* (2), 93–102.

(12) Friel, J. J.; Lyman, C. E. *Microsc. Microanal.* **2006**, *12* (1), 2–25.

(13) Rothen, A. *Rev. Sci. Instrum.* **2004**, *16* (2), 26.

(14) Perkampus, H. *UV-VIS Spectroscopy and Its Applications* ; Springer Science & Business Media, 2013.

(15) Stiles, P. L.; Dieringer, J. A.; Shah, N. C.; Van Duyne, R. P. *Annu. Rev. Anal. Chem.* **2008**, *1*, 601–626.

(16) Moskovits, M. *J. Raman Spectrosc.* **2005**, *36* (6–7), 485–496.

(17) Blackie, E. J.; Le Ru, E. C.; Etchegoin, P. G. *J. Am. Chem. Soc.* **2009**, *131* (40), 14466–14472.

(18) Le Ru, E. C.; Blackie, E.; Meyer, M.; Etchegoint, P. G. *J. Phys. Chem. C* **2007**, *111* (37), 13794–13803.

(19) Two,Three and Four Electrode Systems https://www.gamry.com/application-notes/instrumentation/two-three-four-electrode-experiments/ (accessed Dec 25, 2021).

(20) Douglas A. Skoog, F. James Holler, S. R. C. *Instrumental Analysis Principles*; 2018.

(21) Chronopotentiometry (CP) – Pine Research https://pineresearch.com/shop/kb/software/methods-and-techniques/galvanostatic-methods/chronopotentiometry-cp/ (accessed Dec 25, 2021).

(22) Advances in FDTD Computational Electrodynamics: Photonics and Nanotechnology https://books.google.com/books/about/Advances_in_FDTD_Computational_Electrody.html?id=ynRM33xslM8C (accessed Dec 7, 2021).

(23) Griffiths, D. J. *Introduction to Electrodynamics*; Prentice Hall, 1981.

(24) Reddy, J. N. *An Introduction to the Finite Element Method*; McGraw-Hill, 2005.

(25) Harish, A. What Is FEM & FEA Explained https://www.simscale.com/blog/2016/10/what-is-finite-element-method/ (accessed Dec 10, 2021).

Chapter 4 Controlling Energy Flow in Multimetallic Nanostructures for Plasmonic Catalysis

4.1 Publication Information

This work is a collaboration with Umar Aslam. The work presented in this chapter is a collaboration with Umar Aslam and is published as: Umar Aslam, Steven Chavez, and Suljo Linic. "*Controlling energy flow in multimetallic nanostructures for plasmonic catalysis*." Nature Nanotechnology, 12, 1000, 2017. The images in **Figure 4.1** and the data in **Figure 4.2** belong to Umar Aslam, and are included here for context. The simulation data presented throughout the rest of the chapter is solely my work and is my direct contribution.

I have adapted excerpts from the published work related to my contributions to fit the context of this chapter and added additional data/analysis. This chapter presents the work related to the initial discovery of how a plasmonic metal transfers the energy of visible light to a non-plasmonic metal for applications in plasmonic catalysis.

4.2 Summary

The photo-excitation of plasmonic metal nanoparticles (Ag, Au, and Cu) can directly induce photochemical reactions on their surfaces. However, the widespread application of this technology in catalysis is limited by the relatively poor chemical reactivity of noble metal surfaces. Despite efforts in combining plasmonic and catalytic metals, the physical mechanisms governing energy transfer from plasmonic metals to catalytic metals remains unclear. Here, we show that hybrid core-shell nanostructures in which a core plasmonic metal harvests visible light photons

can selectively channel that energy into catalytically active centers on the nanostructure shell. We developed a synthetic protocol to deposit a few monolayers of Pt onto Ag nanocubes to accomplish this. This model system allows us to conclusively separate the optical and catalytic functions of the hybrid nanomaterial and determine that energy flow is strongly biased towards the excitation of energetic charge carriers in the Pt shell.

4.3 Introduction

It has been recently demonstrated that plasmonic metal nanoparticles illuminated with relatively low-intensity light can perform photochemical transformations.[1–5] These discoveries have led to a new field of chemical conversion termed plasmonic catalysis. Plasmon-driven chemical conversion has been demonstrated mainly on noble metal nanoparticles (Au, Ag, and Cu) for some chemical transformations.[6–8] These nanomaterials exhibit strong localized surface plasmon resonance (LSPR), which is characterized by high extinction of light by these nanostructures and large electric fields at the surface of the nanostructures.[9–11] The combination of these two effects leads to high rates of formation of energetic charge carriers in the nanoparticles, which can result in chemical transformations.[12–14]

The central obstacle to expanding the use of plasmonic catalysis is that it has been limited to chemical transformations that can be performed only on the surfaces of the noble metals, which are inherently not very chemically reactive.[15,16] We and many others have been attempting to understand the nanoscopic mechanisms of plasmon decay in metallic nanoparticles, with the ultimate objective of controlling this decay process.[17–20] In particular, we were interested in designing functioning nanostructures where a plasmonic material concentrates the light energy and this energy is efficiently directed towards a more active catalytic material.

We recently conceptualized the design of such a hybrid plasmonic metal nanostructure.[21] We postulated that a hybrid nanostructure that would meet the critical requirements of such a system should contain a core plasmonic nanoparticle (a metal with low imaginary dielectric function at the LSPR (visible light) frequencies) surrounded by a very thin shell of a more chemically active material (catalytic surface sites), characterized by significantly larger imaginary dielectric function at the LSPR frequency. A material with these dielectric properties has two desired physical features: (i) due to the presence of a large plasmonic core, it can concentrate electromagnetic energy in the LSPR modes, and (ii) the energy stored in the LSPR modes can be selectively dissipated by forming energetic charge carriers (energetic e-h pairs) in the thin shell of the metal with the large imaginary dielectric function. We note that the larger imaginary dielectric function implies that the rate of energy dissipation (i.e., the decay of LSPR modes) through the formation of energetic charge carriers is larger compared to the material with a lower imaginary dielectric function.[22] We hypothesized that this hybrid nanostructure design would allow for a strong concentration of electromagnetic energy and its preferential dissipation through the surface atoms performing the chemical transformation. In addition to these dielectric considerations, the core and shell metals should not be miscible to preserve the core-shell architecture in reactive environments for practical catalytic applications.

In this contribution, we describe a systematic design of such a hybrid nanostructure in the form of Ag-Pt core-shell nanoparticles that contain a very thin shell (~ 1 nm) of epitaxially grown Pt on the surface of cubic Ag nanoparticles. We note that this model system, where plasmonic nanoparticles are completely covered by very thin shells of a catalytically active metal, is the ideal platform for performing these experiments as it allows for complete decoupling of optical and

catalytic functions. We also note that Ag and Pt exhibit the low and high imaginary dielectric function requirements presented in the previous paragraph (See **Figure S 1**).

We performed experimental and theoretical studies showing unambiguously that the optical energy collected at the LSPR conditions by these nanostructures is preferentially dissipated through the Pt shell where the chemical reaction takes place. The work in this chapter focuses on providing us with; (i) a clear pathway for marrying plasmonic and catalytic functions in one material which will allow us to expand the utilization of plasmonic catalysis that can be performed on materials different than the noble metals, and (ii) physical insights into the flow of energy in multicomponent plasmonic systems.

4.4 Results and Discussion

4.4.1 Nanoparticle Synthesis and Characterization

We synthesized hybrid nanostructures by developing a synthetic approach that completely surrounds Ag nanocube cores (~ 75 nm in length) with thin Pt shells (~ 1 nm thickness). To synthesize these core-shell nanostructures we developed a seed-mediated colloidal synthesis approach in which Ag nanocube seeds were coated with Pt by reducing a Pt-metal complex precursor onto the seeds. See **Section 4.7.2** and **Section 4.7.3** for complete synthesis details.

Geometry characterization studies presented in **Figure 4.1** unambiguously show that the synthesis approach yields Ag nanocubes covered by a thin Pt shell. A bright-field transmission electron micrograph (TEM) of a representative Ag-Pt core-shell nanocube is shown in **Figure 4.1a**. The high resolution TEM image in **Figure 4.1c** (atomic resolution in **Figure 4.1d**) shows that the Pt shell thickness in these nanoparticles was approximately 6 atomic layers, which corresponds to 1.2 ± 0.2 nm. A dark-field scanning transmission electron microscope (STEM) image of a core-shell nanoparticle is shown in **Figure 4.1e**. An energy-dispersive X-ray

spectroscopy (EDS) elemental line scan across a single representative nanoparticle (**Figure 4.1b**) and the EDS elemental mapping of Ag and Pt in **Figure 4.1f – h** show that Pt atoms are covering the Ag nanocube (75 nm edge length).

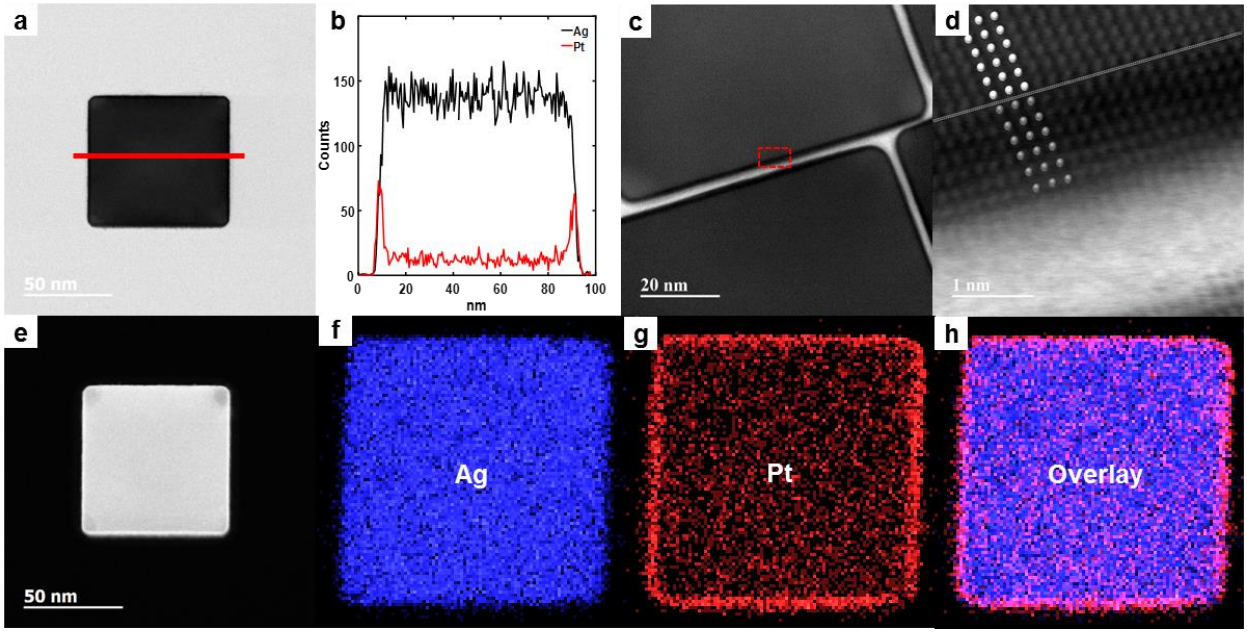

Figure 4.1 Characterization of Ag-Pt nanocubes. a) Bright-field TEM image of a single Ag nanocube coated with a thin layer of Pt. **b)** EDS elemental line scan taken along the red line in **(a)** demonstrating the elemental composition of the core and shell of the nanocube. **c-d)** High resolution and atomic-resolution bright-field TEM images. The thin Pt shell appears darker in contrast owing to the higher elemental weight of Pt. The Ag and Pt atoms are highlighted in **(d)** which clearly shows the boundary between the two materials. **e-h)** Dark-field STEM image of a representative core-shell nanocube and EDS elemental maps of Ag **(f)**, Pt **(g)**, and overlay of the two **(h)** demonstrating the complete coverage of Ag by Pt.

4.4.2 Characterizing the Plasmon Excitation and Decay Pathways

We analyzed the optical properties of these hybrid nanostructures by measuring their extinction, absorption and scattering characteristics and comparing them to the optical behavior of Ag nanocubes of identical size and shape (see **Section 4.7.4** for experimental details). Data in **Figure 4.2a** show that the introduction of the thin Pt shell on the Ag core only slightly affects the optical extinction of the nanostructure. The extinction peak due to the excitation of LSPR is preserved. Small shifts in the position and width of the LSPR peak compared to pure Ag nanocubes

are due to the Pt-induced changes in the dielectric environment from the presence of the Pt shell. Furthermore, we used an integrating optical sphere to measure the absorption and scattering of the pure Ag nanocubes and the Ag-Pt core-shell nanocubes. Data in **Figure 4.2b and Figure 4.2c** show that introducing even a very thin Pt shell fundamentally changes the dominant channel for plasmon decay. Data in **Figure 4.2b** show that photon scattering is the dominant pathway for plasmon decay in pure Ag nanocubes, consistent with previous measurements for Ag nanoparticles of this size.[23,24] Data in **Figure 4.2c** show that photon absorption (formation of energetic e-h pairs) becomes a critical plasmon decay pathway by introducing a thin Pt shell in our design. Based on these experimental data, we hypothesized that Pt introduces a faster plasmon decay channel through the Pt shell and that a large fraction of the electromagnetic energy concentrated in the nanostructure is dissipated through the thin Pt shell via the formation of energetic charge carriers (e-h pairs).

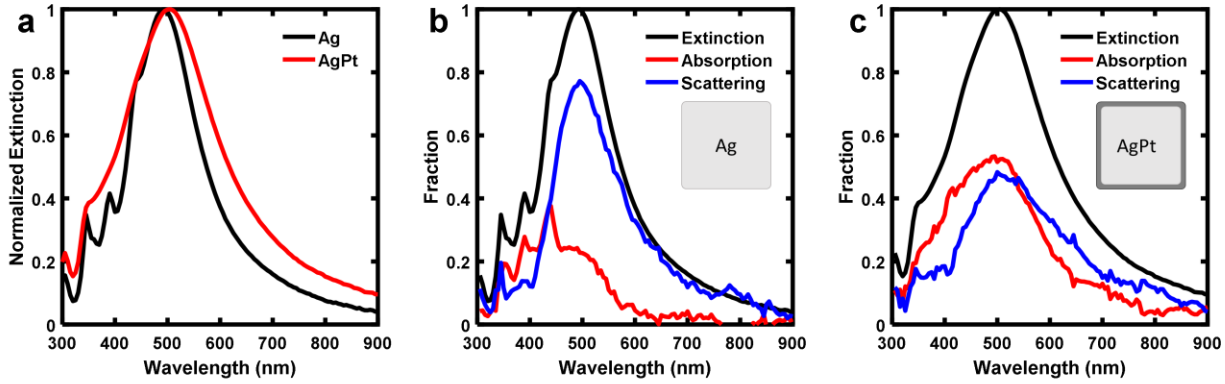

Figure 4.2 Experimental optical characteristics of Ag and AgPt core-shell nanocubes. a) Measured wavelength-dependent normalized extinction of the Ag nanocubes and Ag-Pt core-shell nanocubes. **b)** Measured wavelength-dependent fractional Ag nanocube absorption and scattering. **c)** Measured wavelength-dependent fractional Ag-Pt nanocube absorption and scattering.

To further shed light on the optical behavior of these systems, we performed electro-dynamic finite element method (FEM) simulations. The model system used in our FEM simulations is identical to the nanoparticle geometry measured in the TEM studies (See **Sections**

4.7.5 and 4.7.6 for simulation details). The calculated extinction, absorption and scattering characteristics of pure Ag and Ag-Pt core-shell nanocubes (**Figure 4.3a – c**) are fully consistent with the experimental measurements. They show that the extinction is mainly unchanged with introducing a thin Pt shell and that the absorption is more dominant in the nanomaterials that contain Pt than pure Ag.

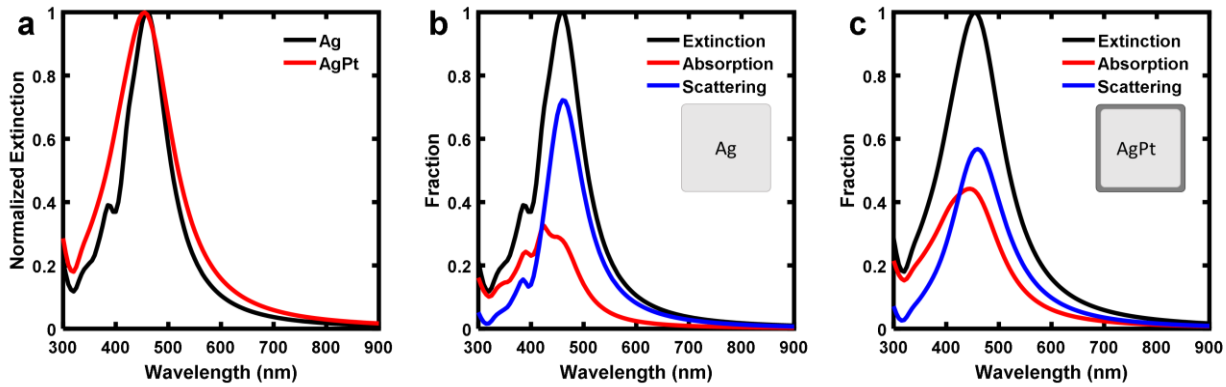

Figure 4.3 Simulated optical characteristics of Ag and AgPt core-shell nanocubes. a) Calculated wavelength-dependent normalized extinction of the Ag nanocubes and Ag-Pt core-shell nanocubes. **b)** Calculated wavelength-dependent fractional Ag nanocube absorption and scattering. **c)** Calculated wavelength-dependent fractional Ag-Pt nanocube absorption and scattering.

We have also used these simulations to analyze the power dissipated (i.e., the rate of photon absorption through the formation of energetic charge carriers, e-h pairs) through the thin Pt shell of an Ag-Pt core-shell nanocube. We compared them to an Ag shell of the equivalent dimensions on a pure Ag nanocube. Comparing the data in **Figure 4.4a – c**, we find that in the Ag-Pt nanoparticles, a large fraction of energy is dissipated through absorption in the Pt shell compared to pure Ag where the energy dissipated through absorption is relatively low at any part of the nanostructure. For example, FEM simulations show that for a Pt shell of 1.2 nm thickness on a core cube of Ag (edge length 75 nm) the rate of absorption per unit volume in the Pt shell is ~ 22 times larger than the rate of absorption in the core over the visible light wavelength range (300-900 nm). In comparison, for the same thickness of an Ag shell in an Ag nanoparticle of identical

size and shape, the rate of absorption per unit volume in the shell is only ~ 3 times larger than the rate of absorption in the core. We note that a similar analysis of our integrating sphere *experimental* data shows the rate of absorption per unit volume in a thin Pt shell (1.2 nm) was ~ 18 times larger than the rate of absorption in the Ag core, in relative agreement with the FEM simulations.

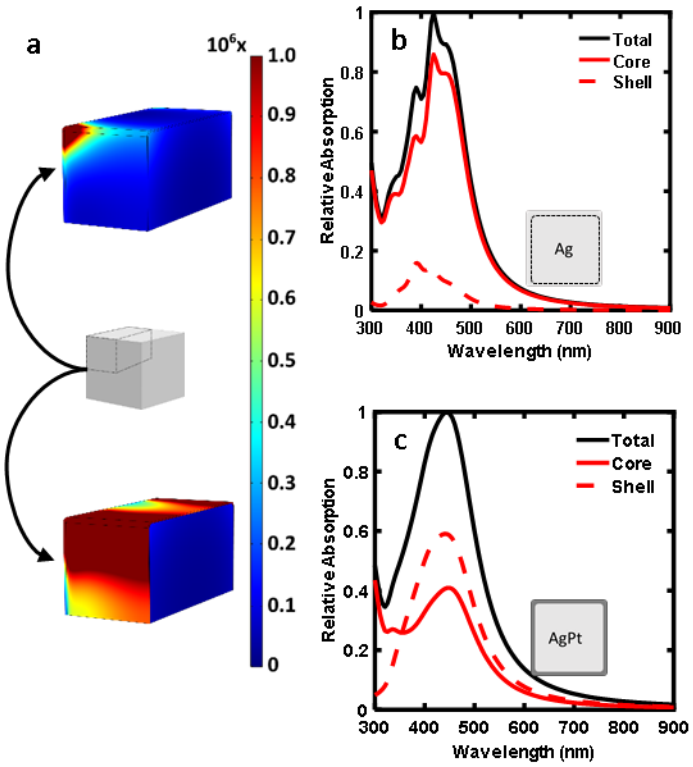

Figure 4.4 Absorption distribution in Ag and AgPt core-shell nanocubes. a) Calculated fractions of the Ag-Pt nanocube absorption and scattering. **b)** Heat maps of power dissipation per volume (W/m^3) at the LSPR peak (455 nm) for the Ag nanocube and at the LSPR peak (460 nm) for the Ag-Pt nanocube. The source field was 1 V/m at the resonant frequency, which for a free space amounts to 2.6 x 10^{-4} mW/cm^2. **c)** Fraction of power absorbed in the 75 nm thick "core" and the 1.2 nm thick "shell" of a pure Ag nanocube. Insert depicts the size of the Ag "core" and Ag "shell" **i,** Fraction of power absorbed in the 75 nm thick Ag "core" and the 1.2 nm thick Pt "shell" of an Ag-Pt nanocube. Inset depicts the size of the Ag "core" and Pt "shell".

4.4.3 Preliminary Analysis of the Energy Transfer Mechanism

For nanostructures of similar shape and size, the plasmon dephasing is governed by the material properties, specifically the value of the material's imaginary part of the dielectric function (referred to as ε_2 or Imag(ε) below). Materials with high ε_2 preferentially dissipate energy through

the excitation of electron-hole pairs but do so at the expense of a strong plasmonic response. On the other hand, plasmonic metals have an inherently low ε_2 at resonant frequencies, allowing them to exhibit strong LSPR (i.e., high fields) at the expense of their hot carrier generation probability. According to Equation 4.1, the absolute absorption in a material depends on a combination of both high ε_2 and high field strength:

$$A = \frac{1}{2}\int \omega\varepsilon_2|E(r)|^2 dr \qquad (4.1)$$

where ω is the frequency of the incoming light, and the integral is calculated over the volume of interest.[25] Our final objective was to use this equation to determine the mechanism for energy transfer from Ag to Pt in the Ag-Pt core-shell nanocubes.

The data in **Figure 4.5a** show the field enhancement calculated in the particle shells as a function of wavelength. As expected, monometallic Ag nanocubes have the highest field enhancements (due to strong LSPR excitation). The data show that coating the Pt shell on Ag significantly dampens the field enhancement (most likely due to slight plasmon dampening). In contrast, monometallic Pt cubes (used here as a reference) show no field enhancement in the simulated wavelength range. The data in **Figure 4.5b** show the effect of the material dielectric function. One can see that ε_2 has a significant effect on the product of ε_2 and $|E|^2$, which is directly proportional to the absorption in the shell via the equation above. Not surprisingly, the quantity plotted in **Figure 4.5b** maps one-to-one with the calculated power dissipated (photon absorption through the formation of electron-hole pairs) in the particle shells shown in **Figure 4.5c.**

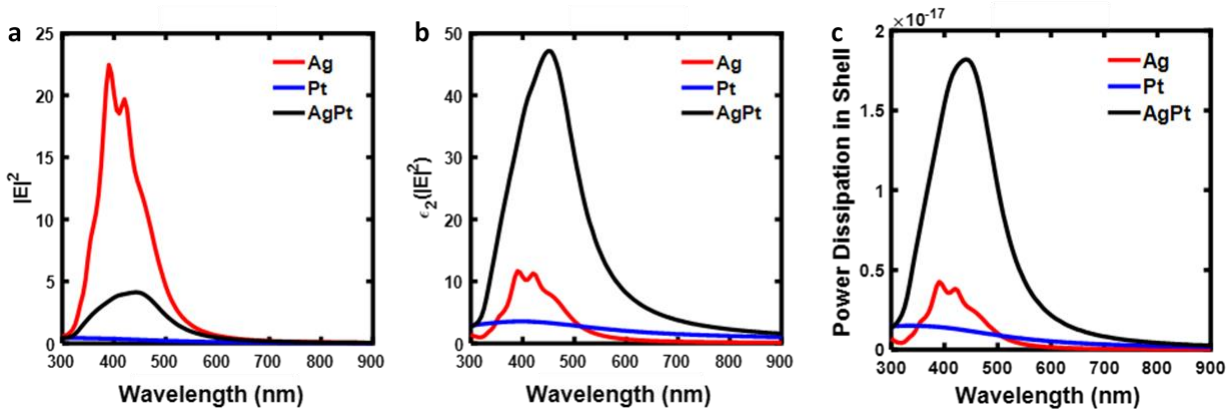

Figure 4.5 Preliminary energy transfer analysis of Ag and Ag-Pt nanocubes. a) Calculated field enhancements in the particle shells. **b)** Product of ε_2 and field enhancement in the particle shells. **c)** Calculated power dissipation as a function of wavelength in the particle shells.

4.5 Conclusion

Based on our experimental (**Figure 4.2**) and simulated (**Figure 4.2 and Figure 4.5b**) data, we can shed light on energy flow in these multicomponent systems. The incoming electromagnetic radiation excites LSPR of the multicomponent plasmonic nanostructures. This excitation results in high overall extinction and elevated electric field intensities near the surface of the nanoparticles. The energy of the LSPR is dissipated through various available dissipation pathways. These dissipation pathways include photon scattering and absorption events (excitation of energetic charge carriers) at various parts of the nanostructure. In metal nanoparticles, these scattering and absorption events have their characteristic rates, with direct, vertical electronic excitations (these are the excitations from d-states below the Fermi level to s-states above the Fermi level) being the fastest plasmon decay channel.[18,26] At visible photon energies, Ag does not allow for the direct, vertical d-to-s transitions since the d-states in Ag are well below the Fermi level, and these electrons cannot be excited by visible photons. On the other hand, Pt supports these fast electronic excitations. By positioning a few layers of Pt on an Ag nanoparticle, we effectively direct the LSPR energy towards selective dissipation through these Pt sites.

Furthermore, this LSPR-decay channel is also enhanced by the presence of very high LSPR-induced electric field intensities at the surface layers of these nanostructures. This energy flow concentrates a large fraction of electromagnetic energy in the surface Pt atoms, effectively "energizing" these active Pt surface sites.

In conclusion, we have demonstrated the ability to control the energy flow in plasmonic systems at the nanoscale through the targeted synthesis of multicomponent plasmonic nanostructures. By completely coating a plasmonic metal (Ag) nanocube possessing low imaginary dielectric function with a few atomic layers of a catalytic metal (Pt) possessing high imaginary dielectric function, a channel for plasmon decay was introduced, leading to the dissipation of light energy through the thin Pt shell. This well-defined model system allowed us to demonstrate plasmon-driven energy transfer to non-plasmonic surfaces via an ultrafast plasmon dephasing mechanism. We hypothesize that this could be similar to recently demonstrated "direct" energy/charge transfer processes recently demonstrates for plasmonic metal-molecule and metal-semiconductor systems.[18,27] We believe that the underlying physical concepts discussed in this work will motivate the rational design of other multicomponent plasmonic systems for controlling energy flow in plasmonic, energy harvesting, and photo-catalytic applications.

4.6 Acknowledgements

This work was primarily supported by the National Science Foundation (CBET-1437601 and CBET- 1702471). The synthesis was developed with the support by the U.S. Department of Energy, Office of Basic Energy Science, Division of Chemical Sciences (FG-02-05ER15686). Secondary support for the development of analytical tools used to analyze the data was provided by NSF (CBET-1436056 and CHE- 1362120). The electron microscopy measurements were supported by the University of Michigan College of Engineering and by NSF (DMR-0723032).

We also acknowledge the partial support of Technical University Munich – Institute for Advance Study.

4.7 Supporting Information

4.7.1 Imaginary Dielectric Function for Ag and Pt

The imaginary component of the dielectric function of a material describes the ability of the material to absorb electromagnetic energy. This is directly related to the electronic structure of the material. For the noble, plasmonic metals (Ag, Au, and Cu), the imaginary component of the dielectric function is small at the LSPR frequencies. This is due to the d-states of the noble metals lying completely below the Fermi level making direct, vertical d-to-s transitions impossible in most of the visible range, particularly for Ag. For many transition metals, the imaginary component of the dielectric function is relatively large through the entire visible range of the electromagnetic spectrum. This means that visible light photons have sufficient energy to excite interband (d-to-s) transitions in the materials. The imaginary component of the dielectric functions for Ag and Pt are shown in **Figure S *1*.** Imaginary dielectric function of Ag and Pt(data from Rakic et. al.).[28] This shows that Pt metal is much more likely to absorb visible light compared to Ag in the visible range (i.e. at LSPR frequencies of Ag).

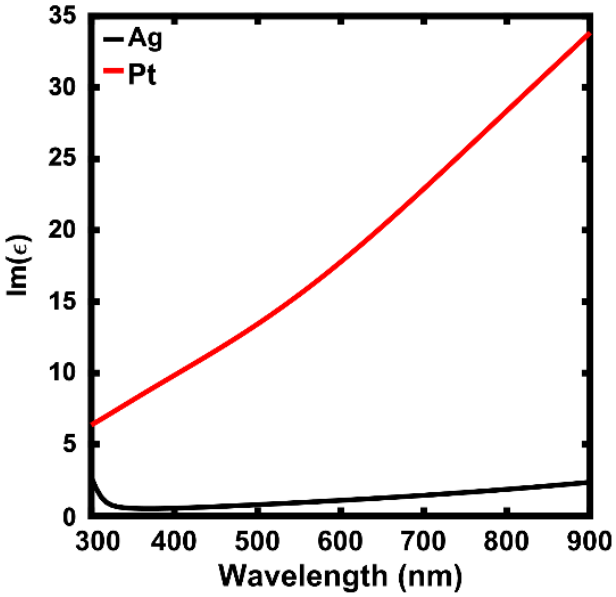

Figure S 1. Imaginary dielectric function of Ag and Pt

4.7.2 Ag Nanocube Synthesis

Ag nanocubes were prepared using a well-established colloidal synthesis in which ethylene glycol (VWR International, semigrade) served as the solvent and reducing agent, $AgNO_3$ (Acros Organics, ultrapure grade 99.5%) as the Ag precursor, and polyvinylpyrrolidone (PVP, MW=55,000 Sigma-Aldrich) as the polymeric stabilizing agent. A 20 mL glass vial was filled with 10 mL of ethylene glycol and allowed to heat at 140°C in a pre-heated oil bath. After 1 hour, 80 µL of a 36 mM aqueous HCl solution was added to the reaction vessel. Next, 5 mL of a 10 mg/mL solution of PVP in ethylene glycol was added to the reaction vessel followed by the addition of 2 mL of a 25 mg/mL solution of $AgNO_3$ in ethylene glycol. A ventilated cap was then placed on top of the reaction vessel to allow air into the reaction mixture, and the vessel was allowed to heat for ~24 hours. After ~24 hours, the reaction vessel is capped close to prevent O_2 from entering and allow Ag nanocubes to grow. After ~8 hours, the solution transmits a vibrant purple color characteristic of Ag nanocubes with an edge length of ~75 nm. The reaction vessel is quenched at

this point and washed via centrifugation with a 1:10 water-to-acetone mixture twice and re-dispersed in DI water.

4.7.3 AgPt Core-Shell Nanoparticle Synthesis

In a typical synthesis, $1/10^{th}$ of a solution of Ag nanocubes is diluted to 3 mL with water and is mixed with 50 mg of PVP. The Pt precursor is prepared fresh in a separate container by adding 12 mg of K_2PtCl_4 (Sigma Aldrich, 99.99%) to 16 mL of DI water. The reducing agent is also prepared in a separate container by adding 100 mg of ascorbic acid to 3 mL of DI water followed by the addition of 600 μL of an aqueous 1.25 M NaOH solution. The reducing agent mixture is then added to the reaction vessel. The Pt precursor solution is slowly added to the reaction vessel using a syringe pump at a rate of 4 mL/hr. Every 2 hours, 50 μL of an aqueous 1.25 M NaOH solution was added to the reaction vessel to maintain a high pH as the pH was found to decrease over time. After 4 hours, the nanoparticles are washed twice with DI water via centrifugation. To prepare enough nanoparticles for a catalyst, 10 individual syntheses were performed and combined. This synthesis strategy was motivated by other recent successes using different materials.

4.7.4 Experimental Optical Measurements

Ag-Pt core-shell nanoparticles for optical measurements were all synthesized from the same sample of Ag seed nanoparticles. Samples for optical measurements were prepared by diluting samples of Ag and Ag-Pt nanocubes in 3 mL of DI water in cuvettes. These samples were prepared to give roughly the same fractional extinction. A sample of just DI water was also prepared, and any contributions from the solvent were subtracted in all measurements. Extinction measurements were performed using a UV-vis spectrophotometer. The instrument passes

monochromated light through the sample and measures the fraction of light that is transmitted and the extinction fraction can simply be calculated as:

$$Extinction\ fraction = 1 - (transmission\ fraction)$$

The extinction fraction is the sum of the absorption fraction and scattering fraction. To decouple absorption from scattering, we use an optical integrative sphere combined with a monochromatic visible light source and photodiode detector. The optical integrative sphere is coated with a highly reflective coating which allows for the collection of scattered and transmitted light. The absorption fraction can be calculated from this data as:

$$Absorption\ fraction = 1 - (transmission + scattering\ fraction)$$

Lastly, the scattering fraction can be calculated as:

$$Scattering\ fraction = extinction\ fraction - absorption\ fraction$$

4.7.5 Finite Element Model Set-up

The extinction, absorption and scattering efficiencies, as well as the absorption ratios in the particle cores vs the particle shells were calculated using COMSOL Multiphysics finite-element based software. We utilized the '*Wave optics*' module to calculate the scattered field resulting from a plane wave incident on a model 3-D nanoparticle. The plane wave was defined as: $E = E_0 e^{-ikx}$ and was polarized in the z-direction. Core-shell nanocubes with a 75 nm core edge length and a 1.2 nm shell were defined and the free space wavelength range from 300 nm to 900 nm was simulated. The corners of the nanocubes in the simulations were smoothed to reflect the particle geometry observed in TEM characterization. Three different particles were simulated: pure Ag, pure Pt and Ag-Pt core-shell particles. Pure Ag and pure Pt were simulated by defining both the core and the shell of the particles as either Ag or Pt respectively. The optical data for Ag and Pt were taken from COMSOL's Optical Materials database (Rakic et. al) and a region of air was

defined around the particle by setting the real part of the dielectric function equal to 1. The width of the region of air around the particle was equal to half the wavelength of the incident plane wave and a perfectly matched layer (PML) was constructed to act as an absorber of the scattered field. Specific calculations are discussed in the following sections.

4.7.6 Simulated Optical Characterization

Calculating the extinction, absorption and scattering cross sections of these nanoparticles is important for determining both the LSPR wavelength as well as information on the dominant channel for plasmon decay. The absorption cross section as a function of wavelength was calculated by integrating the resistive heating losses over the volume of the nanoparticles. The scattering cross section as a function of wavelength was calculated by integrating the dot product of the scattered intensity vector and the normal vector pointing outwards from the particle surface across the entire particle surface. The extinction cross section was calculated by summing the absorption and scattering cross sections. The cross sections were then converted into efficiencies by dividing by the geometric cross section.

Figure S 2 shows the simulated extinction, absorption and scattering efficiencies for the pure Ag, pure Pt, and Ag-Pt core-shell nanoparticles. The LSPR peak for the monometallic Ag particle is around 475 nm and plasmon decay is dominated by radiative scattering. This agrees very well with the experimental optical data for Ag nanoparticles presented in the manuscript, with the experimental red-shift due to the higher dielectric environment of water. The data for monometallic Pt shows a much lower extinction efficiency than for Ag, as expected. The Ag-Pt particle shows a distinct LSPR peak at similar wavelengths to the pure Ag nanoparticle. The LSPR peak is also broadened compared to the Ag nanoparticle. These changes to the optical extinction of Ag nanoparticles coated with a thin layer of Pt are consistent with the changes observed

experimentally. The extinction efficiency is slightly lower for the Ag-Pt nanocubes compared to pure Ag nanocubes likely because of the dielectric properties of Pt metal.

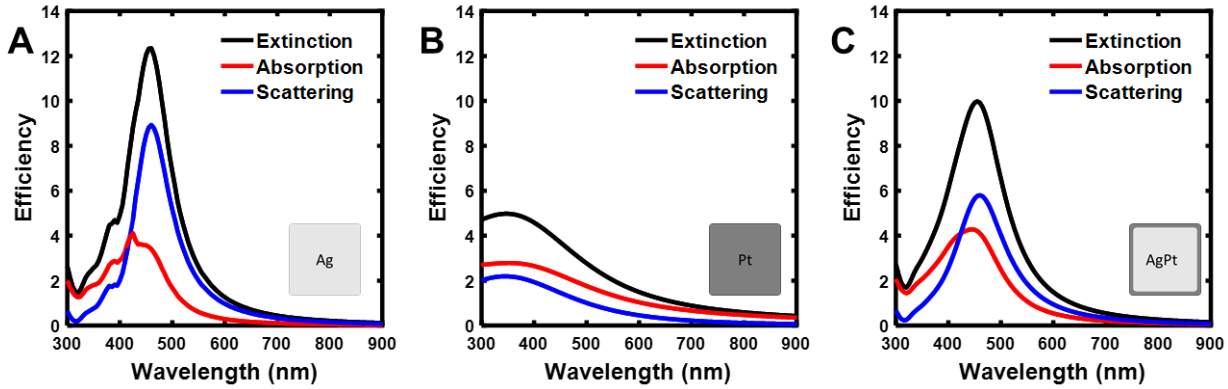

Figure S 2 Simulated optical efficiencies. Simulated, extinction, absorption and scattering efficiencies for: **a)** monometallic Ag; **b)** monometallic Pt; and **c)** core-shell Ag-Pt nanoparticles.

4.7.7 Absorption Ratio Calculations

The absorption in the particle core vs. the particle shell were calculated by integrating the resistive heating losses over volume of the core and the shell respectively. Data in **Figure S 3** show the calculated core vs. shell absorption ratios for the 3 particles (Ag, Pt and Ag-Pt core-shell) normalized by the maximum absorption in each case. The size of the core was 75 nm edge length and the size of the shell was 1.2 nm for all 3 particles. Data in **Figure S 3** show that in the pure Ag and Pt particle cases, photon absorption occurs primarily in the core of the particles across the wavelength range of interest. On the other hand, in the case of the Ag-Pt particles, a higher fraction of the absorption takes place in the Pt shell as opposed to the Ag core. These data show that coating Pt on Ag nanoparticles dramatically biases absorption to the thin Pt shell.

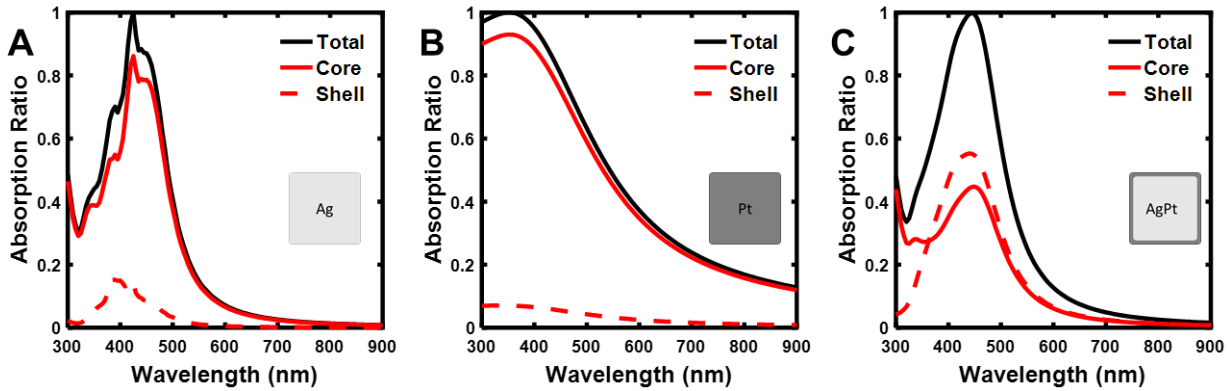

Figure S 3 Simulated absorption ratios. Simulated core-vs shell absorption ratios for: **a)** a Ag nanocube; **b)** a Pt nanocube; and **c)** a core-shell Ag-Pt nanocube.

We calculated the ratio of energy dissipation in the shell to the energy dissipation in the core from our optical simulations by integrating the total rate of absorption in the core and the shell with respect to photon energy and dividing by the respective volumes of the core and shell. This ratio of the rate of absorption per unit volume in the 1.2 nm Pt shell to the rate of absorption in the Ag core was 22.2. In contrast, the same calculation for a monometallic Ag nanocube showed that the rate of absorption per unit volume for a 1.2 nm Ag "shell" is only 2.9 times higher than the Ag core.

We estimated this shell-to-core energy dissipation ratio using our experimental integrative sphere data as well. This was done using the absorption data for Ag-Pt core-shell nanocubes with varying shell thickness. Assuming that the increase in absorption with increasing shell thickness was due only to the additional layers of Pt, we calculated an absorption per nm for the Pt shell. Using this, we calculated Pt shell absorption for a 1.2 nm thick shell. This shell absorption was subtracted from the total experimental absorption for Ag-Pt core-shell nanoparticles with 1.2 nm thick shells to give us the approximate absorption in the Ag core. Integrating the Pt shell and Ag core absorption with respect to energy and dividing by the respective volumes of the shell and core provides a total energy absorption in the shell and core per volume. We calculate an experimental

ratio of shell absorption to core absorption of 18.2 from this back-of-the-envelope calculation which is similar to the value calculated from the FEM simulations.

4.7.8 Calculation of Absolute Power Dissipation

In addition to calculating the ratio of the rate of absorption in the shell per volume to the rate of absorption in the core per volume for the Ag-Pt nanocube and Ag nanocube (the previous section), we calculated the absolute rate of absorption in the 1.2 nm Pt shell and compared it to the absolute rate of absorption in the equivalent shell of Ag in the pure Ag nanocube. This calculation shows that the rate of absorption in the thin Pt shell was 5.1 times larger than the rate of absorption in the equivalent Ag "shell". This means that 5 times more energy is dissipated through the surface layers of the Ag-Pt core-shell nanocube compared to the surface layers of pure Ag.

4.8 References

(1) Christopher, P.; Xin, H.; Linic, S. *Nat. Chem.* **2011**, *3* (6), 467.

(2) Mukherjee, S.; Libisch, F.; Large, N.; Neumann, O.; Brown, L. V; Cheng, J.; Lassiter, J. B.; Carter, E. A.; Nordlander, P.; Halas, N. J. *Nano Lett.* **2013**, *13* (1), 240–247.

(3) Kale, M. J.; Avanesian, T.; Christopher, P. *ACS Catal.* **2014**, *4* (1), 116–128.

(4) Kim, Y.; Dumett Torres, D.; Jain, P. K. *Nano Lett.* **2016**, *16* (5), 3399–3407.

(5) Xiao, Q.; Sarina, S.; Waclawik, E. R.; Jia, J.; Chang, J.; Riches, J. D.; Wu, H.; Zheng, Z.; Zhu, H. *ACS Catal.* **2016**, *6* (3), 1744–1753.

(6) Christopher, P.; Xin, H.; Marimuthu, A.; Linic, S. *Nat. Mater.* **2012**, *11* (12), 1044–1050.

(7) Marimuthu, A.; Zhang, J.; Linic, S. *Science* **2013**, *339* (6127), 1590–1593.

(8) Huang, Y. F.; Zhang, M.; Zhao, L. Bin; Feng, J. M.; Wu, D. Y.; Ren, B.; Tian, Z. Q. *Angew. Chemie Int. Ed.* **2014**, *53* (9), 2353–2357.

(9) Kelly, K. L.; Coronado, E.; Zhao, L. L.; Schatz, G. C. *J. Phys. Chem. B* **2002**, *107* (3), 668–677.

(10) Link, S.; El-Sayed, M. A. *J. Phys. Chem. B* **1999**, *103* (40), 8410–8426.

(11) Linic, S.; Christopher, P.; Ingram, D. B. *Nat. Mater.* **2011**, *10* (12), 911–921.

(12) Linic, S.; Aslam, U.; Boerigter, C.; Morabito, M. *Nat. Mater.* **2015**, *14* (6), 567–576.

(13) Manjavacas, A.; Liu, J. G.; Kulkarni, V.; Nordlander, P. **2014**.

(14) Sundararaman, R.; Narang, P.; Jermyn, A. S.; Goddard III, W. A.; Atwater, H. A. *Nat. Commun.* **2014**, *5*, 5788.

(15) Hammer, B.; Norskov, J. K. *Nature* **1995**, *376* (6537), 238–240.

(16) Hammer, B.; Nørskov, J. K. *Adv. Catal.* **2000**, *45*, 71–129.

(17) Boerigter, C.; Campana, R.; Morabito, M.; Linic, S. *Nat. Commun.* **2016**, *7*, 10545.

(18) Boerigter, C.; Aslam, U.; Linic, S. *ACS Nano* **2016**, *10* (6), 6108–6115.

(19) Brown, A. M.; Sundararaman, R.; Narang, P.; Goddard Iii, W. A.; Atwater, H. A. .

(20) Bernardi, M.; Mustafa, J.; Neaton, J. B.; Louie, S. G. *Nat. Commun.* **2015**, *6*, 7044.

(21) Linic, S.; Aslam, U.; Boerigter, C.; Morabito, M. *Nat. Mater.* **2015**, *14* (6), 567–576.

(22) Amendola, V.; Saija, R.; Maragò, O. M.; Iatì, M. A. *Nanoscale* **2015**, *7* (19), 8782–8792.

(23) David D. Evanoff, J. and; Chumanov*, G. *J. Phys. Chem. B* **2004**, *108* (37), 13948–13956.

(24) Langhammer, C.; Kasemo, B.; Zorić, I. *J. Chem. Phys.* **2007**, *126* (19), 194702.

(25) Christopher, P.; Moskovits, M. *Annu. Rev. Phys. Chem* **2017**, *6817*.

(26) Khurgin, J. B. *Nat. Nanotechnol.* **2015**, *10*.

(27) Wu, K.; Chen, J.; McBride, J. R.; Lian, T. *Science.* **2015**, *349* (6248), 632–635.

(28) Rakić, A. D.; Djurišić, A. B.; Elazar, J. M.; Majewski, M. L. *Appl. Opt.* **1998**, *37* (22), 5271.

Chapter 5 Design Principles for Directing Energy and Energetic Charge Flow in Multicomponent Plasmonic Nanostructures

5.1 Publication Information

The work presented in this chapter is published as: Steven Chavez, Umar Aslam, and Suljo Linic. "*Design principles for directing energy and energetic charge flow in multicomponent plasmonic nanostructures*." ACS Energy Letters, 3, 1590-1596, 2018.

Modifications have been made the published document to adapt the content to this text. This chapter generalizes the framework of energy transfer presented in the previous chapter to include all plasmonic metals and non-plasmonic metals.

5.2 Summary

The decay of localized surface plasmons supported by plasmonic metal nanoparticles results in the formation of energetic charge carriers within the nanoparticles. Once formed, these charge carriers can transfer to chemically attached materials where they can perform a function. The efficient extraction and utilization of these charge carriers in various applications hinges on the ability to design plasmonic nanostructures with highly localized charge carrier generation at specific locations in the nanostructure. Herein, we shed light on the physical mechanisms governing the flow of energy in resonantly excited multimetallic plasmonic nanoparticles. We demonstrate that coating plasmonic nanostructures with non-plasmonic metals can result in the preferential dissipation of energy (i.e. formation of charge carriers) in the non-plasmonic metal, and that the extent of this dissipation depends heavily on the electronic structure of the constituent

metals. We use experimental and modeling studies of various core-shell nanostructures to develop a transparent physical framework of energy transfer in these systems and discuss how this framework can be used to engineer nanostructures that allow for high efficiencies of charge carrier extraction.

5.3 Introduction

Plasmonic metal nanoparticles are promising platforms for manipulating the flow of electromagnetic energy at the nanometer length scale. Upon light illumination, incoming electromagnetic radiation interacts with the delocalized, free electrons of the metallic nanoparticles, resulting in the excitation of localized surface plasmon resonance (LSPR).[1–4] LSPR acts to confine the energy of incoming radiation in the form of amplified electromagnetic fields at the surface of the nanostructure.[5–7] The energy of these elevated fields is dissipated either through radiative scattering of photons or non-radiative excitation of energetic charge carriers (i.e. absorption) in the metal nanoparticle.

There is growing interest in developing a deeper understanding of the energy dissipation pathways in resonantly excited plasmonic nanoparticles with the ultimate aim of designing plasmonic nanostructures that offer a high degree of control over the LSPR decay process in terms of: 1) the partitioning of energy between absorption and scattering and, 2) the spatial distribution of the absorption process.[8–13] For example, manipulating the location of charge carrier excitation (photon absorption) in terms of surface versus bulk excitations is critical in a number of applications, including plasmonic photocatalysis[14–21] plasmon-enhanced photovoltaics[22–25], plasmonic heating[26–28], and photothermal cancer therapy[29–33]. Ideally, these high energy charge carriers would be generated close to the particle surface to minimize their energy loss within the nanoparticle before their extraction.

We recently described the design of a hybrid bimetallic plasmonic nanostructure that allows for a high degree of control over the LSPR decay mechanism in terms of absorption/scattering ratios and the location of the absorption process.[34] In these nanostructures, a very thin shell (1 nm) of a non-plasmonic metal (Pt) was coated onto a larger plasmonic nanoparticle core (75 nm Ag cube). We showed that the energy concentrated via LSPR excitation in the core-shell nanoparticle was preferentially dissipated through the absorption process in the thin Pt shell (i.e. within ~1 nm of the bimetallic nanoparticle surface), increasing the extraction probability of the energetic charge carriers.

Herein, we focus on analyzing the physical framework describing the flow of energy in multimetallic plasmonic nanoparticles. We systematically investigate, through experimental and modeling approaches, the LSPR decay mechanisms in Ag-Pt and Au-Pt core-shell nanoparticles of different shapes and sizes. We demonstrate that the nanoparticle size significantly impacts the plasmon decay pathways, where particle sizes supporting higher electric field intensities at the nanoparticle surface direct more energy to Pt. We also show that the choice of plasmonic metal (Ag vs. Au) strongly impacts the LSPR energy dissipation pathways. We demonstrate that unlike for the Ag-Pt nanoparticles where the energy is dissipated through the Pt shell for all LSPR wavelengths, for the Au-Pt system a significant biasing of the particle absorption in Pt is only achieved at the LSPR wavelengths where the Au interband transitions are inaccessible. Collectively, these studies have allowed us to develop a transparent physical mechanism for the LSPR decay in multimetallic plasmonic nanostructures.

5.4 Results and Discussion

5.4.1 Synthesis and Characterization of AgPt Nanocubes of Varying Size

Ag nanocube seeds of varying sizes were synthesized using an established polyol method and characterized using high-angle annular dark field scanning transmission electron microscopy (HAADF-STEM).[35,36] The Ag nanocube seeds used in this study were ~ 40 nm in edge length (small particles) and ~110 nm in edge length (large particles). A thin layer of Pt was subsequently coated onto the surface of the Ag seeds using a recently reported method.[37] Dark field STEM images of the small and large Ag-Pt nanocubes are shown in **Figure 5.1a** and **Figure *5.1*e**. Energy dispersive X-ray spectroscopy (EDS) elemental maps of the particles (**Figure 5.1b – d** and **Figure 5.1f – h**) show complete coverage of the Ag nanocubes cores by the Pt shell. The average thickness of the Pt shell was determined to be 1.4 nm from the STEM images.

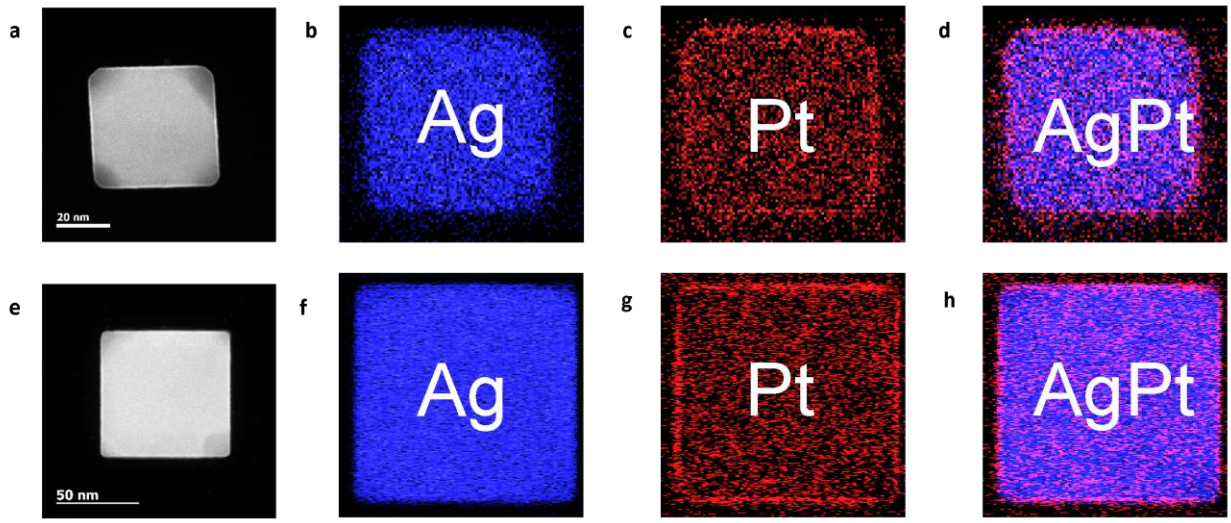

Figure 5.1 Characterization of AgPt nanocubes of varying sizes. a-d) Dark field STEM image of a representative small Ag-Pt nanocube. The average edge length of the nanocubes was ~41±3 nm **(a)** EDS elemental maps of Ag **(b)** Pt **(c)** and their overlay **(d)**. **e-h)** Dark field STEM image of a representative large Ag-Pt nanocube. The average edge length of the nanocubes was ~111±1 nm **(e)** and EDS elemental maps of Ag **(f)** Pt **(g)** and their overlay **(h)**.

We measured the optical extinction, absorption and scattering spectra of the small and large Ag and Ag-Pt nanocubes using transmission UV-vis spectroscopy and an optical integrating

sphere. The data in **Figure 5.2a** show that for the small Ag nanocubes, excited plasmons decay approximately equally through scattering and absorption, while the data in **Figure 5.2c** show that scattering is the dominant decay channel for larger Ag nanocubes. Comparing the extinction, absorption and scattering of monometallic Ag nanocubes (**Figure 5.2a, c**) to that of Ag-Pt nanocubes (**Figure 5.2b, d**), it is clear that the absorption/scattering ratio increases significantly upon the introduction of the thin Pt shell for both large and small particles. Together, the data from these optical measurements (**Figure 5.2a – d**) show that coating plasmonic Ag nanocubes with Pt alters the LSPR decay pathway leading to significantly more absorption as opposed to scattering. We have shown previously that these changes in the absorption to scattering ratio are due to an increased absorption in Pt compared to Ag, i.e., the plasmon energy is dissipated by absorption directly in the Pt shell.[34]

5.4.2 Experimental Absorption Analysis of AgPt Nanocubes of Varying Size

To investigate how the particle size affects the rate of energy dissipation through Pt, we estimated the experimental ratio of the volume-normalized absorption in the Pt shells for the two particle sizes. This is essentially a measure of the effectiveness of these bimetallic systems at dissipating electromagnetic energy through the Pt surface layers (i.e., the surface sites). We can crudely approximate this ratio using the following equation:

$$\frac{Pt_{Abs,40}}{Pt_{Abs,110}} \approx \frac{A_{AgPt,40} - A_{Ag,40}}{V_{Pt,40}} * \frac{V_{Pt,110}}{A_{AgPt,110} - A_{Ag,110}} \tag{5.1}$$

where $A_{Ag,40}$ and $A_{AgPt,40}$ are the experimental absorption for the small Ag and Ag-Pt nanocubes, A_{Ag110} and $A_{AgPt,110}$ are the experimental absorption for the large Ag and Ag-Pt nanocubes, and $V_{Pt,40}$ and $V_{Pt,110}$ are the volumes of the small and large Pt shells respectively. The data in **Figure 5.2e** show that the Pt-shell volume-normalized absorption ratio in the small versus large

nanoparticles is significantly larger than 1 below ~ 640 nm and that it reaches close to 1 above this wavelength. This analysis suggests that below the wavelength of ~ 640 nm, the smaller nanoparticles are much more effective in driving energy to the Pt shell.

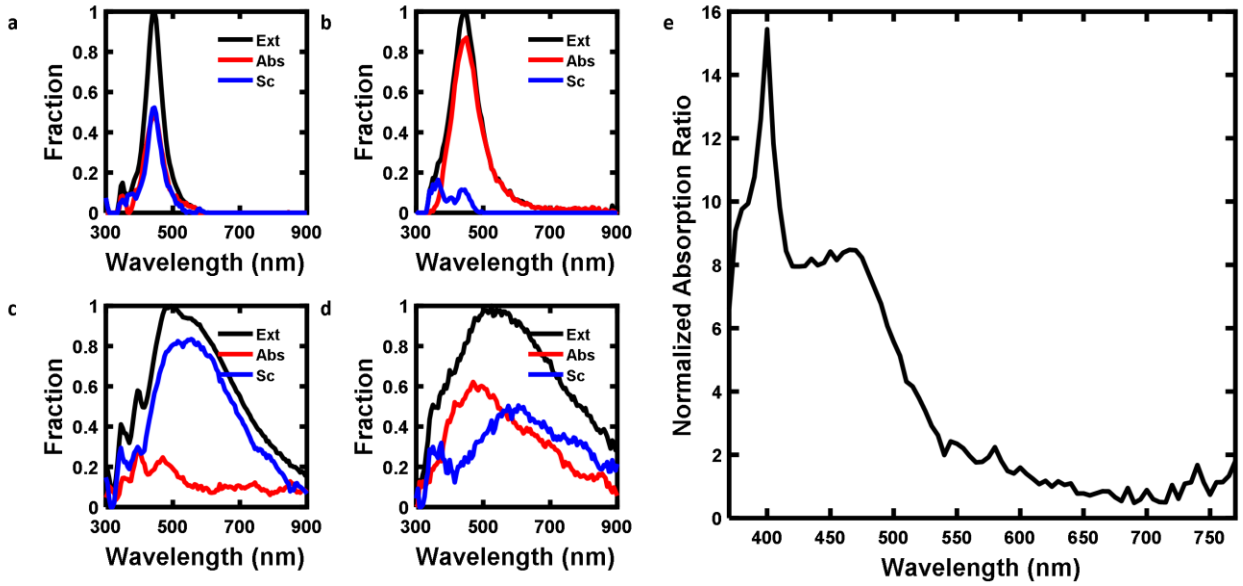

Figure 5.2 Experimental optical characterization of Ag and AgPt nanocubes of varying sizes. a-d) Measured fractional extinction, absorption and scattering of **(a)** small Ag cubes, **(b)** small Ag cubes coated with ~1.4 nm of Pt, **(c)** large Ag cubes, **(d)** large Ag cubes coated with ~1.4 nm of Pt; **e)** Experimental volume-normalized absorption ratio in the Pt shells of the small to large particles.

5.4.3 Theoretical Absorption Analysis of AgPt Nanocubes of Varying Size

To shed light on the experimentally observed difference in the rate of energy dissipation in the surface Pt atoms as a function of particle size, we performed finite element method (FEM) simulations on the systems of interest (simulation details provided in Supplemental Information **Section 5.7.4)**. The simulated optical characteristics (extinction, absorption, and scattering) of both small and large nanocubes (**Figure S 5a-d**) are consistent with the experimental measurements (**Figure 5.2a – d**), showing that the nanoparticle absorption increases upon depositing Pt onto the surface of the Ag nanocube seeds. Since the FEM simulations allow us to compute the absorption in the different parts of the hybrid nanostructures, we also calculated the fractional absorption in

the Pt shell vs the Ag core for each particle size and compared it to a pure Ag particle with a fictitious Ag 'shell' of the dimensions equal to the Pt dimensions in the Ag-Pt nanocubes. The fractional absorption for small (**Figure 5.3a**) and large Ag nanocubes (**Figure 5.3c**) show that for pure monometallic Ag, absorption occurs mainly in the particle core, i.e., a relatively small fraction of energy is absorbed by the few Ag layers close to the surface of the nanoparticles. It is clear that upon deposition of the Pt shell, the particle absorption is moved to the Pt shell for both small (**Figure 5.3b**) and large Ag-Pt nanocubes (**Figure 5.3d**). Furthermore, by normalizing the simulated wavelength-dependent absorption in the Pt shell by the shell volume for the different particle sizes (See Supplemental Information for calculation details), we computed the wavelength dependent absorption ratio in the Pt shell for the two particle sizes. These data show that the absorption in the Pt shell is significantly greater in the small nanoparticles at short wavelengths (less than ~ 560 nm). These simulation results (**Figure 5.3e**) are qualitatively consistent with the experimental analysis (**Figure 5.2e**), showing that small particles dissipate significantly more optical energy per unit volume of Pt than the large particles.

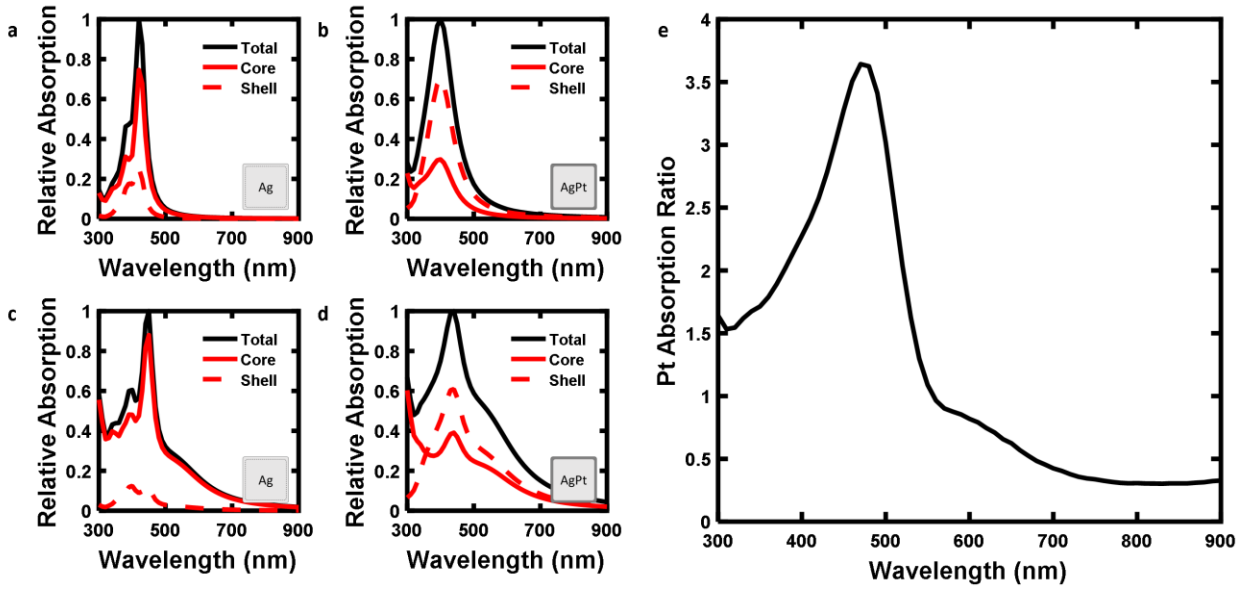

Figure 5.3 Simulated absorption analysis of Ag and AgPt nanocubes of varying sizes. a-d) Relative absorption fractions in the core vs. the shell for **(a)** a 40 nm Ag cube with a 1.4 nm thick Ag shell (**b)** a 40 nm Ag cube with a 1.4 nm thick Pt shell **(c)** a 110 nm Ag cube with a 1.4 nm thick Ag shell (**d)** a 110 nm Ag cube with a 1.4 nm thick Pt shell. **e)** Simulated volume-normalized absorption ratio in the Pt shell of the small to large particles.

5.4.4 Proposing an Energy Transfer Model – Electric Field and Dielectric Function Analysis of AgPt Nanocubes

One feature of plasmonic nanoparticles that is size-dependent at the conditions of LSPR is the intensity of the electric field at the surface of the nanoparticles.[8,38] To investigate the role of the field enhancement on the LSPR decay mechanism, we used the FEM simulations to calculate the average electric field intensity $|E|^2$ at the particle surface as a function of wavelength for both large and small Ag nanocubes (**Figure 5.4a**). These data show field intensity, $|E|^2$, is significantly greater for small Ag nanocubes for the wavelengths at which the ratio of the volume-normalized absorption in the Pt shell of small to large particles (**Figure 5.3e**) is large. This direct mapping between the field intensity and the rate at which energy is deposited into the Pt surface layers suggests that the electric fields generated at the surface of plasmonic particles at LSPR excitation

frequencies play an important role in determining the rate at which the energy is transferred between the plasmonic nanostructure and an attached medium (in this case Pt).

Our data in **Figure 5.2** also show that for a fixed particle size (either 40 or 110 nm) and shape, the ratio of absorption to scattering increases for the Pt coated particles compared to the pure Ag nanostructures. These observations cannot be entirely explained by the E-field intensity around the Ag plasmonic particles, and it is critical to examine additional factors, such as the electronic structure of Pt and Ag. Optical electronic excitations in metals can take place through either the excitation of *s*-electrons below the Fermi level (E_f) to unoccupied *s*-states above E_f (intraband transitions) or through direct excitations of *d*-electrons below E_f to unoccupied *s*-states above E_f (interband transitions).[39] The probability of these optical excitations in a material is described by the imaginary part of the material's dielectric function (ε_2).

The imaginary part of the Pt and Ag dielectric functions are shown in **Figure 5.4b**.[40] It is clear that at the LSPR wavelengths, Pt has a significantly larger ε_2 than Ag. This essentially means that under an identical set of conditions (e.g. identical optical field), the probability of a photon being absorbed by a Pt atom is significantly larger than the probability for photon absorption by an Ag atom. The main reason for this is that Ag is a d^{10} metal characterized by a populated *d* band lying far below E_F.[41] As a consequence, the excitation of *d*-electrons to *s* states just above E_f (interband transitions) requires higher energy photons than those provided at the LSPR wavelengths. Therefore, electronic excitations in Ag at these wavelengths are dominated by transitions between *s* states (intraband transitions), which require a third body to conserve momentum and are therefore characterized by low oscillator strengths (leading to low ε_2).[39]

On the other hand, the *d* states for Pt are not completely full (Pt is a d^9 metal) and the *d* band intersects E_F.[42] This means the *d*-to-*s* (interband) transitions in Pt can be activated at the

LSPR wavelengths. In contrast to intraband transitions, interband transitions are direct, momentum conserved excitations, and are the main contributors to ε_2 of metals when available.[39,43] The availability of these transitions in Pt at visible wavelengths results in the large value of ε_2 for Pt compared to Ag.

In **Figure 5.4c** we plotted the wavelength-dependent ratio of the Pt and Ag dielectric functions.[40] These data show that the value of ε_2 for Pt is between 15-18 times larger than the value for Ag in the visible range. To study the effect of this difference in ε_2 for Ag and Pt, we compared the shell absorption in a Ag-Pt core-shell nanocube to the absorption in the surface layers of a pure Ag nanocube of the same size. The data in **Figure 5.4d** show that the rate of absorption is always larger for a Pt shell compared to the Ag shell for an otherwise identical particle. This suggests that in these systems where a plasmonic nanoparticle core is covered with a thin shell of a non-plasmonic metal, shell metals having a large value of ε_2 relative to the plasmonic metal open up a rapid LSPR dissipation pathway through the shell metal.

We hypothesize that the availability of inherently fast direct electronic transitions (d to s) in these metals acts as a preferential decay pathway for the electric field energy stored at the nanoparticle surface under LSPR conditions. Physically, this manifests itself as highly efficient

energy transfer from the plasmonic core to the non-plasmonic metal shell via direct absorption in the shell metal, which is characterized by a larger ε_2 relative to the plasmonic metal.

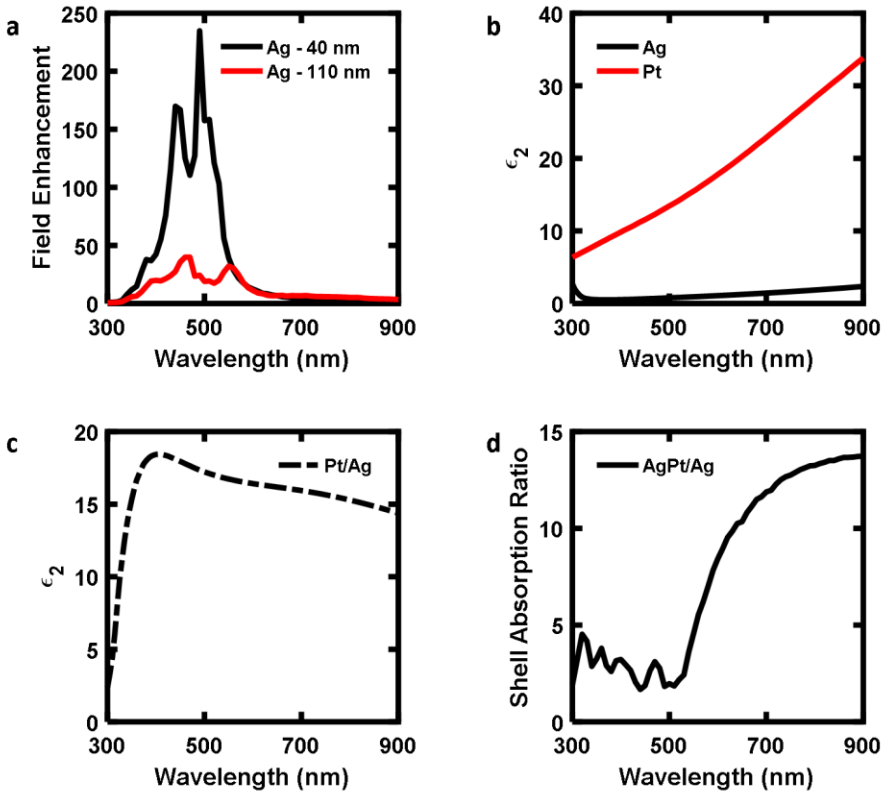

Figure 5.4 Electric field and dielectric function analysis. a) Enhancement of the electric field intensity at the particle surface as a function of wavelength for small and large Ag nanocubes; **b)** Imaginary part of the dielectric function for Ag and Pt as a function of wavelength. Dielectric data taken from ref 18; **c)** Wavelength dependent ratio of the imaginary dielectric function of Pt with Ag; **d)** Ratio of the calculated shell absorption for AgPt/Ag for the 40 nm particles.

5.4.5 Extending the Energy Transfer Model – Analysis of Au and AuPt Nanocubes

The analysis above paints a comprehensive picture of the photon absorption in multimetallic structures under LSPR conditions and informs us about how to design multifunctional materials that can guide the process of photon absorption to a particular spot in the material (i.e., the surface layers). It is clear that any such multicomponent material needs to be able to: (i) concentrate the electric field to the surface, which can be accomplished by the plasmonic

component at the LSPR wavelengths, and (ii) have another component at the surface (where the fields are high) characterized by a high imaginary part of the dielectric function relative to the plasmonic component at the LSPR wavelengths. To further probe this model, we used the FEM modelling to analyze the optical characteristics of a 75 nm Au nanocube coated with 1 nm of Pt. This model system is analogous to the Ag-Pt core-shell system with Au substituted in place of Ag as the plasmonic metal core. The data in **Figure 5.5a** show the LSPR peak at ~ 550 nm for these Au and Au-Pt nanocubes. The data in **Figure 5.5a** and **Figure 5.5b** show that, unlike in the Ag-Pt case, coating the Au nanocube with Pt does not significantly alter the plasmon decay pathway (i.e. absorption vs scattering).

Additionally, the absorption fraction data in **Figure 5.5c** and **Figure 5.5d** show that the presence of the thin Pt shell results in only a marginal biasing of the plasmon decay pathway towards absorption in the Pt shell. This behavior is in contrast to that observed for the Ag-Pt nanoparticles (**Figure 5.2** and **Figure 5.3**) where the Pt shell provided a very effective pathway for plasmon decay via absorption. The key difference between Au and Ag is that Au has a higher ε_2 at these LSPR wavelengths as shown in **Figure 5.5e**, where the ratio of ε_2 of Pt to Au as a function of wavelength is plotted. The data show that at ~550 nm the ratio of ε_2 for Pt and Au is relatively low compared to the large ratios in ε_2 for Ag and Pt (**Figure 5.4c**). According to the model described above, this low ratio in the imaginary part of the dielectric function of Pt and Au indicates that a significant portion of the LSPR energy will be dissipated through absorption in Au, i.e., this Au particle geometry is not effective in driving energy into the surface Pt layers.

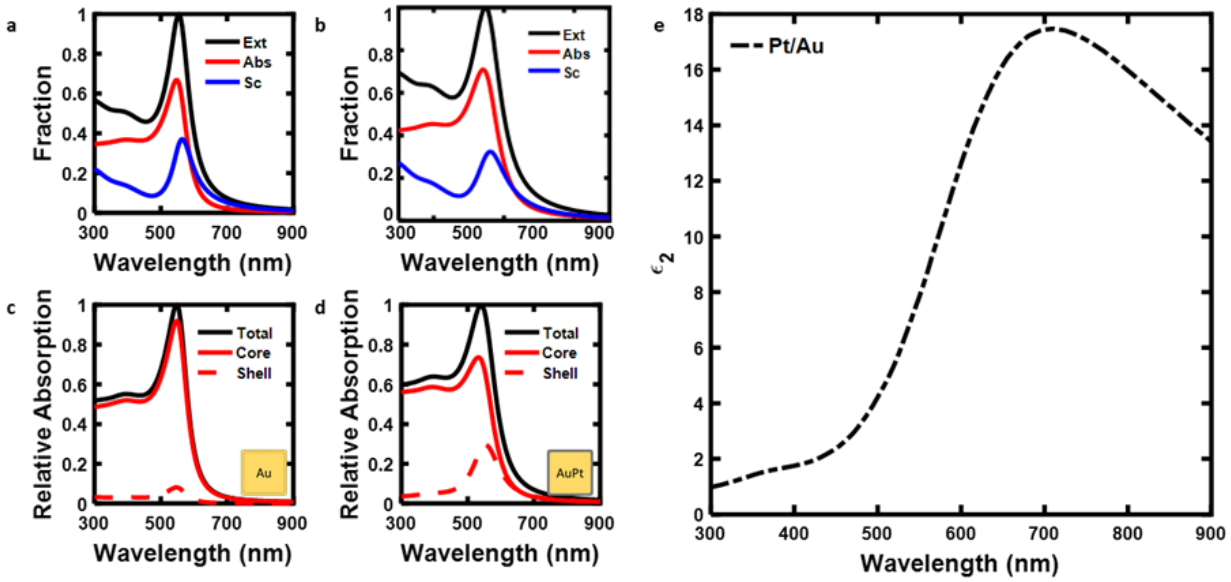

Figure 5.5 Energy transfer analysis of Au and AuPt nanocubes. a) Calculated extinction, absorption and scattering fraction of a 75 nm edge length Au nanocube with a 1 nm Au shell; **b)** Calculated extinction, absorption and scattering fraction of a 75 nm edge length Au nanocube with a 1 nm Pt shell; **c,d)** Relative absorption fractions in the core vs. the shell for c) a 75 nm Au cube with a 1 nm thick Au shell; d) a 75 nm Au cube with a 1 nm thick Pt shell.; **e)** Wavelength dependent ratio of the imaginary dielectric function of Pt with Au.

5.4.6 Extending the Energy Transfer Model – Analysis of Au and AuPt Nanorods

The model proposed above also suggests that moving the LSPR excitation frequency of the plasmonic Au core to longer wavelengths, where the ratio of Pt to Au ε_2 is high (**Figure 5.5e**), should preferentially direct more energy into the Pt shell. To probe this, we used the FEM modelling to examine the behavior of a 20 nm by 80 nm Au nanorod coated with either 1 nm of Au, or 1 nm of Pt. Plasmonic metal nanorods display two LSPR modes, a transverse mode with excitation frequencies at short wavelengths and a longitudinal mode with excitation frequencies at long wavelengths.[44,45] By varying the polarization of incident light in the FEM model, we can tune the LSPR frequency to regions where the ratio Pt to Au ε_2 is low/high, and can therefore study how the plasmon decay pathways are affected by the ratio of ε_2 of the constituent materials.

The data in **Figure 5.6** show the normalized total absorption (solid lines) of the pure Au and Au-Pt nanorod as well as the fractional absorption in the 1 nm Au shell of the pure Au nanorod

and the 1 nm Pt shell of the Au-Pt nanorod (dotted lines) undergoing either longitudinal or transverse plasmon excitation. For the pure Au nanorod undergoing transverse plasmon excitation (**Figure 5.6a**), the shell absorption makes up a very low fraction of the total particle absorption. The same conclusions can be drawn for the pure Au nanorod undergoing longitudinal plasmon excitation (**Figure 5.6b**). The data show that when Pt is coated on the nanorod, the flow of energy is strongly dependent on which plasmon mode is excited. The data in **Figure 5.6c** show that the transverse plasmon peak for the Au-Pt nanorod is located at ~480 nm where the ratio of ε_2 for Pt to Au is low. As a result, very little of the energy dissipation is moved to the Pt shell for the Au-Pt nanorod when this plasmon mode is excited. On the other hand, exciting the longitudinal plasmon mode shifts the LSPR wavelengths to regions where the Pt to Au ε_2 ratio is high. The data show that for the excitation of this plasmon mode, a significant amount of the particle absorption comes from absorption directly in the Pt shell. Together, these data suggest that LSPR energy can be dissipated through the non-plasmonic metal shell when the value of ε_2 of the non-plasmonic metal is high relative to the plasmonic metal at the LSPR frequencies.

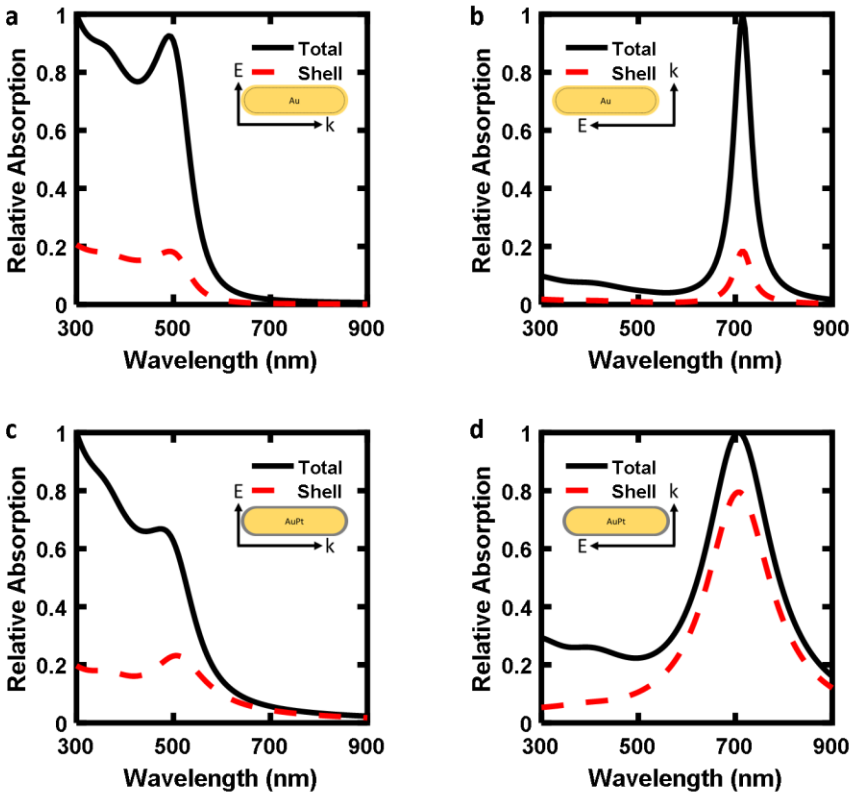

Figure 5.6 Absorption analysis of Au and AgPt nanorods. Relative absorption fractions of a Au and Au-Pt nanorod with a width of 20 nm coated with a 1 nm Au shell and 1 nm Pt shell respectively. The nanorod length was 80 nm, corresponding to an aspect ratio (AR) of 2. The Au nanorod was illuminated with a plane wave polarized in the transverse direction (**a**) and in the longitudinal direction (**b**); the corresponding Au-Pt data for transverse and longitudinal polarizations are shown in **(c)** and **(d)**; In all panels, the black solid lines represent the total particle absorption (normalized by the maximum absorption) and the red dotted lines represent the contribution of the total absorption that is attributed only to the shell. The insets depict the light propagation vector (k) and E-field polarization vector (E).

5.5 Conclusion

The results presented herein paint a clear picture of the physical mechanism governing energy transfer in multimetallic plasmonic nanostructures. By studying core-shell nanoparticles of varying size, shape and composition we demonstrated that the energy flow in multimetallic plasmonic nanostructures is dependent on two critical factors acting in concert: (i) the electric field intensity at the LSPR frequencies, and (ii) the availability of direct transitions in the non-plasmonic metal relative to the plasmonic metal. To isolate the effect of the field intensity, we studied Ag-Pt

and Ag nanocubes of varying sizes. We showed that nanoparticles displaying higher field intensities under LSPR conditions were more effective in dissipating energy through the non-plasmonic metal shell. Additionally, the extent of this energy transfer to the non-plasmonic shell depended on the ratio of ε_2 of the core and shell materials at the LSPR wavelength, where higher shell to core ε_2 ratio resulted in more energy transfer to the shell. This framework not only allows for the design of hybrid nanostructures that localize charge carriers to desired parts of the nanostructure, but also the generation and potential extraction of charge carriers that have entirely different energy distributions than those generated in plasmonic metals.

5.6 Acknowledgements

The work presented in this chapter was primarily supported by the National Science Foundation (NSF) (CBET-1436056 and CBET- 1702471). The synthesis was developed with the support of the US Department of Energy, Office of Basic Energy Science, Division of Chemical Sciences (FG-02-05ER15686). Secondary support for the development of analytical tools used to analyze the optical measurements was provided by NSF (CBET-1437601). We also acknowledges the partial support of Technische Universität München – Institute for Advanced Study, funded by the German Excellence Initiative and the European Union Seventh Framework Programme under grant agreement n°291763

5.7 Supporting Information

5.7.1 Ag Nanocube Synthesis

Ag nanocubes were synthesized utilizing a standard colloidal synthesis method.[46] Ethylene glycol (VWR International, semigrade), $AgNO_3$ (Acros Organics, ultrapure grade 99.5%) and polyvinylpyrrolidone (PVP, MW=55,000 Sigma-Aldrich) were purchased and used as received.

To begin, 10 mL of ethylene glycol were placed in a 20 mL glass vial and allowed to heat to 140°C in an oil bath. Next, 80 μL of a 36 mM aqueous HCl solution was added to the vial after 1h. After 10 min, 5 mL of a 10 mg/mL solution of PVP in ethylene glycol was added to the reaction. Subsequently, 2 mL of a 25 mg/mL solution of $AgNO_3$ in ethylene glycol was added and a ventilated cap was placed on the vial. The vial and its contents were then heated for ~24 h. Once a day has elapsed, the ventilated caps were replaced with non-ventilated caps to prevent O_2 from entering the system. The transmission of the solution is monitored visually over the course of 12 h as the nanocubes begin to grow. The solution transmitted a vibrant orange-red color after ~6 h (corresponding to a ~40 nm edge length) and a faint, dark purple color after ~10 h (corresponding to a ~110 nm edge length). When the appropriate transmission color was visible, the vial was then quenched and the nanoparticles were washed with a 1:10 water:acetone mixture via centrifugation and redispersed in DI water. The washing process was repeated twice.

5.7.2 Coating of Pt onto Ag Nanocube Seeds

Thin shells of Pt were coated onto the Ag nanocube seeds using a recently reported synthesis method.[37] Briefly, 50 mg of PVP was added to 1 mL of Ag nanocubes mixed with 2 mL of DI water in a 20 mL vial. In a separate vessel, a modified Pt precursor solution was prepared by dissolving 12 mg of K_2PtCl_4 (Sigma Aldrich, 99.99%) in 8 mL of DI water and adjusting the pH to 12 with a 1.25 M aqueous NaOH solution. A reducing solution consisting of 100 mg of ascorbic acid (Sigma Aldrich, reagent grade) in 3 mL of DI water was prepared in a separate vial while the Pt solution was allowed to sit for 10 min. Ten minutes after the Pt solution was prepared, 600 μL of 1.25 M NaOH solution was added to the reducing solution, which was then immediately added to the Ag nanocube solution under stirring. The Pt solution was added immediately after. As the reaction proceeded, 50 uL of 1.25 M NaOH was added to the reaction mixture every hour to

maintain a high pH. After 8 h, the nanoparticle solution was washed twice in DI water at pH ~12 via centrifugation and redispersed in 5 mL of ~12 pH water.

5.7.3 Optical Absorption Measurements

For the optical measurements, all Ag-Pt nanoparticles of a particular size were synthesized from the same sample of Ag nanoparticle seeds of that particular size. To prepare the samples for the optical measurements, Ag and Ag-Pt nanoparticles of the 2 different sizes were placed into 3 mL cuvettes and diluted with DI water. The samples were prepared so they gave the same amount of fractional extinction with a total solution volume of 3 mL. A UV-vis spectrometer in transmission mode was used to generate extinction spectra of the samples using the following equation:

$$Extinction = 1 - Transmission\ Fraction.$$

And an integrating sphere set up described previously[34] was used to measure the sum of the transmission and scattering fractions. This allowed the fractional absorption to be calculated via the equation:

$$Absorption\ fraction = 1 - (transmission + scattering\ fraction).$$

The scattering fraction can then be calculated from the extinction and absorption fractions. It is important to note that the extinction and absorption of pure water was also measured and subtracted out of all of the measurements.

5.7.4 Finite Element Model Set-up

The optical characteristics of the studied plasmonic particles were simulated using COMSOL Multiphysics finite-element based software. The '*Wave optics*' module was used to calculate the radiative field resulting from a plane wave impinging on a 3-dimensional

nanoparticle. The plane wave was defined as: $E = E_0 e^{-ikx}$ and was polarized in the z-direction for the nanocubes. For the nanorods, the wave was polarized in either the longitudinal or transverse direction as described in the main text. **Figure S 4** shows a schematic of the model systems used in the simulations, where E is the edge length of the nanocube core, s is the thickness of the nanoparticle shell and D and L are the diameter and the longitudinal length of the nanorods, respectively. The parameters used in the simulations are given in **Table 1**.

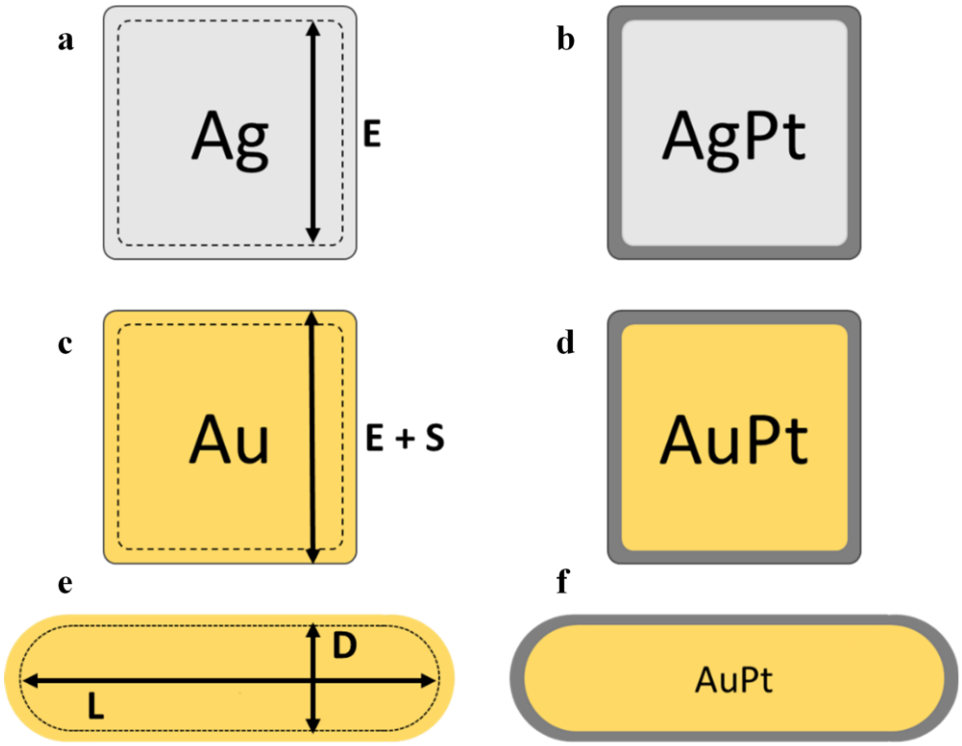

Figure S 4 Schematic of model geometries used in the COMSOL simulations. a,b) Ag and Ag-Pt core-shell nanocubes; **c,d)** Au and Au-Pt core-shell nanocubes; **e,f)** Au and Au-Pt core-shell nanorods.

Table 1Parameters for model geometry

System	E (core material)	S (shell material)	D	L
Small Ag cube	40 nm (Ag)	1.4 nm (Ag)	--	--
Small AgPt cube	40 nm (Ag)	1.4 nm (Pt)	--	--

Large Ag cube	110 nm (Ag)	1.4 nm (Ag)	--	--
Large AgPt cube	110 nm (Ag)	1.4 nm (Pt)	--	--
Au cube	75 nm (Au)	1 nm (Au)	--	--
AuPt cube	75 nm (Au)	1 nm (Pt)	--	--
Au rod (AR=4)	--	1 nm (Au)	20 nm (Au)	80 nm
Au rod (AR=4)	--	1 nm (Pt)	20 nm (Au)	80 nm

Each core-shell material was created in the model and the wavelength range from 300 nm to 900 nm was simulated. The corners of the nanocubes in the simulations were smoothed to reflect the particle geometry observed in TEM characterization. Dielectric data for Ag, Au and Pt were taken from COMSOL's Optical Materials database (Rakic et. al)[47] and a region of air (water for the Ag/AgPt case) was defined around the particle by setting the real part of the dielectric function equal to 1 (or 1.33 for water). The width of the region of air (water) around the particle was equal to half the wavelength of the incident plane wave and a perfectly matched layer (PML) was constructed to act as an absorber of the scattered field. The calculations are discussed in the following sections.

5.7.5 Extinction, Absorption and Scattering Calculations

The absorption cross section as a function of wavelength was calculated by integrating the resistive heating losses over the volume of the nanoparticles. Absorption for a particular region of the nanoparticles (i.e., the core or the shell) were calculated by integrating the heating losses over the core and shell volumes explicitly defined in the model. To calculate the scattering cross section, the dot product of the normal vector pointing outwards from the particle surface area and the scattered intensity vector was integrated across the entire particle surface for each wavelength. The extinction was determined by summing the absorption and scattering cross sections. Fractions were

obtained by defining the maximum value of the extinction (or absorption for the absorption fraction graphs) as 1 and scaling all values relative to that particular value. **Figure S 5** shows the simulated extinction, absorption and scattering fractions of the small/large Ag/AgPt nanocubes described in the main text.

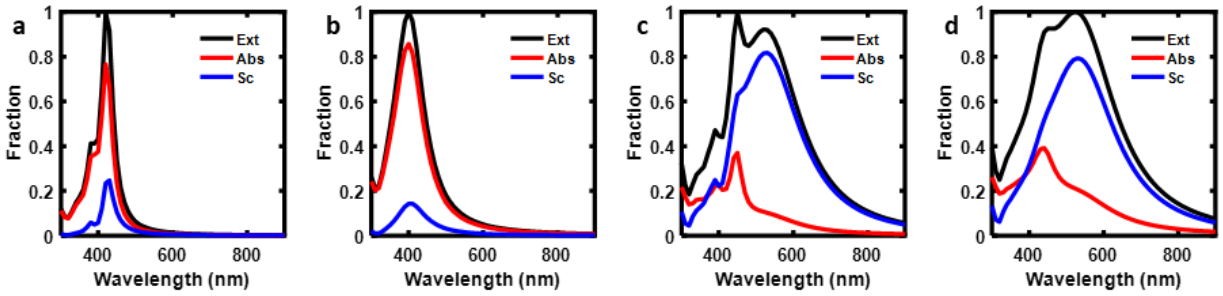

Figure S 5 Simulated optical characteristics of small and large Ag and AgPt nanocubes. a-d) Simulated fractional extinction, absorption and scattering of **(a)** small Ag cubes, **(b)** small Ag cubes coated with ~1.4 nm of Pt, **(c)** large Ag cubes, **(d)** large Ag cubes coated with ~1.4 nm of Pt

5.7.6 Pt Absorption Ratio Calculation

The simulated Pt absorption ratio ($A_{Pt,\ 40\ COMSOL}$/ $A_{Pt,\ 110\ COMSOL}$) in **Figure 5.3e** was calculated using the following equation:

$$\frac{A_{Pt,40\ COMSOL}}{A_{Pt,110\ COMSOL}} = \frac{A_{Shell,\ AgPt\ 40}}{V_{Shell,\ AgPt\ 40}} * \frac{V_{Shell,\ AgPt\ 110}}{A_{Shell,\ AgPt\ 110}} \qquad (S4.1)$$

where $A_{Shell\ AgPt,40}$ and $A_{Shell\ AgPt,110}$ are the calculated absorption in Pt for the 40 nm and 110 nm particles, and $V_{Shell\ AgPt,40}$ and $V_{Shell\ AgPt,110}$ are the volumes of the Pt shell for the 40 nm and 110 nm particles.

5.7.7 Electric Field Calculation

The electric field at the particle dielectric interface (**Figure 5.4a**) was calculated by integrating the field intensity over the surface of the particle. The field intensity was normalized by the

background field intensity (i.e. by the field intensity from the simulation with no particle included). This was done for both the 40 nm Ag particle and 110 nm Ag particle in water.

5.7.8 Shell Absorption Ratio Calculation

The simulated shell absorption ratio in **Figure 5.4d** was calculated using the following equation:

$$A_{Ratio,\ Shell} = \frac{A_{Shell,\ AgPt\ 40}}{A_{Shell,\ Ag\ 40}} \qquad (S4.2)$$

Where $A_{\text{Shell AgPt,40}}$ and $A_{\text{Shell Ag,40}}$ are the simulated shell absorptions in the 40 nm Ag-Pt and Ag nanoparticles respectively.

5.7.9 Dielectric Data for Ag, Au and Pt

The optical data for Ag, Pt and Au were taken from COMSOL's Optical Materials database (Rakic et. al)[47]. The imaginary part of the dielectric function for Ag, Au and Pt are plotted in **Figure S *6***.

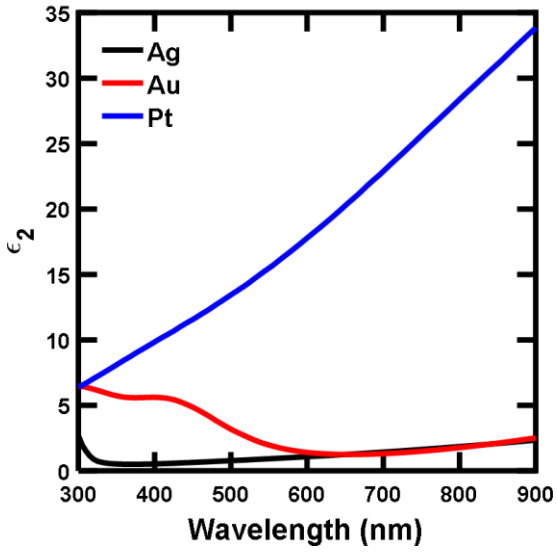

Figure S 6 Imaginary part of the dielectric function for Ag, Au and Pt.

5.8 References

(1) Kelly, K. L.; Coronado, E.; Zhao, L. L.; Schatz, G. C. *J. Phys. Chem. B* **2002**, *107* (3), 668–677.

(2) El-Sayed, M. A. *Acc. Chem. Res.* **2001**, *34* (4), 257–264.

(3) Link, S.; El-Sayed, M. A. *J. Phys. Chem. B* **1999**, *103* (40), 8410–8426.

(4) Bohren, C. F. *Am. J. Phys.* **1983**, *51* (67), 327–510.

(5) Hao, E.; Schatz, G. C. *J. Chem. Phys.* **2004**, *120* (1), 357–366.

(6) Linic, S.; Christopher, P.; Ingram, D. B. *Nat. Mater.* **2011**, *10* (12), 911–921.

(7) Schuller, J. A.; Barnard, E. S.; Cai, W.; Jun, Y. C.; White, J. S.; Brongersma, M. L. *Nat. Mater.* **2010**, *9* (3), 193–204.

(8) Li, K.; Hogan, N. J.; Kale, M. J.; Halas, N. J.; Nordlander, P.; Christopher, P. *Nano Lett.* **2017**, acs.nanolett.7b00992.

(9) Brown, A. M.; Sundararaman, R.; Narang, P.; Goddard, W. A.; Atwater, H. A. *ACS Nano* **2016**, *10* (1), 957–966.

(10) Bernardi, M.; Mustafa, J.; Neaton, J. B.; Louie, S. G. *Nat. Commun.* **2015**, *6*, 7044.

(11) Simoncelli, S.; Li, Y.; Cortés, E.; Maier, S. A. *Nano Lett.* **2018**, acs.nanolett.8b00302.

(12) Joplin, A.; Ali Hosseini Jebeli, S.; Sung, E.; Diemler, N.; Straney, P. J.; Yorulmaz, M.; Chang, W.-S.; Millstone, J. E.; Link, S.; Nano XXXX, A. **2017**.

(13) Swearer, D. F.; Zhao, H.; Zhou, L.; Zhang, C.; Robatjazi, H.; Martirez, J. M. P.; Krauter, C. M.; Yazdi, S.; McClain, M. J.; Ringe, E.; Carter, E. A.; Nordlander, P.; Halas, N. J. *Proc. Natl. Acad. Sci.* **2016**, 201609769.

(14) Mubeen, S.; Lee, J.; Singh, N.; Krämer, S.; Stucky, G. D.; Moskovits, M. *Nat. Nanotechnol.* **2013**, *8* (4), 247–251.

(15) Christopher, P.; Xin, H.; Linic, S. *Nat. Chem.* **2011**, *3* (6), 467.

(16) Christopher, P.; Xin, H.; Marimuthu, A.; Linic, S. *Nat. Mater.* **2012**, *11* (12), 1044–1050.

(17) Mukherjee, S.; Libisch, F.; Large, N.; Neumann, O.; Brown, L. V.; Cheng, J.; Lassiter, J. B.; Carter, E. A.; Nordlander, P.; Halas, N. J. *Nano Lett.* **2013**, *13* (1), 240–247.

(18) Linic, S.; Aslam, U.; Boerigter, C.; Morabito, M. *Nat. Mater.* **2015**, *14* (6), 567–576.

(19) Holewinski, A.; Xin, H.; Nikolla, E.; Linic, S. *Curr. Opin. Chem. Eng.* **2013**, *2* (3), 312–

319.

(20) Schweitzer, N.; Xin, H.; Nikolla, E.; Miller, J. T.; Linic, S. *Top. Catal.* **2010**, *53* (5–6), 348–356.

(21) Boerigter, C.; Campana, R.; Morabito, M.; Linic, S. *Nat. Commun.* **2016**, *7*, 10545.

(22) Atwater, H. a; Polman, A. *Nat. Mater.* **2010**, *9* (3), 205–213.

(23) Mubeen, S.; Hernandez-Sosa, G.; Moses, D.; Lee, J.; Moskovits, M. *Nano Lett.* **2011**, *11* (12), 5548–5552.

(24) Catchpole, K. R.; Polman, A. *Opt. Express* **2008**, *16* (26), 21793.

(25) Moskovits, M. *Nat. Nanotechnol. 2015 101* **2015**.

(26) Baffou, G.; Quidant, R. *Laser Photon. Rev.* **2013**, *7* (2), 171–187.

(27) Carlson, M. T.; Khan, A.; Richardson, H. H. *Nano Lett.* **2011**, *11* (3), 1061–1069.

(28) Chen, X.; Chen, Y.; Yan, M.; Qiu, M. *ACS Nano* **2012**, *6* (3), 2550–2557.

(29) Hirsch, L. R.; Stafford, R. J.; Bankson, J. A.; Sershen, S. R.; Rivera, B.; Price, R. E.; Hazle, J. D.; Halas, N. J.; West, J. L. *Proc. Natl. Acad. Sci. U. S. A.* **2003**, *100* (23), 13549–13554.

(30) Xiaohua Huang, †; Ivan H. El-Sayed, ‡; Wei Qian, † and; Mostafa A. El-Sayed*, †. *J. Am. Chem. Soc.* **2006**, *128* (6), 2115–2120.

(31) Ali, M. R. K.; Wu, Y.; Tang, Y.; Xiao, H.; Chen, K.; Han, T.; Fang, N.; Wu, R.; El-Sayed, M. A. *Proc. Natl. Acad. Sci. U. S. A.* **2017**, *114* (28), E5655–E5663.

(32) Carpin, L. B.; Bickford, L. R.; Agollah, G.; Yu, T.-K.; Schiff, R.; Li, Y.; Drezek, R. A. *Breast Cancer Res. Treat.* **2011**, *125* (1), 27–34.

(33) El-Sayed, I. H.; Huang, X.; El-Sayed, M. A. *Cancer Lett.* **2006**, *239* (1), 129–135.

(34) Aslam, U.; Chavez, S.; Linic, S. *Nat. Nanotechnol.* **2017**, *12*, 1000–1005.

(35) Sun, Y.; Xia, Y. *Science (80-.).* **2002**, *298* (5601), 2176–2179.

(36) Christopher, P.; Linic, S. *ChemCatChem* **2010**, *2* (1), 78–83.

(37) Aslam, U.; Linic, S. *ACS Appl. Mater. Interfaces* **2017**, *9* (49), 43127–43132.

(38) Christopher, P.; Moskovits, M. *Annu. Rev. Phys. Chem* **2017**, *6817*.

(39) Khurgin, J. B. *Nat. Nanotechnol.* **2015**, *10* (1), 2–6.

(40) Rakić, A. D.; Djurišić, A. B.; Elazar, J. M.; Majewski, M. L. *Appl. Opt.* **1998**, *37* (22), 5271.

(41) Kreibig, U.; Vollmer, M. *Optical Properties of Metal Clusters*; 1995.

(42) Hammer, B.; Nørskov, J. K. *Adv. Catal.* **2000**, *45*, 71–129.

(43) Boerigter, C.; Aslam, U.; Linic, S. *ACS Nano* **2016**, *10* (6), 6108–6115.

(44) Eustis, S.; El-Sayed, M. A. *Chem. Soc. Rev.* **2006**, *35*, 209–217.

(45) Jana, N. R.; Gearheart, L.; Murphy, C. J. *J. Phys. Chem. B* **2001**, *105*, 4065–4067.

(46) Sun, Y. *Science* **2002**, *298* (5601), 2176–2179.

(47) Rakić, A. D.; Djurišić, A. B.; Elazar, J. M.; Majewski, M. L. *Appl. Opt.* **1998**, *37* (22), 5271–5283.

Chapter 6 Maximzing Light Absorption in Bimetallic Hybrid Plasmonic Nanostructures

6.1 Publication Information

The data presented in this chapter has been composed as a manuscript, which I will submit for publication with the author list: Steven Chavez*, Vishal Govind Rao* and Suljo Linic. This chapter explores how to engineer the composition and shape of hybrid bimetallic nanoparticles to maximize the amount of light they absorb.

6.2 Summary

Controlling light absorption within photoexcited plasmonic nanostructures is imperative for various applications. In this context, hybrid plasmonic nanostructures created by interfacing plasmonic materials with small amounts of non-plasmonic materials (e.g., another metal, semiconductor, or molecule) can drastically change the systems' absorption properties. Herein, we quantify light absorption in hybrid Ag-Pt core-shell nanocubes by measuring their local temperature using anti-Stokes Raman nanothermometry. We show that Ag-Pt nanocubes exhibit a wavelength-dependent temperature rise under illumination and an overall higher maximum temperature increase than monometallic Ag nanoparticles. We then use computational approaches to demonstrate that the difference in measured nanoparticle temperature results from synergy between plasmon resonance of the Ag core and highly absorbing Pt surface atoms. We use these results to establish guidelines for engineering bimetallic plasmonic materials that can effectively localize light absorption and photothermal heating processes to the nanoscale.

6.3 Introduction

Interfacing nanoparticles of plasmonic metals (e.g., Au, Cu, or Al) with non-plasmonic materials (e.g., molecules, semiconductors, or other metals) has emerged as an attractive option for enabling and improving various solar energy conversion technologies.[1–6] These hybrid plasmonic materials (HPMs) rely on the ability of plasmonic nanoparticles to harvest light energy via localized surface plasmon resonance (LSPR). LSPR enhances the optical cross-section of these nanoparticles and confines light energy to their surface in the form of intense electric fields. [4,7–10] These effects lead to high rates of charge carrier generation (i.e., light absorption) within the nanoparticles.[11,12] In HPMs, these charge carriers can be transferred to the non-plasmonic component to perform a function such as powering an electrical circuit or performing chemical work.[3,5,13–15] This synergy between plasmonic and non-plasmonic materials allows HPNs to open avenues for engineering new families of solar energy conversion devices.[6]

The main concern associated with the utilization of HPN's is associated with the ultrafast (~femtosecond) thermalization of charge carriers within plasmonic nanoparticles.[16,17] These lifetimes suggest that the viability of extracting charge carriers into the non-plasmonic component is low. Our group has shown that interfacing plasmonic nanoparticles with non-plasmonic materials characterized by a large imaginary dielectric function (ε_2) can bypass this thermalization process.[18–20] We show that Ag nanoparticles can dissipate LSPR energy through high ε_2 materials at high rates. This energy transfer effectively results in the direct localization of charge carrier generation in the non-plasmonic material. Further optimizing these HPNs requires understanding how to engineer these systems to maximize their light-harvesting abilities.

This contribution explores how coating plasmonic Ag nanocubes with Pt to form bimetallic Ag-Pt HPNs affects their ability to absorb light. We utilize wavelength-dependent anti-Stokes

surface-enhanced Raman spectroscopy (SERS) to measure the temperature of these systems under photoexcitation. We demonstrate that the Ag-Pt HPNs display a higher temperature rise than Ag nanocubes when LSPR is excited. Electrodynamics modeling shows that the increased photothermal response in Ag-Pt HPNs compared to Ag nanocubes results from enhanced light absorption. We subsequently use this model to elucidate design principles for maximizing light absorption in bimetallic HPNs. We predict these results will motivate the rational design of other HPNs for applications related to solar energy harvesting.

6.4 Results and Discussion

6.4.1 Physical and Optical Characterization of Ag and Ag-Pt Nanocubes

The model systems used in our SERS studies consisted of Ag or Ag-Pt nanocube aggregates deposited onto Si chips. These aggregates are characterized by a large number of hot spots (i.e., the region between closely packed plasmonic nanoparticles) and serve as ideal SERS substrates.[21,22] We synthesized the Ag and Ag-Pt nanocubes using previously reported methods and characterized them using scanning transmission electron microscopy (STEM).[23,24] The dark-field STEM image in **Figure 6.1a** shows that the Ag nanocubes have an average edge length of 50 ± 9 nm. The average Pt shell thickness in the Ag–Pt nanocubes was ~1.2 nm (**Figure 6.1b**). We confirmed the aggregated nature of the nanoparticles by measuring the optical extinction of Ag and Ag-Pt nanocubes deposited onto glass slides (**Figure 6.1c**). The data in **Figure 6.1c** show that both samples exhibit a broad extinction spectrum across the visible wavelengths. This broad spectrum is a key signature of nanoparticle aggregation.[25]

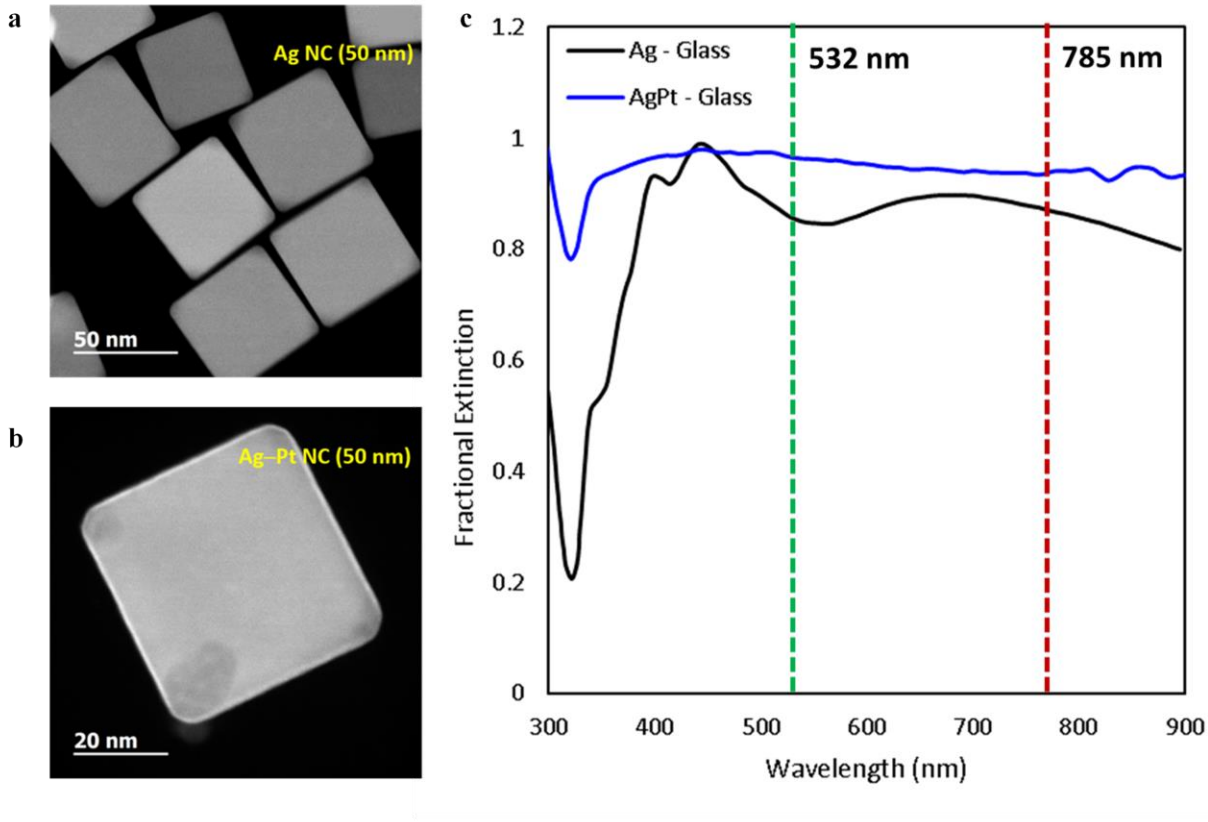

Figure 6.1 Physical and optical characterization of Ag and Ag-Pt nanocubes. a-b) STEM images of Ag (a) and Ag-Pt (b) NCs. **c)** UV-vis measured fractional extinction of Ag and Ag-Pt NCs deposited on glass. The dashed lines indicate the wavelength of the 532 nm (green) and 785 nm (red) lasers used in the Raman measurements.

6.4.2 Nanoparticle Temperature Measurements using anti-Stokes Raman Thermometry

We probed the light absorption (i.e., charge carrier generation) rates in photoexcited Ag and Ag-Pt aggregates by measuring their temperature using wavelength-dependent anti-Stokes SERS inelastic light scattering measurements. The intensity of the anti-Stokes background detected in SERS correlates with the emission rate of anti-Stokes shifted photons (subject to corrections for detector sensitivity and unequal electromagnetic enhancements).[24,26,27] Assuming thermal equilibrium between electrons and phonons (**Sections 6.7.5 and 6.7.6**), we relate the anti-Stokes background intensity ($I_{aS,background}$) to the nanoparticle temperature (T) via the Fermi-Dirac distribution function:

$$I_{\mathrm{aS,background}} = I_{\mathrm{aS},0}\left[e^{E_{\mathrm{Raman}}/k_B T} + 1\right]^{-1} \quad (6.1)$$

where E_{Raman} is the energy of the Raman shift, $I_{aS,0}$ is the intensity of the anti-Stokes SERS at $E_{\mathrm{Raman}} = 0$, and k_{B} is Boltzmann's constant. We calculate the nanocube electron-phonon temperature by fitting the anti-Stokes background signal to equation 6.1.[27,28] We confirmed the viability of using these measurements for nanothermometry on these systems in **Section 6.7.7**.

We performed our Raman measurements utilizing lasers with photon wavelengths of 532 nm and 785 nm at a constant intensity (**Section 6.7.4**). The data in **Figure 6.2a** and **Figure 6.2b** show representative raw anti-Stokes spectra obtained from Ag and AgPt aggregates measured under continuous-wave illumination for 532 nm and 785 nm, respectively. The data show that the anti-Stokes background is significantly higher for the Ag-Pt nanocubes compared to the Ag nanocubes at 532 nm. We observe low signals for both systems under 785 nm illumination. We plot histograms of the corresponding anti-Stokes background derived nanoparticle temperature for these systems in **Figure 6.2c** and **Figure 6.2d**. The data show that the Ag-Pt NCs exhibit a ~150 K higher temperature than Ag NCs under 532 nm illumination. Although we have shown that both Ag and Ag–Pt NCs support SERS at 532 nm and 785 nm[24,26,27], we observed a minimal temperature increase in the NCs under 785 nm illumination.

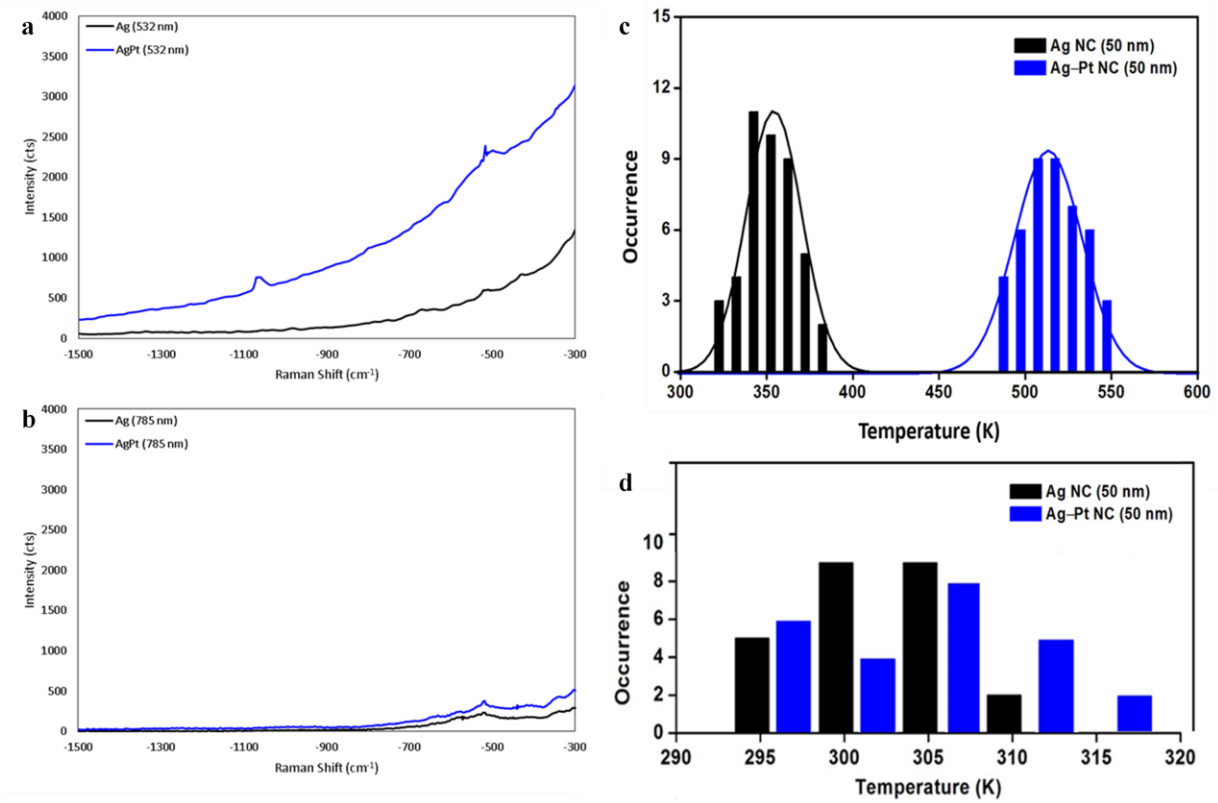

Figure 6.2 Nanoparticle temperature measurements using anti-Stokes Raman thermometry. a-b) Representative anti-Stokes spectra for the ~50 nm Ag and AgPt nanoparticles under 532 nm illumination (a) and 785 nm illumination (b). **c-d)** The measured nanoparticle temperature of ~50nm Ag and Ag–Pt nanocubes under 532 nm illumination (c) and 785 nm illumination (d). The laser intensity used in the measurements was 3.45 mW/cm^2.

We can make two distinct observations from the data presented in **Figure 6.2**. The first is the increased heating of Ag-Pt nanocubes compared to Ag nanocubes under 532 nm illumination. The second is that there is more significant heating of Ag and Ag-Pt nanocubes under 532 nm illumination compared to 785 nm illumination. Based on these observations, we hypothesized that the Pt shell increases the total light absorption rate in Ag-Pt nanocubes compared to Ag nanocubes. We have previously shown that coating Ag nanocubes with thin Pt layers increases their absorption fraction but have not quantified whether Ag-Pt nanocubes exhibit higher net absorption rates than Ag nanocubes of identical size.[18,19] Furthermore, we postulated that the increased heating at 532 nm compared to 785 nm is due to higher absorption rates due to LSPR. We base these hypotheses

on the fact that the temperature increase under illumination is proportional to the magnitude of plasmon energy loss in the nanoparticle.[29]

6.4.3 Simulated Absorption Characteristics and Resulting Temperature Increase in the Nanocube Systems

We tested these hypotheses by developing a finite element method (FEM) electrodynamics model and simulating the systems of interest (**Section 6.7.8**). The model geometry consisted of 50 nm nanocubes surrounded by a 1.2 nm shell and 4 nm of polyvinylpyrrolidone (PVP), which remains on the nanocubes post-synthesis. We set the dielectric properties of the core and shell materials to Ag or Pt using data from Rakic.[30] The refractive index of the PVP layer was set to 1.5 and assumed to be non-absorbing in the simulated wavelength range of 300 nm to 800 nm. The light intensity was identical to the Raman laser intensity after passing through the focusing objective (1 mW/μm^2). We simulated the optical absorption characteristics of core-shell Ag-Ag and Ag-Pt nanocubes with the dimensions described above. We also simulated a 50 nm Pt cube with a 1.2 nm Pt shell and a stand-alone 1.2 nm Pt shell to compare the behavior of Ag and Ag-Pt nanocubes to non-plasmonic systems.

We first address hypothesis one above related to how the Pt layer affects a Ag nanocube's ability to absorb light. We began by calculating the various nanoparticle systems' wavelength-dependent absorption cross-section (σ_{abs}). The data in **Figure 6.3a** shows show that the Ag nanocube exhibits a peak in the σ_{abs} at ~460 nm. This high absorption is due to LSPR and is characteristic of Ag nanoparticles of this size. We note that this is ~5 times higher than the σ_{abs} for the Pt cube at the same wavelength. The data in **Figure 6.3a** similarly show that the Ag-Pt nanocube also exhibits a LSPR peak at 440 nm. Comparing the Ag-Pt spectrum to the stand-alone

Pt shell spectrum confirms that Ag LSPR is critical in allowing the Ag-Pt hybrid nanostructure to harvest light.

While the data show that the Ag-Pt nanocube can harvest light via LSPR, we observe that the magnitude of σ_{abs} for Ag-Pt decreases compared to Ag. This dampening suggests that the Pt shell decreases the light-harvesting efficiency of the Ag core. We investigate this by summing the power dissipated (*P*) throughout the nanostructures across the entire wavelength range. We calculate *P* by multiplying σ_{abs} at each wavelength by the power input into the model. The data in **Figure 6.3b** show that the Ag-Pt nanocube absorbs more energy than the Ag NC. This analysis indicates that the Pt shell ultimately increases the nanoparticle's light absorption efficiency, despite decreasing the plasmonic response.[31]

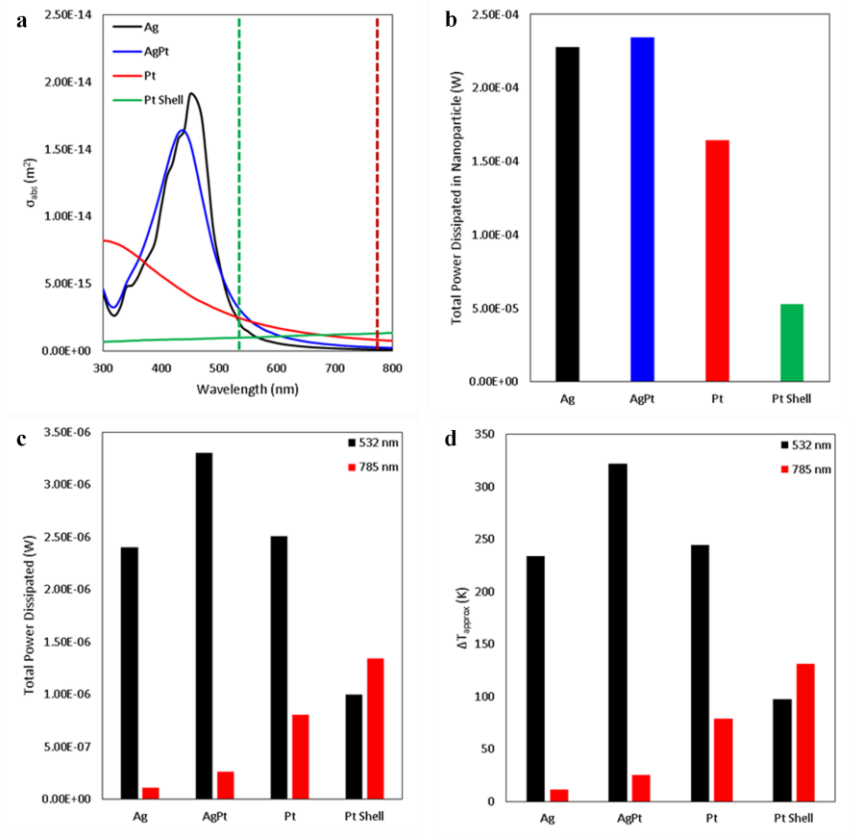

Figure 6.3 Simulated absorption characteristics and resulting temperature increase in the nanocube systems. **a**) The calculated wavelength-dependent absorption cross-section for the four different nanoparticle systems. The

dashed lines indicate the wavelength of the 532 nm (green) and 785 nm (red) lasers used in the Raman measurements. **b)** the total power dissipated throughout the nanoparticles due to the absorption of photons from 300 nm to 800 nm. **c)** total power dissipated throughout the four nanoparticle systems due to the absorption of 532 nm and 785 nm photons. **d)** approximate change in nanoparticle temperature within the four nanoparticle systems at 532 nm and 785 nm calculated using equation 5.2. At each wavelength, the power input into the model was 1 $mW/\mu m^2$.

Our next objective was to address our second hypothesis related to how the excitation of LSPR affects the light absorption in Ag and Ag-Pt nanocubes. The dashed lines in **Figure 6.3a** designate the wavelengths used in the Raman experiments. The data show that the 532 nm laser is resonant with the LSPR peak of both Ag and Ag-Pt, while the 785 nm laser is not resonant. We used the model to calculate *P* throughout the various systems at 532 nm and 785 nm. The data in **Figure 6.3c** show that at 532 nm, Ag-Pt exhibits the highest rates of power dissipation, followed by monometallic Pt and Ag. This trend exactly matches the trend in the magnitudes of σ_{abs} at 532 nm shown in **Figure 6.3a**. On the other hand, the data for 785 nm in **Figure 6.3c** show negligible power dissipation throughout the Ag and Ag-Pt NCs at this wavelength. Comparing this data to the data in **Figure 6.3a**, it is clear that this low power dissipation is due to the lack of LSPR at 785 nm. The moderate power dissipation for the pure Pt systems at 785 nm results from Pt's electronic structure. Pt is characterized by a high ε_2 compared to Ag at long wavelengths, which allows it to absorb photons at 785 nm more efficiently.[5,32,33]

Next, we quantify how the absorbed power affects the nanocube temperature at each wavelength. We approximate the uniform temperature increase of each nanoparticle (ΔT_{NP}) with the following equation[34–36]:

$$\Delta T_{NP} = \frac{P}{4\pi R\kappa} \tag{6.2}$$

where *R* is the radius of a spherical particle with the same volume as each nanocube, and κ is the effective permittivity of the surrounding medium (κ_{air} = 0.0258 W/m K). The data in **Figure 6.3d** show that the Ag-Pt nanocube exhibits a ~90 K higher temperature increase than the Ag nanocube

under 532 nm illumination and that both nanoparticles show ΔT_{NP} < 25 K under 785 nm illumination. This assessment confirms that increased absorption via the addition of Pt leads to significant increases in the nanoparticle temperature at 532 nm. The lack of heating at 785 nm further confirms that this temperature increase is LSPR driven. Collectively, the data in **Figure 6.3** confirm our hypotheses that: 1) adding Pt to the surface of the Ag nanocube increases the total absorption, and 2) the temperature increase is LSPR mediated.

6.4.4 Nanoparticle Composition and Size Effects on the Total Light Absorption

The above data show that Ag-Pt nanocubes exhibit higher LSPR-induced light absorption rates than pure Ag nanocubes. Our final objective was to determine how to engineer these materials to maximize their light absorption ability. We first wanted to determine how the Pt shell thickness affects light absorption in Ag-Pt nanocubes. We accomplished this by modeling Ag-Pt nanocubes with a constant edge length (50 nm) and increasing Pt shell thickness. We compared their absorption characteristics to 50 nm monometallic Ag and Pt nanocubes. The data in **Figure 6.4a** show *P* as a function of wavelength for these systems. We observe a continuous decrease and blue-shift of the LSPR peak as the Pt shell increases. The decrease in LSPR intensity is due to increasing damping as the Pt layer increases, while the blue shift is due to the nanocube's optical behavior becoming more like pure Pt.

We assessed the effect of the Pt shell thickness on the total absorption by calculating the "power dissipation enhancement" (P_{Enh}). We obtained P_{Enh} by calculating the total *P* for the Ag-Pt systems across the 300 nm to 800 nm wavelength range and dividing it by the total *P* within monometallic Ag and Pt systems. The data in **Figure 6.4b** show that any amount of Ag in the system increases *P* compared to pure Pt. However, the data show that adding more than 1 nm of

Pt to an Ag nanoparticle severely diminishes *P*. This observation suggests that maximizing light absorption in Ag-Pt systems requires the thinnest Pt layer possible to minimize plasmon damping.

Next, we assessed the effect of the nanoparticle size on its light absorption capability. We plot the calculated *P* for Ag-Pt, Ag, and Pt nanocubes of varying edge lengths in **Figure 6.4c**. The Pt shell thickness was held constant at 1 nm in the Ag-Pt systems. The data show that *P* increases for all three systems as their size increases. This trend is not surprising since σ_{abs} for metallic nanoparticles is proportional to their volume.[37–39] The data also show that the plasmonic Ag and Ag-Pt systems absorb the most light for small particle sizes, while pure Pt absorbs the most light for large particle sizes.

We further investigate this observation by calculating P_{Enh} for these systems as a function of the size. The data in **Figure 6.4d** show that P_{Enh} compared to Ag is below 1 for small nanocubes and increases as the size increases. We can explain this by noting that the LSPR decay pathway is typically dominated by absorption in small particles (~under 20 nm) and by scattering in large particles (~over 70 nm).[40,41] Small Ag nanocubes absorb more light than Ag-Pt of equivalent size since Pt damps the LSPR. As the Ag size increases, absorption plays a less critical role. In this case, adding the Pt shell (characterized by high ε_2) biases the LSPR decay pathway towards absorption, leading to high enhancements.[18,19] The P_{Enh} data for Ag-Pt/Pt shows that the Ag core significantly increases *P* compared to pure Pt at small particle sizes. We attribute this to Ag LSPR as described above. The data also show that P_{Enh} for Ag-Pt/Pt drops below 1 for large particle sizes. We can explain this by noting the high light absorption rates in large Pt nanoparticles due to their large ε_2 (**Figure 6.4c**). While this data suggests we should utilize large Pt nanocubes for light-harvesting applications, we note that its σ_{abs} is still low compared to plasmonic materials. Thus, the Ag-Pt HPN system serves as the best system for these applications.

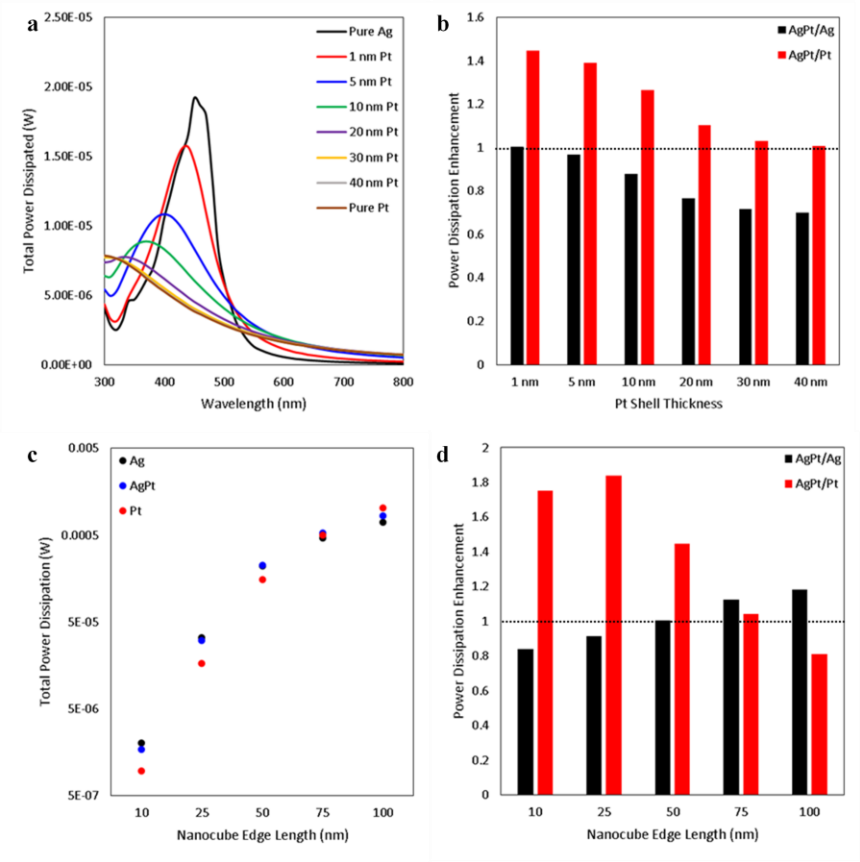

Figure 6.4 The nanoparticle composition and size effects on the total power dissipated throughout the nanocubes. a) Total power dissipated through 50 nm Ag-Pt core-shell nanocubes with varying Pt shell thicknesses. We include the data for 50 nm Ag and Pt nanocubes for comparison. **b)** the enhancement in total power dissipation of 50 nm Ag-Pt nanocubes of varying Pt shell thicknesses compared to 50 nm Ag (AgPt/Ag) or 50 nm Pt nanocubes (AgPt/Pt). **c)** the total power dissipated throughout Ag-Pt nanocubes of varying Ag core sizes and a constant 1 nm Pt shell. **d)** the enhancement in total power dissipation of Ag-Pt nanocubes of varying Ag core sizes and a constant 1 nm Pt shell compared to pure Ag (AgPt/Ag) or pure Pt nanocubes (AgPt/Pt) of the same size.

6.5 Conclusion

The data presented above sheds light on how to design bimetallic HPNs to maximize their light absorption capability. Our anti-Stokes Raman measurements demonstrate that adding a 1 nm Pt shell to Ag nanocubes increases their temperature rise under illumination. We used our model to show that this temperature increase resulted from high light absorption rates in Ag-Pt compared to Ag, despite LSPR damping in the presence of Pt. This analysis demonstrated that coating plasmonic nanoparticles with thin layers of highly absorbing materials results in higher light

absorption rates than each component. We substantiated this by analyzing the light absorption rates Ag-Pt nanocubes of varying geometries. By varying the Pt shell thickness, we show that the thinnest Pt layer leads to the highest absorption rates due to decreases LSPR damping. We additionally show that large Ag nanocubes benefit the most from the Pt layer due to their high scattering rates. These findings present guidelines for engineering multicomponent HPMs that can effectively localize light absorption and photothermal heating processes to the nanoscale.

6.6 Acknowledgements

This research was supported by the U.S. Department of Energy, Office of Science, Office of Basic Energy Sciences, under Award (DE-SC0021362) (experimental work) and National Science Foundation (NSF) (CBET-1803991) (modeling work). Secondary support for the development of analytical tools used in the model was provided by NSF (CBET-1702471 and CHE-1800197).

6.7 Supporting Information

6.7.1 Ag Nanocube Synthesis

The silver nanocubes were synthesized using a polyol method as reported previously. In brief, 10 mL of ethylene glycol were preheated at 140 °C for 1 h. Then 80 μL of 36 mM HCl were introduced to the mixture followed by the addition of 5 mL of a 10 mg/mL solution of polyvinylpyrrolidone (PVP, MW=55,000 Sigma Aldrich) in ethylene glycol. Next 2 mL of a 25 mg/mL solution of $AgNO_3$ (Acros Organics, ultrapure grade 99.5%) were added and a ventilated cap was positioned on the reaction vessel. After allowing the reaction mixture to sit overnight, the ventilated cap was replaced with an air-tight cap. The mixture was allowed to react for ~6 hours to form the Ag nanocubes of size ~ 50 nm. To wash the particles, the sample was diluted to 45 mL

with water and centrifuged for 20 minutes at 8,000 rpm. The supernatant was disposed and the nanocubes were resuspended in 5 mL of DI water. This washing procedure was repeated twice, and the resulting nanoparticles were redispersed in 10 mL of DI water.

6.7.2 Ag-Pt Nanocube Synthesis

The Ag-Pt core-shell nanocubes were synthesized using a recently published method.[18,23,24] A sample of purified Ag nanocubes in 10 mL of DI water was added to a Teflon beaker. Then 200 mg of PVP was dissolved in the reaction mixture. The Pt precursor solution was made by adding 32 mg of K_2PtCl_4 (Sigma Aldrich, 99.99%) in 5 mL of DI water. The pH of this solution was adjusted to ~12 by adding 50 μL of a 1.25 M aqueous NaOH solution. To prepare the reducing solution, 250 mg of ascorbic acid were dissolved in 3.5 mL of DI water. The pH of this mixture was increased to ~12 by adding 1.5 mL of a 1.25 M NaOH solution. This reducing solution was then added to the reaction mixture under stirring followed by the addition of the Pt precursor solution. Every hour, 100 μL of 1.25 M NaOH were added to the reaction mixture to maintain a high pH. The mixture was allowed to react for 2 hours and then promptly washed via centrifugation by diluting to 45 mL basic (~12 pH) DI water, and centrifuged for 20 minutes at 10,000 rpm. After discarding the supernatant, the nanoparticles were washed once more.

6.7.3 Characterization of Ag and Ag-Pt nanocubes

We characterized the Ag and Ag-Pt nanocubes using scanning transmission electron microscopy (STEM). The STEM images were obtained on a JEOL 3100 double CS-corrected transmission electron microscope utilizing an accelerating voltage of 300 kV. The samples for STEM characterization were prepared by drop casting the nanoparticle solution onto 200 mesh carbon-on-copper grids.

6.7.4 Raman Sample Preparation and Raman Measurements

Samples for anti-Stokes background collection and for Raman measurements were prepared by drop-casting ~40 μL of the nanoparticle solution onto a cleaned silicon chip and allowing the solvent to evaporate at ~323 K. The wavelength-dependent Raman studies were conducted using a Horiba LabRAM HR DuoScan™ system under excitation from either a 532 nm diode-pumped solid-state laser or a 785 nm diode laser. Unless mentioned otherwise we have used ~3.45 mW/cm^2 laser intensity for both the lasers. The laser beam was focused onto nanoparticles with an objective microscope at a magnification of 50×. Raman scattering was detected at an angle of 180° using a Peltier-cooled (-71 ℃) charge coupled device (CCD) camera. The spot size of the two lasers was ~3.14 μm^2.

6.7.5 Measuring Local Nanoparticle Temperature using anti-Stokes Raman Thermometry

The anti-Stokes emission occurs at higher energy than the incident light, this process requires additional energy to be supplied either from multiple photon excitations or a thermal bath (phonons). Since we have used continuous wave (CW) laser irradiation in all our experiments, we do not see multiple photon excitation under our experimental condition.[27] Furthermore, the electron–phonon coupling occurs on a similar time scale as consecutive photon absorption. Therefore, the anti-Stokes emission from plasmonic nanostructures can be attributed to interactions of charge carriers with phonons, either directly through phonon-mediated charge carrier recombination[42] or indirectly through a thermal-activated electronic Raman scattering.[28,43–45] This weak recombination emission/scattering gets enhanced due to the localized surface plasmon resonance, acting as an antenna and the emission spectrum resembles the plasmon spectrum. The anti-Stokes intensity was thus corrected for unequal electromagnetic enhancements and detector sensitivity for these measurements.

6.7.6 Methodology Behind anti-Stokes Raman Thermometry

We have used the steps outlined in **Figure S 7a-d** to determine the local temperature of the nanoparticles. First, we collected anti-Stokes spectra of the Ag and Ag-Pt nanocubes under continuous wave illumination by the 532 and 785 nm laser (**Figure S *7*a**). The measured background anti-Stokes intensities were then exponentially fit to the Fermi–Dirac electron distribution function (**Figure S *7*b**). To extract the temperature from this fit, we can rearrange equation 6.1 in the main manuscript to:

$$\ln\left(\frac{I_{\mathrm{aS},0}}{I_{\mathrm{aS,background}}}-1\right)=\frac{E_{\mathrm{Raman}}}{k_B T} \qquad (S6.1)$$

The theoretical $I_{\mathrm{aS},0}$ value can be derived by considering anti-Stokes background signal at high Raman shifts, where:

$$e^{E_{\mathrm{Raman}}/k_B T} \gg 1 \qquad (S6.2)$$

Under this condition we can write equation 5.1 in the main manuscript as:

$$I_{\mathrm{aS,background}} = I_{\mathrm{aS},0}\, e^{-E_{\mathrm{Raman}}/k_B T} \qquad (S6.3)$$

Which can be further simplified to equation S6.4:

$$\ln(I_{\mathrm{aS}}) = \ln\left(I_{\mathrm{aS},0}\right) - \frac{E_{Raman}}{k_B T} \qquad (S6.4)$$

According to equation S5.4, we can extract $\ln(I_{\mathrm{aS},0})$ as the intercept of the $\ln(I_{\mathrm{aS}})$ versus E_{Raman} plot (**Figure S 7c**). Once we obtain $I_{\mathrm{aS},0}$, we can use equation S5.1 to determine the local temperature by including lower energy Raman shifts and plotting $\ln(I_{\mathrm{aS},0}/I_{\mathrm{aS}} - 1)$ versus E_{Raman}. We can then obtain the local nanoparticle temperature from the slope of the plot, which is $1/k_B T$ (**Figure S 7d**).

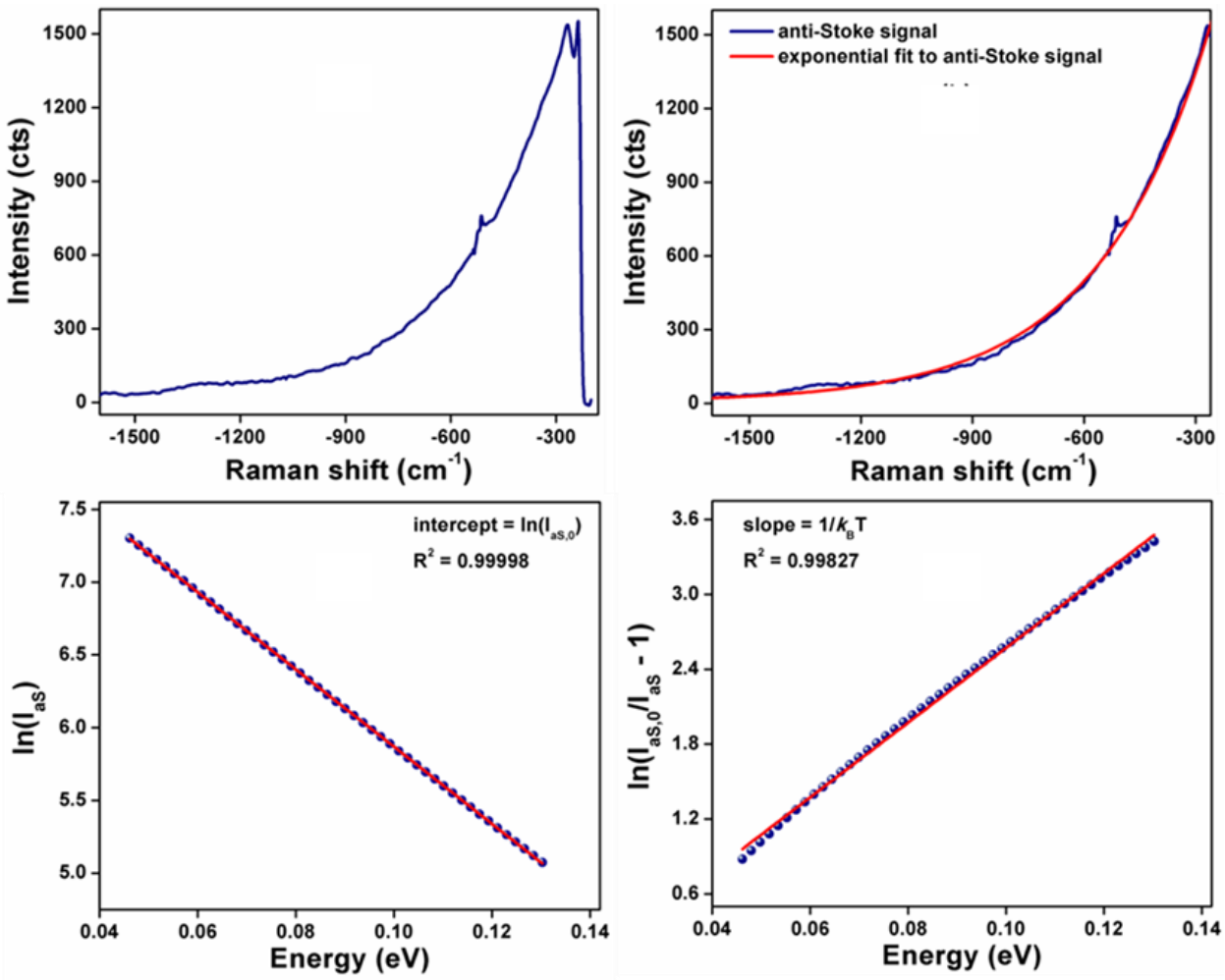

Figure S 7 How to measure the local nanoparticle temperature using anti-Stokes Raman scattering measurements. a-d) Representative example showing steps involved in measuring the nanoparticle temperature. The first step is to collect the anti-Stokes spectra via laser excitation (a). Next, the anti-Stokes background signal is fit to an exponential function (b). The third step is to obtain the intercept of the best fit line for $\ln(I_{aS})$ versus Energy (Raman, in eV), which is equal to $\ln(I_{aS,0})$ (c). Finally, the local nanoparticle temperature is obtained by plotting $\ln(I_{aS,0}/I_{aS} - 1)$ versus Energy (Raman, in eV), where the slope represents $1/k_BT$ (d).

6.7.7 Confirming anti-Stokes Measurements Can be Used for Thermometry

We confirmed the viability of using anti-Stokes scattering measurements for nanothermometry by measuring the local nanoparticle temperature of Ag nanocubes using 785 nm laser light as the excitation source (since Ag nanocubes do not show signs of heating at this excitation wavelength) as a function of external temperature. In this control experiment, the Ag coated Si chip was placed inside a reaction chamber equipped with a thermocouple located directly

underneath the sample within the reactor vessel. We varied the temperature in the reactor from 298 K to 398 K using an external heat source and simultaneously measured the reactor temperature using the thermocouple and the nanoparticle temperature using anti-Stokes scattering spectra. The data in **Figure S *8*** show the local temperature of the Ag nanocubes measured under continuous-wave illumination by the 785 nm laser as a function of externally controlled reactor temperature. The measured temperature using the anti-Stokes background clearly reflect the applied temperature, which indicates that this method of measuring temperature can be used for nanothermometry.

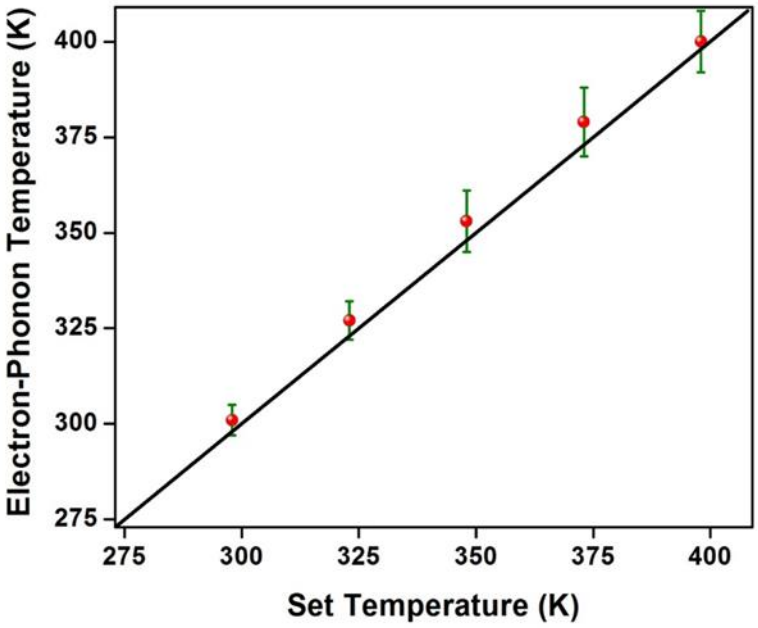

Figure S 8 The calculated electron-phonon temperature as a function of the externally set reactor temperature under 785 nm illumination. The red spheres indicate average temperature of Ag nanoparticles, and the error bars represent the standard deviation of all data points. The black solid line is used to guide the viewer, and it represents the measured nanoparticle temperature equal to set temperature in the reactor.

6.7.8 Details of Optoelectronic Simulations

The model geometries used in the simulations consisted of a 50 nm Ag cube coated with a 1.2 nm shell of either Ag or Pt encapsulated by a 5 nm layer of polyvinylpyrrolidone (PVP). A 50 nm Pt cube with a 1.2 nm Pt shell and a stand-alone 1.2 nm Pt shell (each coated with 5 nm of

PVP) were also simulated as control systems. The dielectric and thermal properties for Ag and Pt were obtained from COMSOL's materials database[46], while the refractive index of the PVP coating was set to 1.5. The optical behavior of the nanoparticle systems was simulated using COMSOL Multiphysics finite-element based software. The '*Wave Optics*' module was used to calculate the scattered field resulting from a transverse-electric polarized plane wave impinging on a 3-dimensional nanoparticle. A top port (Port 1) is set to send the light wave at a specified incident power (P = 3.45 mW/cm^2 i.e., the same power used in the experiments) and a bottom port (Port 2) is set to absorb the transmitted light. The corners of the nanocubes in the simulations were smoothed to reflect the particle geometry observed in TEM characterization. The height of the region of air above the nanoparticle systems was equal to half the wavelength of the incident plane wave, and a perfectly matched layer (PML) was constructed to act as an absorber of the scattered field.

6.8 References

(1) Atwater, H. a; Polman, A. *Nat. Mater.* **2010**, *9* (3), 205–213.

(2) Li, J.; Cushing, S. K.; Meng, F.; Senty, T. R.; Bristow, A. D.; Wu, N. *Nat. Photonics* **2015**, *9* (9), 601–607.

(3) Moskovits, M. *Nat. Nanotechnol. 2015 101* **2015**.

(4) Brongersma, M. L.; Halas, N. J.; Nordlander, P. *Nat. Nanotechnol.* **2015**, *10* (1), 25–34.

(5) Aslam, U.; Rao, V. G.; Chavez, S.; Linic, S. *Nat. Catal.* **2018**, *1*, 656–665.

(6) Linic, S.; Chavez, S.; Elias, R. *Nat. Mater.* **2021**, 1–9.

(7) Linic, S.; Christopher, P.; Ingram, D. B. *Nat. Mater.* **2011**, *10* (12), 911–921.

(8) Ciracì, C.; Hill, R. T.; Mock, J. J.; Urzhumov, Y.; Fernández-Domínguez, A. I.; Maier, S. A.; Pendry, J. B.; Chilkoti, A.; Smith, D. R. *Science* **2012**, *337* (6098), 1072–1074.

(9) El-Sayed, M. A. *Acc. Chem. Res.* **2001**, *34* (4), 257–264.

(10) Hao, E.; Schatz, G. C. *J. Chem. Phys.* **2004**, *120* (1), 357–366.

(11) Manjavacas, A.; Liu, J. G.; Kulkarni, V.; Nordlander, P. *ACS Nano* **2014**, *8* (8), 7630–7638.

(12) Sundararaman, R.; Narang, P.; Jermyn, A. S.; Goddard III, W. A.; Atwater, H. A. *Nat. Commun.* **2014**, *5*, 5788.

(13) Brongersma, M. L.; Halas, N. J.; Nordlander, P. *Nat. Nanotechnol.* **2015**, *10* (1), 25–34.

(14) Enrichi, F.; Quandt, A.; Righini, G. C. *Renew. Sustain. Energy Rev.* **2018**, *82*, 2433–2439.

(15) Govorov, A. O.; Zhang, H.; Gun'ko, Y. K. *J. Phys. Chem. C* **2013**, *117* (32), 16616–16631.

(16) Voisin, C.; Fatti, N. Del; Christofilos, D.; Vallee, F. *J. Phys. Chem. B* **2001**, *105* (12), 2264–2280.

(17) Khurgin, J. B. *Nat. Nanotechnol.* **2015**, *10*.

(18) Aslam, U.; Chavez, S.; Linic, S. *Nat. Nanotechnol.* **2017**, *12*, 1000–1005.

(19) Chavez, S.; Aslam, U.; Linic, S. *ACS Energy Lett.* **2018**, *3* (7), 1590–1596.

(20) Chavez, S.; Rao, V. G.; Linic, S. *Faraday Discuss.* **2019**.

(21) Sun, L.; Song, Y.; Wang, L.; Guo, C.; Sun, Y.; Li, Z.; Liu, Z. *J. Phys. Chem. C* **2008**, *112* (5), 1415–1422.

(22) Sharma, B.; Fernanda Cardinal, M.; Kleinman, S. L.; Greeneltch, N. G.; Frontiera, R. R.; Blaber, M. G.; Schatz, G. C.; Van Duyne, R. P. *MRS Bull.* **2013**, *38* (8), 615–624.

(23) Aslam, U.; Linic, S. *ACS Appl. Mater. Interfaces* **2017**, *9* (49), 43127–43132.

(24) Rao, V. G.; Aslam, U.; Linic, S. *J. Am. Chem. Soc* **2019**, *141*, 647.

(25) Sun, L.; Zhao, D.; Ding, M.; Xu, Z.; Zhang, Z.; Li, B.; Shen, D. *J. Phys. Chem. C* **2011**, *115* (33), 16295–16304.

(26) Boerigter, C.; Campana, R.; Morabito, M.; Linic, S. *Nat. Commun.* **2016**, *7*, 10545.

(27) Boerigter, C.; Aslam, U.; Linic, S. *ACS Nano* **2016**, *10* (6), 6108–6115.

(28) Hugall, J. T.; Baumberg, J. J. *Nano Letters*. American Chemical Society April 8, 2015, pp 2600–2604.

(29) Baffou, G.; Cichos, F.; Quidant, R. *Nat. Mater.* **2020**, *19*, 946–958.

(30) Rakić, A. D.; Djurišić, A. B.; Elazar, J. M.; Majewski, M. L. *Appl. Opt.* **1998**, *37* (22),

5271.

(31) Engelbrekt, C.; Crampton, K. T.; Fishman, D. A.; Law, M.; Apkarian, V. A. *ACS Nano* **2020**, acsnano.0c01653.

(32) Antosiewicz, T. J.; Apell, S. P.; Wadell, C.; Langhammer, C. *J. Phys. Chem. C* **2012**, *116* (38), 20522–20529.

(33) Langhammer, C.; Kasemo, B.; Zorić, I. *J. Chem. Phys.* **2007**, *126* (19), 194702.

(34) Baffou, G.; Quidant, R.; García De Abajo, F. J. **2010**, *4*.

(35) Baffou, G.; Quidant, R. *Laser Photon. Rev.* **2013**, *7* (2), 171–187.

(36) Rej, S.; Mascaretti, L.; Santiago, E. Y.; Tomanec, O.; Kment, Š.; Wang, Z.; Zbořil, R.; Fornasiero, P.; Govorov, A. O.; Naldoni, A. *ACS Catal.* **2020**, *10* (9), 5261–5271.

(37) Li, K.; Hogan, N. J.; Kale, M. J.; Halas, N. J.; Nordlander, P.; Christopher, P. *Nano Lett.* **2017**, acs.nanolett.7b00992.

(38) Christopher, P.; Moskovits, M. *Annu. Rev. Phys. Chem* **2017**, *6817*.

(39) Hartland, G. V. *Chem. Rev.* **2011**, *111* (6), 3858–3887.

(40) Bohren, C. F. *Am. J. Phys.* **1983**, *51* (67), 327–510.

(41) Jain, P. K.; Lee, K. S.; El-Sayed, I. H.; El-Sayed, M. A. *J. Phys. Chem. B* **2006**, *110* (14), 7238–7248.

(42) Carattino, A.; Caldarola, M.; Orrit, M. *Nano Lett.* **2018**, *18* (2), 874–880.

(43) Xie, X.; Cahill, D. G. *Appl. Phys. Lett.* **2016**, *109* (18), 183104.

(44) Huang, J.; Wang, W.; Murphy, C. J.; Cahill, D. G. *Proc. Natl. Acad. Sci. U. S. A.* **2014**, *111* (3), 906–911.

(45) Jones, S.; Andrén, D.; Karpinski, P.; Käll, M. *ACS Photonics* **2018**, *5* (7), 2878–2887.

(46) Rakić, A. D.; Djurišić, A. B.; Elazar, J. M.; Majewski, M. L. *Appl. Opt.* **1998**, *37* (22), 5271–5283.

Chapter 7 Unearthing the Factors Governing Site Specific Rates of Electronic Excitations in Multicomponent Plasmonic Systems and Catalysts

7.1 Publication Information

The work presented in this chapter is published as: Steven Chavez, Vishal Govind Rao, and Suljo Linic. "*Unearthing the factors governing site specific rates of electronic excitations in multicomponent plasmonic systems and catalysts*." Faraday Discussions, 214, 441-453, 2019.

Modifications have been made the published document to adapt the content to this text. This chapter extends the energy transfer framework presented in the previous three chapters to multicomponent plasmonic systems containing semiconductors and molecules.

7.2 Summary

We use experimental and computational studies of core-shell metal-semiconductor and metal-molecule systems to investigate the mechanism of energy flow and energetic charge carrier generation in multicomponent plasmonic systems. We demonstrate that the rates of plasmon decay through the formation of energetic charge carriers are governed by two factors: (1) the intensity of the local plasmon induced electric fields at a specific location in the multicomponent nanostructure, and (2) the availability of direct, momentum conserved electronic excitations in the material located in that specific location. We propose a unifying physical framework that describes the flow of energy in all multicomponent plasmonic systems and leads us towards molecular control of the energy flow and excited charge carrier generation in these systems.

7.3 Introduction

Localized surface plasmon resonance (LSPR) is a collective and coherent oscillation of free electrons in plasmonic nanoparticles stimulated by electromagnetic radiation.[1–3] LSPR is accompanied by large optical extinction cross-sections at the resonant frequencies as well as elevated oscillating electric fields at the surface of the nanostructures. Compared to the electric fields of an incoming photon flux, these fields can be enhanced anywhere from 10^3 times at the surface of single particles to 10^6 times in between two particles separated by ~1 nm.[4–7] LSPR essentially acts to confine incoming electromagnetic energy within small volumes at the surface of the nanoparticles. The energy of these enhanced fields is dissipated either radiatively via reemission of photons into the far field (scattering) or non-radiatively via the excitation of charge carriers (i.e. the formation of energetic electron/hole pairs) within the nanoparticle (absorption). In clean nanoparticles, the energy of these charge carriers is thermalized, i.e., it is dissipated as heat directly within the nanostructure via electron-electron and subsequently electron-phonon collisions. This thermalization process leads to direct heating of the plasmonic nanostructure under LSPR conditions.[8,9]

Due to their high optical extinction cross-section and their ability to localize electric fields in small volumes, plasmonic nanoparticles are emerging as one of the most promising materials platforms for various applications. Many potential applications of plasmonic nanoparticles rely on spatially controlling the electronic excitation processes in plasmonic nanostructures. Specifically, there is a great deal of interest in creating multifunctional nanostructures where plasmonic nanoparticles that serve as nanoscopic light-energy concentrators are coupled with another material (metal, semiconductor or molecular entities) that utilizes this energy to perform a function.[10–17] In these multifunctional materials, energetic charge carriers would need to transfer

from the plasmonic material to the other material before they are thermalized in the plasmonic metal, or preferentially form at high rates (stimulated by LSPR) directly in the other material rather than in the plasmonic metal (**Figure 7.1**). For example, the efficient creation of energetic charge carriers in semiconductors or molecules or the efficient transfer of energetic charge carriers from plasmonic nanoparticles to the attached semiconductors or molecules is crucial in numerous applications including plasmon-enhanced photovoltaics[18,19], plasmonic sensing[20], plasmonic photocatalysis[21–25] and photothermal cancer therapy[26–29]. To be able to design such multifunctional nanostructures, a deeper understanding of the energy dissipation pathways in resonantly excited plasmonic multicomponent nanostructures and the factors that govern the flow of energy within these multicomponent plasmonic nanostructures is required.

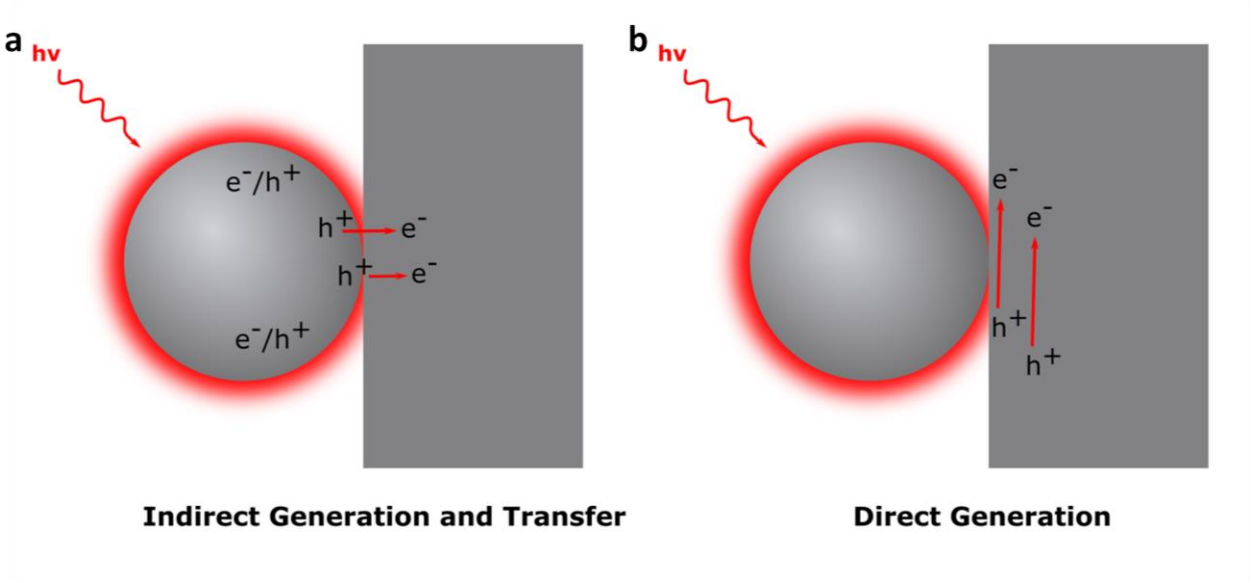

Figure 7.1 Mechanisms of energetic charge generation/extraction from plasmonic nanoparticles to surrounding materials. **a)** the electron-hole pairs are generated directly in the plasmonic nanostructure. A number of charge carriers with enough energy have an opportunity to transfer over to an attached material. The rest will be thermalized within the bulk of the plasmonic nanostructure; **b)** the electron-hole pairs are generated directly in the attached material in regions close to the plasmonic nanostructure. This bypasses thermalization processes in the plasmonic nanostructure.

We have previously reported the design of bimetallic plasmonic nanostructures in the form of Ag-Pt core-shell nanocubes in which relatively large Ag cubes (tens of nanometers) were covered

with very thin Pt shells (~ 1 nm).[30] We demonstrated that in these multimetallic nanostructures, the plasmonic Ag core served to harvest the light energy through the excitation of LSPR and that this LSPR energy was dissipated preferentially through the formation of energetic charge carriers in the thin non-plasmonic Pt shell. We also developed a transparent physical framework that could describe the energy flow in this bimetallic plasmonic system.[31] We postulated that the local rate of formation of energetic charge carriers in the multimetallic nanostructures is to a large degree governed by two factors: (1) the local intensity of the electric field, and (2) the magnitude of the imaginary part of the dielectric function (ε_2) of the non-plasmonic metal relative to the plasmonic metal. In the above-mentioned Ag-Pt core-shell system, the Ag core confined the high field to the surface due to the plasmonic effect, and Pt has significantly higher ε_2 than Ag at the LSPR frequencies (due to the availability of direct d to s electronic excitations). This led to the dissipation of LSPR energy through the formation of energetic e-h pairs directly in thin Pt shell. This proposed model and the experimental results provided us with a framework for the rational design of multicomponent systems where a plasmonic material guides the light energy to specific, sub-diffraction-limit volumes where this energy is dissipated through the formation of energetic charge carriers at high rates.

To further validate the proposed model for the flow of LSPR energy in multicomponent plasmonic systems, we move away from the above-mentioned bimetallic systems and focus on multicomponent metal-semiconductor and metal-molecule systems. We use experimental and theoretical studies to systematically investigate the LSPR decay mechanisms in core-shell Ag-Cu_2O (metal-semiconductor) and Ag-Methylene Blue (MB) (metal-molecule) multicomponent nanostructures. We show that the high fields generated at the LSPR wavelength can direct energy into the thin Cu_2O and MB shells respectively, in a manner similar to the one described for the

Ag-Pt core-shell structures. This results in the increased absorption in Cu_2O and the MB dye molecules respectively.

7.4 Results and Discussion

7.4.1 Physical Characterization of AgCu_2O Core-Shell Nanocubes

To synthesize the Ag-Cu_2O core-shell nanostructures, we first synthesized Ag nanocube seeds using a well-established polyol-based method.[32–34] The resulting nanocubes were characterized using high-angle annular dark field scanning transmission electron microscopy (STEM). The average edge length of the Ag nanocubes was determined to be ~75 nm. The Ag nanocube seeds were then coated with a thin layer of Cu_2O by modifying a recently reported method.[35] Briefly, the Ag-Cu_2O nanoparticles were prepared by reducing a copper (II) nitrate precursor onto the Ag nanocube seeds with hydrazine in the presence of sodium hydroxide and polyvinylpyrrolidone. This resulted in the conformal coating of Cu_2O onto the surface of the Ag nanocubes. **Figure 7.2a** shows a representative bright field STEM image of the Ag-Cu_2O nanocubes investigated in this study. Elemental mapping of the particles (**Figure 7.2b – e**) using energy dispersive x-ray spectroscopy (EDS) show that the Ag nanocube cores are covered by the Cu_2O shells. From the STEM images, we determined the average thickness of the Cu_2O shell to be ~ 5 nm.

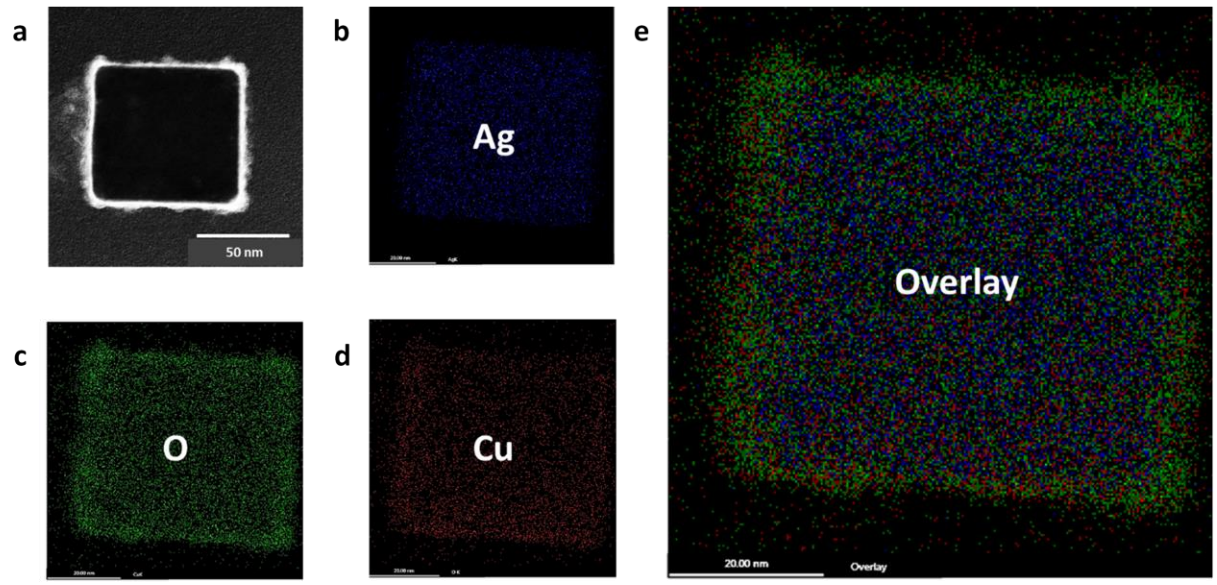

Figure 7.2 Characterization of $AgCu_2O$ core-shell nanocubes. a-e) Bright field STEM image of a representative $AgCu_2O$ nanocube. The average edge length of the nanocubes was ~75±2 nm **(a)** EDS elemental maps of Ag **(b)** O **(c)** Cu **(d)** and their overlay **(e)**.

7.4.2 Optical Characterization of Ag and $AgCu_2O$ Core-Shell Nanocubes

To investigate the impact of the thin Cu_2O shell on the energy flow in these core-shell nanostructures, we studied the optical properties of the Ag-Cu_2O nanostructures by measuring their extinction, absorption and scattering and comparing these to the optical properties of the pure Ag nanocube seeds of comparable size. The extinction characteristics of the nanocubes were measured using transmission UV-vis spectroscopy. The UV-vis data in **Figure 7.3a** show that the introduction of the thin Cu_2O shell results in a slight red-shift and an increased linewidth of the LSPR extinction peak. This red-shift in the LSPR peak is the result of the higher refractive index of Cu_2O compared to air.[36] Additionally, the extinction linewidth is related to the plasmon lifetime, where larger linewidths correspond to shorter plasmon lifetimes.[37] Furthermore, an optical integrating sphere was used to measure the partitioning between absorption and scattering for the Ag-Cu_2O nanocubes as well as the pure Ag nanocubes. The data in **Figure 7.3b** and **Figure 7.3c** show that the introduction of the Cu_2O shell modifies the LSPR decay pathway, resulting in an

increased ratio of absorption to scattering when compared to the pure Ag nanocubes. Based on this data, we hypothesized that: (1) the Cu_2O shell was providing a faster pathway for the dissipation of the electromagnetic energy than Ag, and that the energy was preferentially dissipated through the absorption process in the thin Cu_2O shell. In other words, the introduction of Cu_2O at the surface increased the rate of formation of energetic e-h pairs at the surface of the nanostructure compared to the case of pure Ag, and (2) the presence of the Ag core increases the absorption rates (the rate of formation of charge carriers) in the Cu_2O shell, compared to the identical Cu_2O shell without the Ag plasmonic core effect.

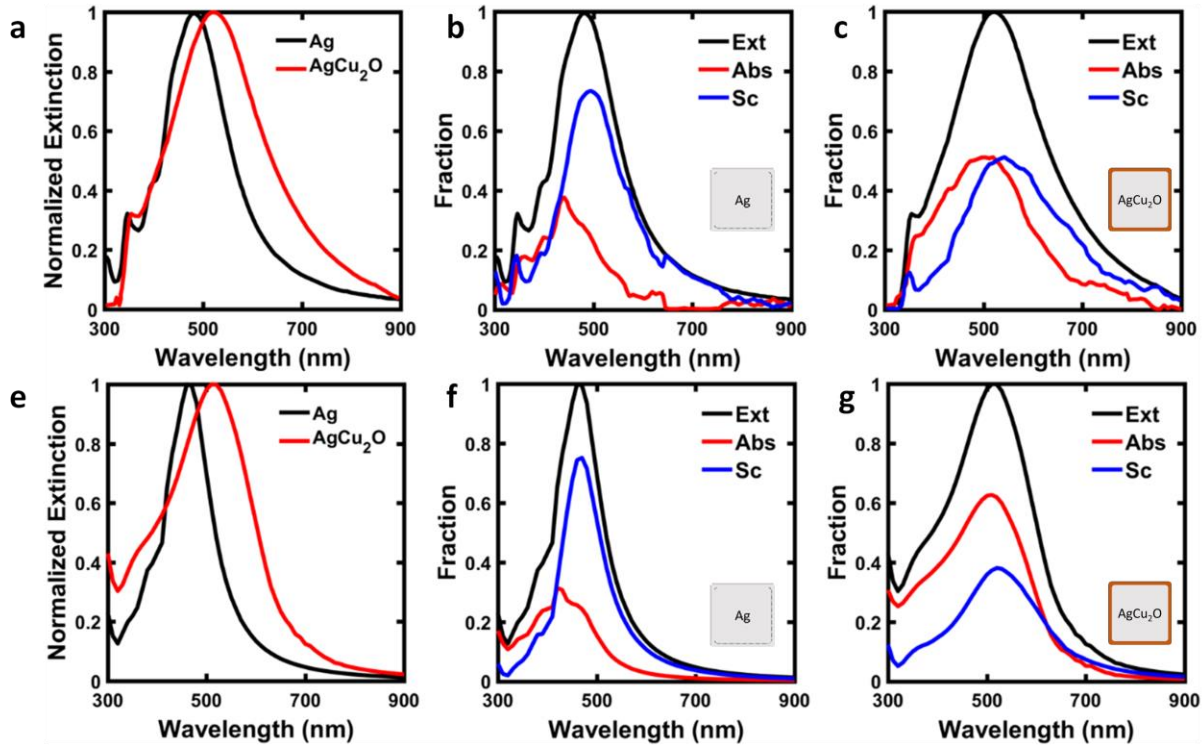

Figure 7.3 Optical characterization of Ag and $AgCu_2O$ core-shell nanocubes. a) Measured normalized extinction of the Ag and Ag-Cu_2O nanocubes; **b-c)** Measured fractional extinction, absorption and scattering of **(b)** the Ag nanocubes, and **(c)** the Ag-Cu_2O nanocubes; **e)** Calculated normalized extinction of the Ag and Ag-Cu_2O nanocubes; **f-g)** Calculated fractional extinction, absorption and scattering of **(f)** the Ag nanocubes, and **(g)** the Ag-Cu_2O nanocubes. The edge dimensions of the Ag cube in the calculations was 75 nm and the thickness of the Cu_2O shell was 5 nm.

Since the experimental data in **Figure 7.3** does not inform us about the location of the energetic e-h pair formation under the LSPR conditions, we performed finite element method (FEM) electrodynamic simulations to spatially resolve the absorption process within the nanostructures. The geometry constructed for the FEM model consisted of a 75 nm Ag nanocube surrounded by a 5 nm shell (corresponding to the dimensions determined from the STEM images) and the dielectric properties for Ag and Cu_2O were obtained from standard databases.[38,39] The data in **Figure 7.3e – g** show that the calculated extinction, absorption and scattering properties for the Ag and Ag-Cu_2O core-shell nanocubes are consistent with the experimental measurements, showing that scattering is the dominant plasmon decay pathway for pure Ag cubes while absorption dominates for the Ag-Cu_2O particles.

7.4.3 Power Dissipation Analysis of Ag and AgCu_2O Core-Shell Nanocubes

We used the FEM model to shed light on the two hypotheses, (1) and (2) discussed above, that emerged from our experimental measurement of the optical properties. The data in **Figure 7.4a** show the calculated power dissipated as a function of wavelength in the Cu_2O shell for the Ag-Cu_2O particle compared to the calculated energy dissipation rate in a virtual Ag 'shell' of a reference Ag-Ag core-shell nanocube of identical dimensions. The calculated power is essentially a measure of the wavelength-dependent rate of the formation on energetic e-h pairs in the shell. The data in **Figure 7.4a** show that, as was hypothesized, the introduction of the thin Cu_2O shell increased the rate of formation of energetic e-h pairs at the surface of the nanostructure (in the thin Cu_2O shell region) compared to the case of pure Ag, i.e., the process of photon absorption is shifted to the surface layers of the multicomponent nanostructure. This is further shown in **Figure 7.4b**, which shows simulated contour maps of the power dissipated throughout the pure Ag nanocube compared to the Ag-Cu_2O nanocube. Upon integrating the power dissipated throughout the shells

in these systems (i.e. the data in **Figure 7.4a**) with respect to energy, we determined that ~ 6 times as much energy was being deposited through the shell of the Ag-Cu_2O particle than in the Ag shell of the pure Ag particle of identical size. To test the second hypotheses, we calculated the rate of absorption in the Cu_2O shell of the Ag-Cu_2O nanoparticle and compared it to the absorption of a Cu_2O shell with identical dimensions, supported on either a pure Cu_2O core or in the absence of a core (i.e. the core was defined as air). The data in **Figure 7.4c** show that the absorption (i.e. generation of charge carriers) in the semiconductor (Cu_2O) shell, at the LSPR wavelengths, is significantly larger for the particle with the Ag plasmonic core. This suggests that in systems where a thin semiconductor shell is surrounding a plasmonic nanoparticle core, the plasmonic core can serve to enhance the rates of absorption in the shell compared to when the shell is supported on non-plasmonic materials.

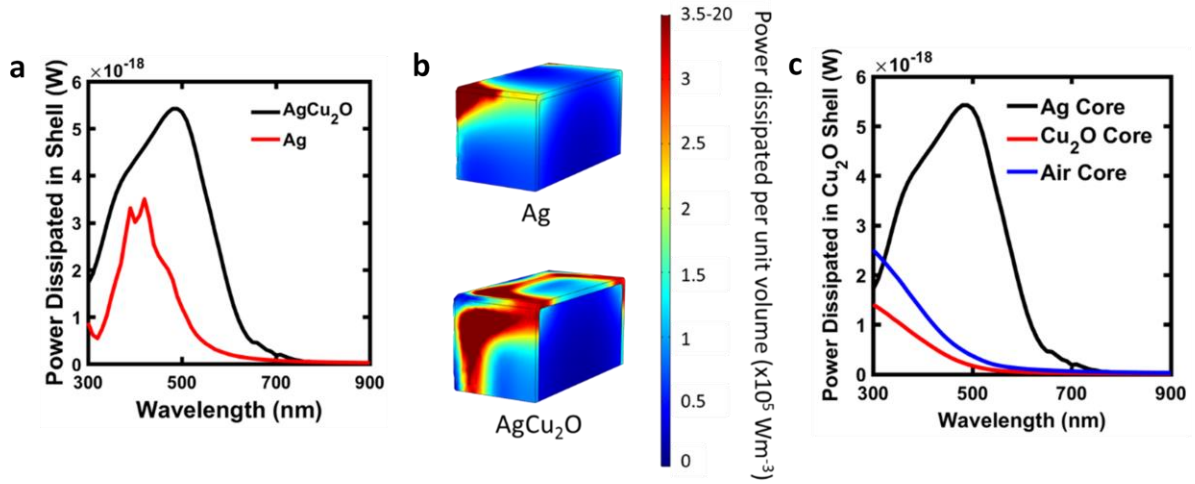

Figure 7.4 Power dissipation analysis of Ag and $AgCu_2O$ core-shell nanocubes. a) Total power dissipated as a function of wavelength in the particle shells for the Ag-Cu_2O particle and the Ag-Ag core-shell particle; **b)** Contour maps of the power dissipation per unit volume at the LSPR frequencies for the pure Ag particle and the Ag-Cu_2O particle. Due to the symmetry of the structures, we show the maps for a quarter of the cubes; **c)** Total power dissipated in the Cu_2O shell of core-shell particles with varying core materials. The source field for all simulations was 1 V m^{-1} at all frequencies, which for a free space amounts to 2.6×10^{-4} mW cm^{-2}.

7.4.4 Electric Field and Dielectric Analysis of Ag and AgCu₂O Core-Shell Nanocubes

As discussed above, we postulated that the site-specific rate of formation of energetic charge carriers in the multicomponent plasmonic nanostructures is to a large degree governed by two factors: (1) the intensity of the LSPR-induced electric field at the specific site, and (2) the magnitude of ε_2 of the material that resides at the site. We used the data in **Figure *7.3*** and **Figure 7.4** to test the validity of the model. The first question is related to the impact of the local E-field on the rate of energy dissipation via absorption (i.e., the rate of LSPR decay via localized absorption). It is well established that plasmonic nanostructures generate high electric fields that are confined to the surface of the nanostructure.[5,40] To investigate how the LSPR decay is affected by the field enhancement, we used the FEM model to calculate the electric field intensity $|E|^2$ as a function of wavelength at the surface of the Ag nanoparticle (specifically, at the Ag-Cu2O interface) with the Cu_2O shell (**Figure 7.5a**). Comparing these wavelength-dependent E-field intensities with the wavelength-dependent rate of absorption in the surface-bound thin Cu_2O shell (**Figure 7.4c**). shows that that the wavelength-dependent rate of absorption in the Cu_2O shell is heavily influenced by the magnitude of the electric field, where larger wavelength-dependent fields induce higher absorption rates.

Furthermore, we have also divided the rate of absorption in the Cu_2O shell of the Ag-Cu_2O core-shell nanoparticle by the rate of absorption in the Cu_2O shell with identical dimensions, supported on either a pure Cu_2O core or on an air-filled core (as described above), and compared these ratios to ratios in the E-field intensity of the respective systems. The data in **Figure 7.5b** show there is a quantitative agreement between the ratios in the local field intensities and the ratios in the local rates of absorption in the Cu_2O shells. This analysis shows that for a given multicomponent plasmonic material, it is the electric field induced by the plasmonic component

that drives the process of photon absorption, i.e., higher local field will induce higher rates of absorption. For a given material (in this case Cu_2O), these local plasmonic E-field can significantly increase the rates of absorption compared to the situations where these fields are not present.

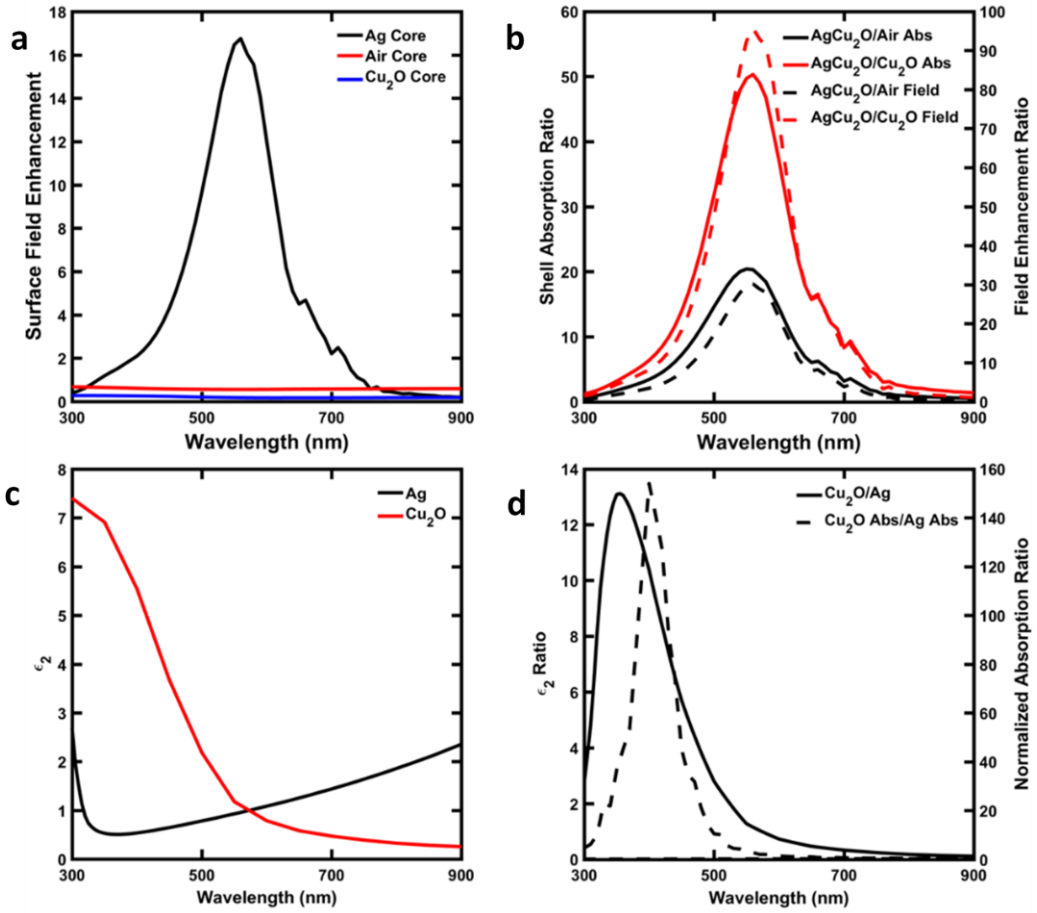

Figure 7.5 Electric field and dielectric analysis of Ag and $AgCu_2O$ core-shell nanocubes. a) Calculated electric field enhancements at the core-Cu_2O interface for the varying core materials (Ag, air or Cu_2O); **b)** Field enhancement ratios (solid lines) and shell absorption ratios (dashed lines) for Ag-Cu_2O with respect to both the Cu_2O-Cu_2O and the Cu_2O-air core-shell systems; **c)** The imaginary part of the dielectric function (ε_2) for both Ag and Cu_2O; **d)** The ratio of ε_2 of Cu_2O and Ag (solid line) and the E-field-normalized shell absorption ratios of Cu_2O in the Ag-Cu_2O system and Ag in the Ag-Ag system (dashed line).

The second issue we address is related to the impact of the local imaginary part of the dielectric function (ε_2) on the energy dissipation pathway in multicomponent plasmonic nanostructures. The data in **Figure 7.4a** show that the rate of energy dissipation is higher in the Cu_2O shell of the Ag-Cu_2O core-shell nanoparticle than in the Ag shell of the virtual Ag-Ag core-

shell structure over a wide range of wavelengths. To explain this result, we plotted the value of ε_2 as a function of wavelength for Cu_2O and Ag in **Figure 7.5c**. The data show that ε_2 is larger for Cu_2O than for Ag at wavelengths below ~590 nm, i.e., at the wavelengths where the LSPR is excited. This difference in the value of ε_2 of the shell material can qualitatively explain the higher rate of energy dissipation through the Cu_2O shell compared to the virtual Ag shell. We note that this discrepancy in the magnitudes of ε_2 for Ag and Cu_2O stems from the difference in electronic structure. The magnitude of ε_2 of a material is directly related to the availability of direct-momentum conserving electronic transitions in the material. Since Ag is a d^{10} metal, its d band lies low in energy and direct, momentum conserved transitions are improbable at low photon energies, resulting in a low value of ε_2 in the visible range.[22] Above 2.1 eV, Cu_2O has a direct band gap, meaning its electronic transitions are momentum-conserved and it can efficiently the UV-visible photons with energy higher than 2.1 eV, resulting in a high ε_2 above this threshold energy.

Comparing these values of ε_2 for Cu_2O and Ag (**Figure 7.5c**) with the rate of absorption in the Cu_2O shell in the Ag-Cu_2O particle and the equivalent Ag shell of a pure Ag nanoparticle (**Figure 7.4a**) suggests that the availability of these direct electronic excitations in Cu_2O (that lead to high ε_2) is responsible for the elevated rates of plasmon decay in the Cu_2O shell. We note that the plasmonic E-field is different for the virtual Ag shell of the pure Ag nanocube compared to the Ag-Cu_2O nanocube. This difference in the E-field leads to some deviation in the agreement between the rate of energy dissipation through the Ag and Cu_2O shells and the relative magnitudes of ε_2 of the shell material. To account for this difference in the E-field we have normalized the shell absorption ratio in the Cu_2O and Ag shells on the Ag-Cu_2O and Ag-Ag nanostructures with the ratio of their respective E-field intensities. The data in **Figure 7.5d** shows that the quantity that we obtain this way scales very well with the ratio of ε_2 for Cu_2O and Ag. This essentially means,

that for the systems where the local E-field is similar, the rate of energy dissipation via absorption can be nicely approximated by the value of ε_2. Simply put, by positioning a material with a larger ε_2 (compared to the plasmonic material) on the surface of a plasmonic nanostructure, the absorption channel is preferentially directed to that material.

7.4.5 Analysis of Ag and AgMB Core-Shell Nanocubes

The analysis presented above describes that the ability of plasmonic nanostructure to guide and dissipate energy in particular locations of a multicomponent plasmonic nanosystem is governed by two critical factors: (i) the local intensity of the electric field, and (ii) the availability of direct electronic transitions (high ε_2) at the wavelengths where the electric fields are high. To further generalize this model, we experimentally and computationally analyzed the optical properties of 75 nm Ag nanocubes interacting with methylene blue (MB) dye molecules. We created our Ag-MB solution by mixing a solution of ~75 nm Ag nanocubes dispersed in water with MB dye molecules. The resulting concentration of the MB in solution was 340 nM. It has been shown that at these low concentrations, the Ag particles are essentially surrounded by thin layers of MB, i.e., solid state MB is adsorbed on the surface of Ag nanoparticles.[41] We used an integrating sphere to measure the optical characteristics (i.e. extinction, absorption and scattering) of our Ag-MB samples and compared them to the optical properties of a pure Ag nanocube solution of the same Ag cube concentration.

The optical data in **Figure 7.6a** and **Figure 7.6b** show that the introduction of MB into the solution increases the overall absorption in the region around ~665 nm. MB is a dye molecule characterized by strong absorption at ~665 nm. To determine the effect of the Ag nanocubes on the MB absorption, we calculated the absorption in MB on the Ag nanocube surface by subtracting the pure Ag absorption from the Ag-MB absorption (the MB concentration 340 nM) and

comparing it to the absorption of a pure MB solution (340 nM). The data in **Figure 7.6c** show that at the wavelength where MB absorbs, the absorption in MB in the presence of the Ag nanocubes is larger than without the Ag nanocubes.

We used the FEM model to simulate the optical characteristics of these systems. The MB dielectric properties were determined by measuring the absorption cross section of the 340 nM MB solution (with UV-vis spectroscopy) and applying the Kramers-Kronig relations as shown previously.[42] The model system used in the FEM simulations consisted of a Ag nanocube with an edge length of 75 nm covered with a 1 nm MB "shell". To draw conclusions about the factors that govern the energy flow in these systems, we also modeled the behavior of two control model systems: an Ag-Ag core-shell nanocube (similar to one used above) and an MB-MB core-shell nanocube, both of identical dimensions to the Ag-MB nanocube. The data in **Figure 7.6d** show that the simulated absorption spectra for MB on Ag (i.e., the shell of the Ag-MB core shell model system) qualitatively match the experiments. The discrepancy in the spectral peak shape of the simulated MB absorption for the Ag-MB core-shell system compared to the experimentally measured absorption (**Figure 7.6c**, dark line) stems from the fact that the absorption data in **Figure 7.6c** is for solid MB films attached to Ag while the simulated spectra uses the MB dielectric function derived for low concentration mainly isolated MB molecules.

We study the impact of the LSPR E-field on the absorption in this system by calculating the ratio in the absorption of MB in the Ag-MB core-shell system to the absorption in the MB shell of a model MB-MB core-shell system and comparing it to the ratio in field intensity at the respective core-shell interfaces (i.e. the ratio of the fields with and without a plasmonic Ag core). The data in **Figure 7.6e** show that, like in the Ag-Cu_2O case, the absorption ratio tracks with the field ratio, demonstrating that the enhanced absorption in the shell is plasmon induced.

Additionally, we explored the effect of ε_2 in this system by calculating the ratio of shell absorption in the Ag-MB particle to the shell absorption in the pure Ag particle and correcting it by the respective field contributions (in a similar manner to the Ag-Cu_2O case described above). The obtained quantitatively tracks very well the calculated ratio of ε_2 for MB and Ag (**Figure 7.6f**).

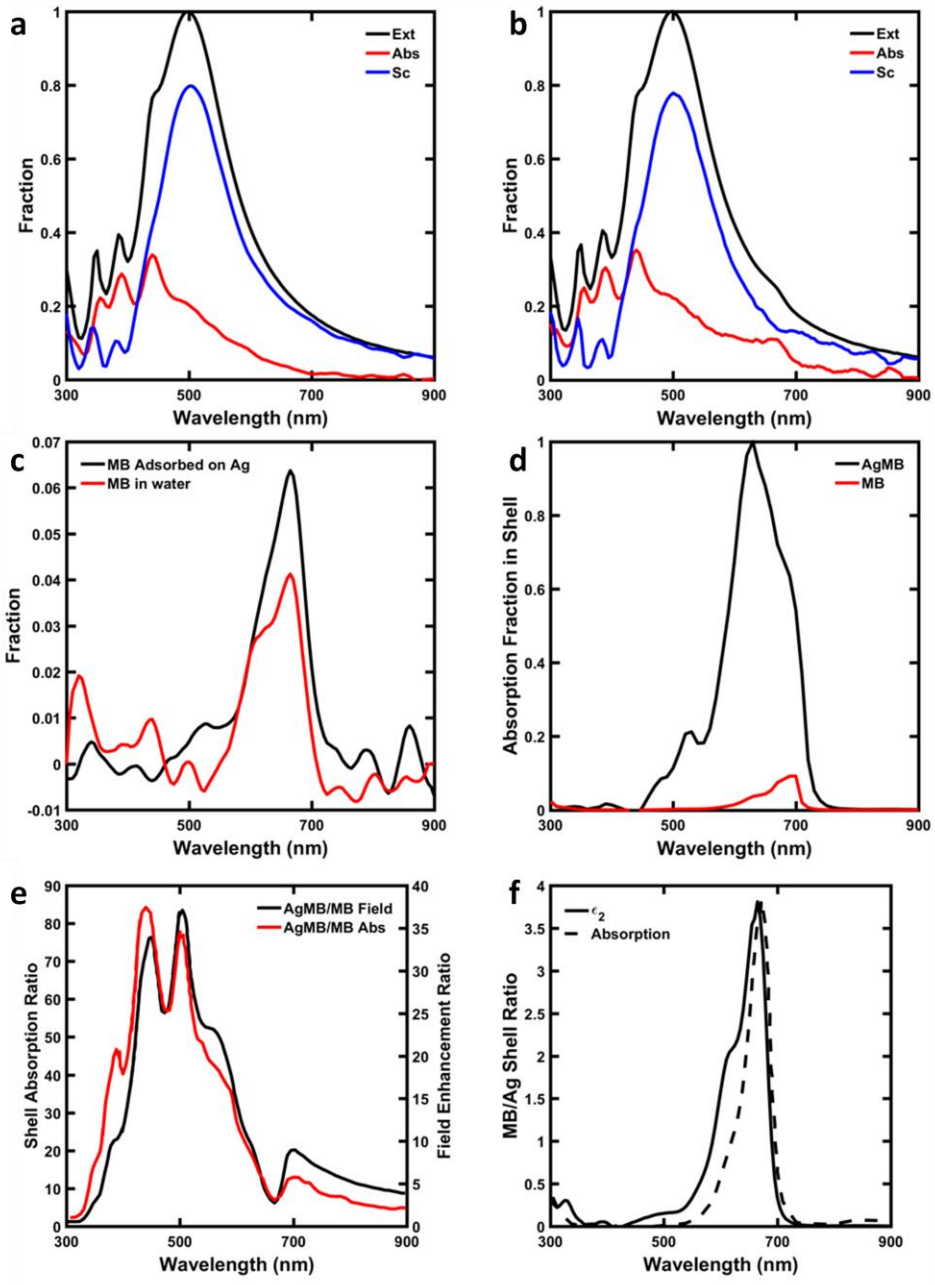

Figure 7.6 Absorption analysis of Ag and AgMB core-shell nanocubes. a-b) Measured fractional extinction, absorption and scattering of **(a)** the Ag nanocubes, and **(b)** the Ag-MB system; **c)** Absorption of MB in water (red

line) and absorption of MB on the Ag nanoparticle surface; **d)** Calculated absorption in the Ag-MB shell vs the MB shell in a reference MB shell with an MB core system; **e)** Field enhancement ratios and shell absorption ratios for Ag-MB with respect to the pure MB system; **f)** The ratio of ε_2 of MB and Ag vs the field normalized shell absorption ratios of MB in the Ag-MB system and Ag in the Ag-Ag system.

7.5 Conclusion

In summary, by studying multicomponent (i.e. core-shell metal-semiconductor and metal-molecule) systems, we demonstrated that both the electric field intensity under resonant LSPR conditions and the value of ε_2 of the shell relative to the core are the critical factors governing the flow of energy in these systems. In the metal-semiconductor case, we studied core-shell Ag-Cu_2O nanocubes. We showed that the presence of the Cu_2O shell altered the LSPR decay pathway, resulting in high absorption directly in the Cu_2O shell. We showed that this enhanced absorption process was field driven and that the field energy was dissipated to a greater extent when the shell material had higher ε_2 with respect to the core material. Additionally, we showed that this framework also described the flow of energy in metal-molecule systems for the case of MB adsorbed on Ag nanocubes.

7.6 Acknowledgements

The work presented in this document was supported by the National Science Foundation (NSF) (CHE-1800197). Secondary support was provided by the National Science Foundation (NSF) (CHE-1702471) (analysis of molecular interactions with nanostructures) and Office of Basic Energy Science, Division of Chemical Sciences (FG-02-05ER15686) (materials synthesis). We also acknowledge the partial support of the Technische Universität München – Institute for Advanced Study, funded by the German Excellence Initiative and the European Union Seventh Framework Programme under grant agreement no. 291763. CBET-

7.7 Supporting Information

7.7.1 Ag Nanocube Synthesis

Ag nanocubes were synthesized utilizing a standard colloidal synthesis method.[43] Ethylene glycol (VWR International, semigrade), $AgNO_3$ (Acros Organics, ultrapure grade 99.5%) and polyvinylpyrrolidone (PVP, MW=55,000 Sigma-Aldrich) were purchased and used as received. First, 10 mL of ethylene glycol were placed in a 20 mL glass vial and allowed to heat to 140°C in an oil bath. Next, 80 µL of a 36 mM aqueous HCl solution was added to the vial after 1h. After 10 min, 5 mL of a 10 mg/mL solution of PVP in ethylene glycol was added to the reaction. Subsequently, 2 mL of a 25 mg/mL solution of $AgNO_3$ in ethylene glycol was added and a ventilated cap was placed on the vial. The vial and its contents were then heated for ~24 h. next, the ventilated caps were replaced with non-ventilated caps to prevent O_2 from entering the system. After ~8-10h, the nanoparticle solution transmits a vibrate pink/purple, corresponding to ~75 nm cubes. The vial was then quenched and the nanoparticles were washed with a 1:10 water:acetone mixture via centrifugation and redispersed in DI water to 10 mL. The washing process was repeated twice.

7.7.2 Coating Cu_2O onto Ag Nanocube Seeds

Thin shells of Cu_2O were coated onto the Ag nanocube seeds by modifying a recently reported synthesis method.[35] Briefly, 5 mL of a 2500 mg/25 mL stock solution of PVP in water was added to a centrifuge tube. Next, 2 mL of the Ag cube seed solution (after washing) was added to the PVP solution under constant stirring, followed by 20 µL of an aqueous 0.1 M $Cu(NO_3)_2$ solution. Next, 11.2 µL of a 5 M NaOH solution was added. Finally, 5 µL of a hydrazine solution

(30 wt% hydrazine) in water was added as a reducing agent. After 10 min, the particles were centrifuged, washed twice in ethanol and redispersed in 10 mL of water.

7.7.3 Extinction, Absorption and Scattering measurements

For the optical measurements, all Ag-Cu_2O nanoparticles were synthesized from the same sample of Ag nanoparticle seeds. To prepare the samples for the optical measurements, Ag and Ag-Cu_2O nanoparticles solutions were placed into 3 mL cuvettes and diluted with DI water. The samples were prepared so they gave the same amount of fractional extinction with a total solution volume of 3 mL. A UV-vis spectrometer in transmission mode was used to generate extinction spectra of the samples using the following equation:

$$Extinction = 1 - Transmission\ Fraction.$$

And an integrating sphere set up described previously[30] was used to measure the sum of the transmission and scattering fractions. This allowed the fractional absorption to be calculated via the equation:

$$Absorption\ fraction = 1 - (transmission + scattering\ fraction).$$

The scattering fraction can then be calculated from the extinction and absorption fractions. It is important to note that the extinction and absorption of pure water was also measured and subtracted out of all of the measurements.

7.7.4 Finite Element Model Set-up

The optical characteristics of the studied plasmonic particles were simulated using COMSOL Multiphysics finite-element based software. The '*Wave optics*' module was used to calculate the radiative field resulting from a plane wave impinging on a 3-dimensional nanoparticle. The plane wave was defined as: $E = E_0 e^{-ikx}$ and was polarized in the z-direction for

the nanocubes. Each core-shell material was created in the model and the wavelength range from 300 nm to 900 nm was simulated. The corners of the nanocubes in the simulations were smoothed to reflect the particle geometry observed in TEM characterization. Dielectric data for Ag was taken from COMSOL's Optical Materials database (Rakic et. al)[38], and from the handbook of optical properties for Cu_2O[39]. A region of air (water for the Ag-MB case) was defined around the particle by setting the real part of the dielectric function equal to 1 (or 1.33 for water). The width of the region of air (water) around the particle was equal to half the wavelength of the incident plane wave and a perfectly matched layer (PML) was constructed to act as an absorber of the scattered field. The calculations are discussed in the following sections.

7.7.5 Extinction, Absorption and Scattering Calculations

The absorption cross section as a function of wavelength was calculated by integrating the resistive heating losses over the volume of the nanoparticles. Absorption for a particular region of the nanoparticles (i.e. the core or the shell) were calculated by integrating the heating losses over the core and shell volumes explicitly defined in the model. To calculate the scattering cross section, the dot product of the normal vector pointing outwards from the particle surface area and the scattered intensity vector was integrated across the entire particle surface for each wavelength. The extinction was determined by summing the absorption and scattering cross sections. Fractions were obtained by defining the maximum value of the extinction (or absorption for the absorption fraction graphs) as 1 and scaling all values relative to that particular value.

7.7.6 Electric field Calculation

The electric field at the core-shell interface was calculated by integrating the field intensity over the surface of the particle. The field intensity was normalized by the background field intensity (i.e. by the field intensity from the simulation with no particle included).

7.7.7 Normalized Shell Absorption Ratio Calculation

The simulated shell absorption ratio (corrected for the fields) in **Figure 7.5d** and **Figure 7.6f** was calculated using the following equation (using Cu_2O as an example):

$$Ratio = \frac{A_{Shell,\ AgCu2O}}{A_{Shell,\ Ag}} * \frac{E_{Ag}}{E_{AgCu2O}} \qquad (S7.1)$$

where $A_{Shell\ AgCu2O}$ (E_{AgCu2O}) and $A_{Shell\ Ag}$ (E_{Ag}) are the calculated absorption (field enhancements) in the Cu_2O shell of the Ag-Cu_2O particle and the absorption in the Ag shell of the Ag-Ag particle respectively. The fields were calculated at the interface between the core and the shell. For the Ag-MB case (**Figure 7.6f**), the Cu_2O shell absorption/fields was replaced by the MB shell absorption/fields.

7.7.8 AgMB Absorption Measurements

To measure the extinction, absorption and scattering contribution for Ag nanoparticles and Ag-MB system we used diluted solutions of Ag nanoparticles (extinction ~ 1.1) and we used low MB concentration (340 nm) to avoid any dye-dye interaction.[41] We removed any contribution from the solvent by using a sample of just DI water and subtracting it from all the measurements. Extinction measurements were performed using a UV-vis spectrophotometer.

The extinction fraction is the sum of the absorption fraction and scattering fraction. To decouple absorption from scattering contribution, we performed an optical integrating sphere

measurement (as described above). Similarly, to measure the enhanced optical absorption of MB in the proximity of Ag, we used integrating sphere measurement and we observed noticeable change in the absorption spectrum of MB in the vicinity of Ag nanoparticle.[41]

7.8 References

(1) El-Sayed, M. A. *Acc. Chem. Res.* **2001**, *34* (4), 257–264.

(2) Kelly, K. L.; Coronado, E.; Zhao, L. L.; Schatz, G. C. *J. Phys. Chem. B* **2003**, *107* (3), 668–677.

(3) Bohren, C. F.; Huffman, D. R. *Wiley* **1998**, 544.

(4) Gunnarsson, L.; Rindzevicius, T.; Prikulis, J.; Kasemo, B.; Käll, M.; Zou, S.; Schatz, G. C. *J. Phys. Chem. B* **2005**, *109* (3), 1079–1087.

(5) Hao, E.; Schatz, G. C. *J. Chem. Phys.* **2004**, *120* (1), 357.

(6) Jiang Jiang; Ken Bosnick; Mathieu Maillard, and; Brus*, L. **2003**.

(7) Linic, S.; Christopher, P.; Ingram, D. B. *Nat. Publ. Gr.* **2011**, *10*.

(8) Frischkorn, C.; Wolf, M. *Chem. Rev.* **2006**, *106*, 4207–4233.

(9) Brongersma, M. L.; Halas, N. J.; Nordlander, P. *Nat. Nanotechnol.* **2015**, *10*, 25–34.

(10) Brown, A. M.; Sundararaman, R.; Narang, P.; Goddard, W. A.; Atwater, H. A. *ACS Nano* **2016**, *10* (1), 957–966.

(11) Li, K.; Hogan, N. J.; Kale, M. J.; Halas, N. J.; Nordlander, P.; Christopher, P. *Nano Lett.* **2017**.

(12) Bernardi, M.; Mustafa, J.; Neaton, J. B.; Louie, S. G. *Nat. Commun.* **2015**, *6*, 7044.

(13) Joplin, A.; Ali Hosseini Jebeli, S.; Sung, E.; Diemler, N.; Straney, P. J.; Yorulmaz, M.; Chang, W.-S.; Millstone, J. E.; Link, S.; Nano XXXX, A. *ACS Nano* **2017**, *11*, 12346–12357.

(14) Linic, S.; Aslam, U.; Boerigter, C.; Morabito, M. *Nat. Mater.* **2015**, *14* (6), 567–576.

(15) Wu, K.; Chen, J.; McBride, J. R.; Lian, T. *Science* **2015**, *349* (6248), 632–635.

(16) Boerigter, C.; Aslam, U.; Linic, S. *ACS Nano* **2016**, *10* (6), 6108–6115.

(17) Boerigter, C.; Campana, R.; Morabito, M.; Linic, S. *Nat. Commun.* **2016**, *7*, 10545.

(18) Atwater, H. a; Polman, A. *Nat. Mater.* **2010**, *9* (3), 205–213.

(19) Beck, F. J.; Polman, A.; Catchpole, K. R. *J. Appl. Phys.* **2009**, *105* (11), 114310.

(20) Knight, M. W.; Sobhani, H.; Nordlander, P.; Halas, N. J. *Science (80-.).* **2011**, *332* (6030).

(21) Christopher, P.; Xin, H.; Linic, S. *Nat. Chem.* **2011**, *3* (6), 467.

(22) Aslam, U.; Rao, V. G.; Chavez, S.; Linic, S. *Nat. Catal.* **2018**, *1*, 656–665.

(23) Mukherjee, S.; Libisch, F.; Large, N.; Neumann, O.; Brown, L. V.; Cheng, J.; Lassiter, J. B.; Carter, E. A.; Nordlander, P.; Halas, N. J. *Nano Lett.* **2013**, *13* (1), 240–247.

(24) Mubeen, S.; Lee, J.; Singh, N.; Krämer, S.; Stucky, G. D.; Moskovits, M. **2013**.

(25) Christopher, P.; Xin, H.; Marimuthu, A.; Linic, S. *Nat. Mater.* **2012**, *11* (12), 1044.

(26) Xiaohua Huang, †; Ivan H. El-Sayed, ‡; Wei Qian, † and; Mostafa A. El-Sayed*, †. *J. Am. Chem. Soc.* **2006**, *128* (6), 2115–2120.

(27) Carpin, L. B.; Bickford, L. R.; Agollah, G.; Yu, T.-K.; Schiff, R.; Li, Y.; Drezek, R. A. *Breast Cancer Res. Treat.* **2011**, *125* (1), 27–34.

(28) Ali, M. R. K.; Wu, Y.; Tang, Y.; Xiao, H.; Chen, K.; Han, T.; Fang, N.; Wu, R.; El-Sayed, M. A. *Proc. Natl. Acad. Sci. U. S. A.* **2017**, *114* (28), E5655–E5663.

(29) El-Sayed, I. H.; Huang, X.; El-Sayed, M. A. *Cancer Lett.* **2006**, *239* (1), 129–135.

(30) Aslam, U.; Chavez, S.; Linic, S. *Nat. Nanotechnol.* **2017**, *12*, 1000–1005.

(31) Chavez, S.; Aslam, U.; Linic, S. *ACS Energy Lett.* **2018**, *3* (7), 1590–1596.

(32) Sun, Y.; Xia, Y. *Science* **2002**, *298* (5601), 2176–2179.

(33) Linic, S.; Christopher, P. *ChemCatChem* **2010**, *2* (9), 1061–1063.

(34) Van Cleve, T.; Gibara, E.; Linic, S. *ChemCatChem* **2016**, *8* (1), 256–261.

(35) Jing, H.; Large, N.; Zhang, Q.; Wang, H. *J. Phys. Chem. C* **2014**, *118*, 19948–19963.

(36) Kreibig, U.; Vollmer, M. *Optical Properties of Metal Clusters*; 1995.

(37) Maier, S. A. *Plasmonics : fundamentals and applications*; Springer, 2007.

(38) Rakić, A. D.; Djurišić, A. B.; Elazar, J. M.; Majewski, M. L. *Appl. Opt.* **1998**, *37* (22), 5271–5283.

(39) Ribbing, C. G.; Roos, A. *Handb. Opt. Constants Solids* **1997**, 875–882.

(40) Stiles, P. L.; Dieringer, J. A.; Shah, N. C.; Van Duyne, R. P. *Annu. Rev. Anal. Chem* **2008**, *1*, 601–626.

(41) Darby, B. L.; Auguié, B.; Meyer, M.; Pantoja, A. E.; Le Ru, E. C. *Nat. Photonics* **2016**, *10*, 40–46.

(42) Djorovic, A.; Meyer, M.; Darby, B. L.; Le Ru, E. C. *ACS Omega* **2017**, *2*, 1804–1811.

(43) Sun, Y. *Science* **2002**, *298* (5601), 2176–2179.

Chapter 8 Quantifying Light Absorption in the Strong Light-Matter Coupling Regime

8.1 Publication Information

The data presented in this chapter has been composed as a manuscript, which I will submit for publication with the author list: Steven Chavez and Suljo Linic. This chapter looks at light absorption and energy transfer/localization in plasmonic/photonic nanostructures that are strongly coupled to molecules.

8.2 Summary

The strong coupling of optical absorbers (e.g., molecules or semiconductors) to confined photonic modes fundamentally alters the physical properties of the coupled system via the formation of hybrid light-matter states. One potential application of strong light-matter coupling relies on exploiting it to localize light-induced charge excitation processes to small volumes of material. Applications that would benefit from this localization include thin-film photovoltaics, photodetection, photocatalysis, and others, where the overall performance depends on the ability of a material to amplify light absorption (i.e., the formation of electron-hole pairs) within specific locations in space. This contribution investigates how strong light-matter coupling affects light absorption rates in molecular absorbers coupled to photonic nanostructures. Our results show that the molecular light absorption efficiencies are highest in configurations where the strongly coupled molecules interact directly with the incoming photon flux. We also identify a nonlinear dependence in the molecular absorption as a function of concentration, unique to the strongly coupled systems. Based on these results, we propose design principles for engineering

nanostructured systems that allow for high efficiencies of charge carrier localization into strongly coupled absorbers.

8.3 Introduction

Interactions between light and matter can significantly change when confined inside a photonic structure.[1–6] For example, electronic transitions in an absorber (emitter) such as a dye molecule can hybridize with a confined electromagnetic field. This light-matter hybridization is similar to the hybridization of electronic states when atoms form chemical bonds. This hybridization can be achieved experimentally by placing the emitter within the vicinity (or inside) of a photonic or plasmonic structure that supports high-intensity electric fields. A typical example is a Fabry-Perot optical cavity consisting of two parallel metallic mirrors.[6,7] In this case, a simple dipole interaction governs the interaction strength (V) between an emitter and the cavity:

$$V = \vec{d} \cdot \vec{E} \tag{8.1}$$

where, $\vec{d}$ is the transition dipole moment of the emitter in the cavity, and $\vec{E}$ is an operator representing the electric field of electromagnetic radiation confined by the cavity.[8] Physically, V is proportional to the rate of energy exchange between the emitter and the cavity.

The extent of the light-matter hybridization depends on the magnitude of V relative to the rate of the energy dissipation pathways in the system (**Figure 8.1**). These dissipation pathways include the decay rate of the emitter excited state (described by the decay constant Γ_e) and the decay rate of the photon in the cavity (described by the decay constant Γ_c). In the limit of slow cavity-emitter energy exchange compared to the energy dissipation rates, i.e., when $V << (\Gamma_e, \Gamma_c)$, the system is in the *weak coupling* regime (**Figure 8.1a**). When weakly coupled, the individual energy levels of the emitter and the cavity remain distinct. However, we can still observe some modifications of the emitter's physical behavior. A common example is the enhanced fluorescence

of an emitter placed in an optical cavity due to the alteration of the emitter emission channels – known as the Purcell effect.[9] When the rate of energy exchange becomes faster than any available energy dissipation pathway in the system, i.e., when $V >> (\Gamma_e, \Gamma_c)$, the system enters the *strong coupling* regime (**Figure 8.1b**). The strong emitter-cavity coupling results in the emergence of two hybrid light-matter energy states known as polaritons, resulting from the splitting of the emitter energy levels. The upper (P+) and lower (P-) polaritons are separated equally from the initial energy of the emitter electronic transition (when the cavity resonance and emitter energy perfectly overlap). The total splitting is given by the Rabi splitting energy ($\hbar\Omega_R$). In the absence of dissipation, the expression for $\hbar\Omega_R$ is given by[6]:

$$\hbar\Omega_R = 2V_N = 2\,\vec{d}\cdot\vec{E} = 2d\sqrt{\frac{\hbar\omega}{2\varepsilon_0 v}}\times\sqrt{n_{ph}+1} \tag{8.2}$$

where V_N is the collective interaction strength for N molecules in the cavity, ε_0 is the vacuum permittivity, v is the volume of the confined electromagnetic mode, $\hbar\omega$ is the resonant energy, and n_{ph} is the number of photons in the cavity.

Equation 8.2 indicates several mechanisms to increase the value of $\hbar\Omega_R$ and thus the probability that the system will enter the strong coupling regime. These include ensuring that the electromagnetic mode of the cavity is resonant with the emitter electronic transition (allowing them to exchange photons of the same energy), designing cavities with high electric fields compared to the free space electric field, which can be accomplished by confining the electric field into small volumes (i.e., decreasing v), and increasing the magnitude of dipole moment (d) of the emitter coupled to the cavity. For N emitters in the cavity, d is a collective dipole moment and can be increased by increasing the concentration of molecules in the cavity. Experimentally, the

transition from the weak to strong coupling regime can be probed by monitoring the splitting in the cavity absorption peak (i.e., the emergence of P+ and P-) via optical spectroscopy.

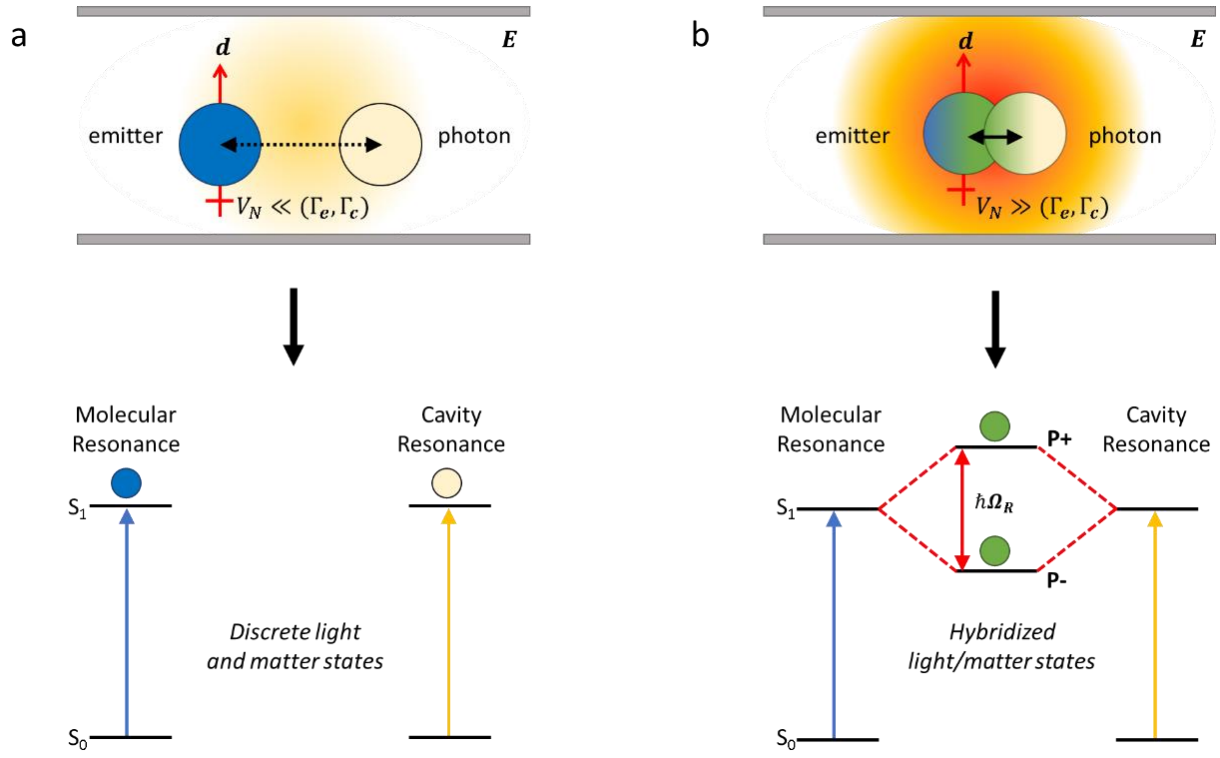

Figure 8.1 Light-matter coupling in the weak and strong coupling regime. Schematic and molecular state diagrams of an emitter with a transition dipole moment, $\vec{d}$, interacting with a photon confined in a metallic Fabry-Perot optical cavity (i.e., between two metallic mirrors). In the weak coupling regime **(a)**, the interaction energy (V_N) between N emitters and the photon in the cavity is low. As a result, the emitter electronic transition and cavity resonance retain their individual character. If V_N becomes sufficiently high, the system enters the strong coupling regime **(b)**, and two hybrid light-matter states (P+ and P-) separated by the Rabi splitting energy $\hbar\Omega_R$ emerge. Here, S_0 and S_1 represent the ground and the excited state of the emitter and $\vec{E}$ corresponds to the magnitude of the electric field confined by the optical cavity.

The emergence of polaritons in strongly coupled systems implies that the system's physical properties are fundamentally altered.[4–6,8,10,11] For example, it has been demonstrated that strong coupling induces modifications of the work function of dye molecule films[12], increases the rate/distance of nonradiative energy transfer between donor and acceptor molecules[13–17], enhances electron transfer in metal-semiconductor systems[18,19], increases the charge conductivity of organic semiconductors[20–22], and changes the rate/selectivity of chemical reactions by coupling of

electronic/vibrational modes of the reacting molecules to a cavity.[23–28] Another potential application of strong light-matter coupling relies on exploiting it to localize light-induced charge excitation processes to small volumes of material strongly coupled to a cavity. Practical applications that would benefit from these processes include thin-film photovoltaics, photodetection, photocatalysis, and other applications where the overall performance often depends on the ability of a material to localize and amplify light absorption (i.e., the formation of electron-hole pairs) to small volumes.[29–36]

While a few reports have shown that strong coupling can enhance light absorption in the strongly coupled systems (e.g., a cavity plus the materials coupled to the cavity), it is unclear how the absorption process is spatially distributed throughout the system.[37,38] For example, in Fabry-Perot optical cavities that contain two metallic mirrors, one would expect a significant fraction of absorption to occur directly in the mirrors. Due to the short lifetime of charge carriers in metals, this absorption would lead to parasitic heating losses in the mirrors.[39] This work aims to quantify the impact of strong coupling on the localization of the absorption process in dye molecules coupled to a cavity. Localizing the light absorption to the dye molecules is critical for hot electron (hole) technologies because of the long lifetimes of charge carriers generated in molecules compared to metals. These longer lifetimes allow the potential extraction of these charge carriers to perform functions such as driving photo-catalytic reactions or serving as a driving force to enhance the electrochemical potential of charge carriers.

To answer these questions, we use a combination of experimental and modeling approaches to investigate how the local light absorption rates (i.e., charge carrier generation) are modified within strongly coupled molecular absorbers. Our model system consists of 5,6-dichloro-2-[[5,6-dichloro-1-ethyl-3-(4-sulphobutyl)-benzimidazol-2-ylidene]-propenyl]-1-ethyl-3-(4-

sulphobutyl)-enzimidazolium hydroxide, sodium salt, inner salt (TDBC) J-aggregate molecules coupled to a Fabry-Perot optical cavity consisting of two parallel silver (Ag) mirrors. We tune the system in and out of the strong coupling regime by varying the concentration of TDBC inside the cavities (i.e., increasing/decreasing *d*). We use this model system to analyze the critical parameters that govern the rate of charge excitation in the coupled system. Our results show that strong coupling offers opportunities to significantly amplify the absorption rates in the molecules coupled to the cavity. We demonstrate that effectively designed systems require significantly lower volumes and molecular concentrations to induce identical absorption rates as stand-alone molecular systems or the same system adsorbed on metallic mirrors. Based on these studies, we propose design principles for engineering nanostructured systems that allow for high efficiencies of charge carrier localization into strongly coupled absorbers.

8.4 Results and Discussion

8.4.1 Nanofabrication of Cavity and Control Systems

We fabricated three Fabry-Perot cavity systems for this study: one containing a high concentration of TDBC, one containing a low concentration of TDBC, and one containing no TDBC. These cavities were fabricated to ensure their optical mode was resonant (tuned) to the TDBC electronic transition at 590 nm (See **Figure 8.2a**). The cavities were fabricated by first depositing a 200 nm Ag film onto a piranha cleaned glass slide via electron beam evaporation at a rate of 5 A/s. Next, TDBC-polymer solutions of varying TDBC concentrations were prepared by dissolving either 1 wt% (low concentration) or 33 wt% (high concentration) of TDBC into aqueous solutions of polyvinyl alcohol (PVA). Here, wt% is the mass of TDBC divided by the total mass of TDBC and PVA in the solution. These solutions were filtered through a 0.22 um nylon mesh and spin-cast onto the glass-supported Ag film to create PVA thin films loaded with the TDBC

dye molecules. We determined the TDBC-PVA film thicknesses to be ~337 nm (PVA only), ~332 nm (low concentration), and ~203 nm (high concentration) using a combination of ellipsometry and profilometry measurements. We completed the cavities by evaporating a second, semi-transparent 30 nm Ag layer on top of the TDBC-PVA film.

8.4.2 Optical Characterization of Cavity and Control Systems

We characterized the optical characteristics of the fabricated systems by analyzing their wavelength-dependent fractional absorption spectra using an optical integrating sphere. The fractional absorption (*A*) spectra for the cavity and mirror were obtained by measuring the samples' fractional reflection (R) at normal incidence and utilizing the equation $A = 1 - R - T$. We compared these absorption spectra to the absorption spectra of a few control samples (see **Figure S *9***): 1) *mirror systems* with the low and high concentration TDBC-PVA films coated onto 200 nm Ag films (with no top mirror), and 2) *stand-alone TDBC-PVA films* of the low and high concentrations coated directly onto glass slides (with no top mirror). The thicknesses and concentrations of the TDBC-PVA layers in these control systems were identical to the thicknesses and concentrations of the TDBC layers in the cavity systems.

The data in **Figure 8.2a** show that the pure PVA-Ag cavity supports two optical modes: one at ~400 nm and one at ~590 nm. The latter directly overlaps with the TDBC electronic transition. In the case of the low TDBC concentration (**Figure 8.2b**), the cavity mode overlapping with the TDBC transition remains unperturbed (i.e., there is a single absorption band at 590nm). This retention of the single cavity mode indicates that the concentration of TDBC in the cavity is not high enough to push the sample into the strong coupling regime. On the other hand, the data for the high concentration cavity (**Figure 8.2c**) show an apparent splitting of the cavity mode due to the coupling of the cavity and TDBC electronic excitations. The absorption Rabi splitting energy

between the P+ and P- peaks is measured to be ~200 meV. To confirm that the high concentration cavity system had entered the strong coupling regime, we used the following equation that defines the magnitude of Rabi splitting required for strong coupling:

$$\hbar\Omega_R > \sqrt{\frac{\Gamma_{UP}^2}{2} + \frac{\Gamma_{LP}^2}{2}} \tag{8.3}$$

where Γ_{UP} and Γ_{LP} are the linewidths of the upper and lower polariton branch modes.[37] **Figure 8.2d** shows the baseline-corrected absorption spectra of the high TDBC concentration cavity system taken from **Figure 8.2c** and its spectral separation. The values of Γ_{UB} and Γ_{LB} are estimated to be 185 meV and 84 meV, corresponding to a $\sqrt{\frac{\Gamma_{UB}^2}{2} + \frac{\Gamma_{LB}^2}{2}}$ value of 144 meV. This is smaller than the Rabi splitting energy of ~200 meV, which confirms that the high concentration TDBC cavity has entered the strong coupling regime.

We compared the absorption spectra of the cavity systems to those of the mirror and stand-alone TDBC-PVA control systems to assess the impact of strong coupling on the light absorption (**Figure 8.2b** and **Figure 8.2c**). For the non-cavity samples, where light interacts directly with the TDBC-PVA films, we observe the absorption due to the TDBC electronic transition at 590 nm. In the case of the high concentration TDBC film in the mirror configuration, we observe a broadening of the absorption resulting from reflection off the bottom Ag mirror. To quantify how effective the cavity and mirror systems are at absorbing incident light energy, we calculated an "absorption enhancement" factor where we compare the absorption of these systems to the absorption by the stand-alone TDBC-PVA system via the following equation:

$$Abs\ Enhancement = \frac{A_{total}}{v_{total}} \times \frac{v_{TDBC}}{A_{TDBC}} \tag{8.4}$$

where A_{total} is the total energy absorbed in either the cavity or mirror system, v_{total} is the volume of absorbing material in that system (i.e., Ag layers + TDBC-PVA layer), A_{TDBC} is the total energy absorbed in the stand-alone TDBC-PVA layer (of the same thickness and concentration as the TDBC-PVA layer used in the corresponding cavity or mirror systems), and v_{TDC} is the total volume of just the TDBC-PVA layer in each respective system. We calculated the values of A_{total} and A_{TDBC} by integrating the fractional absorption curves in **Figure 8.2b-c** with respect to energy across the wavelength range of 450nm to 750 nm, where strong coupling is relevant. The data in **Figure 8.2e** show the volume-normalized absorption enhancement for the cavity and mirror systems compared to their stand-alone TDBC-PVA counterparts. We observe that for the low concentration systems, the volume-normalized absorption enhancement is always larger than 1, meaning both the mirror and cavity systems absorb more than the stand-alone TDBC-PVA films at this concentration. In contrast, the data for the high concentration systems show that the absorption enhancement is only greater than one for the mirror configuration.

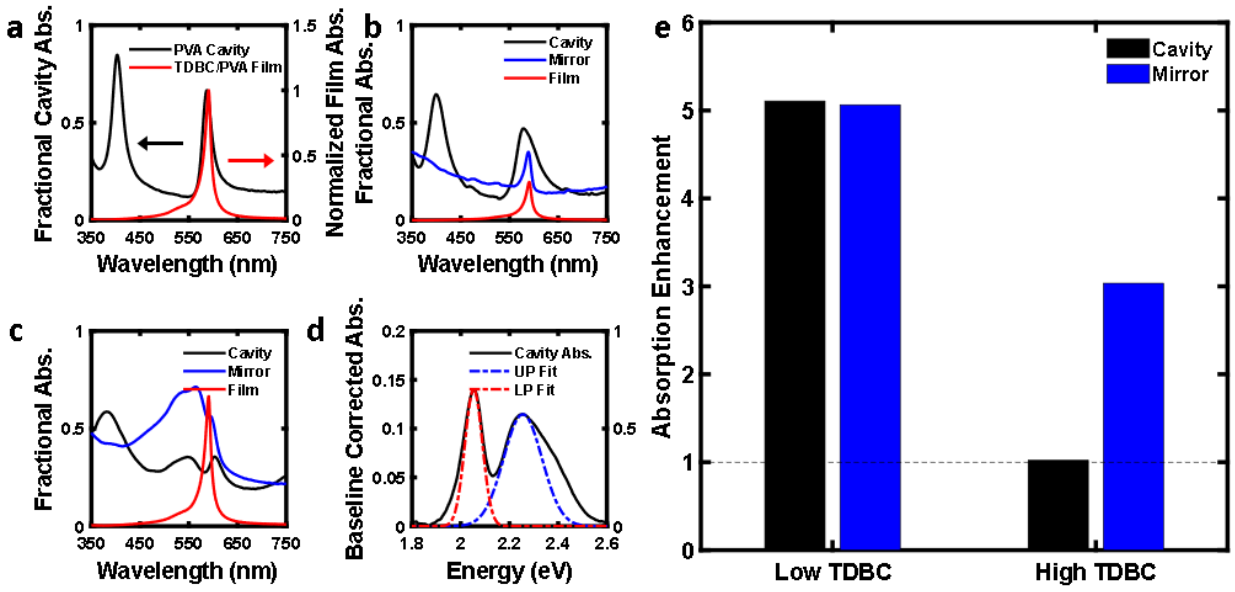

Figure 8.2 Optical characterization of cavity and control systems. a) Wavelength-dependent fractional absorption spectra of a PVA cavity tuned to the TDBC resonance at 590 nm (black) and the normalized absorption spectra of a

TDBC-PVA film on glass (red). **b-c**) Experimentally measured fractional absorption spectra for the low concentration (b) and high concentration (c) TDBC-PVA cavity, mirror, and stand-alone film systems. **d**) The baseline-corrected absorption of the high concentration cavity system and its spectral separation. **e**) Experimental absorption enhancements calculated for the cavity and mirror systems via equation 4.

8.4.3 Efficiency Analysis of Cavity and Control Systems

While the experimental data presented in **Figure 8.2** shows how effectively these different systems absorb light, they do not give us any information about the system's *local* light absorption rate (i.e., charge carrier generation) in various components (Ag and TDBC). It is usually preferred to absorb light in the desired part of the system (for example, the dye molecules) rather than in the metallic Ag mirrors, where the absorbed energy is dissipated as a parasitic heat loss.[39,40] To answer questions related to the local rates of charge carrier formation, we developed a finite element method (FEM) model and performed simulations on the systems of interest (see supplemental **Section S2**). Our objective was to determine how the rate of charge carrier generation is distributed throughout the different components of the systems. The FEM model geometry consisted of TDBC-PVA films (of thicknesses corresponding to the experimentally measured thicknesses) sandwiched between a 30 nm Ag top film and 200 nm Ag bottom film for the cavity systems, or without the respective top/bottom Ag films for the mirror and stand-alone TDBC-PVA systems. We measured the dielectric properties for the TDBC-PVA films of varying concentrations using variable angle spectroscopic ellipsometry (see **Section S3** and **Figure S 10**) and obtained the dielectric data for Ag from standard databases.[41] We validated the model's accuracy by calculating the wavelength-dependent fractional absorption of the high and low concentration cavity/control systems. The calculated spectra in **Figure S 11** show good agreement with the experimental spectra presented in **Figure 8.2**.

We used the model to calculate the absorption enhancement factors for the simulated systems using equation 4 above. We calculated the total absorption in various components of the

system (e.g., the Ag mirrors and the dye layer) by integrating the resistive heating losses within the entire volume of each component across the wavelength range of 450 nm to 750 nm. The data in **Figure 8.3a** show good qualitative agreement with the experimental data in **Figure 8.2e**. Differences in the magnitude and relative values are likely a result of experimental error such as inhomogeneities/roughness in the spin-coated films that are not present in the simulations. We next used the FEM model to shed light on the rate of energy dissipation (i.e., charge carrier excitation) through the TDBC molecules in each system (**Figure 8.3b-d**). We calculated the TDBC absorption enhancement by dividing the total energy absorbed directly in the TDBC layers in each system by the total energy absorbed in a stand-alone TDBC-PVA layer of the same thickness and concentration across the wavelength range of 450 to 750 nm. The data in **Figure 8.3b** show that the TDBC absorption enhancement for the cavity system is higher than for the mirror system in the case of low concentration. We attribute this enhancement to an electric field-induced energy transfer from the cavity mode to the TDBC molecules.[34,42] The data also show that the high concentration cavity system (i.e., the strongly coupled system) has lower TDBC absorption enhancements than the mirror systems. The high concentration mirror system exhibits the most prominent enhancement.

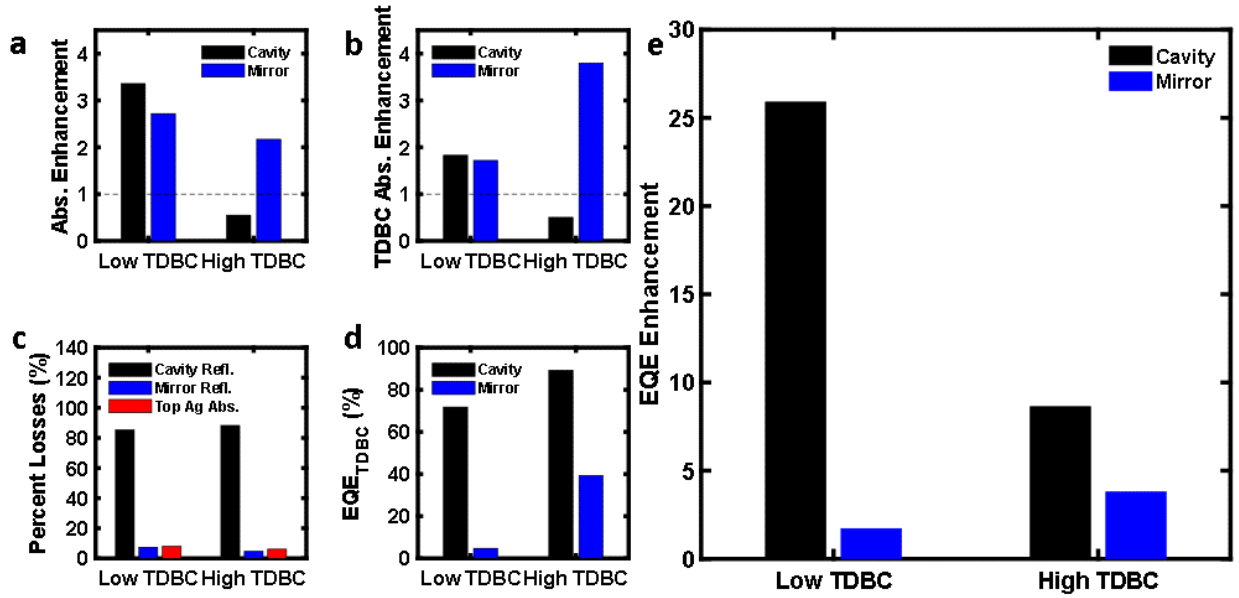

Figure 8.3 Efficiency analysis of cavity and control systems. Absorption enhancement calculated for the simulated cavity and mirror systems via equation 4. **b**) The TDBC absorption enhancement calculated for the simulated cavity and mirror systems compared stand-alone TDBC-PVA films of the same thickness and concentration. **c**) Percentage of energy lost due to reflection (black/red) or to absorption within the top Ag mirror (blue) in the simulated cavity and mirror systems. **d)** Calculated external quantum efficiency for TDBC absorption (EQE_{TDBC}) of the simulated cavity and mirror systems. **e)** Calculated EQE_{TDBC} enhancement for the simulated cavity and mirror systems.

One crucial aspect to consider when comparing the absorption enhancement of the cavity systems to the mirror systems is related to the presence of the top Ag mirror in the cavity systems. Specifically, losses related to reflection from the top Ag mirror and absorption within the top Ag mirror itself play a significant role in the overall absorption efficiencies of the cavity systems. We quantified these losses by using the FEM model to calculate the fraction of light reflected off the cavity/mirror systems and the absorption losses directly in the top Ag mirror for the cavity systems. The data in **Figure 8.3c** show that introducing a top Ag mirror to form the cavities increases the total reflection losses compared to the mirror systems. These losses increase from ~5% and ~8% (for no top mirror configurations) to ~85% and ~88% (with the top Ag mirror) for the low and high TDBC concentration systems. The 30 nm top Ag mirror results in an additional loss of about 6-8% of the incoming light energy due to parasitic absorption directly in the Ag film.

Next, we investigated how strong coupling affects the local rates of charge carrier excitation in TDBC without these additional losses due to the top Ag mirror. We accomplished this by calculating the absorption external quantum efficiency within the TDBC molecules (EQE_{TDBC}) in the cavity and mirror systems. Specifically, we subtracted the amount of light reflected by and absorbed within the top Ag mirror from the total light impinging on the system to obtain the amount of light directly reaching the TDBC layer for the wavelength range of 450 nm to 750 nm. The EQE_{TDBC} was then determined by dividing the amount of light absorbed by the TDBC-PVA layer by the amount of light reaching the TDBC-PVA layer (multiplied by 100). The data in **Figure 8.3d** show that the cavity system surpasses the mirror system efficiencies for both the low and high TDBC concentrations, with the strongly coupled cavity reaching an EQE_{TDBC} value of ~89%. While this data suggests that entering the strong coupling regime enhances the light absorption EQE within these molecular dyes, we need to consider that simply increasing the concentration of molecules in the cavity increases the absorption in the system. To normalize for this concentration effect, we calculated the enhancement in EQE for the cavity and mirror systems by dividing their EQE by the EQE for the stand-alone TDBC film of equivalent concentration. The data in **Figure 8.3e** show that the cavity systems exhibit much higher EQE than the mirror systems, with the lowest concentration systems exhibiting the largest enhancement.

8.4.4 Thickness Analysis of TDBC-Nanohole Array Systems

Our analysis presented in **Figure 8.3** allows us to postulate the optimal system for directing light energy into molecules or other absorbers. We hypothesized that an open system with strongly coupled absorbers directly interacting with the incoming photon flux would yield the highest light absorption efficiencies. The corollary to this hypothesis is that these open systems would be ideal for enhancing light absorption in extremely thin films of molecular absorbers (i.e., tens of

nanometers and less), which we expect to absorb poorly even in the mirror configuration. This corollary stems from the data in **Figure 8.3**, where the low concentration systems (which are inherently poor absorbers) exhibit the most significant EQE enhancements. As we noted above, enhancing the rates of absorption in exceptionally thin layers of material is critical for various applications, including photovoltaics and photocatalysis.[36,43–45]

We tested these hypotheses by using the FEM model to study the light absorption rates within TDBC-PVA films of decreasing thickness deposited on an Ag film containing a hexagonal array of nanoholes. The Ag nanohole array system couples incoming light to the metal film via a grating coupling mechanism. This coupling results in surface plasmon polaritons (SPP) that significantly enhance the electromagnetic field confinement to the surface of the Ag array. Coupling molecules to these SPP modes can give rise to strong light-matter coupling similar to the coupling of Fabry-Perot cavities.[46–48] We tune the SPP wavelength (λ_{sp}) of the nanohole array for a constant Ag film thickness and nanohole diameter (D) by varying the periodicity (P) of the nanoholes. We note that the optical signature of the plasmon resonance for these array systems is a peak in the nanohole transmission (and absorption) spectra.[49,50]

We chose the model parameters to ensure the TDBC-PVA thin films coupled to the Ag nanohole array system entered the strong coupling regime. We set the Ag film thickness for the array systems to 200 nm and varied the thickness of the TDBC-PVA layer on top of the array from 40 nm to 5 nm. We set D to 130 nm, and P was varied to ensure λ_{sp} overlapped with the TDBC electronic transition at 590 nm (**Table 2**). Finally, we set the dielectric properties for the TDBC-PVA films equal to those experimentally extracted from a 66 wt% TDBC-PVA film (**Figure S 12**). These parameters were used in the FEM model to study the effectiveness of these systems to localize the absorption process into these molecular dyes.

The data in **Figure 8.4a** show the simulated absorption spectra for the TDBC-PVA nanohole array systems with varying film thicknesses. We observe a peak centered at 590 nm for all systems due to absorption from uncoupled TDBC molecules. We also observe the emergence of strongly coupled P+ and P- peaks for each system, where the Rabi splitting increases with increasing film thickness due to the higher number of coupled TDBC molecules. To ensure these systems have entered the strong coupling regime, we compared the Rabi splitting energy of the thinnest TDBC-PVA array system (~181.5 meV) with the linewidths of its upper and lower polariton branches via equation 3. The data in **Figure S 13** show that the linewidths of the P+ and P- branches correspond to Γ_{UP} and Γ_{LP} values of 76.89 meV and 60.91 meV, respectively, which results in a $\sqrt{\frac{\Gamma_{UP}^2}{2}+\frac{\Gamma_{LP}^2}{2}}$ value of 69.7 meV. This analysis confirms that these systems have entered the strong coupling regime.

We next calculated EQE_{TDBC} for these systems as described above (we note that there is no top Ag mirror in these systems). We plotted the calculated EQE_{TDBC} in **Figure 8.4b** along with the EQE_{TDBC} for the corresponding control systems. The data show that the nanohole array systems coupled to TDBC exhibit significantly higher EQE_{TDBC} values than their corresponding mirror and stand-alone TDBC-PVA systems. The EQE_{TDBC} is highest for the thickest TDBC-PVA film (40 nm), which approaches 37%, compared to 19% for the mirror system and 13% for the respective stand-alone TDBC-PVA layer. This analysis supports our hypotheses that strongly coupled open systems enhance molecular absorption compared to their mirror counterparts.

Additionally, we calculated the EQE_{TDBC} enhancement for the array and mirror configurations of varying TDBC-PVA layer thickness relative to the stand-alone TDBC system and plotted them in **Figure 8.4c**. We observe that the highest enhancements in TDBC absorption compared to the stand-alone TDBC-PVA films occur for the thinnest samples. These observations

demonstrate that entering the strong coupling regime is critical for designing systems that localize energetic charge carrier formation rates in increasingly small volumes. We can see this in **Figure 8.4d**, where we plot the TDBC-PVA layer thicknesses required for the mirror and stand-alone film configurations to reach the same EQE_{TDBC} as the array configuration with identical TDBC-PVA layer thickness and concentration. The data show that for the 40 nm TDBC-PVA thickness, the film thicknesses required to reach the same EQE_{TDBC} as the array system are ~75 nm and ~107 nm for the mirror and stand-along systems, respectively.

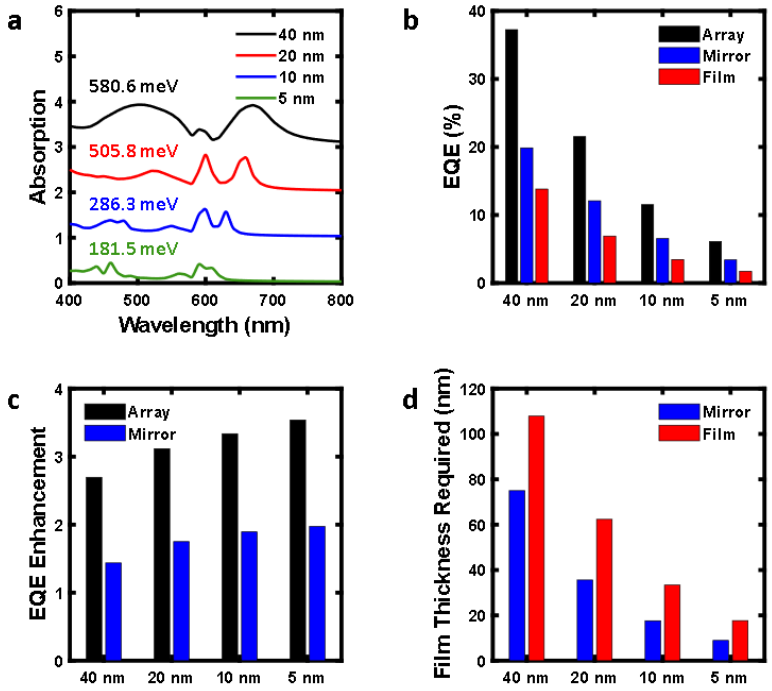

Figure 8.4 Thickness analysis of TDBC-nanohole array systems. a) Simulated fractional absorption spectra of TDBC-PVA films of varying thicknesses coupled to a Ag nanohole array. We show the values of the absorption Rabi splitting next to each spectrum. We vertically offset the spectra for improved visibility. **b)** Calculated EQE_{TDBC}'s of the simulated TDBC-PVA nanohole array systems of varying thicknesses compared to the corresponding mirror systems and stand-alone TDBC-PVA systems of the same thickness and concentration. **c)** Calculated EQE_{TDBC} enhancement for the simulated nanohole array and mirror systems of varying thickness. **d)** Film thicknesses required to achieve the same EQE_{TDBC} as a TDBC-PVA layer at a given thickness strongly coupled to the Ag nanohole array for both the mirror and stand-alone film configurations.

8.4.5 Concentration Analysis of TDBC-Nanohole Array Systems

We also studied the impact of the TDBC concentration on the absorption rates within a TDBC-PVA film of constant thickness (40 nm) coupled to a nanohole array. The TDBC-PVA optical properties were obtained by preparing spin-coated films from solutions of varying TDBC concentration (20 wt% TDBC, 33 wt% TDBC, 50 wt% TDBC, and 66 wt % TDBC) and extracting their optical properties via ellipsometry. We set the array geometric parameters equal to those presented above, except we adjusted *P* to ensure the array systems were resonant with the TDBC electronic transition for each concentration film.

The data in **Figure 8.5a** show the simulated absorption spectra for the 40 nm TDBC-PVA films of varying concentrations coupled to the nanohole array systems. We again observe the emergence of P+ and P- peaks in each system in addition to the bare TDBC absorption peak at 590 nm, suggesting these systems have entered the strong coupling regime. We verify this by plotting the absorption Rabi splitting as a function of the square root of the TDBC concentration in the TDBC-PVA films. The data in **Figure 8.5b** show that the Rabi splitting exhibits a linear dependence on the square root of the TDBC concentration, following equation 2 above. This analysis confirms that these systems have entered the strong coupling regime.

We used the model to study energy dissipation rates through the 40 nm TDBC-PVA films of varying concentrations coupled to the nanohole array. We compared these rates to the energy dissipation rates through TDBC-PVA films in the mirror and stand-alone TDBC-PVA film configurations of the same thickness and TDBC concentration. We calculated the total power dissipated within the TDBC-PVA layer for these array, mirror, and stand-alone systems by summing the power absorbed throughout the TDBC layer at each wavelength from 450 nm to 750 nm and plotted it as a function of TDBC concentration (**Figure 8.5c**). The data show that the power

dissipated through TDBC in the array systems is significantly higher than the mirror and stand-alone TDBC-PVA systems. In these control systems, the power dissipation (absorption) in the TDBC layer exhibits a linear dependence on the TDBC concentration, as expected from Beer's law.

Interestingly, the power dissipation throughout TDBC layers coupled to the nanohole arrays is nonlinear with respect to the TDBC concentration. Upon coupling the TDBC film to the nanohole array, we observe a significant initial increase at low concentrations that beings to plateau at higher concentrations. The data in **Figure S 14** show that the power dissipated through the TDBC-PVA films coupled to the array systems exhibits a linear dependence on the square root on the TDBC concentration. This concentration dependence is unique to the strongly coupled films and demonstrates how strong coupling can modify the absorption characteristics in molecular films compared to the weak coupling regime. Additionally, we plotted the enhancement in the total power dissipation throughout the TDBC-PVA films in the array configuration at a given concentration compared to the mirror and stand-alone TDBC-PVA configurations at the equivalent concentration. The data in **Figure 8.5d** again show that the enhancements are most prominent for the low concentration systems.

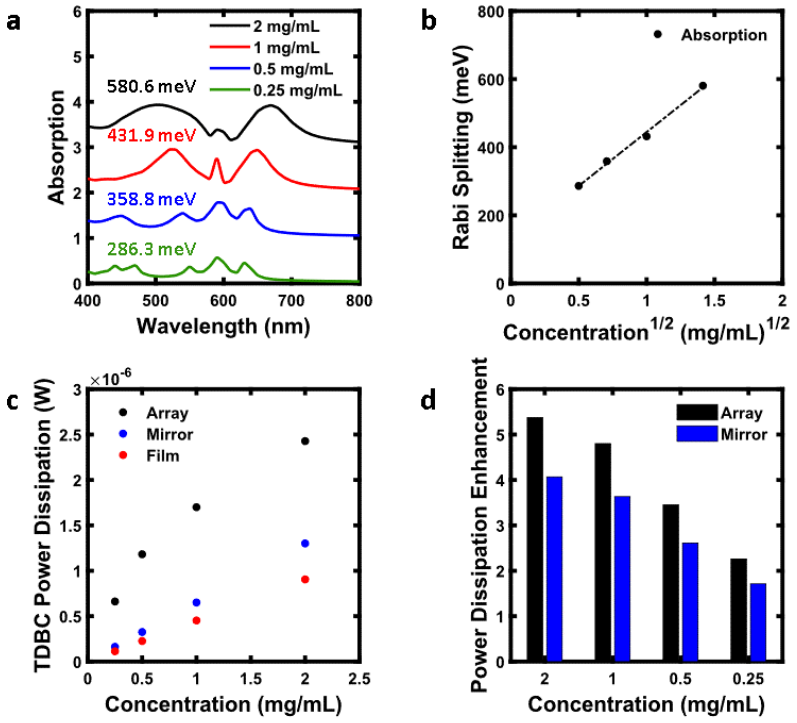

Figure 8.5 Concentration analysis of TDBC-nanohole array systems. a) Simulated fractional absorption spectra of TDBC-PVA films of varying concentrations coupled with a Ag nanohole array. We show the values of the absorption Rabi splitting next to each spectrum. We vertically offset the spectra for improved visibility. **b)** The value of the absorption Rabi splitting for the simulated 40 nm TDBC-PVA nanohole array systems as a function of the TDBC film concentration square root. **c)** The total power dissipated throughout the TDBC-PVA films as a function of the TDBC film concentration in either the array, mirror, or film configuration for the wavelength range of 450 nm to 750 nm. At each wavelength, the power input into the model was 2.1×10^{-7} W. **d)** Calculated power dissipation enhancement for the simulated 40 nm TDBC-PVA nanohole array systems of varying TDBC concentration. In (a-d), the concentration of TDBC is listed in units of mg TDBC/mL water used to prepare the spin coating solution. The amount of PVA used can be calculated from the corresponding wt% values listed in the text.

8.5 Conclusion

The analysis above paints a comprehensive picture of light absorption within molecular thin films coupled to photonic nanostructures. By analyzing the light absorption rates within thin films of dye molecules strongly coupled to Fabry-Perot optical cavities, we demonstrate that light absorption within the molecular layer is highest in systems free from extraneous absorbers that could lead to parasitic absorption losses. We corroborate this by studying the light absorption rates of molecular thin films coupled to plasmonic nanohole arrays. By varying the molecular

concentration within the films, we show that molecules strongly coupled to the arrays exhibit the most significant rates of molecular light absorption compared to weakly coupled systems. We additionally show that strong coupling is ideal for enhancing light absorption in optically thin films by varying the thickness of the films coupled to the arrays. We note that the efficiency enhancement relative to other systems becomes limited at high concentrations (or large thicknesses) due to the ability of the uncoupled systems to absorb increasing amounts of light energy under these conditions. This limited absorption enhancement at high concentrations is also inherently limited by the square root dependence of the power dissipation within TDBC on the molecular concentration, which we show is unique to the strong coupling regime. Overall, these findings provide guidelines for exploiting strong light-matter coupling to improve both traditional solar energy conversion technologies that rely on localizing the charge carrier generation process into small volumes of material and novel polariton-based solar energy conversion systems that rely on the unique properties of photoexcited polaritons to operate at unprecedented efficiencies.[51,52]

8.6 Acknowledgements

This research was supported by the U.S. Department of Energy, Office of Science, Office of Basic Energy Sciences, under Award (DE-SC0021362) (experimental work) and National Science Foundation (NSF) (CBET-1803991) (modeling work). Secondary support for the development of analytical tools used in the model was provided by NSF (CBET-1702471 and CHE-1800197).

8.7 Supporting Information

8.7.1 Fabrication of Cavity and Control Systems

The cavity and control systems were fabricated by first depositing a 200 nm Ag film onto a piranha cleaned glass slide via electron beam evaporation at a rate of 5 A/s and a pressure of 4.0×10^{-6} torr. TDBC-PVA solutions of varying TDBC (Few chemicals) concentrations were prepared by dissolving either 1 wt% (low concentration) or 33 wt% (high concentration) of TDBC into aqueous solutions of PVA (Acros Organics, MW 20000-3000). These solutions were filtered through a 0.22 um nylon mesh and spin-cast onto the glass-supported Ag film to create PVA thin films loaded with the TDBC dye molecules. We completed the cavities by evaporating a second, semi-transparent 30 nm Ag layer on top of the TDBC-PVA film at a rate of 1 A/s. We fabricated control systems by omitting either the top (mirror systems) or both (stand-alone films) Ag depositions.

Figure S 9 Schematics of cavity and control systems. Left) a pure TDBC-PVA film deposited onto glass; **Middle)** a TDBC-PVA film deposited onto a 200 nm Ag mirror without a top Ag mirror. **Right)** a standard TDBC/PVA cavity system as described in the main text.

8.7.2 Finite Element Method Simulations

The optical characteristics of the experimentally fabricated systems were simulated using COMSOL Multiphysics finite-element based software. The '*Wave optics*' module was used to calculate the transmission and reflection fractions of light impinging on a three-dimensional cavity system. The model is set up for one-unit cell where Floquet boundary conditions are describing

the periodicity of the system. A top port (Port 1) is set to send the light wave at a specified incident power and a bottom port (Port 2) is set to absorb the transmitted light. The S-parameters for transmission and reflection are calculated at Port 2 and Port 1 respectively to obtain the transmission and reflection fractions. The dimensions of the top and bottom Ag mirrors were 30 nm and 200 nm respectively and the thickness of the TDBC-PVA layer was varied to match the thicknesses of the films created experimentally. The optical properties for Ag used in the model were taken from the COMSOL database (Rakic) and the data for the TDBC-PVA layers was obtained via ellipsometry (as described in the text and shown in **Figure S 10** below). The simulations for the control systems were performed by removing the respective top/bottom Ag films.

8.7.3 Measuring the Thickness and Dielectric Properties of TDBC-PVA Films

The dielectric properties for the TDBC-PVA films used in the FEM model were extracted from the experimentally fabricated samples. First, TDBC-PVA solutions of low and high TDBC concentration were spin-cast onto optically thick (200 nm) Ag films supported on glass substrates. The refractive index (n) and extinction coefficient of the films were subsequently extracted via Variable Angle Spectroscopic Ellipsometry measurements using a Woollam M-2000 ellipsometer. Briefly, reflection measurements at 3 different angles (55°, 65° and 75°) were performed to obtain measurements for the p- and s- components of the elliptically polarized light. The reflection data was then fit to a thin film model, allowing the optical properties to be extracted. The refractive index (n) and the extinction coefficient (k) for TDBC-PVA films of are shown in **Figure S 10**.

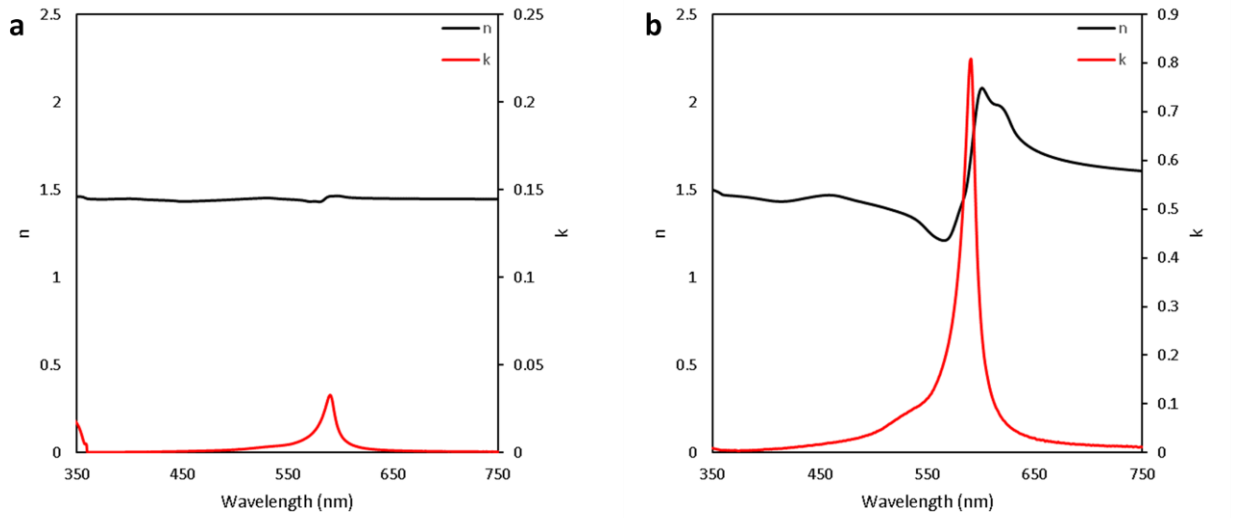

Figure S 10 Dielectric data for the TDBC/PVA films. Ellipsometry extracted refractive index (n) and extinction coefficient (k) of TDBC-PVA films prepared from TDBC-PVA solutions with low **(a)** and high **(b)** concentrations of TDBC.

8.7.4 Simulated Absorption Spectra of Cavity and Control Systems

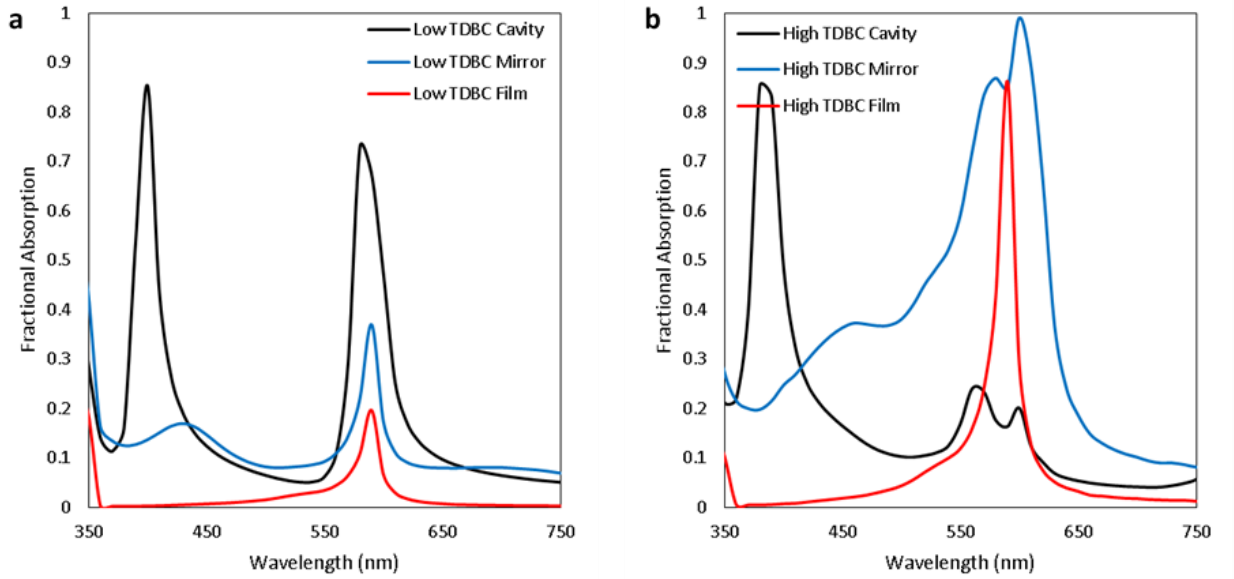

Figure S 11 Simulated optical characteristics of cavity and control systems. Calculated fractional absorption spectra for the low concentration **(a)** and high concentration **(b)** TDBC-PVA cavity, mirror, and stand-alone film systems.

8.7.5 Parameters used in the TDBC-PVA Nanohole Array Analysis

Table 2 Model parameters for the nanohole arrays.

Film Thickness	Period	Hole Diameter	Ag Thickness
40 nm	250 nm	130 nm	200 nm
20 nm	450 nm	130 nm	200 nm
10 nm	590 nm	130 nm	200 nm
5 nm	620 nm	130 nm	200 nm

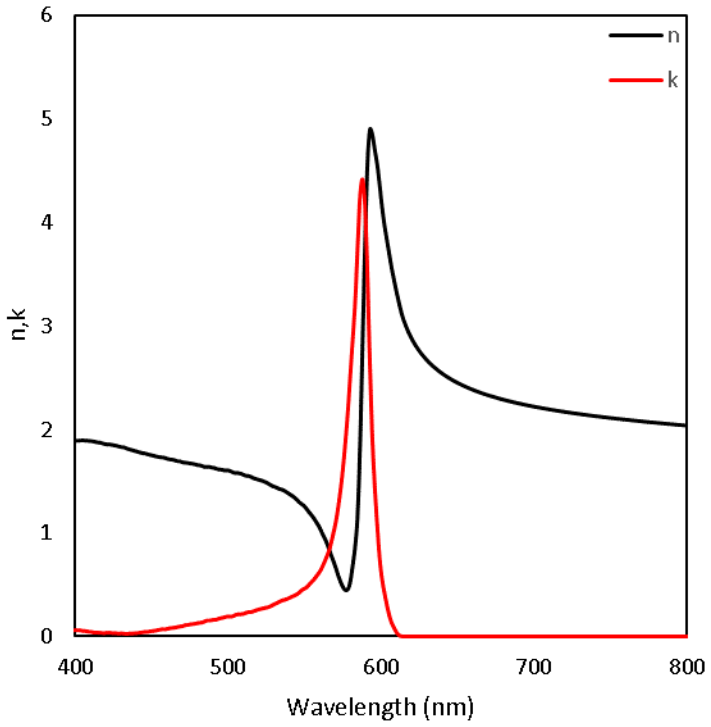

Figure S 12 Dielectric data for 66 wt% TDBC-PVA films. The refractive index (n) and extinction coefficient (k) used in the TDBC-PVA nanohole array models obtained via variable angle spectroscopic ellipsometry measurements.

8.7.6 Strong Coupling in TDBC-PVA Thin Films Supported on Ag Nanohole Arrays

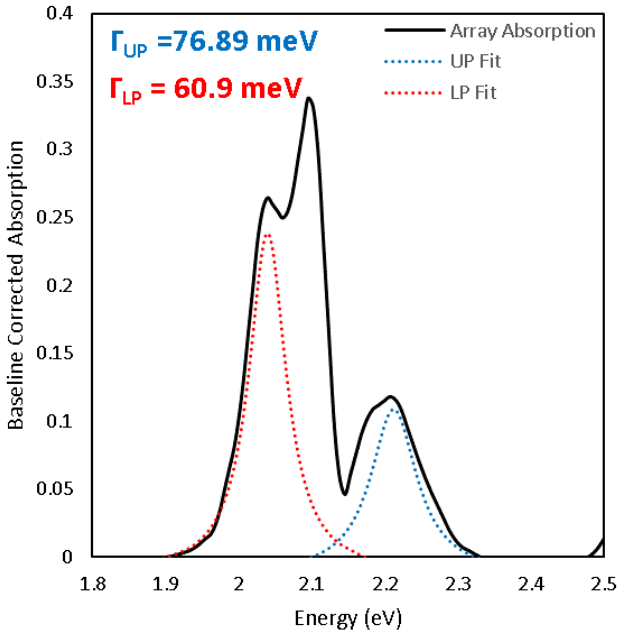

Figure S 13 Confirming the nanohole arrays are in the strong coupling regime. The baseline-corrected absorption of the 5 nm TDBC-PVA film coupled to the Ag nanohole array. The values of Γ_{LP} and Γ_{UP} were extracted by fitting the spectra to a Lorentzian function and extracting the linewidth.

8.7.7 Power Dissipation through Strongly Coupled TDBC-PVA Thin Films

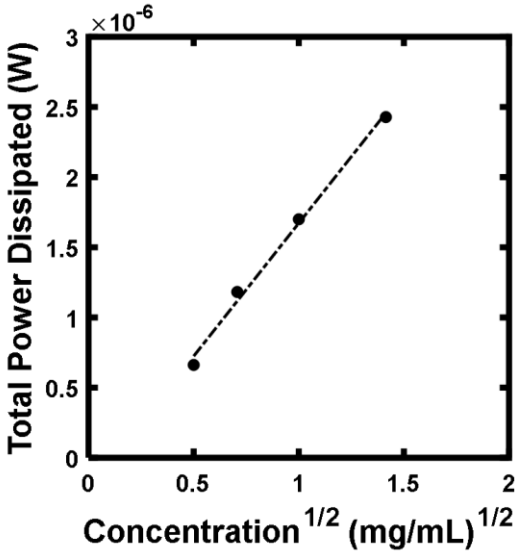

Figure S 14. Power dissipation in strongly coupled nanohole array systems. The total power dissipated throughout the TDBC-PVA films as a function of the square root of TDBC film concentration in the array configuration for the wavelength range of 450 nm to 750 nm. At each wavelength, the power input into the model was 2.1×10^{-7} W.

8.8 References

(1) Skolnick, M. S.; Fisher, T. A.; Whittaker, D. M. *Semiconductor Science and Technology*. IOP Publishing July 1, 1998, pp 645–669.

(2) Kasprzak, J.; Richard, M.; Kundermann, S.; Baas, A.; Jeambrun, P.; Keeling, J. M. J.; Marchetti, F. M.; Szymańska, M. H.; André, R.; Staehli, J. L.; Savona, V.; Littlewood, P. B.; Deveaud, B.; Dang, L. S. *Nature* **2006**, *443* (7110), 409–414.

(3) Raimond, J. M.; Brune, M.; Haroche, S. *Rev. Mod. Phys.* **2001**, *73* (3), 565–582.

(4) Törmä, P.; Barnes, W. L. *Rep. Prog. Phys.* **2015**, *78* (1), 013901.

(5) Vasa, P.; Lienau, C. *ACS Photonics* **2018**, *5* (1), 2–23.

(6) Ebbesen, T. W. *Acc. Chem. Res.* **2016**, *49* (11), 2403–2412.

(7) Baranov, D. G.; Wersäll, M.; Cuadra, J.; Antosiewicz, T. J.; Shegai, T. *ACS Photonics* **2018**, *5*, 24–42.

(8) Hertzog, M.; Wang, M.; Rgen Mony, J.; Bö, K. *Chem. Soc. Rev.* **2019**, *48*, 937–961.

(9) Purcell, E. M. *Phys. Rev.* **1946**, *69* (681).

(10) Dovzhenko, D. S.; Ryabchuk, S. V; Rakovich, Y. P.; Nabiev, I. R. *Nanoscale* **2018**, *10*.

(11) Sanvitto, D.; Kéna-Cohen, S. *Nature Materials*. Nature Publishing Group October 1, 2016, pp 1061–1073.

(12) Hutchison, J. A.; Liscio, A.; Schwartz, T.; Canaguier-Durand, A.; Genet, C.; Palermo, V.; Samorì, P.; Ebbesen, T. W. *Adv. Mater.* **2013**, *25* (17), 2481–2485.

(13) Coles, D. M.; Somaschi, N.; Michetti, P.; Clark, C.; Lagoudakis, P. G.; Savvidis, P. G.; Lidzey, D. G. *Nat. Mater.* **2014**, *13*, 712–719.

(14) Zhong, X.; Chervy, T.; Zhang, L.; Thomas, A.; George, J.; Genet, C.; Hutchison, J. A.; Ebbesen, T. W. *Angew. Chemie - Int. Ed.* **2017**, *56* (31), 9034–9038.

(15) Zhong, X.; Chervy, T.; Wang, S.; George, J.; Thomas, A.; Hutchison, J. A.; Devaux, E.; Genet, C.; Ebbesen, T. W. *Angew. Chemie* **2016**, *128* (21), 6310–6314.

(16) Rozenman, G. G.; Akulov, K.; Golombek, A.; Schwartz, T. *ACS Photonics* **2018**, *5* (1), 105–110.

(17) Georgiou, K.; Michetti, P.; Gai, L.; Cavazzini, M.; Shen, Z.; Lidzey, D. G. *ACS Photonics* **2018**, *5* (1), 258–266.

(18) Zeng, P.; Cadusch, J.; Chakraborty, D.; Smith, T. A.; Roberts, A.; Sader, J. E.; Davis, T. J.; Gómez, D. E. *Nano Lett.* **2016**, *16* (4), 2651–2656.

(19) Shan, H.; Yu, Y.; Wang, X.; Luo, Y.; Zu, S.; Du, B.; Han, T.; Li, B.; Li, Y.; Wu, J.; Lin, F.; Shi, K.; Tay, B. K.; Liu, Z.; Zhu, X.; Fang, Z. *Light Sci. Appl.* **2019**, *8* (1), 9.

(20) Orgiu, E.; George, J.; Hutchison, J. A.; Devaux, E.; Dayen, J. F.; Doudin, B.; Stellacci, F.; Genet, C.; Schachenmayer, J.; Genes, C.; Pupillo, G.; Samorì, P.; Ebbesen, T. W. *Nat. Mater.* **2015**, *14*, 1123–1130.

(21) Nagarajan, K.; George, J.; Thomas, A.; Devaux, E.; Chervy, T.; Azzini, S.; Aziz, J.; Hosseini, M. W.; Kumar, A.; Genet, C.; Bartolo, N.; Ciuti, C.; Ebbesen, T. *ACS Nano* **2020**, *14* (8), 10219–10225.

(22) Hagenmüller, D.; Schachenmayer, J.; Schütz, S.; Genes, C.; Pupillo, G. *Phys. Rev. Lett.* **2017**, *119* (22), 223601.

(23) Canaguier-Durand, A.; Devaux, E.; George, J.; Pang, Y.; Hutchison, J. A.; Schwartz, T.; Genet, C.; Wilhelms, N.; Lehn, J.-M.; Ebbesen, T. W. *Angew. Chemie Int. Ed.* **2013**, *52* (40), 10533–10536.

(24) Schwartz, T.; Hutchison, J. A.; Genet, C.; Ebbesen, T. W. *Phys. Rev. Lett.* **2011**, *106*, 196405.

(25) Hutchison, J. A.; Schwartz, T.; Genet, C.; Devaux, E.; Ebbesen, T. W. *Angew. Chemie Int. Ed.* **2012**, *51* (7), 1592–1596.

(26) Munkhbat, B.; Wersäll, M.; Baranov, D. G.; Antosiewicz, T. J.; Shegai, T. *Sci. Adv.* **2018**, *4*, eaas9552.

(27) Thomas, A.; Lethuillier-Karl, L.; Nagarajan, K.; Vergauwe, R. M. A.; George, J.; Chervy, T.; Shalabney, A.; Devaux, E.; Genet, C.; Moran, J.; Ebbesen, T. W. *Science* **2019**, *363* (6427), 615–619.

(28) Hirai, K.; Hutchison, J. A.; Uji-i, H. *Chempluschem* **2020**, *85* (9), 1981–1988.

(29) Schuller, J. A.; Barnard, E. S.; Cai, W.; Jun, Y. C.; White, J. S.; Brongersma, M. L. *Nat. Mater.* **2010**, *9* (3), 193–204.

(30) Moskovits, M. *Nat. Nanotechnol.* **2015**, *10* (1), 6–8.

(31) Ndukaife, J. C.; Shalaev, V. M.; Boltasseva, A. *Science* **2016**, *351* (6271), 334–335.

(32) Clavero, C. *Nat. Photonics* **2014**, *8* (2), 95–103.

(33) Aslam, U.; Rao, V. G.; Chavez, S.; Linic, S. *Nat. Catal.* **2018**, *1*, 656–665.

(34) Linic, S.; Chavez, S.; Elias, R. *Nat. Mater.* **2021**, 1–9.

(35) Brongersma, M. L.; Halas, N. J.; Nordlander, P. *Nat. Nanotechnol.* **2015**, *10* (1), 25–34.

(36) Aslam, U.; Chavez, S.; Linic, S. *Nat. Nanotechnol.* **2017**, *12*, 1000–1005.

(37) Shi, X.; Ueno, K.; Oshikiri, T.; Sun, Q.; Sasaki, K.; Misawa, H. *Nat. Nanotechnol.* **2018**, 1.

(38) Gómez, D. E.; Shi, X.; Oshikiri, T.; Roberts, A.; Misawa, H. *Nano Lett.* **2021**, *21* (9), 3864–3870.

(39) Khurgin, J. B. *Nat. Nanotechnol.* **2015**, *10*.

(40) Maier, S. A. *Plasmonics: Fundamentals and applications*; 2007.

(41) Rakić, A. D.; Djurišić, A. B.; Elazar, J. M.; Majewski, M. L. *Appl. Opt.* **1998**, *37* (22), 5271.

(42) Li, J.; Cushing, S. K.; Meng, F.; Senty, T. R.; Bristow, A. D.; Wu, N. *Nat. Photonics* **2015**, *9* (9), 601–607.

(43) Atwater, H. a; Polman, A. *Nat. Mater.* **2010**, *9* (3), 205–213.

(44) Chavez, S.; Aslam, U.; Linic, S. *ACS Energy Lett.* **2018**, *3* (7), 1590–1596.

(45) Chavez, S.; Rao, V. G.; Linic, S. *Faraday Discuss.* **2019**.

(46) Salomon, A.; Genet, C.; Ebbesen, T. W. *Angew. Chemie Int. Ed.* **2009**, *48* (46), 8748–8751.

(47) Salomon, A.; Wang, S.; Hutchison, J. A.; Genet, C.; Ebbesen, T. W. *ChemPhysChem* **2013**, *14* (9), 1882–1886.

(48) Kang, E. S.; Chen, S.; Sardar, S.; Tordera, D.; Armakavicius, N.; Darakchieva, V.; Shegai, T.; Jonsson, M. P. *ACS Photo* **2018**, *5* (10), 4046–4055.

(49) Ebbesen, T. W.; Lezec, H. J.; Ghaemi, H. F.; Thio, T.; Wolff, P. A. *Nature* **1998**, *391* (6668), 667–669.

(50) Genet, C.; Ebbesen, T. W. *Nature* **2007**, *445*, 39–46.

(51) Nikolis, V. C.; Mischok, A.; Siegmund, B.; Kublitski, J.; Jia, X.; Benduhn, J.; Hörmann, U.; Neher, D.; Gather, M. C.; Spoltore, D.; Vandewal, K. *Nat. Commun. 2019 101* **2019**, *10* (1), 1–8.

(52) Bujalance, C.; Esteso, V.; Caliò, L.; Lavarda, G.; Torres, T.; Feist, J.; García-Vidal, F. J.; Bottari, G.; Míguez, H. *J. Phys. Chem. Lett.* **2021**, *12*, 10706–10712.

Chapter 9 Investigating Charge Extraction from Strongly Coupled Molecular Absorbers

9.1 Summary

This chapter presents preliminary work investigating the possibility of extracting photogenerated charge carriers from strongly coupled molecular absorbers. We show that strongly coupled systems demonstrate signatures of enhanced transport of photogenerated carriers. These signatures include lower system resistances and possibly generation of photocurrent under illumination. Overall, this data suggests that extracting photogenerated charge from strongly coupled molecules is possible due to increased charge transport. More experiments need to be performed to verify these conclusions.

9.2 Introduction

Strong light-matter coupling has emerged as an attractive avenue for modifying materials properties in various systems.[1–9] Recent research demonstrates that the hybridization of molecules or semiconductors with confined optical modes induces modifications of the work function of dye molecule films[10], increases the rate/distance of nonradiative energy transfer between donor and acceptor molecules[11–15], enhances electron transfer in metal-semiconductor systems[16,17], increases the charge conductivity of organic semiconductors[18–20], and changes the rate/selectivity of chemical reactions by coupling of electronic/vibrational modes of the reacting molecules to a cavity.[21–26] However, only a few studies have studied the ramifications of strong light-matter coupling on phenomena related to solar energy conversion such as light absorption. [27,28] In the previous chapter of this dissertation, we showed that strongly coupled systems can amplify and

localize light absorption into optical absorbers coupled to plasmonic/photonic structures. We hypothesized that we could extract charge generated in the coupled molecules because of their enhanced charge transport properties. [18–20,29]

This chapter uses a combination of experimental and modeling approaches to investigate whether we can extract photogenerated charge from strongly coupled molecular absorbers. We study systems comprising of 5,6-dichloro-2-[[5,6-dichloro-1-ethyl-3-(4-sulphobutyl)-benzimidazol-2-ylidene]-propenyl]-1-ethyl-3-(4-sulphobutyl)-enzimidazolium hydroxide, sodium salt, inner salt (TDBC) J-aggregate molecules coupled to Fabry-Perot optical cavities. We tune the systems in and out of the strong coupling regime by varying the thickness of the TDBC molecular films used in the cavities and the TDBC concentration. Our results suggest that strong coupling offers opportunities to extract photogenerated charge from molecules coupled to the cavities. We demonstrate that strongly coupled systems exhibit signatures of enhanced charge transport. Preliminary data suggest that photocurrent measured in strongly coupled systems exhibits contributions from photoelectronic current produced by charge carriers.

9.3 Results and Discussion

9.3.1 Fabrication of Cavity and Control Systems

We fabricated four Fabry-Perot cavity systems and four mirror control systems for this study (**Figure 9.1**). We fabricated these systems to contain either low TDBC concentration, high TDBC concentration, or no TDBC. The thicknesses of the cavities were tuned to ensure one of their optical modes was resonant with the TDBC electronic transition at ~590 nm. We purposely detuned one of the high concentration cavities from the TDBC electronic transition to act as a control. We fabricated these cavities by using electron beam evaporation to deposit 200 nm of Ag onto degenerately doped p^+-Si wafers with a resistivity of ~0.005 Ω-cm (Addison Engineering).

The p^+-Si wafers were cleaned with piranha solution and etched with HF before the deposition. We performed the Ag evaporation at ~$4x10^{-6}$ torr and a rate of 5 A/s. We next prepared TDBC-polymer solutions of varying concentrations to deposit onto the Ag films. We dissolved either 1.25 wt% (low concentration) or 33 wt% (high concentration) of TDBC into aqueous solutions of PVA at room temperature. We filtered these solutions through nylon mesh with pore diameters of 0.22 μm. These solutions were spin-coated onto the Ag films to form TDBC-loaded PVA films. We used variable angle spectroscopic ellipsometry to measure the thicknesses of the TDBC-PVA films. The film thicknesses were ~339 nm, ~334 nm, ~220 nm, and ~133 nm for the PVA, low TDBC concentration, high TDBC concentration (tuned), and high TDBC concentration (detuned) systems, respectively. Finally, we evaporated a second, 30 nm layer of Ag on top of the TDBC-PVA films to complete the cavities. We fabricated the control mirror systems by repeating the steps above and stopping before adding the 30 nm Ag layer.

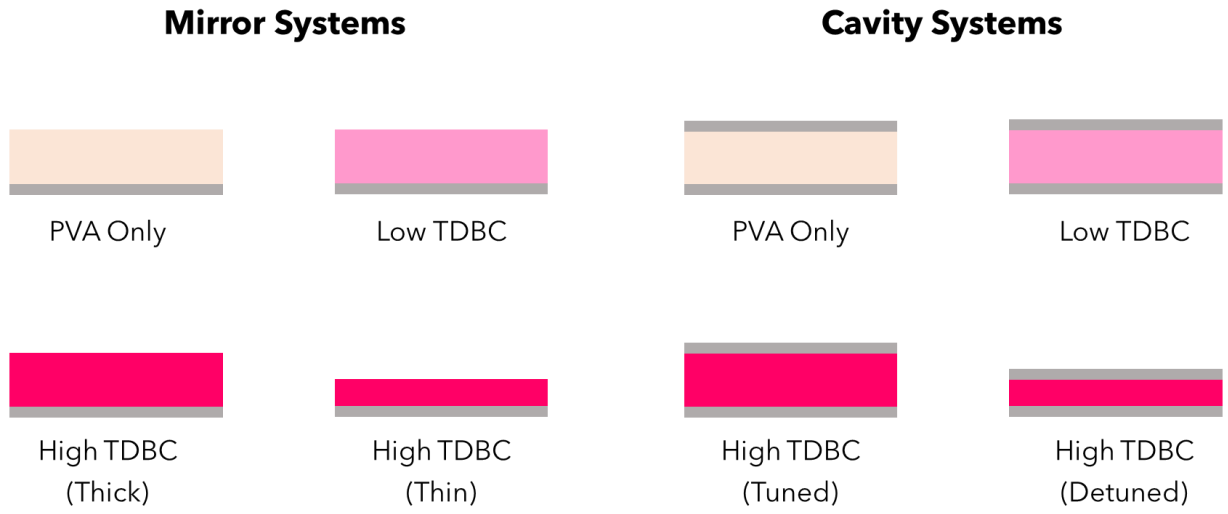

Figure 9.1 Schematic of cavity and control systems used in these studies. Left) TDBC-PVA (or only PVA) films deposited onto a 200 nm Ag mirror supported on p+-Si to form mirror systems. **Right)** standard TDBC-PVA (or PVA only) optical cavities as described in the main text.

9.3.2 Optical Characterization of Cavity and Control Systems

We characterized the optical characteristics of the fabricated systems by using an optical integrating sphere to measure their wavelength-dependent fractional absorption spectra. We obtained the fractional absorption (*A*) spectra by measuring the samples' fractional reflection (R) at normal incidence and utilizing the equation $A = 1 - R - T$. First, we confirmed that the low and high TDBC films' optical spectra exhibit similar absorption characteristics to rule out aggregation effects. The data in **Figure 9.2a** show that the normalized absorption spectra of low and high concentration TDBC-PVA films (deposited on glass) exhibit similar optical behavior, both showing strong absorption at 590 nm. We show the absorption spectra of the mirror systems in **Figure 9.2b**. The broad baseline absorption in the PVA-only system is due to absorption in the optically thick bottom Ag film. We observe that increasing the TDBC concentration to 1.25 wt% results in narrow absorption at 590 nm. Further increasing the TDBC concentration to 33 wt% results in a considerable broadening of the TDBC absorption spectra. This broadening is due to the multiple reflections through the TDBC/PVA caused by the bottom Ag mirror.

The optical absorption spectra for the cavity systems are shown in **Figure 9.2c**. The data show that the PVA-Ag cavity exhibits two optical modes: the first-order mode at ~400 nm and the second-order mode at ~590 nm. This data confirms that the second-order mode is tuned to the TDBC electronic transition. The low and high concentration (tuned) cavity systems also exhibit first-order modes at ~400 nm, indicating their second-order mode is tuned to the TDBC transition. In the case of low TDBC concentration, the cavity mode remains unperturbed, demonstrating that the TDBC concentration in the system is not high enough to enable strong light-matter coupling. Conversely, the high concentration tuned cavity data shows an apparent splitting of the cavity

mode with a measured absorption Rabi splitting energy of ~185 meV. We confirmed strong light-matter coupling in this system using the following criteria:

$$\hbar\Omega_R > \sqrt{\frac{\Gamma_{UP}^2}{2} + \frac{\Gamma_{LP}^2}{2}} \tag{9.1}$$

where the linewidths of the upper and lower polariton branch modes are Γ_{UP} and Γ_{LP}, respectively.[27] We estimated Γ_{UP} and Γ_{LP} the high concentration tuned cavity to be 156 meV and 116 meV from spectral separation of the baseline-corrected absorption spectra (**Figure 9.2d**). This corresponds to a $\sqrt{\frac{\Gamma_{UB}^2}{2} + \frac{\Gamma_{LB}^2}{2}}$ value of 137 meV, which confirms this cavity exhibits strong light-matter coupling according to equation 9.1. Finally, we observe that the high concentration detuned cavity exhibits a blue-shifted second-order mode at ~520 nm. This cavity mode remains intact and thus, the detuned sample is also in the weak coupling regime.

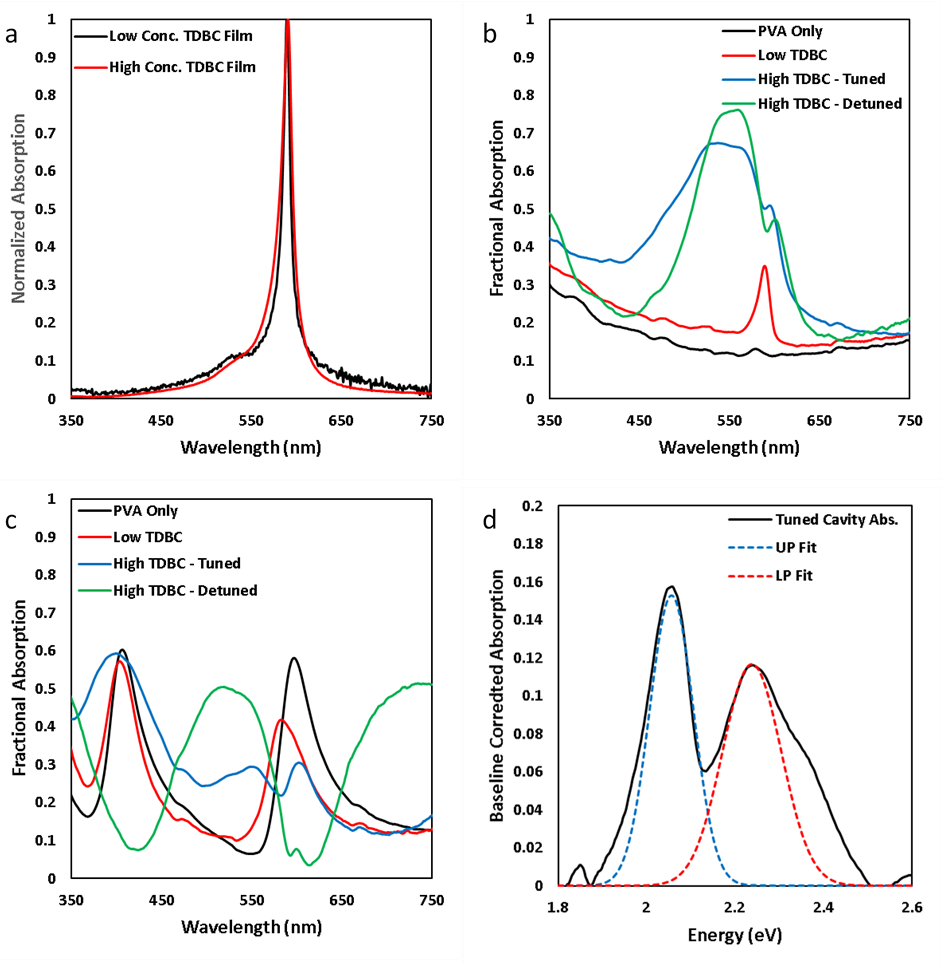

Figure 9.2 Optical characterization of cavity and control systems. a) Normalized absorption spectra of low and high concentration TDBC-PVA films deposited onto glass slides. **b-c**) Experimentally measured fractional absorption spectra for the mirror (b) and cavity (c) systems. **d**) The baseline-corrected absorption of the high concentration, tuned cavity system, and its spectral separation.

9.3.3 Photovoltage Measurements of Cavity and Control Systems

Our first objective was to determine whether these systems built up photovoltage under illumination. We accomplished this by performing open-circuit chronopotentiometry experiments in the dark and under broadband illumination. **Figure 9.3a** shows a schematic of the experimental set-up. Using a potentiostat, we measured the voltage across the top and bottom of the cavity (and mirror) systems. We set the current flowing through the two electrodes to zero and measured the open-circuit voltage over time. We allowed the voltage to equilibrate entirely in the dark upon

starting the experiment. After equilibration, we illuminated the systems with broadband light (Incident Power = 0.016 W) for 100 seconds and recorded the change in voltage. We turned off the light after the photovoltage stabilized under illumination. **Figure 9.3b** shows an example of the measured data for the low concentration cavity and control systems. We observe no change in voltage over the entire period in the dark. Under illumination, we see a steady buildup of negative voltage. This voltage returns to the baseline after illumination. We define the photovoltage in these systems as the difference in equilibrated voltage under illumination and the dark voltage.

The data in **Figure 9.3c** show the measured photovoltage for the various cavity and mirror systems. We observe that the cavity systems generate more photovoltage than the mirror systems, except for the high concentration tuned cavity (i.e., the strongly coupled cavity). To explain this observation, we need to consider the possible origins of the photovoltage in these systems are. One possible origin is via the buildup of a thermal voltage via photothermal heating of the cavity systems. Absorption in the cavity/mirror systems could lead to resistive heating and establish a temperature gradient across the system. In this case, these temperature gradients would be higher (i.e., the photovoltage is larger) in systems with more Ag since metals exhibit high parasitic absorption losses. A second possible origin for the photovoltage could be the generation of photogenerated charge in the system, similar to photovoltages in semiconductor systems. In this case, the photoelectronic voltage comes from the steady-state generation of charge carriers in the TDBC layer that cannot flow through the system. The rate of charge carrier generation dictates the magnitude of this photovoltage and is therefore limited by charge carrier recombination in the TDBC layer.

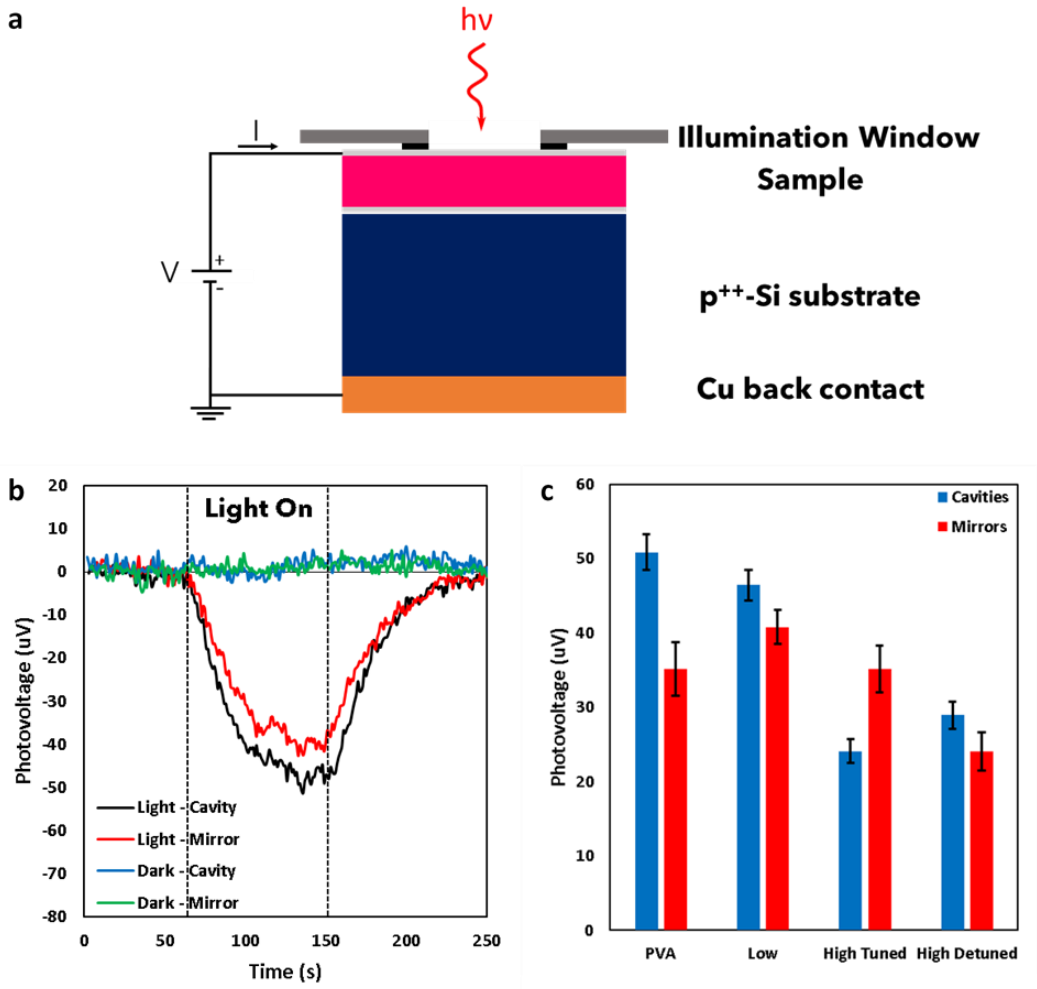

Figure 9.3 Measuring photovoltage in the cavity and control systems. a) Schematic of the 2-electrode configuration used to perform the (photo)electrical measurements. **b)** An example of the raw photovoltage data for the low TDBC concentration mirror and cavity systems in the dark and under illumination. **c)** the photovoltage measured under illumination for the cavity and control systems. Error bars represent the standard deviation of 3 different measurements.

With this in mind, we began investigating the different origins of the photovoltage by calculating the fractional absorption in the cavity and mirror systems. We hypothesized that the photovoltage should trend with the total light absorption. We base this on the fact that photothermal and photoelectronic voltages are proportional to light absorption. We calculated the total fractional absorption by integrating the fractional absorption curves in **Figure 9.2b-c** with respect to energy across the wavelength range of 350nm to 750 nm and dividing it by the total energy input across

the same wavelength range. The data in **Figure 9.4a** show that the high TDBC concentration systems exhibit the highest fractional absorption, directly contrasting with the photovoltage data in **Figure 9.3c.** We note that high absorption in these systems likely originated from high light absorption in the TDBC film. Based on this, we hypothesized that a majority of the photovoltage originates from photothermal heating of the top and bottom Ag mirrors.

We needed to approximate the fraction of total light absorption resulting solely from Ag to test this hypothesis. Determining the Ag absorption requires direct measurement of the top Ag absorption, which is impossible to do experimentally. We circumvented this problem by building a finite element model (See **Section 9.6**) to simulate the optical properties of the cavity and mirror systems. Our goal was to use the model to approximate absorption in the top Ag layer. We would then use the model to help us figure out how to determine the top Ag absorption experimentally. The data in **Figure S 16** show that the model can accurately reproduce the experimental absorption data. We used the model to calculate the absorption spectra of the cavity systems with and without top/bottom Ag mirrors and used linear combinations of the resulting absorption spectra to approximate the top Ag absorption. **Section 9.6.2** shows that the linear combinations of absorption spectra for the systems shown in **Figure S 17** can accurately approximate the model calculated top Ag absorption (**Figure S 18**). We then fabricated the systems shown in **Figure S 17** and used the linear combination to approximate the top Ag. The data in **Figure 9.4b** show that the experimentally approximated top Ag absorption matches the model calculated top Ag absorption shown in **Figure S 18**.

We used the top Ag absorption to calculate the total Ag absorption. We approximated the bottom Ag absorption in all of the systems by using the absorption spectra of the PVA-only mirror system. The data in **Figure 9.4c** show that the Ag absorption data trend perfectly with the

photovoltage data, again with the exception of the strongly coupled cavity system. We can see this more clearly by calculating the "enhancement" in the Ag absorption and the photovoltage. We calculated this by dividing the absorption (or photovoltage) in the cavity systems by the absorption (or photovoltage) in the mirror systems. The data in **Figure 9.4d** show that the cavity/mirror enhancement for the photovoltage and top Ag absorption trend together well except for the strongly coupled cavity.

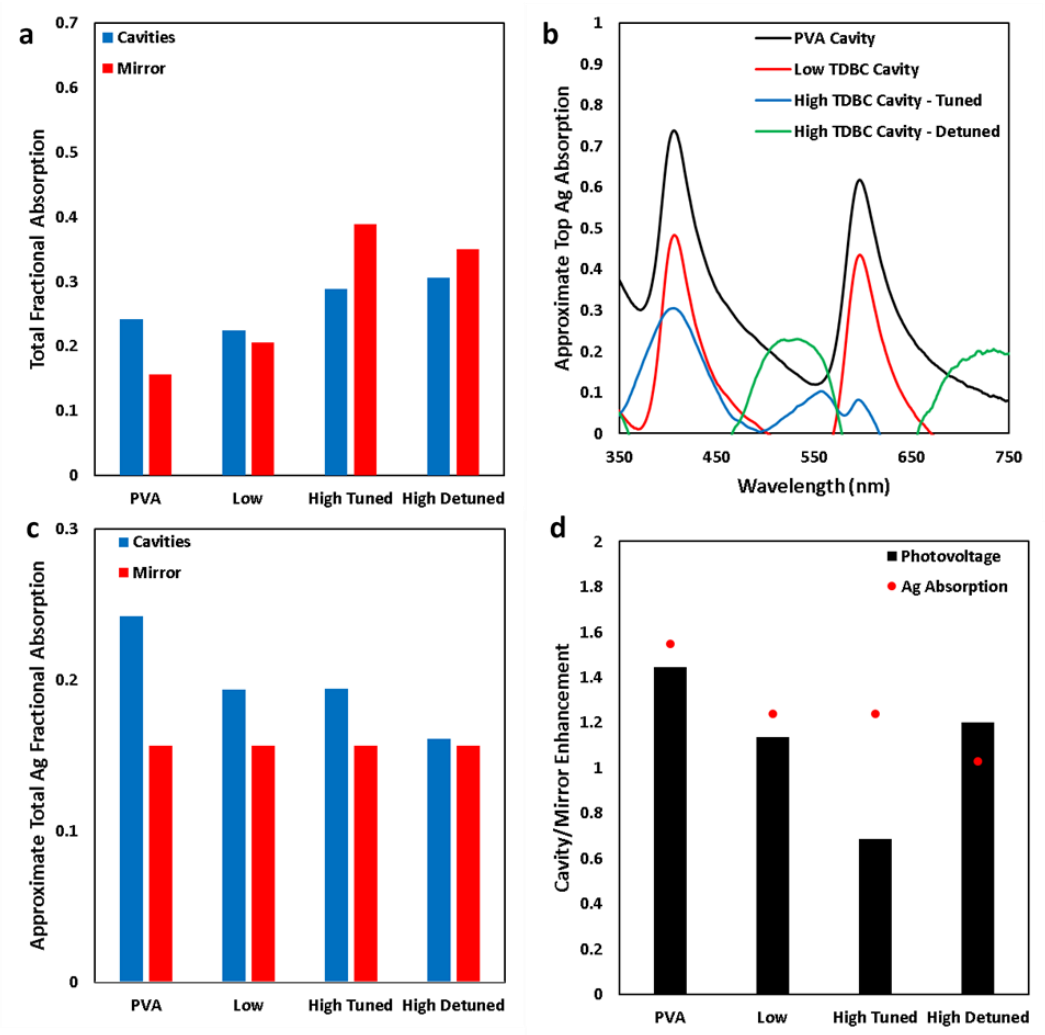

Figure 9.4Absorption analysis of cavity and control systems. a) the experimentally determined total fractional absorption of the various systems from 350 nm to 750 nm. **b-c)** the experimentally approximated top Ag absorption (b) and total Ag absorption (c) in the cavity and mirror systems.

It is clear from the data in **Figure 9.4c** that a majority of the measured photovoltage in these systems likely results from thermal gradients due to Ag absorption. It is also clear that the strongly coupled system does not follow this trend. We hypothesized that charge carrier recombination in TDBC limits photovoltage generation in the strongly coupled system. We based this hypothesis on the fact that charge carrier mobility/transport can significantly increase in the strong light-matter coupling regime.[18–20,29] In this case, increased charge transport/mobility would lead to higher recombination rates and limit photovoltage. We tested this hypothesis by measuring the current-voltage characteristics of the cavity and mirror systems in the dark. The data in **Figure 9.5a-b** show that the difference in the measured current as a function of voltage increases significantly only in the case of the strongly coupled cavity. This data suggests that the conductivity between the two mirrors is higher for the strongly coupled cavity.

Additionally, impedance spectroscopy data for the cavity and mirror systems (**Figure 9.5c-d)** show that the resistance is the least for the strongly coupled cavity system. We note that the magnitude of current measured in these systems is several orders of magnitude higher than what is reported in other studies. [18–20,29] We attribute this to measuring current between the top of the cavity and the bottom of the p^+-Si substrate. Data in **Figure S 19** show current-voltage data measured between the top and bottom Ag mirrors for methylene blue dye molecules coupled to optical cavities. We again observe a large increase in the measured current for the tuned, strongly coupled system. This data suggests that this phenomenon applies to any system in the strong coupling regime.

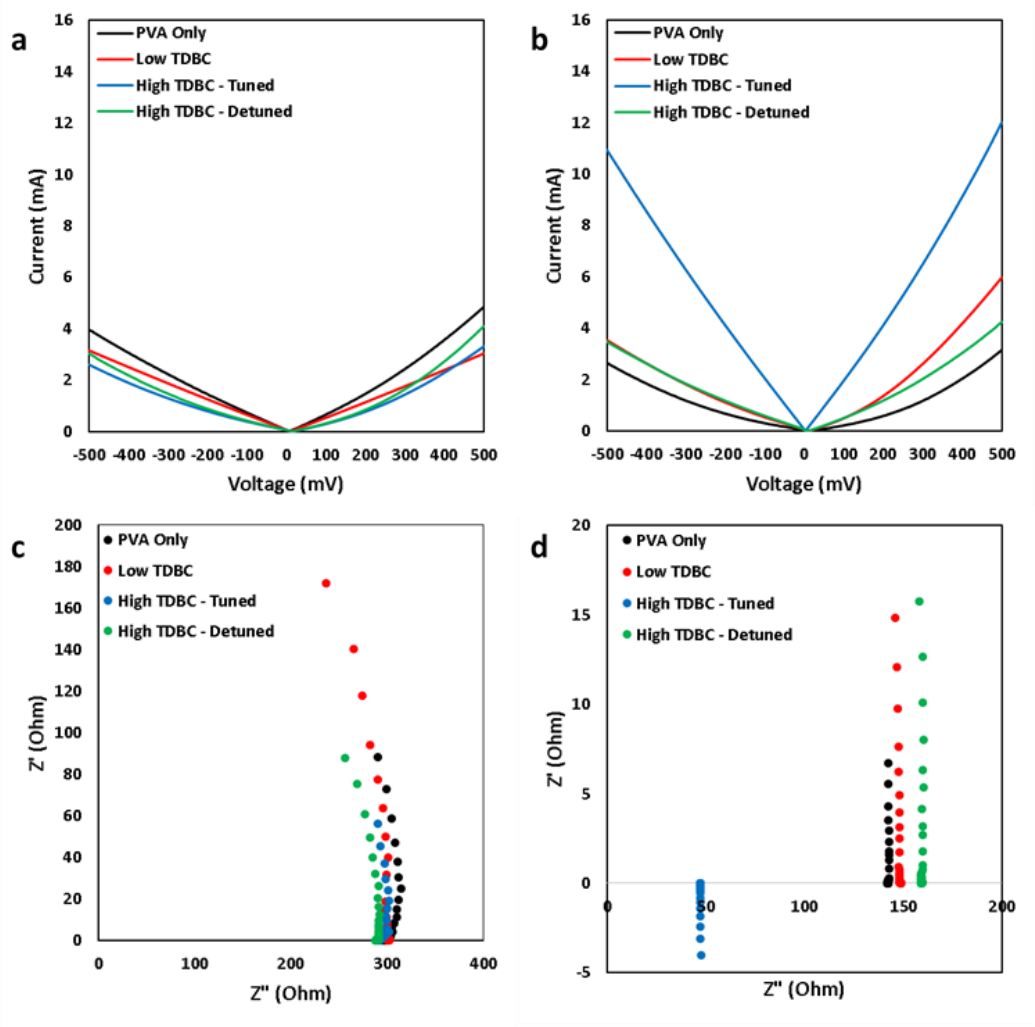

Figure 9.5 Electrical measurements of cavity and control systems. a-b) experimentally measured current-voltage characteristics of the mirror (a) and cavity (b) systems. **c-d)** experimentally measured electrochemical impedance spectra of the mirror (c) and cavity (d) systems.

The data in **Figure 9.5** suggest that the conductivity of the TDBC layer increases in the strong light-matter coupling regime. Our final objective was to determine whether this increase in conductivity allows us to extract photogenerated charge from the strongly coupled molecules. We accordingly used chronoamperometry experiments to measure the photocurrent generated by the cavity systems over time at various applied voltages. We biased the cavities as shown in **Figure 9.3a.** We let the current equilibrate in the dark for each experiment and then illuminated the sample with broadband light for 30 seconds. The data in **Figure 9.6a-b** show the change in current (i.e.,

the photocurrent) for the detuned and tuned high TDBC concentration cavities. We observe that we can measure a photocurrent for both the detuned and tuned cavity systems under these conditions. The photocurrent increases as a function of voltage for both systems, and the strongly coupled systems generate less photocurrent at a given voltage.

Interestingly, we see that the strongly coupled systems generate photocurrent immediately upon illumination. The photocurrent stops increasing immediately when we remove the illumination. This observation contrasts with what we observe in the detuned system, where the generation of the photocurrent occurs only after a 5-10 second delay. Additionally, the photocurrent continues to increase after we stop the illumination. We note that immediate responses to light are key signatures of a photoelectronic current, while slow responses to light are signatures of a photothermal current.[30] We demonstrate this in **Figure 9.6c-d**, where we show lineshapes of photothermal/photoelectronic current and the effect of varying their contributions to the lineshape. We see that larger photothermal contributions result in slower time response. Together, the data in **Figure 9.6** suggest that photoelectronic currents could contribute significantly to the photocurrent in the strongly coupled system while not in the detuned system.

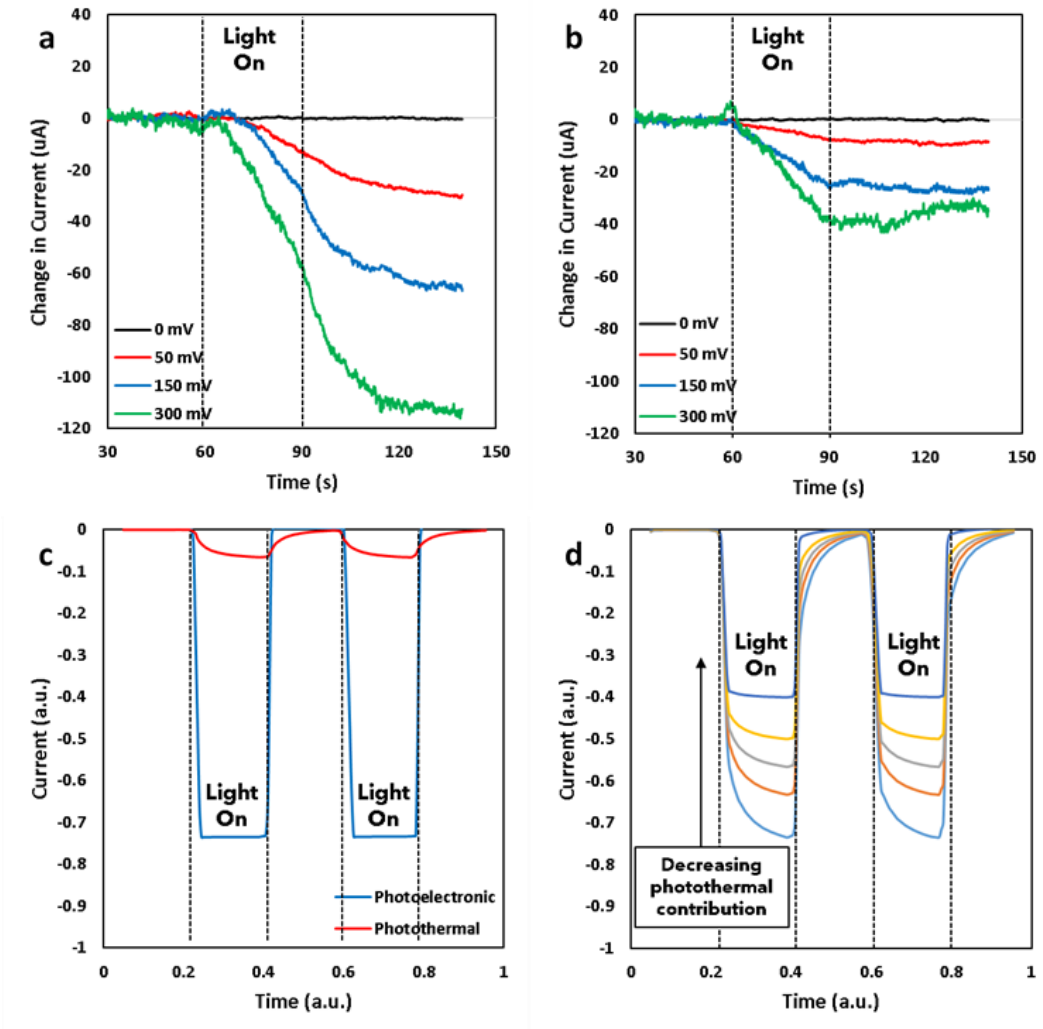

Figure 9.6 Photocurrent analysis of cavity and control systems. a-b) experimentally measured photocurrent for the high concentration detuned (a) and tuned (b) cavity systems over time at varying applied voltages. **c)** data illustrating the photocurrent lineshape as a function of time for electronic and thermal contributions. **d)** photocurrent lineshape over time for varying photoelectronic/photothermal contributions.

9.4 Conclusion

In conclusion, the data we present in this chapter suggests that we can possibly extract photogenerated charge from strongly coupled molecular absorbers. This extraction is due to increased charge carrier mobility in the strong light-matter coupling regime. However, we need to perform more experiments in order to determine whether this is possible. Specifically, we need to perform photocurrent measurements under forward/reverse biases and at different voltages to

ensure charge carriers are contributing to the photocurrent. We expect the photoelectronic current to be more sensitive to the applied voltage than the photothermal current. Overall, this chapter presents a first step into investigating charge extraction from strongly coupled molecular absorbers.

9.5 Acknowledgements

This research was supported by the U.S. Department of Energy, Office of Science, Office of Basic Energy Sciences, under Award (DE-SC0021362) (experimental work) and National Science Foundation (NSF) (CBET-1803991) (modeling work). Secondary support for the development of analytical tools used in the model was provided by NSF (CBET-1702471 and CHE-1800197).

9.6 Supporting Information

9.6.1 Measuring the Thickness and Dielectric Properties of TDBC-PVA Films

We extracted the dielectric properties for the TDBC-PVA films used in the FEM model from the experimentally fabricated samples using variable angle spectroscopic ellipsometry. First, we spin-cast TDBC-PVA solutions of low and high TDBC concentration onto optically thick (200 nm) Ag films supported on glass substrates. We then extract the films' refractive index (n) and extinction coefficient using a Woollam M-2000 ellipsometer. The refractive index (n) and the extinction coefficient (k) for TDBC-PVA films of the low and high concentration TDBC film are shown in **Figure S 15**.

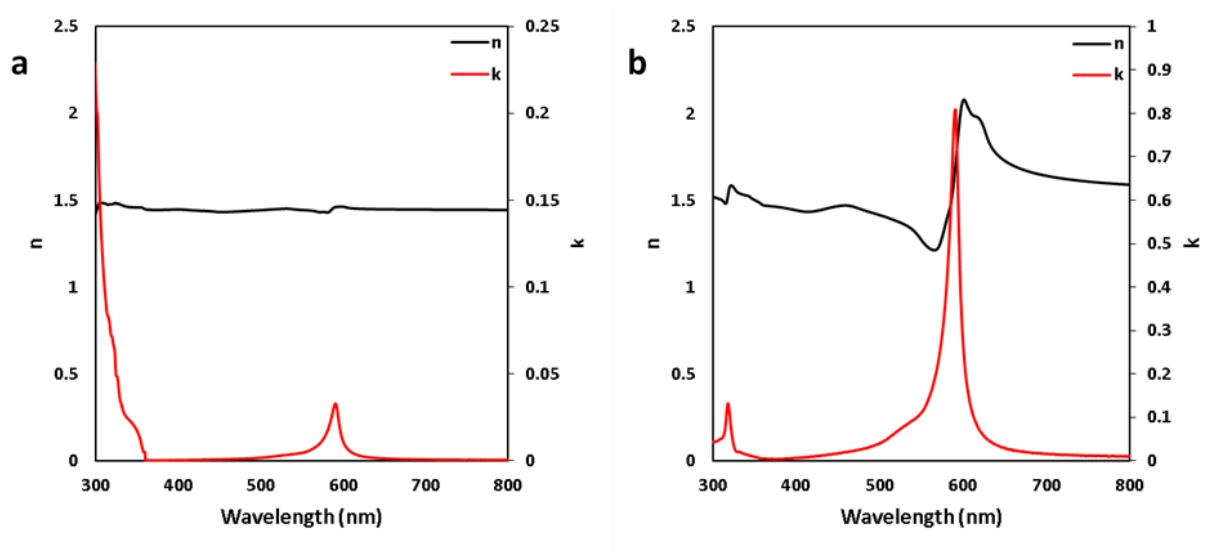

Figure S 15 Experimentally measured dielectric data for the TDBC-PVA films. Ellipsometry extracted refractive index (n) and extinction coefficient (k) of TDBC-PVA films prepared from TDBC-PVA solutions with low **(a)** and high **(b)** concentrations of TDBC.

9.6.2 Simulating absorption characteristics of the cavity and control systems

We simulated the absorption characteristics of the experimentally fabricated systems using COMSOL Multiphysics finite-element based software. We used the '*Wave optics*' module to calculate the transmission and reflection fractions of light impinging on a three-dimensional cavity system. The model is set up for one-unit cell where Floquet boundary conditions describe the system's periodicity. We set a top port (Port 1) to send the light wave at a specified incident power, and a bottom port (Port 2) to absorb the transmitted light. The transmission and reflection are calculated at Port 2 and Port 1, respectively, to obtain the transmission and reflection fractions. The dimensions of the top and bottom Ag mirrors were 30 nm and 200 nm, and the thickness of the TDBC-PVA layer was varied to match the thicknesses of the films created experimentally. We obtained the optical properties for Ag from the COMSOL database (Rakic) and the data for the TDBC-PVA layers was obtained via ellipsometry (as described in the next section). We performed the simulations for the mirror systems by removing the respective top/bottom Ag films.

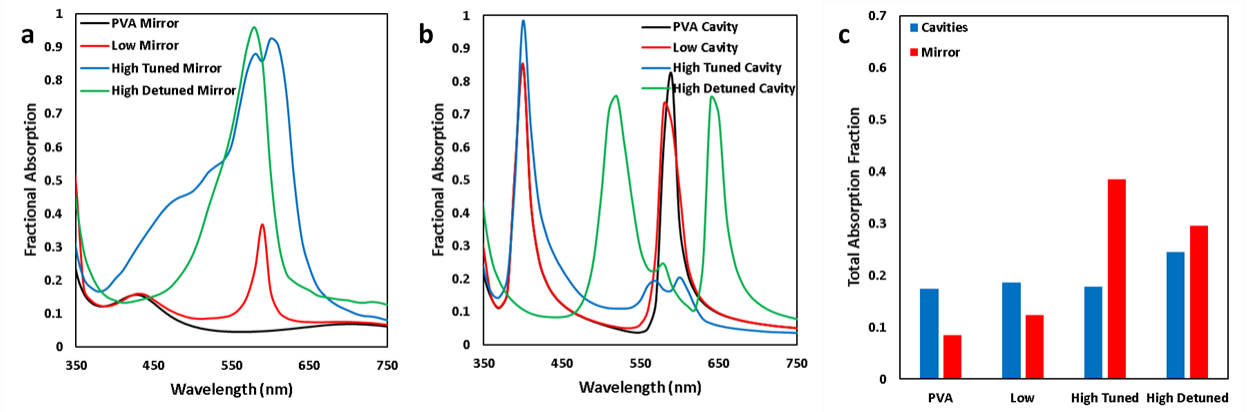

Figure S 16 Simulated absorption characteristics of cavity and control systems. a-b) Calculated fractional absorption spectra for the TDBC-PVA mirros (a), and cavity (b) systems. **c)** Simulated total fractional absorption of the various systems from 350 nm to 750 nm.

9.6.3 Approximating Top Ag Absorption

We approximated the top Ag absorption in the cavity systems by first fabricating the various systems shown in **Figure S 17**. We measured the fractional absorption spectra of the fabricated systems and performed the linear combination shown below to approximate the top Ag absorption. We checked the accuracy of this method by performing the same linear combinations with the calculated fractional absorption spectra using the model. The data in **Figure S 18** show that the approximation matches the direct calculation relatively well.

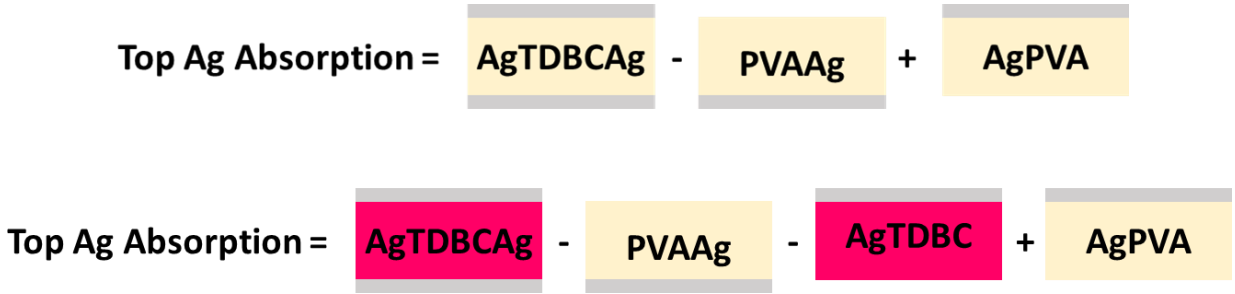

Figure S 17 Schematic of how to experimentally approximate top Ag absorption in optical cavities. We used the operations shown in the schematic to approximate the top Ag absorption in the PVA (top) and TDBC-PVA (bottom) cavities. Each sum corresponds to the sum of the fractional absorption spectra of each system shown schematically. These systems were fabricated accordingly and their spectra was used to approximate the top Ag absorption.

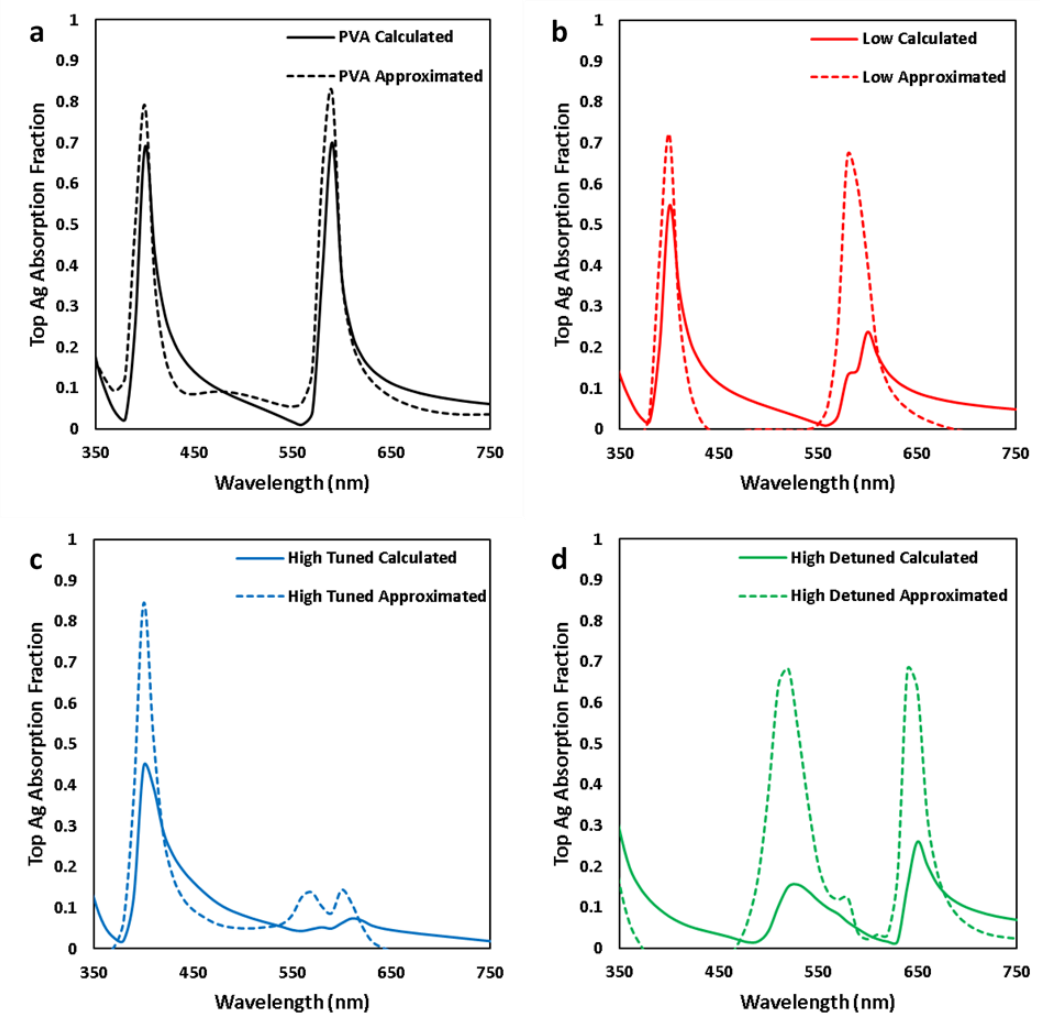

Figure S 18 Simulated top Ag absorption in optical cavities. The approximated (dashed) and calculated (solid) top Ag absorption in the various systems. We obtained the approximated Ag absorption by performing the calculations shown in **Figure S 17** using simulated data. We obtained the calculated data by directly calculating it in the model.

9.6.4 Improved Conductivity in other Strongly Coupled Systems

We used optical cavities coupled to methylene blue (MB) dye molecules to prove the generalizability of the current-voltage measurements. We prepared the spin coating solutions for these samples by dissolving 20 mg mL^{-1} of MB into 1.5 wt% aqueous solutions of polyvinyl alcohol (PVA, 88000 g mol^{-1}). The average thickness of the tuned sample in **Figure S 19b** is ~335 nm. We prepared the detuned cavities by incorporating thinner MB-PVA layers. We measured the current between the top and bottom Ag mirrors in these measurements since the cavities were

supported on glass. The measured current for each of the MB-PVA cavities is shown in **Figure S 19c.**

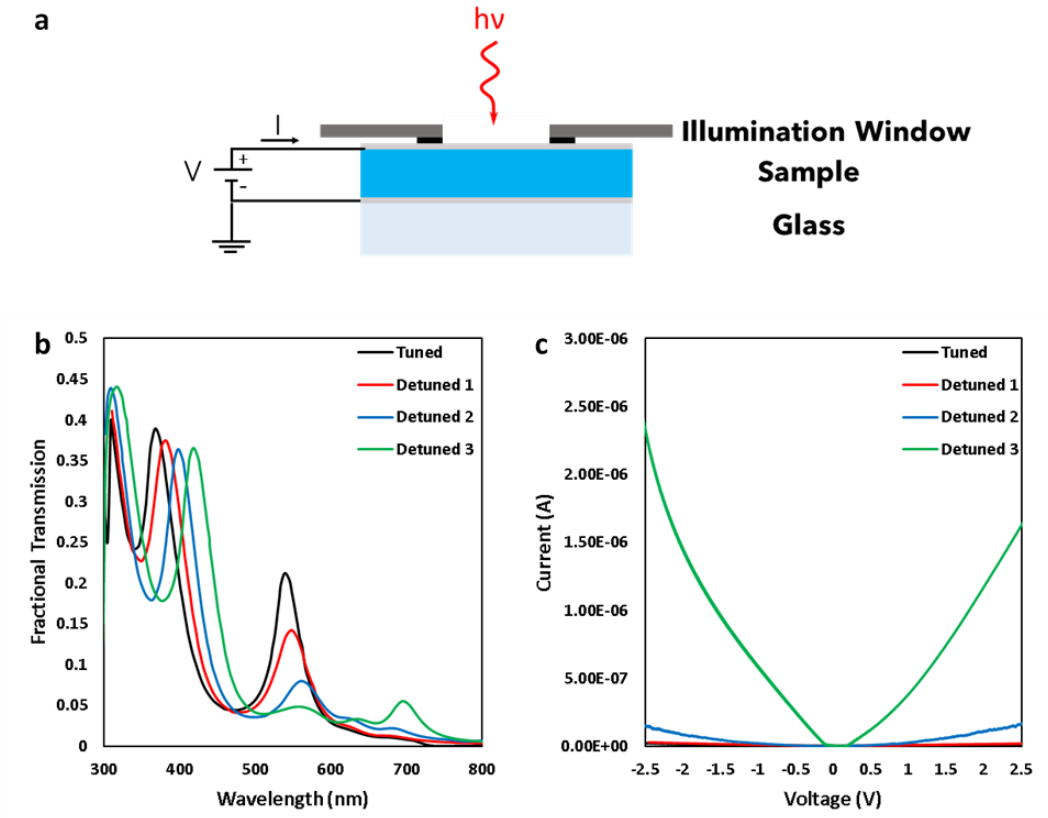

Figure S 19 Electrical characterization of methylene blue molecules strongly coupled to optical cavities. a) Schematic of the 2-electrode configuration used to perform the electrical measurements of the methylene blue-Ag optical cavities. **b)** measured fractional transmission spectra of a strongly coupled methylene blue cavity (black) as well as methylene blue cavities with increased detuning. **c)** the measured current-voltage characteristics of the systems shown in (b).

9.7 References

(1) Skolnick, M. S.; Fisher, T. A.; Whittaker, D. M. *Semiconductor Science and Technology*. IOP Publishing July 1, 1998, pp 645–669.

(2) Kasprzak, J.; Richard, M.; Kundermann, S.; Baas, A.; Jeambrun, P.; Keeling, J. M. J.; Marchetti, F. M.; Szymańska, M. H.; André, R.; Staehli, J. L.; Savona, V.; Littlewood, P. B.; Deveaud, B.; Dang, L. S. *Nature* **2006**, *443* (7110), 409–414.

(3) Raimond, J. M.; Brune, M.; Haroche, S. *Rev. Mod. Phys.* **2001**, *73* (3), 565–582.

(4) Törmä, P.; Barnes, W. L. *Rep. Prog. Phys.* **2015**, *78* (1), 013901.

(5) Vasa, P.; Lienau, C. *ACS Photonics* **2018**, *5* (1), 2–23.

(6) Ebbesen, T. W. *Acc. Chem. Res.* **2016**, *49* (11), 2403–2412.

(7) Hertzog, M.; Wang, M.; Rgen Mony, J.; Bö, K. *Chem. Soc. Rev.* **2019**, *48*, 937–961.

(8) Dovzhenko, D. S.; Ryabchuk, S. V; Rakovich, Y. P.; Nabiev, I. R. *Nanoscale* **2018**, *10*.

(9) Sanvitto, D.; Kéna-Cohen, S. *Nature Materials*. Nature Publishing Group October 1, 2016, pp 1061–1073.

(10) Hutchison, J. A.; Liscio, A.; Schwartz, T.; Canaguier-Durand, A.; Genet, C.; Palermo, V.; Samorì, P.; Ebbesen, T. W. *Adv. Mater.* **2013**, *25* (17), 2481–2485.

(11) Coles, D. M.; Somaschi, N.; Michetti, P.; Clark, C.; Lagoudakis, P. G.; Savvidis, P. G.; Lidzey, D. G. *Nat. Mater.* **2014**, *13*, 712–719.

(12) Zhong, X.; Chervy, T.; Zhang, L.; Thomas, A.; George, J.; Genet, C.; Hutchison, J. A.; Ebbesen, T. W. *Angew. Chemie - Int. Ed.* **2017**, *56* (31), 9034–9038.

(13) Zhong, X.; Chervy, T.; Wang, S.; George, J.; Thomas, A.; Hutchison, J. A.; Devaux, E.; Genet, C.; Ebbesen, T. W. *Angew. Chemie* **2016**, *128* (21), 6310–6314.

(14) Rozenman, G. G.; Akulov, K.; Golombek, A.; Schwartz, T. *ACS Photonics* **2018**, *5* (1), 105–110.

(15) Georgiou, K.; Michetti, P.; Gai, L.; Cavazzini, M.; Shen, Z.; Lidzey, D. G. *ACS Photonics* **2018**, *5* (1), 258–266.

(16) Zeng, P.; Cadusch, J.; Chakraborty, D.; Smith, T. A.; Roberts, A.; Sader, J. E.; Davis, T. J.; Gómez, D. E. *Nano Lett.* **2016**, *16* (4), 2651–2656.

(17) Shan, H.; Yu, Y.; Wang, X.; Luo, Y.; Zu, S.; Du, B.; Han, T.; Li, B.; Li, Y.; Wu, J.; Lin, F.; Shi, K.; Tay, B. K.; Liu, Z.; Zhu, X.; Fang, Z. *Light Sci. Appl.* **2019**, *8* (1), 9.

(18) Orgiu, E.; George, J.; Hutchison, J. A.; Devaux, E.; Dayen, J. F.; Doudin, B.; Stellacci, F.; Genet, C.; Schachenmayer, J.; Genes, C.; Pupillo, G.; Samorì, P.; Ebbesen, T. W. *Nat. Mater.* **2015**, *14*, 1123–1130.

(19) Nagarajan, K.; George, J.; Thomas, A.; Devaux, E.; Chervy, T.; Azzini, S.; Aziz, J.; Hosseini, M. W.; Kumar, A.; Genet, C.; Bartolo, N.; Ciuti, C.; Ebbesen, T. *ACS Nano* **2020**, *14* (8), 10219–10225.

(20) Hagenmüller, D.; Schachenmayer, J.; Schütz, S.; Genes, C.; Pupillo, G. *Phys. Rev. Lett.* **2017**, *119* (22), 223601.

(21) Canaguier-Durand, A.; Devaux, E.; George, J.; Pang, Y.; Hutchison, J. A.; Schwartz, T.; Genet, C.; Wilhelms, N.; Lehn, J.-M.; Ebbesen, T. W. *Angew. Chemie Int. Ed.* **2013**, *52* (40), 10533–10536.

(22) Schwartz, T.; Hutchison, J. A.; Genet, C.; Ebbesen, T. W. *Phys. Rev. Lett.* **2011**, *106*, 196405.

(23) Hutchison, J. A.; Schwartz, T.; Genet, C.; Devaux, E.; Ebbesen, T. W. *Angew. Chemie Int. Ed.* **2012**, *51* (7), 1592–1596.

(24) Munkhbat, B.; Wersäll, M.; Baranov, D. G.; Antosiewicz, T. J.; Shegai, T. *Sci. Adv.* **2018**, *4*, eaas9552.

(25) Thomas, A.; Lethuillier-Karl, L.; Nagarajan, K.; Vergauwe, R. M. A.; George, J.; Chervy, T.; Shalabney, A.; Devaux, E.; Genet, C.; Moran, J.; Ebbesen, T. W. *Science (80-.).* **2019**, *363* (6427), 615–619.

(26) Hirai, K.; Hutchison, J. A.; Uji-i, H. *Chempluschem* **2020**, *85* (9), 1981–1988.

(27) Shi, X.; Ueno, K.; Oshikiri, T.; Sun, Q.; Sasaki, K.; Misawa, H. *Nat. Nanotechnol.* **2018**, 1.

(28) Gómez, D. E.; Shi, X.; Oshikiri, T.; Roberts, A.; Misawa, H. *Nano Lett.* **2021**, *21* (9), 3864–3870.

(29) Feist, J.; Garcia-Vidal, F. J. *Phys. Rev. Lett.* **2015**, *114* (19), 196402.

(30) Zhan, C.; Liu, B.-W.; Huang, Y.-F.; Hu, S.; Ren, B.; Moskovits, M.; Tian, Z.-Q. .

Chapter 10 Conclusions, Impact, and Future Directions

10.1 Summary

We began this dissertation work with the initial goal of designing multicomponent plasmonic materials that could enable and enhance various solar energy conversion technologies. We hypothesized that we could use plasmonic nanostructures to localize light energy into non-plasmonic materials by interfacing them together. While this concept seemed straightforward, we quickly realized that engineering such materials demands a fundamental understanding of how these two components interact physically, optically, and chemically. Specifically, it requires a deep understanding of how energy flows across plasmonic/non-plasmonic interfaces. Our first studies focused on energy transfer between plasmonic metals and catalytic metals for applications in plasmonic catalysis. We discovered that coating plasmonic nanoparticles with thin layers of catalytically active material results in the localization of light energy into the catalytic component. We developed a physical framework to understand this energy transfer process and demonstrated that this framework describes energy transfer in any multicomponent plasmonic system. We termed this burgeoning field "hybrid plasmonics."

These initial results provided general design rules for engineering hybrid plasmonic systems that could localize light absorption into specific locations in space (i.e., the non-plasmonic component). Our next goal was to maximize this energy localization process by manipulating light-matter interactions. This pursuit led us to the field of strong light-matter coupling, where extremely high rates of energy exchange characterize interactions between light and absorbing materials. We showed that typical configurations used in the light-matter coupling literature are

insufficient for solar energy conversion technologies. Changing the configuration showed that strong light-matter coupling increases the energy localization compared to weakly coupled systems, and charge carriers generated in this regime (termed "polaritons") display favorable charge transport properties. Overall, this work opens the door for several exciting new directions in multicomponent materials design, interface engineering, and polariton-based solar energy conversion technologies.

10.2 Overview of Major Contributions

10.2.1 Engineering Energy Flow in Hybrid Plasmonic Systems

When starting this dissertation work, our initial objective was to expand the applications of plasmonic catalysis beyond the surface chemistry of noble metals.[1–3] The approach typically adopted in the literature to solve this problem was to interface plasmonic metals with catalytically active metal clusters.[4–7] The idea is that the plasmonic component first harvests light energy and then transfers the energy to the catalytic component to drive photochemistry. While this is an attractive approach, these studies mainly employed plasmonic nanomaterials (either free standing[4,5] or coated with thin metal oxides[6,7]) that were randomly decorated with small clusters of a catalytic metal. These specific systems are inherently limited because both components are exposed to the reactant molecules and can therefore potentially act as active sites for surface chemistry. Not only does this prevent one from showing that photochemistry is being driven exclusively on the catalytic metal, but it makes identifying the exact mechanism by which the plasmonic metal transfers the light energy to the catalytic metal impossible. Nevertheless, these systems were routinely utilized in the literature, and the mechanism of energy transfer from the plasmonic component to the catalytic component was considered to be well established as the indirect transfer mechanism (**Figure 10.1a,c**).[4,5,8,9]

Accepting the indirect mechanism as the primary energy transfer mechanism in bimetallic hybrid plasmonic systems implies that charge carriers generated in the plasmonic component migrate to the catalytic component at high rates. The issue with this argument is that non-thermal charge carriers generated in metals have extremely short lifetimes.[2,10,11] These carriers initially lose energy via electron-electron scattering on ~500 fs and subsequently equilibrate with phonon modes on the order of ~1-100 ps (**Figure 10.2a**). Thus, there should be a low probability of charge transfer to the catalytic component unless charge transport and transfer occur on timescales faster than these relaxation processes.

We note that direct photodiode measurements report that charge carriers can cross metal-semiconductor interfaces with relatively high quantum efficiencies.[12] Additionally, researchers have reported significant enhancements in the rates of chemical reactions, large kinetic isotope effects, and changes in product selectivity that phonon heating effects cannot fully explain.[3,13–18] These reports suggest that non-thermal charge carriers readily sample the surface even in clean plasmonic nanostructures. It is important to understand that these metal-semiconductor and metal-molecule systems often have interface energetics that favor charge extraction via the indirect mechanism, such as Schottky junctions. In the case of plasmonic metals interfaced with catalytic metals, the voltage generated at the interface via equilibration of the Fermi level's would prevent charge transfer from the plasmonic metal to the catalytic metal.[19] This is because plasmonic metals typically have smaller work functions than catalytic metals.[20] Regardless, the large charge carrier densities in metals screen any charge carrier separation effects from built-in voltages. [19] This screening effect results in no net driving force for charge carrier extraction in these bimetallic systems.

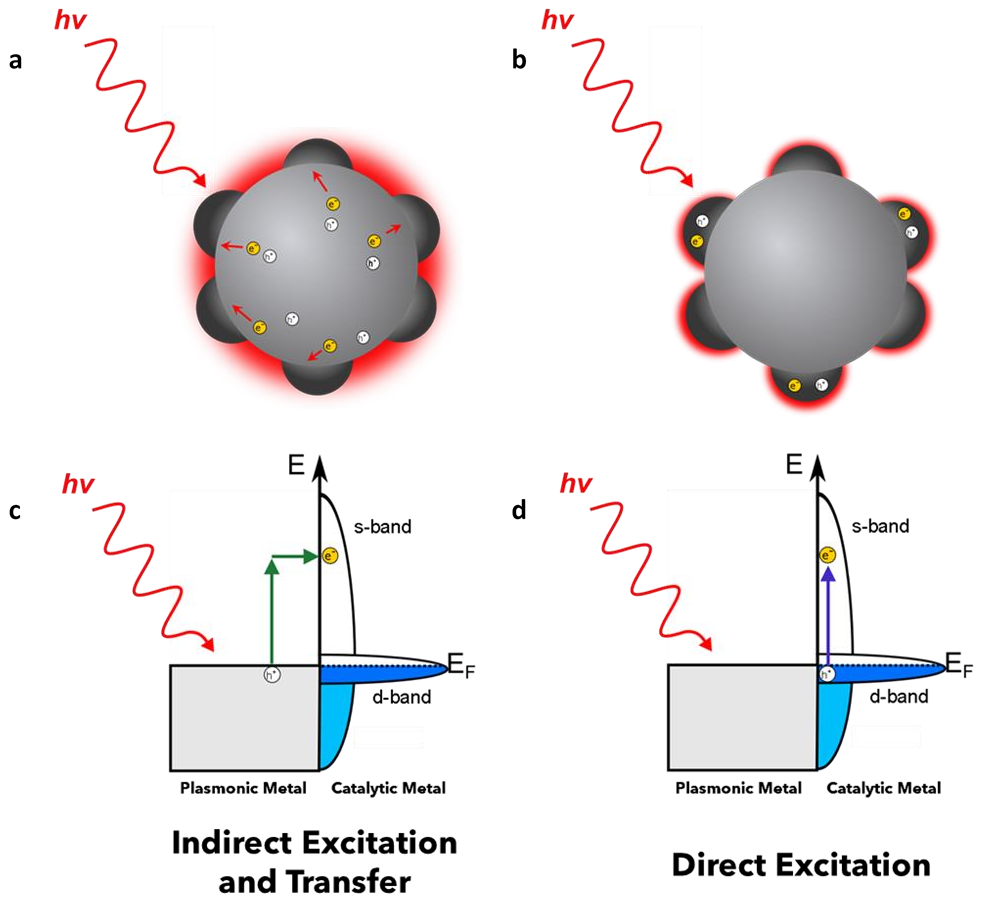

Figure 10.1 Energy transfer in bimetallic hybrid plasmonic systems. a,c) Schematic and corresponding band diagram of energy/charge transfer between a plasmonic metal and a catalytic metal before this dissertation work. The plasmon decays via the formation of energetic charge carriers in the plasmonic component that subsequently transfers to the catalytic component. **b,d)** Schematic and corresponding band diagram of energy/charge transfer between a plasmonic metal and a catalytic metal after this dissertation work. The plasmon decays via the direct excitation of momentum-conserved d-to-s transitions in the catalytic component.

Chapter 4 presents the first results suggesting a direct excitation mechanism governs energy transfer in bimetallic plasmonic systems (**Figure 10.1b,d**).[21] We studied the optical characteristics of plasmonic Ag nanocubes encapsulated by a 1 nm shell of catalytically active Pt. This nanostructure completely decouples each component's optical/catalytic contributions since no underlying Ag facets are exposed, and the Pt shell is thin enough to transmit light. The FEM model developed in this dissertation showed that Ag nanocubes dissipate LSPR energy directly through the 1 nm Pt shell. We hypothesized that this was due to direct, momentum-conserved

electronic transitions in the Pt shell. These transitions are characterized by extremely fast excitation rates on the order of 10^{15} s^{-1}, which is 1-2 orders of magnitude faster than the excitation of non-thermal charge carriers in monometallic plasmonic nanoparticles (**Figure 10.2a**).[10,22] They are prevalent in catalytic metals, which feature high-energy d-bands that allow them to occur in the visible range.[23]

We confirmed this hypothesis in **Chapter 5** by studying bimetallic plasmonic nanoparticles of varying shapes and sizes.[24] We demonstrated that energy transfer from a plasmonic metal to a catalytic metal only occurs when these direct, momentum-conserved transitions are available at energies where LSPR occurs. Physically, we describe this energy transfer process as the dissipation of LSPR-confined electromagnetic energy directly through these ultrafast d-to-s transitions (**Figure 10.1d)**. In theory, this direct energy transfer mechanism should bypass efficiency losses resulting from the initial generation in the Ag core (i.e., from the indirect mechanism). Recent transient absorption studies of energy transfer in bimetallic AuPt nanoparticles support our hypothesis.[25] This illustrates that both the timescales of plasmon excitation/decay and the spatial location of the charge carrier generation process fundamentally differ in bimetallic plasmonic systems (**Figure 10.2b)**. We present design principles for exploiting this energy transfer process to maximize light absorption in these bimetallic systems in **Chapter 6**.

The studies in **Chapter 4**, **Chapter 5**, and **Chapter 6** allow us to determine the factors governing energy transfer in bimetallic hybrid plasmonic systems. They reveal that the generation of charge carriers in the presence of a non-plasmonic metal is governed by: (1) the intensity of the electric field generated by the plasmonic nanostructure under LSPR conditions, and (2) the availability of direct, electronic excitations in the non-plasmonic material. As mentioned throughout the dissertation, the probability of direct transitions in a material is described by its wavelength-dependent

imaginary dielectric function (ε_2). **Chapter 7** investigated whether this framework could describe energy transfer in other hybrid plasmonic systems by studying the light absorption rates within core-shell metal-semiconductor and metal-molecule systems.[26] The data showed that the direct excitation mechanism dominates in these systems when direct transitions are available at LSPR energies. These results align with conventionally accepted mechanisms of plasmon-induced resonance energy transfer.[27]

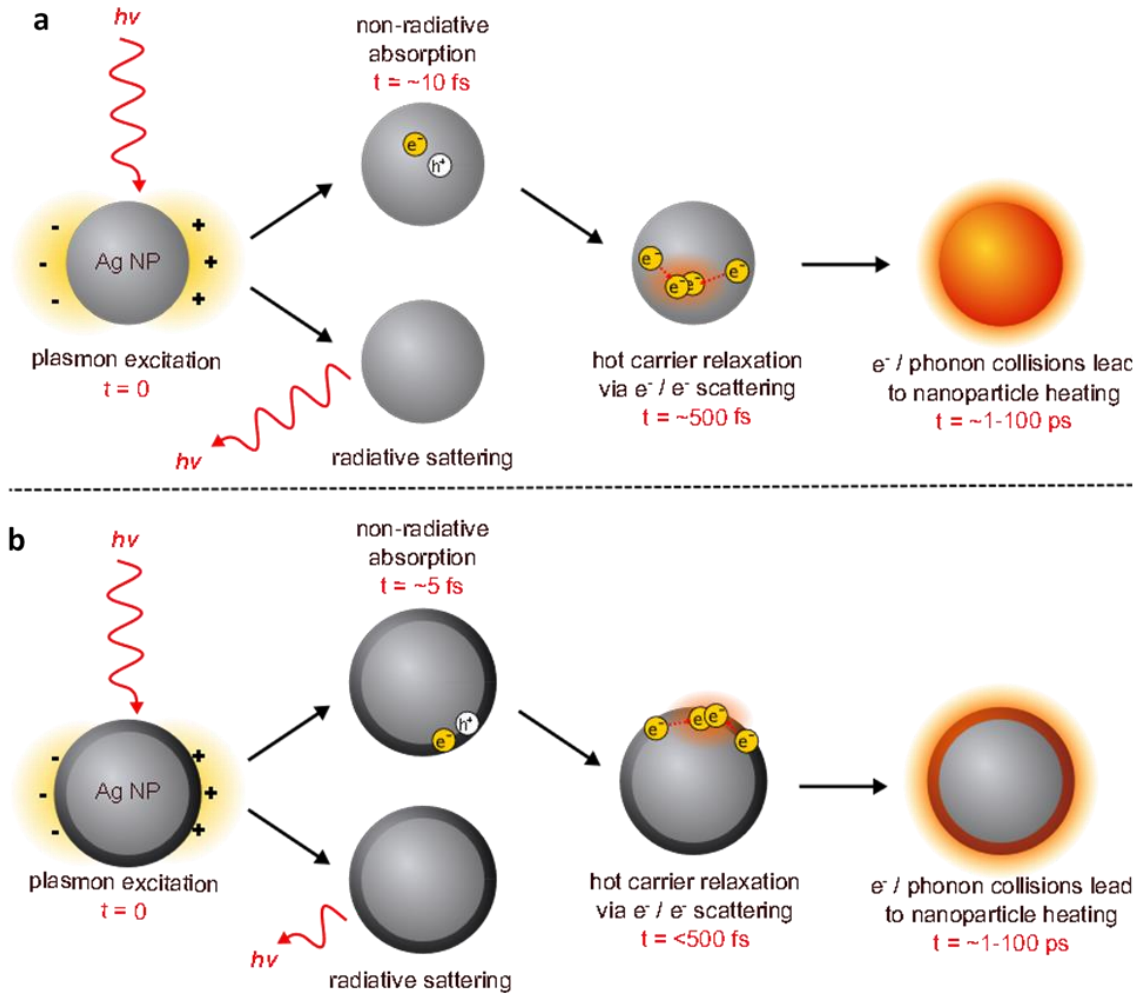

Figure 10.2 Plasmon decay in bimetallic hybrid plasmonic systems. Illustration of sequential plasmon excitation and decay processes in: (1) an illuminated monometallic Ag nanoparticle and (2) Ag nanoparticle with another material attached to the nanoparticle surface. In the hybrid materials, a large fraction of carriers are generated either directly in the non-plasmonic shell or at the interface between the nanoparticle and the attached material. Adapted from Ref. [28]

Collectively, the chapters summarized above allow us to propose a unifying physical framework that leads us towards molecular control of charge carrier generation in all multicomponent hybrid plasmonic systems.[28] First, the plasmonic component harvests the energy of visible light via LSPR in the form of high electric field intensities present at the nanoparticle surface. In the case of a clean plasmonic nanoparticle, these charge carriers are generated throughout the bulk of the nanostructure (**Figure 10.3b** – left). While some of these charge carriers can transfer to attached materials via the indirect charge transfer mechanism (e.g., in metal-semiconductor and metal-molecule systems), most charge carriers thermalize before extraction due to ultrafast recombination rates in metals. However, when the attached material is characterized by a large number of direct transitions (i.e., the material has high ε_2), the electric field energy present under LSPR conditions is preferentially dissipated through the non-plasmonic material (**Figure 10.3b** – right). This process results in the localization of charge carrier generation in the non-plasmonic material. Physically, this results in high rates of charge carrier extraction compared to the indirect mechanism. Since ε_2 can be easily measured for a wide variety of materials (**Figure 10.3**a), our proposed physical framework should enable the design of highly efficient nanomaterials relevant to various solar energy conversion technologies.

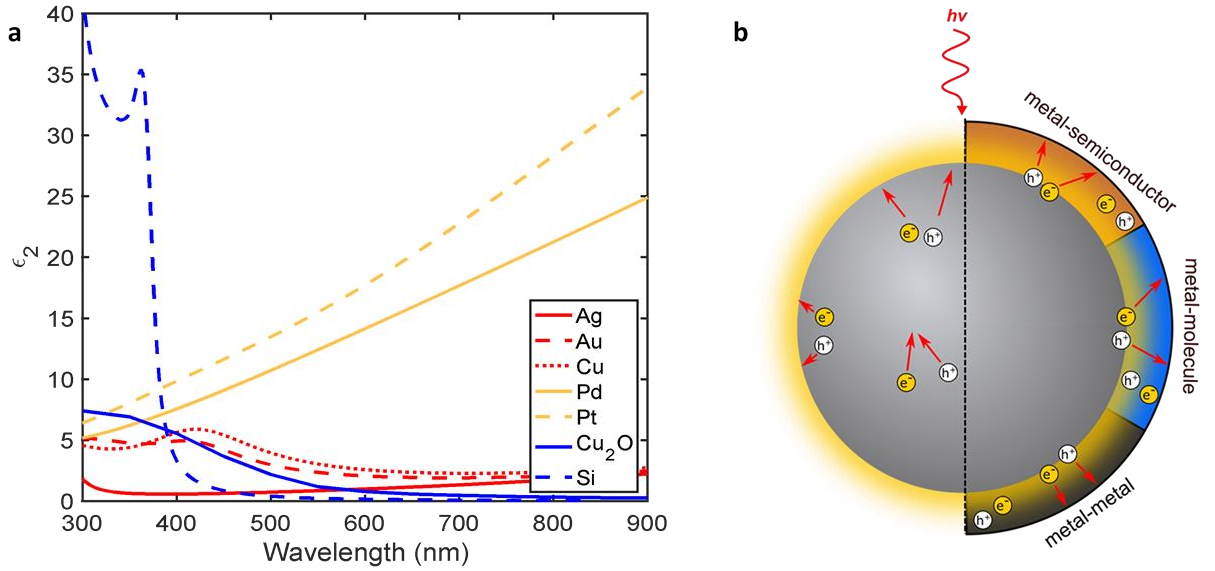

Figure 10.3 Plasmon excitation and decay in hybrid plasmonic systems. a) The imaginary part of the dielectric function for various plasmonic and non-plasmonic materials. b) Electron–hole pair generation and transport in a clean plasmonic nanostructure (left) and in one coated with either a semiconductor, molecules, or another metal (right). The charge carriers are generated throughout the entire volume of the clean plasmonic nanoparticle, while the process is confined to either the attached material or the interface between the attached material and the nanoparticle in the hybrid system. Adapted from Ref. [28]

10.2.2 Strong Light-Matter Coupling for Enhanced Charge Localization and Transport

The physical framework summarized in the above section provides design principles for localizing and amplifying the rates of charge carrier generation (i.e., light absorption) into small volumes of material. The framework implies that one way to maximize this energy localization process is to place absorbers into increasingly large electric fields. Our pursuit of maximizing light-absorption rates in absorbing materials led us to the field of strong light-matter coupling.[29–35] Strong light-matter coupling between photonic/plasmonic nanostructures and absorbing materials occurs when they exchange energy at extremely high rates. It is characterized by the formation of "polaritons," which are hybrid states that simultaneously exhibit light and matter properties. While there is significant interest in understanding the physical and chemical characteristics of these coupled light-matter states, researchers have primarily focused on the

potential of the coupled states to improve quantum information technologies or alter chemical reaction pathways.[36–41]

Chapter 8 of this dissertation explores how strong light-matter coupling affects photophysical processes related to solar energy harvesting. Specifically, we investigate how strong coupling affects the rates of charge carrier generation in molecular absorbers coupled to photonic structures. Our results utilizing Fabry-Perot optical cavities show that strongly coupled systems confine light into the coupled molecules with higher quantum efficiencies than weakly coupled systems (**Figure 10.4a,b**). While a few reports have shown that strong coupling can enhance light absorption in the strongly coupled systems[42,43], this is the first demonstration that absorption can be localized to the molecular layer. We also identify that the multiple metallic mirrors in optical cavities lead to substantial reflection and parasitic absorption losses. We showed that open systems (i.e., molecules strongly coupled to plasmonic nanohole arrays - **Figure 10.4c**) supported the highest light absorption efficiencies. In this context, **Chapter 9** suggests that photoexcited polaritons exhibit improved charge transport properties. While this has been demonstrated previously in thin films of organic semiconductors and 2D materials[44–46], it has not been demonstrated for molecular systems. Collectively, these findings provide guidelines for exploiting strong light-matter coupling to improve both traditional solar energy conversion technologies that rely on maximizing light absorption and new polariton-based solar energy conversion systems that rely on the unique properties of photoexcited polaritons to operate at unprecedented efficiencies.[47,48]

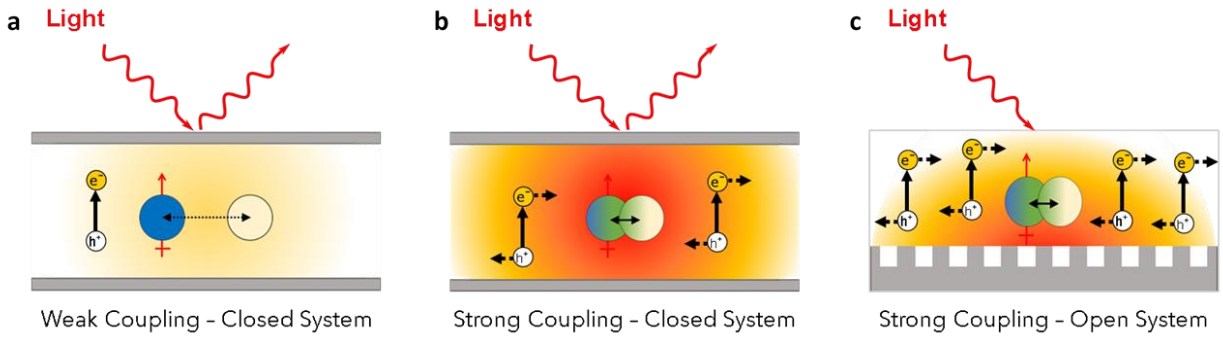

Figure 10.4 Charge carrier generation and transport in the coupled cavity and array systems. a) Light absorption is low in molecular absorbers weakly coupled to an optical cavity due to high reflection losses from the top mirror and low energy exchange rates between the cavity and the molecules. **b)** Light absorption in molecules strongly coupled to an optical cavity is high, and the carriers exhibit enhanced charge transport. However, absorption in these systems are inherently limited by losses due to the top metallic mirror. **c)** the optical system to take advantage of light absorption and charge transport requires coupling molecules to an open system such as a plasmonic nanohole array.

10.3 Future Directions

10.3.1 Moving Hybrid Plasmonics Forward

This dissertation work revealed the critical role of direct, momentum-conserved electronic transitions in controlling how LSPR energy flows throughout hybrid plasmonic materials. Simply introducing a material with a large ε_2 at the LSPR energy to the surface of a plasmonic nanoparticle funnels the harvested electromagnetic energy directly into the attached material. While these findings present a significant advance in the new field of hybrid plasmonics, steady-state experiments and time-independent models limited our studies. A proper understanding of hybrid plasmonic systems will only result from recognizing that the electric field and dielectric function are highly inhomogeneous throughout these systems.[28] This inhomogeneity impacts both the initial location of charge carrier generation and how they move throughout the system at femtosecond time scales and atomic spatial scales. The result of this inhomogeneity is shown schematically in **Figure 10.5a.** Even in a clean plasmonic nanoparticle, charge carriers form at higher rates near the nanoparticle surface due to high surface electric fields. Surface-induced decay processes such as geometry-induced intraband transitions further augment the rates of surface excitations. Finally, introducing non-plasmonic materials further

shifts charge carrier formation near the nanoparticle surface. Properly capturing these behavior necessitates the development of ab-initio, time-dependent models that incorporate the plasmonic component, the non-plasmonic component, and their interface.

Quantum effects arising from extremely small nanoparticles or chemisorption of molecules/semiconductors onto metal surfaces also play a critical role in the rates and location of charge carrier formation.[49,50] For example, Kale et al. attribute direct excitation of molecules adsorbed onto Pt nanoparticles to the large surface area to volume ratios present in their sub-5-nanometer particles.[51] Additionally, it is well known in the heterogeneous catalysis community that chemisorption of molecules onto metals can form hybrid metal-adsorbate states at the interface.[23] Transitions between hybridized states located at the metal-adsorbate interface can also act as reservoirs for charge transfer.[52] In the context of this dissertation, the formation of interfacial states between metals and molecules/semiconductors can introduce direct, momentum-conserved transitions at the interface. We hypothesize that these interfacial states can additionally be excited by LSPR (**Figure 10.5b**). Recent studies from our group looking at charge transfer in metal-molecule systems support this hypothesis.[22,53] The community has also recognized the importance of interfacial states, as demonstrated by several recent studies.[54–62] To this end, our community desperately needs experimental and theoretical methods to address the interplay between quantum and classical effects. From the theory perspective, hybrid models that can predict the formation of interfacial states (which are quantum in nature) in multicomponent systems are necessary. These models will allow the prediction of hybrid plasmonic materials that can localize excitations to hybridized states of specific energy, which would have significant implications in photocatalysis.[2,3,24] Experimentally, ultrafast measurements at plasmonic-nonplasmonic interfaces that monitor charge transfer in real-time and synthesis/fabrication techniques that allow the nanoscale control of how multicomponent materials interact (**Figure 10.5c**) are

necessary. Despite these hurdles, the plasmonics community consistently demonstrates the utility of hybrid plasmonic nanomaterials in various technologies, and the field is extremely promising.[24,28,63–67]

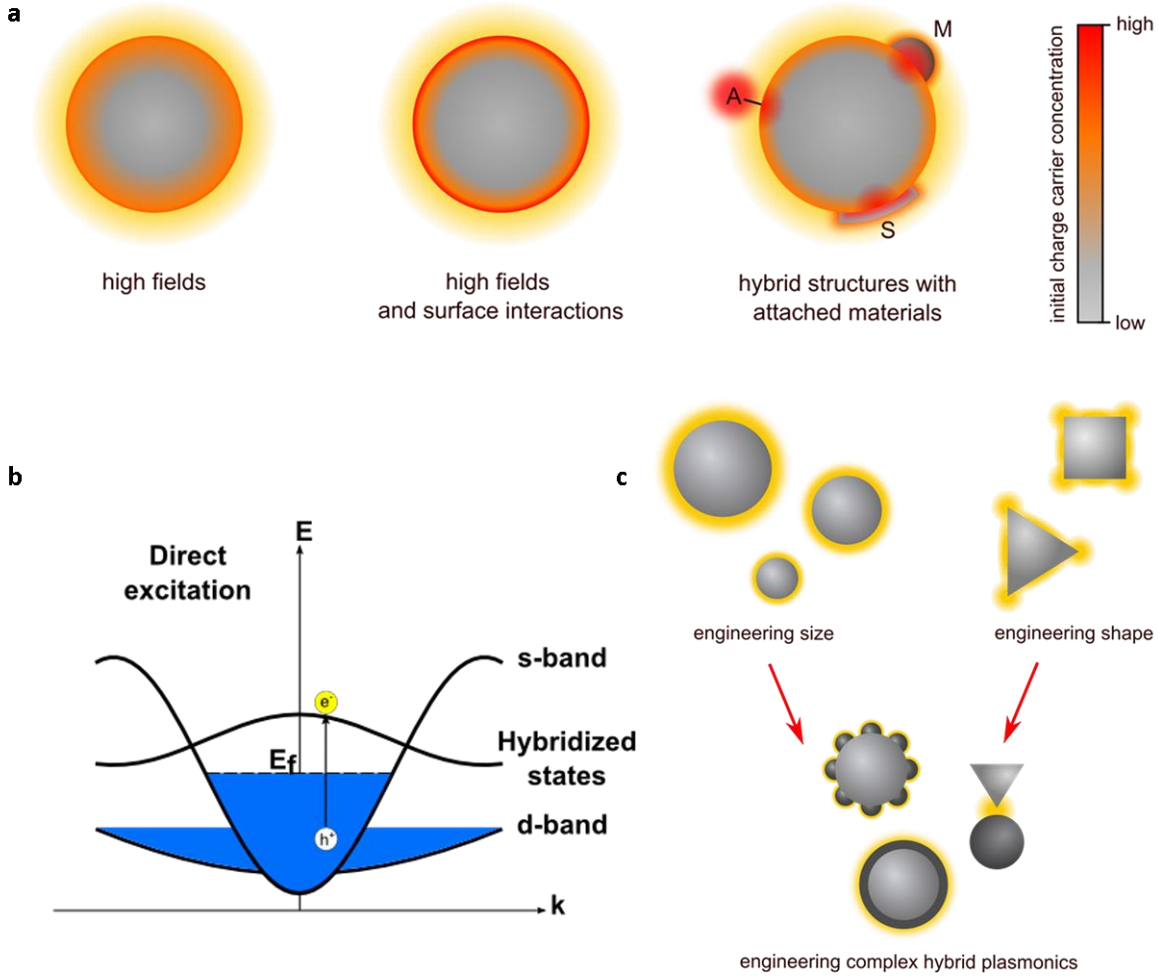

Figure 10.5 Engineering energy and charge flow in hybrid plasmonic systems. a) Illustration of the factors that impact the location-specific initial rates of charge carrier formation due to LSPR decay. The rates are impacted by: high surface fields (left), the rate at which the plasmon collides with the surface—which is higher for small particles (middle), and the presence of non-plasmonic materials at the surface (or interfacial states at the plasmonic/non-plasmonic interface) that allow for the direct electronic excitations (right). Non-plasmonic materials could be a molecule (A), a metal nanoparticle (M), and/or a semiconductor (S). **b)** A band structure representation of the direct energy transfer mechanism. The adsorption of molecules on the metal surface creates new metal–molecule states at the interface that allow for direct, momentum-conserved electronic excitations between the metal and these new states. **c)** Schematic of various geometries and configurations of hybrid plasmonic nanostructures. Material science advances in the synthesis of uniform and stable nanostructures, with precise control over size, shape, and complexity in composition, are needed to explore these materials' potential further. Adapted from Refs. [24,28]

10.3.2 Polariton-Driven Solar Energy Conversion

This dissertation demonstrated enhanced light absorption and charge transport in molecules strongly coupled to photonic/plasmonic structures. These demonstrations follow several others reporting similar phenomena in organic semiconductors and other systems.[42,44–47,68] We explain the enhanced light absorption due to the presence of high electric fields and the broadening of the absorption spectrum under strong coupling conditions, but the enhanced charge transport is less straightforward. Ebbesen et al. attribute the increased charge carrier mobility in semiconductors to the delocalization of the semiconductor wavefunction in the strong coupling regime.[44] This wavefunction delocalization is a signature of strongly coupled systems resulting from quantum entanglement.[29,69] One key feature of these delocalized/entangled states is their coherent behavior.[29,70] While researchers have probed the effect of coherence on optical properties of strongly coupled systems, such as their emission[71,72], they have not explored the effects of coherence on parameters relevant to solar energy conversion.

One field where coherence plays a significant role is in natural photosynthesis.[73,74] Specifically, coherence plays a major factor in the >90% energy transfer efficiency from the light absorbing aggregates to catalytic reaction centers in plants and algae.[75,76] These discoveries have inspired great efforts into mimicking the coherent energy transfer in photosynthesis to enable high-efficiency chemical conversion systems.[73,74,77–80] Unfortunately, this literature is confined to the realms of inorganic and physical chemistry, which know little to nothing about quantum electrodynamics. In this context, exploiting strong light-matter coupling to induce coherence in molecular systems could potentially open avenues for engineering the next generation of polariton-driven solar energy conversion technologies.

10.4 References

(1) Linic, S.; Christopher, P.; Ingram, D. B. Plasmonic-Metal Nanostructures for Efficient Conversion of Solar to Chemical Energy. *Nat. Mater.* **2011**, *10*, 911–921.

(2) Linic, S.; Aslam, U.; Boerigter, C.; Morabito, M. Photochemical Transformations on Plasmonic Metal Nanoparticles. *Nat. Mater.* **2015**, *14*, 567–576.

(3) Kale, M. J.; Avanesian, T.; Christopher, P. Direct Photocatalysis by Plasmonic Nanostructures. *ACS Catal.* **2014**, *4*, 116–128.

(4) Zheng, Z.; Tachikawa, T.; Majima, T. Single-Particle Study of Pt-Modified Au Nanorods for Plasmon-Enhanced Hydrogen Generation in Visible to Near-Infrared Region. *J. Am. Chem. Soc.* **2014**, *136*, 6870–6873.

(5) Zheng, Z.; Tachikawa, T.; Majima, T. Plasmon-Enhanced Formic Acid Dehydrogenation Using Anisotropic Pd–Au Nanorods Studied at the Single-Particle Level. *J. Am. Chem. Soc.* **2015**, *137*, 948–957.

(6) Swearer, D. F.; Zhao, H.; Zhou, L.; Zhang, C.; Robatjazi, H.; Martirez, J. M. P.; Krauter, C. M.; Yazdi, S.; McClain, M. J.; Ringe, E.; *et al.* Heterometallic Antenna−reactor Complexes for Photocatalysis. *Proc. Natl. Acad. Sci.* **2016**, 201609769.

(7) Zhang, C.; Zhao, H.; Zhou, L.; Schlather, A. E.; Dong, L.; McClain, M. J.; Swearer, D. F.; Nordlander, P.; Halas, N. J. Al–Pd Nanodisk Heterodimers as Antenna–Reactor Photocatalysts. *Nano Lett.* **2016**, acs.nanolett.6b03582.

(8) Xiao, Q.; Sarina, S.; Bo, A.; Jia, J.; Liu, H.; Arnold, D. P.; Huang, Y.; Wu, H.; Zhu, H. Visible Light-Driven Cross-Coupling Reactions at Lower Temperatures Using a Photocatalyst of Palladium and Gold Alloy Nanoparticles. *ACS Catal.* **2014**, *4*, 1725–1734.

(9) Xiao, Q.; Sarina, S.; Waclawik, E. R.; Jia, J.; Chang, J.; Riches, J. D.; Wu, H.; Zheng, Z.; Zhu, H. Alloying Gold with Copper Makes for a Highly Selective Visible-Light Photocatalyst for the Reduction of Nitroaromatics to Anilines. *ACS Catal.* **2016**, *6*, 1744–1753.

(10) Khurgin, J. B. How to Deal with the Loss in Plasmonics and Metamaterials. *Nat. Nanotechnol.* **2015**, *10*, 2–6.

(11) Brongersma, M. L.; Halas, N. J.; Nordlander, P. Plasmon-Induced Hot Carrier Science and Technology. *Nat. Nanotechnol.* **2015**, *10*, 25–34.

(12) Al-Kuhaili, M. F.; Saleem, M.; Durrani, S. M. A. Optical Properties of Iron Oxide (α-Fe2O3) Thin Films Deposited by the Reactive Evaporation of Iron. *J. Alloys Compd.* **2012**, *521*, 178–182.

(13) Cortés, E.; Xie, W.; Cambiasso, J.; Jermyn, A. S.; Sundararaman, R.; Narang, P.;

Schlücker, S.; Maier, S. A. Plasmonic Hot Electron Transport Drives Nano-Localized Chemistry. *Nat. Commun.* **2017**, *8*.

(14) Christopher, P.; Xin, H.; Linic, S. Visible-Light-Enhanced Catalytic Oxidation Reactions on Plasmonic Silver Nanostructures. *Nat. Chem.* **2011**, *3*, 467.

(15) Mukherjee, S.; Libisch, F.; Large, N.; Neumann, O.; Brown, L. V; Cheng, J.; Lassiter, J. B.; Carter, E. A.; Nordlander, P.; Halas, N. J. Hot Electrons Do the Impossible: Plasmon-Induced Dissociation of H2 on Au. *Nano Lett.* **2013**, *13*, 240–247.

(16) Christopher, P.; Xin, H.; Marimuthu, A.; Linic, S. Singular Characteristics and Unique Chemical Bond Activation Mechanisms of Photocatalytic Reactions on Plasmonic Nanostructures. *Nat. Mater.* **2012**, *11*, 1044.

(17) Seemala, B.; Therrien, A. J.; Lou, M.; Li, K.; Finzel, J. P.; Qi, J.; Nordlander, P.; Christopher, P. Plasmon-Mediated Catalytic O $_2$ Dissociation on Ag Nanostructures: Hot Electrons or Near Fields? *ACS Energy Lett.* **2019**, *4*, 1803–1809.

(18) Kim, Y.; Smith, J. G.; Jain, P. K. Harvesting Multiple Electron–Hole Pairs Generated through Plasmonic Excitation of Au Nanoparticles. *Nat. Chem.* **2018**.

(19) Giubileo, F.; Di Bartolomeo, A. The Role of Contact Resistance in Graphene Field-Effect Devices. *Prog. Surf. Sci.* **2017**, *92*, 143–175.

(20) Zhang, X.; Chen, Y. L.; Liu, R.-S.; Tsai, D. P. Plasmonic Photocatalysis. *Reports Prog. Phys.* **2013**, *76*, 046401.

(21) Aslam, U.; Chavez, S.; Linic, S. Controlling Energy Flow in Multimetallic Nanostructures for Plasmonic Catalysis. *Nat. Nanotechnol.* **2017**, *12*, 1000–1005.

(22) Boerigter, C.; Aslam, U.; Linic, S. Mechanism of Charge Transfer from Plasmonic Nanostructures to Chemically Attached Materials. *ACS Nano* **2016**, *10*, 6108–6115.

(23) Hammer, B.; Norskov, J. K. Why Gold Is the Noblest of All the Metals. *Nature* **1995**, *376*, 238–240.

(24) Aslam, U.; Rao, V. G.; Chavez, S.; Linic, S. Catalytic Conversion of Solar to Chemical Energy on Plasmonic Metal Nanostructures. *Nat. Catal.* **2018**, *1*, 656–665.

(25) Engelbrekt, C.; Crampton, K. T.; Fishman, D. A.; Law, M.; Apkarian, V. A. Efficient Plasmon-Mediated Energy Funneling to the Surface of Au@Pt Core–Shell Nanocrystals. *ACS Nano* **2020**, acsnano.0c01653.

(26) Chavez, S.; Rao, V. G.; Linic, S. Unearthing the Factors Governing Site Specific Rates of Electronic Excitations in Multicomponent Plasmonic Systems and Catalysts. *Faraday Discuss.* **2019**.

(27) Li, J.; Cushing, S. K.; Meng, F.; Senty, T. R.; Bristow, A. D.; Wu, N. Plasmon-Induced

Resonance Energy Transfer for Solar Energy Conversion. *Nat. Photonics* **2015**, *9*, 601–607.

(28) Linic, S.; Chavez, S.; Elias, R. Flow and Extraction of Energy and Charge Carriers in Hybrid Plasmonic Nanostructures. *Nat. Mater.* **2021**, 1–9.

(29) Ebbesen, T. W. Hybrid Light-Matter States in a Molecular and Material Science Perspective. *Acc. Chem. Res.* **2016**, *49*, 2403–2412.

(30) Vasa, P.; Lienau, C. Strong Light-Matter Interaction in Quantum Emitter/Metal Hybrid Nanostructures. *ACS Photonics* **2018**, *5*, 2–23.

(31) Skolnick, M. S.; Fisher, T. A.; Whittaker, D. M. Strong Coupling Phenomena in Quantum Microcavity Structures. *Semiconductor Science and Technology*, **1998**, *13*, 645–669.

(32) Raimond, J. M.; Brune, M.; Haroche, S. Manipulating Quantum Entanglement with Atoms and Photons in a Cavity. *Rev. Mod. Phys.* **2001**, *73*, 565–582.

(33) Baranov, D. G.; Wersä, M.; Cuadra, J.; Antosiewicz, T. J.; Shegai, T. Novel Nanostructures and Materials for Strong Light−Matter Interactions. *ACS Photonics* **2018**, *5*, 24–42.

(34) Hertzog, M.; Wang, M.; Rgen Mony, J.; Bö, K. Strong Light-Matter Interactions: A New Direction within Chemistry. *Chem. Soc. Rev.* **2019**, *48*, 937–961.

(35) Garcia-Vidal, F. J.; Ciuti, C.; Ebbesen, T. W. Manipulating Matter by Strong Coupling to Vacuum Fields. *Science (80-.).* **2021**, *373*, eabd0336.

(36) Bosman, S. J.; Gely, M. F.; Singh, V.; Bruno, A.; Bothner, D.; Steele, G. A. Multi-Mode Ultra-Strong Coupling in Circuit Quantum Electrodynamics. *npj Quantum Inf. 2017 31* **2017**, *3*, 1–6.

(37) Qin, W.; Miranowicz, A.; Li, P. B.; Lü, X. Y.; You, J. Q.; Nori, F. Exponentially Enhanced Light-Matter Interaction, Cooperativities, and Steady-State Entanglement Using Parametric Amplification. *Phys. Rev. Lett.* **2018**, *120*, 093601.

(38) Thomas, A.; Lethuillier-Karl, L.; Nagarajan, K.; Vergauwe, R. M. A.; George, J.; Chervy, T.; Shalabney, A.; Devaux, E.; Genet, C.; Moran, J.; *et al.* Tilting a Ground-State Reactivity Landscape by Vibrational Strong Coupling. *Science* **2019**, *363*, 615–619.

(39) Hutchison, J. A.; Schwartz, T.; Genet, C.; Devaux, E.; Ebbesen, T. W. Modifying Chemical Landscapes by Coupling to Vacuum Fields. *Angew. Chemie - Int. Ed.* **2012**, *51*, 1592–1596.

(40) Munkhbat, B.; Wersäll, M.; Baranov, D. G.; Antosiewicz, T. J.; Shegai, T. Suppression of Photo-Oxidation of Organic Chromophores by Strong Coupling to Plasmonic Nanoantennas. *Sci. Adv.* **2018**, *4*, eaas9552.

(41) Flick, J.; Rivera, N.; Narang, P. Strong Light-Matter Coupling in Quantum Chemistry and Quantum Photonics. *Nanophotonics*, **2018**, *7*, 1479–1501.

(42) Shi, X.; Ueno, K.; Oshikiri, T.; Sun, Q.; Sasaki, K.; Misawa, H. Enhanced Water Splitting under Modal Strong Coupling Conditions. *Nat. Nanotechnol.* **2018**, 1.

(43) Gómez, D. E.; Shi, X.; Oshikiri, T.; Roberts, A.; Misawa, H. Near-Perfect Absorption of Light by Coherent Plasmon–Exciton States. *Nano Lett.* **2021**, *21*, 3864–3870.

(44) Orgiu, E.; George, J.; Hutchison, J. A.; Devaux, E.; Dayen, J. F.; Doudin, B.; Stellacci, F.; Genet, C.; Schachenmayer, J.; Genes, C.; *et al.* Conductivity in Organic Semiconductors Hybridized with the Vacuum Field. *Nat. Mater.* **2015**, *14*, 1123–1130.

(45) Nagarajan, K.; George, J.; Thomas, A.; Devaux, E.; Chervy, T.; Azzini, S.; Aziz, J.; Hosseini, M. W.; Kumar, A.; Genet, C.; *et al.* Conductivity and Photoconductivity of a P-Type Organic Semiconductor under Ultra-Strong Coupling. *ACS Nano* **2020**, *14*, 10219–10225.

(46) Bhatt, P.; Kaur, K.; George, J. Enhanced Charge Transport in Two-Dimensional Materials through Light-Matter Strong Coupling. *ACS Nano* **2021**, *15*, 13616–13622.

(47) Nikolis, V. C.; Mischok, A.; Siegmund, B.; Kublitski, J.; Jia, X.; Benduhn, J.; Hörmann, U.; Neher, D.; Gather, M. C.; Spoltore, D.; *et al.* Strong Light-Matter Coupling for Reduced Photon Energy Losses in Organic Photovoltaics. *Nat. Commun. 2019 101* **2019**, *10*, 1–8.

(48) Bujalance, C.; Esteso, V.; Caliò, L.; Lavarda, G.; Torres, T.; Feist, J.; García-Vidal, F. J.; Bottari, G.; Míguez, H. Ultrastrong Exciton–Photon Coupling in Broadband Solar Absorbers. *J. Phys. Chem. Lett.* **2021**, *12*, 10706–10712.

(49) Khurgin, J. B.; Levy, U. Generating Hot Carriers in Plasmonic Nanoparticles: When Quantization Does and Does Not Matter? **2019**.

(50) Yan, J.; Jacobsen, K. W.; Thygesen, K. S. First-Principles Study of Surface Plasmons on Ag(111) and H/Ag(111). *Phys. Rev. B - Condens. Matter Mater. Phys.* **2011**, *84*, 235430.

(51) Kale, M. J.; Avanesian, T.; Xin, H.; Yan, J.; Christopher, P. Controlling Catalytic Selectivity on Metal Nanoparticles by Direct Photoexcitation of Adsorbate–Metal Bonds. *Nano Lett.* **2014**, *14*, 5405–5412.

(52) Lindstrom, C. D.; Zhu, X.-Y. Photoinduced Electron Transfer at Molecule−Metal Interfaces. *Chem. Rev.* **2006**, *106*, 4281–4300.

(53) Boerigter, C.; Campana, R.; Morabito, M.; Linic, S. Evidence and Implications of Direct Charge Excitation as the Dominant Mechanism in Plasmon-Mediated Photocatalysis. *Nat. Commun.* **2016**, *7*.

(54) Foerster, B.; Spata, V. A.; Carter, E. A.; Sönnichsen, C.; Link, S. Plasmon Damping

Depends on the Chemical Nature of the Nanoparticle Interface. *Sci. Adv.* **2019**, *5*.

(55) Lee, S. A.; Link, S. Chemical Interface Damping of Surface Plasmon Resonances. *Acc. Chem. Res.* **2021**, *21*, acs.accounts.0c00872.

(56) Foerster, B.; Hartelt, M.; Collins, S. S. E.; Aeschlimann, M.; Link, S.; Sönnichsen, C. Interfacial States Cause Equal Decay of Plasmons and Hot Electrons at Gold–Metal Oxide Interfaces. *Nano Lett.* **2020**, acs.nanolett.0c00223.

(57) Therrien, A. J.; Kale, M. J.; Yuan, L.; Zhang, C.; Halas, N. J.; Christopher, P. Impact of Chemical Interface Damping on Surface Plasmon Dephasing. *Faraday Discuss.* **2019**, *214*, 59–72.

(58) Tan, S.; Argondizzo, A.; Ren, J.; Liu, L.; Zhao, J.; Petek, H. Plasmonic Coupling at a Metal/Semiconductor Interface. *Nat. Photonics* **2017**, *11*, 806–812.

(59) Dą, M.; Dai, Y.; Petek, H. Ultrafast Photoemission Electron Microscopy: Imaging Plasmons in Space and Time. **2020**.

(60) Liu, Y.; Chen, Q.; Cullen, D. A.; Xie, Z.; Lian, T. Efficient Hot Electron Transfer from Small Au Nanoparticles. *Nano Lett* **2020**, *20*, 24.

(61) Wu, K.; Chen, J.; McBride, J. R.; Lian, T. Efficient Hot-Electron Transfer by a Plasmon-Induced Interfacial Charge-Transfer Transition. *Science* **2015**, *349*, 632–635.

(62) Khurgin, J. B.; Petrov, A.; Eich, M.; Uskov, A. V. Direct Plasmonic Excitation of the Hybridized Surface States in Metal Nanoparticles. *ACS Photonics* **2021**, acsphotonics.1c00167.

(63) Lopez-Sanchez, O.; Lembke, D.; Kayci, M.; Radenovic, A.; Kis, A. Ultrasensitive Photodetectors Based on Monolayer MoS2. *Nat. Nanotechnol. 2013 87* **2013**, *8*, 497–501.

(64) Atwater, H. a; Polman, A. Plasmonics for Improved Photovoltaic Devices. *Nat. Mater.* **2010**, *9*, 205–213.

(65) Li, Y.; DiStefano, J. G.; Murthy, A. A.; Cain, J. D.; Hanson, E. D.; Li, Q.; Castro, F. C.; Chen, X.; Dravid, V. P. Superior Plasmonic Photodetectors Based on Au@MoS_2 Core–Shell Heterostructures. *ACS Nano* **2017**, *11*, 10321–10329.

(66) An, X.; Stelter, D.; Keyes, T.; Reinhard, B. M. Plasmonic Photocatalysis of Urea Oxidation and Visible-Light Fuel Cells. *Chem* **2019**, *5*, 2228–2242.

(67) Corte, E.; Besteiro, L. V; Alabastri, A.; Baldi, A.; Tagliabue, G.; Demetriadou, A.; Narang, P. Challenges in Plasmonic Catalysis. *ACS Nano* **2021**, *18*, 22.

(68) Gómez, D. E.; Shi, X.; Oshikiri, T.; Roberts, A.; Misawa, H. Near-Perfect Absorption of Light by Coherent Plasmon–Exciton States. *Nano Lett.* **2021**, acs.nanolett.1c00389.

(69) Kfir, O. Entanglements of Electrons and Cavity Photons in the Strong-Coupling Regime. *Phys. Rev. Lett.* **2019**, *123*, 103602.

(70) Scholes, G. D. Emergence of Collective Coherent States from Strong-Light Coupling of Disordered Systems. *J. Phys. Chem. A* **2021**, *125*, 6750.

(71) Aberra Guebrou, S.; Symonds, C.; Homeyer, E.; Plenet, J. C.; Gartstein, Y. N.; Agranovich, V. M.; Bellessa, J. Coherent Emission from a Disordered Organic Semiconductor Induced by Strong Coupling with Surface Plasmons. *Phys. Rev. Lett.* **2012**, *108*, 066401.

(72) Shi, L.; Hakala, T. K.; Rekola, H. T.; Martikainen, J.-P.; Moerland, R. J.; Törmä, P. Spatial Coherence Properties of Organic Molecules Coupled to Plasmonic Surface Lattice Resonances in the Weak and Strong Coupling Regimes. *Phys. Rev. Lett.* **2014**, *112*, 153002.

(73) Scholes, G. D.; Fassioli, F.; Dinshaw, R.; Arpin, P. C. Photosynthetic Light Harvesting: Excitons and Coherence. *J. R. Soc. Interface* **2013**, *11*.

(74) Scholes, G. D.; Fleming, G. R.; Olaya-Castro, A.; van Grondelle, R. Lessons from Nature about Solar Light Harvesting. *Nat. Chem.* **2011**, *3*, 763–774.

(75) Engel, G. S.; Calhoun, T. R.; Read, E. L.; Ahn, T. K.; Mančal, T.; Cheng, Y. C.; Blankenship, R. E.; Fleming, G. R. Evidence for Wavelike Energy Transfer through Quantum Coherence in Photosynthetic Systems. *Nature* **2007**, *446*, 782–786.

(76) Collini, E.; Wong, C. Y.; Wilk, K. E.; Curmi, P. M. G.; Brumer, P.; Scholes, G. D. Coherently Wired Light-Harvesting in Photosynthetic Marine Algae at Ambient Temperature. *Nat. 2010 4637281* **2010**, *463*, 644–647.

(77) Brédas, J. L.; Sargent, E. H.; Scholes, G. D. Photovoltaic Concepts Inspired by Coherence Effects in Photosynthetic Systems. *Nature Materials*, **2016**, *16*, 35–44.

(78) Scholes, G. D. Coherence from Light Harvesting to Chemistry. *Journal of Physical Chemistry Letters*, 2018, *9*, 1568–1572.

(79) Scholes, G. D.; Fleming, G.; chen, L. X.; aspuru-Guzik, alán; Buchleitner, andreas; coker, D. F.; Engel, G. S.; van Grondelle, rienk; ishizaki, akihito; Jonas, D. M.; *et al.* Using Coherence to Enhance Function in Chemical and Biophysical Systems. **2017**.

(80) Proppe, A. H.; Li, Y. C.; Aspuru-Guzik, A.; Berlinguette, C. P.; Chang, C. J.; Cogdell, R.; Doyle, A. G.; Flick, J.; Gabor, N. M.; van Grondelle, R.; *et al.* Bioinspiration in Light Harvesting and Catalysis. *Nat. Rev. Mater.* **2020**, *5*, 828–846.